NanoScience and Technology

Anatolie Sidorenko *Editor*

# Functional Nanostructures and Metamaterials for Superconducting Spintronics

## From Superconducting Qubits to Self-Organized Nanostructures

Springer

# NanoScience and Technology

The series NanoScience and Technology is focused on the fascinating nano-world, mesoscopic physics, analysis with atomic resolution, nano and quantum-effect devices, nanomechanics and atomic-scale processes. All the basic aspects and technology-oriented developments in this emerging discipline are covered by comprehensive and timely books. The series constitutes a survey of the relevant special topics, which are presented by leading experts in the field. These books will appeal to researchers, engineers, and advanced students.

More information about this series at http://www.springer.com/series/3705

Anatolie Sidorenko
Editor

# Functional Nanostructures and Metamaterials for Superconducting Spintronics

## From Superconducting Qubits to Self-Organized Nanostructures

Springer

*Editor*
Anatolie Sidorenko
Institute of Electronic Engineering
and Nanotechnologies
Academy of Sciences of Moldova
Chisinau
Moldova

ISSN 1434-4904 ISSN 2197-7127 (electronic)
NanoScience and Technology
ISBN 978-3-319-90480-1 ISBN 978-3-319-90481-8 (eBook)
https://doi.org/10.1007/978-3-319-90481-8

Library of Congress Control Number: 2018939141



Printed on acid-free paper

This Springer imprint is published by the registered company Springer International Publishing AG
part of Springer Nature
The registered company address is: Gewerbestrasse 11, 6330 Cham, Switzerland

# Foreword

Last two decades techniques of preparation and materials processing at the nanometer scale have been developed rapidly and led to invention of novel principles for a new generation of devices and sensors: quantum detectors, qubits, pi- and fi-junctions, spin-valves, single-molecule electronic devices, SAW-sensors, smart gas sensors "artificial nose" and other interesting and useful applications of Nanoscience and Nanotechnologies. On the other hand, huge progress in the theoretical investigation of the matter peculiarities at the nanoscale led to understanding of the intrinsic properties, to prediction and description of possible novel phenomena in nano-objects and nanostructures. There exist a correlated process of mutual stimulation of experiment, technology and theory: from one side, the progress in nanotechnologies and in measurement techniques opens to experimentalists new horizon of investigation of properties of the matter at nanoscale and detection of novel phenomena. From the other side, the intensive theoretical investigations give possibilities to predict the appearance of a novel effects, even more—to calculate a special functional nanostructures and nanomaterials. This two processes, two big streams, take place in Nanoscience simultaneously, giving rapid development of this area of human activity. The novel ideas, approaches, predicted and detected effects and phenomena, are presented in various reports at conferences and their proceedings, in scientific reports of the projects and programs, in articles of scientific journals and patents, but are still not included in the textbooks of university courses and manuals.

The main goal of the present book, prepared and edited by Prof. Anatolie Sidorenko, Director of the Institute of Electronic Engineering and Nanotechnologies, consists in the attempt to fill the gap between the textbook and the ocean of scientific publications and to present the result of such dramatic competition and mutual stimulation of the theory and experiment at nanometer scale. *Molecular electronics, superconducting spintronics and qubits, quantum-coherent devices for quantum computing* are the modern and rapid developing ranges of activity. They include numerous coherent effects induced in normal and ferromagnetic metals by contact with nearby superconductors: electron, spin and heat transfer due to Andreev reflection processes, as well as anomalous

properties of the Josephson current via ferromagnetic metals, leading to the development of novel sensors and switching elements.

All these topics are strongly interrelated with respect to fundamental aspects and fabrication technologies. They address key topics in very active research fields along the borderline between nanoscience, nanotechnology, super-conductivity, and magnetism. The related phenomena are highly promising for application in novel functional devices, computer logics, sensing and detection of low concentrated chemicals, weak and extremely weak magnetic and microwave fields, infrared and ultraviolet radiation.

I think that this book will be very useful for graduate and post-graduate students, engineers and researchers, who would like to gain knowledge about novel effects at nanoscale and their possible applications.

Karlsruhe, Germany Horst Hahn
June 2018

# Preface

The idea of writing this book arose as a result of communication with students and doctorants: I realized that there exists a clear visible gap between the university text books and a huge amount of special literature on nanoscience and superconductivity at nanometer scale. In my lectures for students, I tried to "fill" this gap by giving examples of the rapid development of superconductivity at nanoscale, newly discovered phenomena, and their applications in new devices and sensors.

Recently, a number of very interesting effects in layered nanostructures have been predicted theoretically and then detected experimentally; among these effects, triplet superconductivity, spin-valve effect, crossed Andreev reflection, pi-shift, and Josephson fi-junctions are especially intriguing. After the detection of those phenomena, researchers developed a fabrication technology for functional nanostructures operating as novel electronic devices and circuits: superconducting spin-valves, full switching memory element MRAM, and superconducting Q-bit for ultra rapid computers of the twenty-first century. To highlight some of the raised issues, well-known experts were invited to write chapters for this book.

We believe that the book can attract attention of researchers, engineers, Ph.D. students, and all other people who would like to gain knowledge about novel effects at nanoscale.

Chisinau, Moldova
June 2018

Anatolie Sidorenko

# Contents

**Basic Superconducting Spin Valves** . . . . . 1
V. N. Kushnir, Anatolie Sidorenko, L. R. Tagirov and M. Yu. Kupriyanov
1 Introduction . . . . . 2
2 Superconductor–Metallic Ferromagnet Proximity Effect . . . . . 4
3 Elementary Superconducting Spin Valve: Diffusive Limit . . . . . 6
4 Elementary Spin Valve with Strong Ferromagnets . . . . . 10
4.1 Normal and Inverse Spin Valve Effects in the Elementary Structures . . . . . 10
4.2 Superconducting Spin Valve Effect and the Domain Structures of Ferromagnets . . . . . 11
4.3 Theory of Spin Valve in the Clean Limit . . . . . 14
4.4 Parametric Spin Valve . . . . . 15
5 Superconducting Spin Valve Effect in the S/F1/N/F2 Structures . . . . . 19
6 Discussion and Conclusion . . . . . 22
References . . . . . 24

**Superconducting Triplet Proximity and Josephson Spin Valves** . . . . . 31
L. R. Tagirov, M. Yu. Kupriyanov, V. N. Kushnir
and Anatolie Sidorenko
1 Introduction . . . . . 32
2 Superconductor–Ferromagnet Proximity Spin Valves . . . . . 33
3 Superconducting Spin-Valve Effect in the S/F1/N/F2 Structures . . . . . 35
4 Josephson Spin Valves with Ferromagnetic Weak Links . . . . . 40
References . . . . . 44

**Compact Josephson $\varphi$-Junctions** . . . . . 49
S. V. Bakurskiy, N. V. Klenov, I. I. Soloviev, Anatolie Sidorenko,
M. Yu. Kupriyanov and A. A. Golubov
1 Introduction . . . . . 50
2 Model . . . . . 52

3 Ramp- and Overlap-Type Geometries . . . . . 55
4 Discussion and Conclusion . . . . . 67
References . . . . . 69

**Magnetic Proximity Effect and Superconducting Triplet Correlations at the Heterostructure of Cuprate Superconductor and Oxide Spin Valve** . . . . . 73
K. Y. Constantinian, G. A. Ovsyannikov, V. V. Demidov and Yu. N. Khaydukov
1 Introduction . . . . . 74
2 Experimental . . . . . 75
3 Magnetic Proximity Effect . . . . . 77
4 Superconducting Triplet Correlations . . . . . 82
5 Conclusion . . . . . 87
References . . . . . 88

**Nanodevices with Normal Metal—Insulator—Superconductor Tunnel Junctions** . . . . . 91
M. Tarasov and V. Edelman
1 Introduction: The NIS Junction at a Glance . . . . . 92
2 Fabrication Technology . . . . . 93
3 Terahertz Band Conventional SINIS Bolometer . . . . . 95
4 Mechanisms of Energy Relaxation and Time Scale . . . . . 100
5 Electron Cooling of Absorber and Overheating of Superconductor . . . . . 105
6 NIS Thermometer . . . . . 107
7 Andreev Current and Hot Electron Traps . . . . . 109
8 Current Response, Quantum Efficiency, and Thermalization . . . . . 113
9 Conclusion . . . . . 114
References . . . . . 115

**Multichroic Polarization Sensitive Planar Antennas with Resonant Cold-Electron Bolometers for Cosmology Experiments** . . . . . 117
L. S. Kuzmin and A. V. Chiginev
1 Introduction. ESA Requirements . . . . . 117
2 Seashell Antenna . . . . . 118
3 Cross-Slot Antenna . . . . . 121
4 Comparison and Discussion . . . . . 125
References . . . . . 126

**Passive Millimeter-Wave Imaging Technology for Concealed Contraband Detection** . . . . . 129
Jing-Hui Qiu, Jiaran Qi, Nan-nan Wang and Aleksandr Denisov
1 Introduction . . . . . 129

2 Theory of Passive Millimeter-Wave Imaging . . . . . 130
2.1 Planck's Radiation Law–Blackbody Radiation Detection Theory . . . . . 131
2.2 Radiation Temperature Transfer Model of the Passive Millimeter-Wave Near-Field Imaging . . . . . 134
3 Millimeter-Wave Radiometer . . . . . 135
3.1 Key Technical Parameters of Millimeter-Wave Radiometer . . . . . 135
3.2 Millimeter-Wave Direct Detection Radiometer . . . . . 137
3.3 Calibration Method for the Radiometer Array Adopted in the Passive Millimeter-Wave Imaging System . . . . . 139
4 Passive Millimeter-Wave Near-Field Imaging Feed Antenna . . . . . 141
5 Quasi-optical Theory and Focusing Antenna for Passive Millimeter-Wave Near-Field Imaging . . . . . 146
5.1 Quasi-optics Design Method . . . . . 146
5.2 The Design of the Optical System Parameters . . . . . 148
5.3 Design of Lens Curvature . . . . . 149
6 Passive Millimeter-Wave Near-Filed Imaging System . . . . . 152
6.1 20-Channel FPA System for Hidden Object Detection Under Human Clothing . . . . . 153
6.2 High Spatial Resolution 70-Channel FPA System for Concealed Object Detection Under Human Clothing . . . . . 154
References . . . . . 158

**Coupled Spin and Heat Transport in Superconductor Hybrid Structures** . . . . . 161
Detlef Beckmann
1 Introduction . . . . . 161
2 Nonlocal Spin Transport . . . . . 162
3 Spin-Dependent Thermoelectric Effects . . . . . 164
4 Possible Applications . . . . . 168
4.1 Thermometry . . . . . 168
4.2 Cooling . . . . . 170
5 Conclusion and Outlook . . . . . 172
References . . . . . 172

**Lasing in Circuit Quantum Electrodynamics** . . . . . 175
G. Oelsner and E. Il'ichev
1 Introduction . . . . . 175
2 Requirements for Lasing . . . . . 176
3 Circuit QED with Superconducting Quantum Systems . . . . . 178
4 Lasing by Single Superconducting Artificial Atoms . . . . . 182
4.1 Standard Lasing Scheme . . . . . 182
4.2 Dressed-State Lasing . . . . . 183
4.3 Landau–Zener–Stückelberg Lasing . . . . . 189

5 Summary and Conclusion . . . . . 192
References . . . . . 193

**Topology-Driven Effects in Advanced Micro- and Nanoarchitectures** . . . . . 195
V. M. Fomin
1 Introduction . . . . . 196
2 Topologic Effects in Quantum Rings by Virtue of Doubly Connectedness . . . . . 197
3 Topologic Effects in Möbius Rings . . . . . 200
4 Superconducting Vortices: Topological Defects in Micro- and Nanoarchitectures . . . . . 206
5 Topologic States of Light in Microcavities . . . . . 211
5.1 Resonant Modes of Light in a Möbius-Ring Resonator . . . . . 211
5.2 Optical Spin–Orbit Coupling and Non-Abelian Evolution of Light in Asymmetric Microcavities . . . . . 213
5.3 Non-Abelian Evolution of Light Polarization . . . . . 214
6 Conclusions . . . . . 217
References . . . . . 218

**Functional Magnetic Metamaterials for Spintronics** . . . . . 221
Yu. P. Sharaevsky, A. V. Sadovnikov, E. N. Beginin, A. Yu. Sharaevskaya, S. E. Sheshukova and S. A. Nikitov
1 Introduction . . . . . 222
2 Spin Waves in Width-Modulated Magnonic Crystal . . . . . 224
3 Defect Spin-Wave Modes Coupling in Magnonic Crystals . . . . . 228
4 Multimode Surface Magnetostatic Wave Propagation in Irregular Planar Magnonic Structure . . . . . 233
5 Transverse Mode Coupling in Confined Multiferroics . . . . . 239
6 Conclusion . . . . . 243
References . . . . . 244

**Quantum Transport, Superconductivity, and Weak Ferromagnetism at Bicrystal Interfaces of Bi and 3D Topological Insulator BiSb** . . . . . 247
Fiodor M. Muntyanu, Andrzej Gilewski, Andrzej J. Zaleski, Vitalie Chistol, Viorel Munteanu, Krzysztof Rogacki and Anatolie Sidorenko
1 Introduction . . . . . 248
2 Samples and Experimental Procedure . . . . . 250
3 Results and Discussion . . . . . 251
3.1 Fermi Surface Rearrangement in Bi and $Bi_{1-x}Sb_x$ ($x < 0.18$) Bicrystals . . . . . 251
3.2 High-Field Quantum Transport in Bi and BiSb Bicrystals . . . . . 254

3.3 Superconductivity and Weak Ferromagnetism at the Interface of Bicrystals of Bi and 3D Topological Insulator BiSb . . . . . 256
4 Conclusions . . . . . 262
References . . . . . 262

**Index** . . . . . 265

# Contributors

**S. V. Bakurskiy** Lomonosov Moscow State University, Skobeltsyn Institute of Nuclear Physics, Moscow, Russia; Moscow Institute of Physics and Technology, State University, Dolgoprudniy, Moscow region, Russia

**Detlef Beckmann** Institute of Nanotechnology, Karlsruhe Institute of Technology, Karlsruhe, Germany

**E. N. Beginin** Laboratory "Metamaterials", Saratov State University, Saratov, Russia; Kotel'nikov Institute of Radioengineering and Electronics, Russian Academy of Sciences, Moscow, Russia

**A. V. Chiginev** Institute for Physics of Microstructures, Russian Academy of Science (RAS), Nizhny Novgorod, Russian Federation; Nizhny Novgorod State Technical University n.a. R.E. Alekseev, Nizhny Novgorod, Russian Federation

**Vitalie Chistol** Technical University of Moldova, Chisinau, Moldova

**K. Y. Constantinian** Kotelnikov Institute of Radio Engineering and Electronics RAS, Moscow, Russia

**V. V. Demidov** Kotelnikov Institute of Radio Engineering and Electronics RAS, Moscow, Russia

**Aleksandr Denisov** Department of Microwave Engineering, School of Electronics and Information Engineering, Harbin Institute of Technology, Harbin, China

**V. Edelman** P.Kapitza Institute for Physical Problems, Russian Academy of Sciences, Moscow, Russia

**V. M. Fomin** Institute for Integrative Nanosciences (IIN), Leibniz Institute for Solid State and Materials Research (IFW) Dresden, Dresden, Germany

**Andrzej Gilewski** Magnet, Wroclaw, Poland

**A. A. Golubov** Lomonosov Moscow State University, Skobeltsyn Institute of Nuclear Physics, Moscow, Russia; Faculty of Science and Technology and MESA + Institute for Nanotechnology, University of Twente, Enschede, The Netherlands

**E. Il'ichev** Leibniz Institute of Photonic Technology, Jena, Germany; Novosibirsk State Technical University, Novosibirsk, Russia

**Yu. N. Khaydukov** Max-Planck Institute for Solid State Research, Stuttgart, Germany

**N. V. Klenov** Lomonosov Moscow State University, Skobeltsyn Institute of Nuclear Physics, Moscow, Russia; Moscow Institute of Physics and Technology, State University, Dolgoprudniy, Moscow region, Russia; Physics Faculty, Lomonosov Moscow State University, Moscow, Russia; N. L. Dukhov All-Russia Research Institute of Automatics, Moscow, Russia

**M. Yu. Kupriyanov** Kazan Federal University, Kazan, Russia; Skobeltsyn Institute of Nuclear Physics, Moscow State University, Moscow, Russia

**V. N. Kushnir** Physics Faculty, Belarus State University, Minsk, Belarus; Belarus State University of Informatics and Radioelectronics, Minsk, Belarus

**L. S. Kuzmin** Chalmers University of Technology, Gothenburg, Sweden; Nizhny Novgorod State Technical University n.a. R.E. Alekseev, Nizhny Novgorod, Russian Federation

**Viorel Munteanu** Institute of Electronic Engineering and Nanotechnologies, Academy of Sciences of Moldova, Chisinau, Moldova

**Fiodor M. Muntyanu** Institute of Electronic Engineering and Nanotechnologies, Academy of Sciences of Moldova, Chisinau, Moldova

**G. Oelsner** Leibniz Institute of Photonic Technology, Jena, Germany

**S. A. Nikitov** Laboratory "Metamaterials", Saratov State University, Saratov, Russia; Kotel'nikov Institute of Radioengineering and Electronics, Russian Academy of Sciences, Moscow, Russia

**G. A. Ovsyannikov** Kotelnikov Institute of Radio Engineering and Electronics RAS, Moscow, Russia

**Jiaran Qi** Department of Microwave Engineering, School of Electronics and Information Engineering, Harbin Institute of Technology, Harbin, China

**Jing-Hui Qiu** Department of Microwave Engineering, School of Electronics and Information Engineering, Harbin Institute of Technology, Harbin, China

**Krzysztof Rogacki** Institute of Low Temperatures and Structural Research, Polish Academy of Sciences, Wroclaw, Poland

**A. V. Sadovnikov** Laboratory "Metamaterials", Saratov State University, Saratov, Russia; Kotel'nikov Institute of Radioengineering and Electronics, Russian Academy of Sciences, Moscow, Russia

**A. Yu. Sharaevskaya** Laboratory "Metamaterials", Saratov State University, Saratov, Russia; Kotel'nikov Institute of Radioengineering and Electronics, Russian Academy of Sciences, Moscow, Russia

**Yu. P. Sharaevsky** Laboratory "Metamaterials", Saratov State University, Saratov, Russia; Kotel'nikov Institute of Radioengineering and Electronics, Russian Academy of Sciences, Moscow, Russia

**S. E. Sheshukova** Laboratory "Metamaterials", Saratov State University, Saratov, Russia; Kotel'nikov Institute of Radioengineering and Electronics, Russian Academy of Sciences, Moscow, Russia

**Anatolie Sidorenko** Institute of Electronic Engineering and Nanotechnologies, Academy of Sciences of Moldova, Chisinau, Moldova; Institut für Physik, Universität Augsburg, Augsburg, Germany

**I. I. Soloviev** Lomonosov Moscow State University, Skobeltsyn Institute of Nuclear Physics, Moscow, Russia; Moscow Institute of Physics and Technology, State University, Dolgoprudniy, Moscow region, Russia

**L. R. Tagirov** Zavoisky Physical-Technical Institute of Russian Academy of Sciences, Kazan, Russia; Kazan Federal University, Kazan, Russia; Universität Augsburg, Augsburg, Germany

**M. Tarasov** V.Kotelnikov Institute of Radio Engineering and Electronics, Russian Academy of Sciences, Moscow, Russia

**Nan-nan Wang** Department of Microwave Engineering, School of Electronics and Information Engineering, Harbin Institute of Technology, Harbin, China

**Andrzej J. Zaleski** Institute of Low Temperatures and Structural Research, Polish Academy of Sciences, Wroclaw, Poland

# Basic Superconducting Spin Valves


**V. N. Kushnir, Anatolie Sidorenko, L. R. Tagirov and M. Yu. Kupriyanov**

**Abstract** The short review is devoted to the state of the art of a booming field of research in spintronics—superconducting spintronics. The spin valve properties of hybrid structures consisting of alternating layers of superconductor (S) and ferromagnetic (F) of nanoscale thicknesses and superconducting due to the proximity effect are considered in detail. The experimental data for the weak and strong ferromagnetic materials are analyzed; the role of the domain structure of the ferromagnet and the scattering of electrons with spin flip at the SF interfaces in the magnitude of the valve effect is considered. Theoretical works describing the effects of the spin valve for diffusive and clean limits are analyzed. The necessity of consideration of the multiplicity of configurations of the superconducting order parameter in multilayer SF heterostructures is underlined.

V. N. Kushnir (✉)
Physics Faculty, Belarus State University, 220000 Minsk, Belarus
e-mail: vnkushnir@gmail.com

V. N. Kushnir
Belarus State University of Informatics and Radioelectronics, 220013 Minsk, Belarus

A. Sidorenko
Institute of Electronic Engineering and Nanotechnologies, Academy of Sciences of Moldova, 2028 Chisinau, Moldova
e-mail: anatoli.sidorenko@kit.edu

L. R. Tagirov
Zavoisky Physical-Technical Institute of Russian Academy of Sciences, Kazan 420029, Russia
e-mail: ltagirov@mail.ru

L. R. Tagirov · M. Yu. Kupriyanov
Kazan Federal University, Kazan 420008, Russia

L. R. Tagirov
Universität Augsburg, Universitätsstraße 1, 86159 Augsburg, Germany

M. Yu. Kupriyanov
Skobeltsyn Institute of Nuclear Physics, Moscow State University, Moscow 119992, Russia
e-mail: mkupr@pn.sinp.msu.ru



A. Sidorenko (ed.), *Functional Nanostructures and Metamaterials for Superconducting Spintronics*, NanoScience and Technology,
https://doi.org/10.1007/978-3-319-90481-8_1

## 1 Introduction

The term "spintronics" (SPIN Transport electrONICS), introduced in 2000 [1, 2], designates a field of electronics aimed to fabricate devices, the electrical characteristics of which are controlled by changing its spin state. The emerging of spintronics is usually associated with observation of giant magnetoresistance effect (GMR 1988) in three-layer and multilayer metallic F/N structures (F, N—ferromagnetic and normal metal, respectively) [3, 4]. Indeed, this discovery, at first, initiated a drastic increase of research in this area and second, almost immediately found application, being put in the basis of reading heads for hard drives and rising to a new level of information storage capacities. However, as emphasized in [5, 6], the fundamental researches which can be attributed to spintronics were initiated long before these events. The starting point was the work by Mott [7] (1936), in which, to explain the temperature dependence of the resistivity of Ni, the "two-current conduction model" was proposed which introduces two relaxation times for the electrons with spin projections parallel and antiparallel to the magnetization vector. The model had been confirmed in experiments (started in 1966) that provided the basis for the formulation of the applied problem: control of the solid-state conduction by acting on the spin degrees of freedom of the system. This, in turn, stimulated research in basic areas of spintronics, namely magnetization dynamics (magnetodynamics), spin transport, and spin relaxation processes in magnetic solid-state heterostructures [5, 6, 8–11]. Rapid advances in solving these problems occurred after development of the high-precision technologies of layered nanostructure preparation in high and ultra-high vacuum conditions in the early 1980s [11]. In addition to key experiments performed during the subsequent 15–20 years (detailed analysis is given in the review [5]), the theoretical apparatus of spintronics was elaborated, which includes the kinetic Boltzmann equation formalism and the Kubo linear response theory, see [1–11] and references therein.

It is interesting that the idea to control superconductivity with magnetism was invented by de Gennes [12] in 1966, well before the giant magnetoresistance experiments in F/N structures. In his proposal, thin superconducting (S)-film with the thickness $d_S < \xi_S$ ($\xi_S$ being the superconducting coherence length) was sandwiched between two ferromagnetic insulators (FIs). By exchange interaction of the superconductor electrons with the first magnetized atomic layers of the ferromagnets, these electrons acquire the exchange fields causing splitting of their spin states. Because of small S-layer thickness, the average exchange field (exchange splitting energy) $\bar{h}$ was considered homogeneous (the so-called Cooper limit) and dependent on the angle $\theta$ between magnetic moments $\boldsymbol{M}_1$ and $\boldsymbol{M}_2$ of the ferromagnets:

$$\bar{h} = 2|\Gamma|(a/d_S)S\,\cos(\theta/2), \tag{1}$$

where $\Gamma$ is exchange integral, $a$ is interatomic distance, and $S$ is the ferromagnet atom spin (here, we keep original notations). On the qualitative level, as far as the maximum $\bar{h}$ is above the Clogston–Chandrasekhar limit $\Delta/\sqrt{2}$ (see in [13]), the S-

layer is normal conducting in a domain of angles close to $\theta = 0$ (magnetic moments $\boldsymbol{M}_1$ and $\boldsymbol{M}_2$ are parallel—"*P*" magnetic state, and the exchange fields induced by the both ferromagnets are summed up). Turning magnetic moment of the magnetically more soft (whatever the reason does not matter) ferromagnet against the other to increase the angle $\theta$, the superconductivity can be restored provided that the $\bar{h}$ shifts below the Clogston–Chandrasekhar limit (partial or complete cancelation of the exchange fields at antiparallel $\boldsymbol{M}_1$ and $\boldsymbol{M}_2$—"*AP*" state). In a more rigorous basis, de Gennes has shown that the free energy of the structure FI/S/FI is a monotonically decreasing function of the angle $\theta$ between $\boldsymbol{M}_1$ and $\boldsymbol{M}_2$. For a given temperature range, the structure can be either in the normal state, when the vectors $\boldsymbol{M}_1$ and $\boldsymbol{M}_2$ are in P-state, or superconducting in the opposite AP case. On this basis, de Gennes [12] suggested spintronic (in modern terms) storage device which has (*verbatim*:) zero resistance for $\theta = \pi$ and a finite resistance for $\theta = 0$.

Inspired by the De Gennes prediction, Deutscher and Meunier [14] and Hauser [15] have made experiments, the former sandwiching the 250-nm-thick indium layer between the permalloy and pure nickel layers each of 150 nm thick. The ferromagnets were isolated from direct contact by the oxidizing of the layer materials. The condition $d_S < \xi_{BCS}(\mathrm{In}) = 330$ nm [16] was fulfilled, but the others are hardly to estimate, however, the difference between transition temperatures of parallel (P) alignment ($T_c^P$) and antiparallel (AP) alignment ($T_c^{AP}$) of the F-layer magnetizations, $\Delta T_c = T_c^{AP} - T_c^P$, was found positive and as large as 200 mK (see Fig. 1 in [14]). In the Hauser experiment, indium film of the thickness 150–4400 nm was sandwiched between 200-nm-thick magnetite $Fe_3O_4$ films grown in a magnetic field to premagnetize each of the magnetic layers in a predetermined direction. Transition temperature measurements have shown that $T_c^{AP} > T_c^P$, and the difference $\Delta T_c$ was found as large as 2 K [15], hardly available until now.

Looking at the formulation of the problem by de Gennes (see also [17]) from the modern point of view, an alternative approach to the FI/S/FI spin valve operating physics can be drawn considering FI/S interface as spin-active one [18–20]. The concept of the spin-active interface implies that electrons acquire spin-dependent phase shifts when reflecting from an interface with ferromagnetic insulator (for the pictorial view see [21], Fig. 7). As far as a Cooper pair in the S-layer consists of two electrons with opposite spins, the pair acquires a total phase and may be decomposed on the singlet and triplet components (see [21], Fig. 8) affecting superconducting $T_c$. Indeed, calculations within the quasiclassical theory [22] have shown that $\Delta T_c$ in this approach is positive and can be as large as a dozen percents of the BSC $T_S$. Modern experiments with FI/S/FI system (FI = EuS, 1.5 and 4.0 nm, and S = Al, 3.5 nm thick) [23] have shown that $\Delta T_c$ can be large enough to switch the system between superconducting- and normal-conducting states; however, the scenario of singlet–triplet mixing at interfaces of SF heterostructures has not been discussed as switching physics (see, however, discussion of the difference between FI/S/FI and F/S/F spin valve physics in [24]). Most of the recent studies were dedicated to proximity effect between a superconductor and a metallic ferromagnet.

In the situations discussed above, the FI-layers were sufficiently thick, and the back influence of S-film superconductivity on the mutual orientation of FI magnetization

vectors was negligibly small. However, if one decreases the thickness of one of the FI-films in FI/S/FI system and/or reduces its magnetic anisotropy by any other means, the situation may change to the opposite. Namely, the *S*-film in FI/S/FI spin valve can impose antiferromagnetic ordering of magnetizations of the sandwiching FI-layers as if there is a kind of exchange interaction between the FI-layers [25, 26]. Zhu and co-workers used a series of GdN/Nb/GdN trilayer configurations with various thicknesses of superconducting Nb interlayer and studied the resistance and magnetization hysteresis as a function of applied magnetic field. These measurements allow them to demonstrate the new type of exchange coupling due to the superconductivity in the interlayer. To prove the key role of the superconductivity in their experiments, they made a number of tests, including the substitution of Nb by nonsuperconducting Ta interlayer and adding thin dielectric AlN-layers between GdN and Nb. In both cases, the effects vanished, confirming that it is indeed due to superconductivity in the interlayer and does not stem from stray fields. Thus, the observed antiferromagnetic alignment of magnetic moments in the GdN/Nb/GdN heterostructure can be a manifestation of the long-range, RKKY-type indirect exchange of magnetic moments in superconductors [27]. This exchange is always antiferromagnetic between magnetic moments of the same kind; manifestations of this unconventional interaction in magnetic resonance measurements have been analyzed in [28–30].

## 2 Superconductor–Metallic Ferromagnet Proximity Effect

Usually, superconductivity and ferromagnetism are considered as antagonistic long-range orders which cannot coexist in a homogeneous medium [31]. Indeed, ferromagnetism is expected to suppress singlet superconductivity, because the presence of an exchange splitting of the conduction band breaks the time reversal symmetry of a Cooper pair. Fulde–Ferrell and Larkin–Ovchinnikov (FFLO) [32, 33] have shown that, nevertheless, superconductivity may survive in the presence of the magnetic background, however, restricted to an extremely narrow range of parameters [34]. The idea was that the Cooper pair keeping zero total spin acquires nonzero pairing momentum. This idea became much more applicable for systems in which superconductivity and ferromagnetism are separated in a nanometer scale because of artificial layering. The latter systems will be in focus of the current review.

The artificially layered metallic systems are ultra-thin-film heterostructures in which superconductivity and ferromagnetism locate at different adjoining or closely lying layers but strongly interact via interfaces. This coupling of superconductors with nonsuperconducting metals through interfaces, so-called *proximity effect*, was brought into play by de Gennes and Guyon [35] and Werthamer [36] and precisely formulated by de Gennes as a boundary problem [37]. The early-stage experimental results, summarized in a review by Jin and Ketterson [38], have mostly shown the expected suppression of superconductivity by proximity to an adjacent ferromagnet; however, some indications of the nonmonotonous dependence of this suppression on the ferromagnetic layer thickness in multilayers had been already noticed.

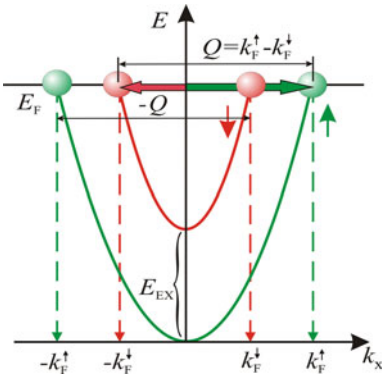


**Fig. 1** Origin of the FFLO state in S/F heterostructures. Paired electrons (red and green balls) from the minority (red) and majority (green) spin subbands (wave vectors are indicated in the respective colors) establish the FFLO-like paired state with finite momentum along the $x$-axis $\hbar Q_{\mathrm{FM}} = \hbar \Delta k_{\mathrm{F}} = E_{ex}/v_{\mathrm{F}}$. Reproduced from [A.S. Sidorenko, Low Temp. Phys. **43**, 766 (2017); http://dx.doi.org/10.1063/1.4995623], with permission of AIP Publishing

The continued progress in the thin-film deposition techniques has led to a burst of activity in the field of superconductor–ferromagnet SF heterostructures, both experimentally and theoretically. It was quickly realized that due to proximity between superconductor and ferromagnet, in the latter, the FFLO-like finite-momentum pairing is induced by singlet Cooper pairs penetrating into the ferromagnetic metal via the S/F interface. It is because of exchange splitting of the ferromagnetic metal conduction band which makes Fermi momenta of the conduction spin subbands nonequal, as it is shown in Fig. 1 [39] for the simplest model of parabolic conduction band.

The resulting pairing wave function oscillates in space along the normal to the S/F interface. When the oscillation scale and the pairing function decay length are comparable with ferromagnetic layer thickness, various interference effects can be expected, namely oscillating superconducting transition temperature $T_c$ as a function of the ferromagnetic layer thickness $d_F$ in S/F bilayers; oscillations of $T_c$ in S/F multilayers as a result of switching between "zero" and "π" phase difference between the neighboring S-layers in a stack; re-entrant superconductivity as a function of the F-layer thickness; Josephson π-junctions—the junctions with intrinsic phase difference of π across the ferromagnetic week link; and some others. Most of these unusual properties of the SF heterostructures are described and explained in detail in several reviews [13, 21, 40–48]. An example of the spectacular unconventional behavior of $T_c(d_F)$ in SF bilayers is given in Fig. 2.

Special attention has been drawn to nonzero spin pairing that could be realized in SF heterostructures atop of the ferromagnetic background. Indeed, it has been shown by Bergeret, Volkov, and Efetov that the triplet s-wave pairing can be induced by a conventional superconductor in proximity with the ferromagnetic subsystem containing noncollinear magnetizations (see review [45] and references therein). This pairing is nonoscillating and extraordinary long range [45, 46] that makes it

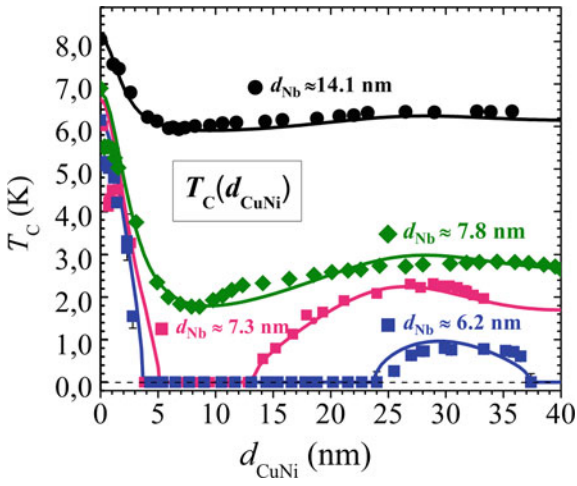


**Fig. 2** Nonmonotonous $T_c(d_F)$ dependence for the $Nb/Cu_{1-x}Ni_x$ bilayers ($x$ = 0.59). Solid curves are calculated with the quasiclassical theory. The calculations give no further re-entrance of superconductivity for the sample series above $d_{CuNi}$ > 40 nm. Reproduced from [A.S. Sidorenko, Low Temp. Phys. **43**, 766 (2017); http://dx.doi.org/10.1063/1.4995623], with permission of AIP Publishing

promising mediator of the spin-polarized Josephson current. The triplet spin valves are considered in chapter "Superconducting Triplet Proximity and Josephson Spin Valves".

## 3 Elementary Superconducting Spin Valve: Diffusive Limit

The elementary spintronic binary logic device, based on the superconducting proximity effect systems, is «*P*−*AP*» superconducting spin valve (SSV) with F1/S/F2 structure [49, 50] as a core (a faraway similarity with conventional F/N/F spin valve [51], but with completely different physics). The metallic ferromagnetic layers in the structure are considered to be monodomain and without the exchange coupling between them. Practically, significant effect, which arises on the reversal of the magnetic moment of one of the F-layers, has defined by the criterion: The difference $\Delta T_c$ between the critical temperatures of *AP* and *P* magnetic states ($T_c^{AP}$ and $T_c^P$, respectively) is larger than the width $\delta T_c$ of the resistive transitions. Besides, the observability condition means that one of the critical temperatures is higher than the other.

In [49, 50], the *P*–*AP* SSV problem was solved in a single-mode approximation of the diffusive limit of the microscopic theory of superconductivity [52]. As a result, it has been found:

(1) For all values of parameters of an S/F structure, the relation $T_c^{AP} > T_c^P$ fullfils.
(2) For $d_S$ values substantially larger than the coherence length of the diffusive limit, $\xi_S$, the difference $\Delta T_c = T_c^{AP} - T_c^P$ is very small; it becomes tangible as the thicknesses $d_S$ approach $\xi_S$.

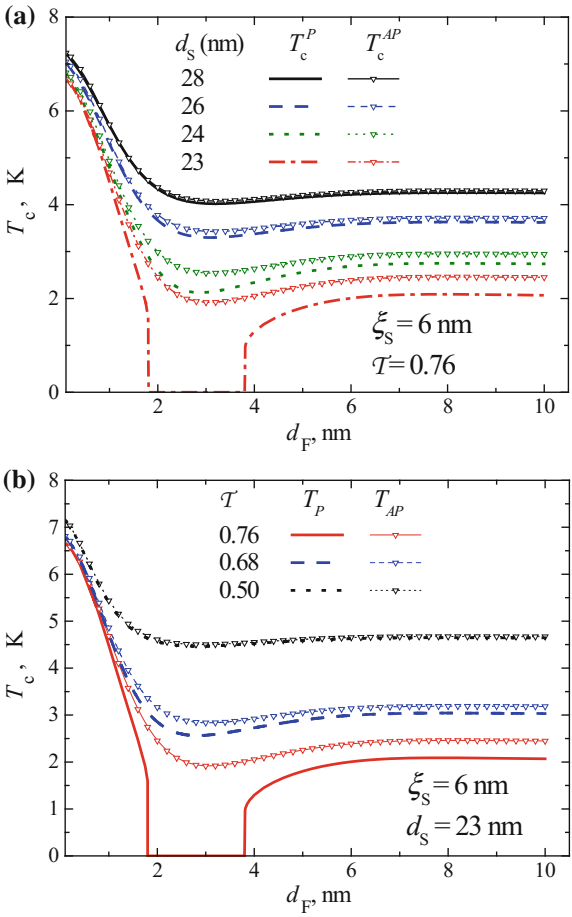


**Fig. 3** Critical temperature versus F-layer thickness for *P* and *AP* magnetic states of the F0/S/F structure with different S-layer thicknesses $d_S$ (**a**) and different S/F interface transparencies T (**b**). The values of the other parameters of the system are $d_{F0} = 8$ nm, $\rho_S/\rho_F = 0.29$ (where $\rho_S$ and $\rho_F$ are the normal specific resistances of S- and F-layer, respectively), $\zeta_F = 3$ nm ($\zeta_F$ the characteristic length of the order parameter decay in ferromagnet), $T_S = 8.8$ K ($T_S$ is the critical temperature of the bulk superconductor)

(3) If the value of $d_S$ satisfies condition of the «re-entrance effect» [53, 54] (for a review see [39]), namely $d_S \sim d_{S,cr}$ (where the critical thickness $d_{S,cr}$ is defined by the relation $T_c^P(d_S \to d_{S,cr}) \to 0$), the relative magnitude of the switching effect can amount 100% (see Fig. 3a).

(4) The magnitude of the *P*–*AP* effect, $\Delta T_c$, is strongly influenced by the quantum-mechanical transparency of SF interface, $\mathcal{T}$; namely, the value of $\Delta T_c$ increases with increasing $\mathcal{T}$ (Fig. 3b).

All these results were confirmed by calculations based on the asymptotically exact multimode solution of the Usadel equations [55].

As it follows from the first result of the theory, the antiferromagnetic (AP) alignment of magnetic moments of the F-layers is less harmful to superconductivity in the diffusive limit F1/S/F2 structures, which is realized in most of experiments on S/F systems with dilute ferromagnets. This statement is valid for temperatures below $T_c$,

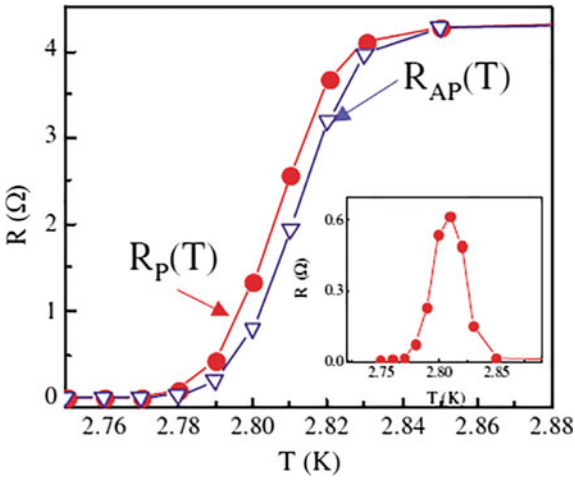


**Fig. 4** Resistive transitions into the superconducting state of the $Cu_{0,47}Ni_{0,53}/Nb(18)/Cu_{0,47}Ni_{0,53}$ structure in *P* and *AP* magnetic configurations; inset: $\Delta R(T) = R_P(T) - R_{AP}(T)$. Reprinted Fig. 3b from [J.Y. Gu, C.-Y. You, J.S. Jiang, J. Pearson, Ya.B. Bazaliy, and S.D. Bader, Phys. Rev. Lett. **89**, 144505 (2002)] with permission by the American Physical Society. Copyright APS 2014

as it follows from the analysis of the temperature dependences of the order parameter, the free energy, the entropy, and the specific heat [56, 57]. It should be noted here that the metallic proximity physics behind the SSV effect in F/S/F systems [49, 50] is essentially different of the spin-active interface physics behind the FI/S/FI SSV utilizing ferromagnetic insulators [12, 24]. So SSV proposal by [49, 50] is not a re-discovery of the de Gennes SSV as can be read in some papers on the topic.

Experimental observations of the SSV effect in structures with weak ferromagnets appeared controversial. The paper [58] reported the detection of the effect in experiments with the structure $AF/Cu_{0.47}Ni_{0.53}/Nb/Cu_{0.47}Ni_{0.53}$ (here, AF is an antiferromagnet). In accordance with the theory, the $\Delta T_c$ value was positive; its maximum, $\Delta T_{c,\max} = 6$ mK, was achieved at the thicknesses $d_S = 18$ nm and $d_F = 5$ nm (see Fig. 4). So small effect has led to an assumption that the theory of the SSV effect describes the experimental data only at a qualitative level [58, 59].

This statement was based on the unavailing of the simultaneous fitting of the experimental dependences $T_c(d_F)$ and $\Delta T_c(d_F)$ by the theoretical curves, calculated both in one-mode approximation and utilizing the exact numerical solution of Usadel equations [59]. It turned out that when the satisfactory fit of the $T_c(d_F)$ dependence is achieved, the theoretical $\Delta T_c$ values are of two orders of magnitude higher than the experimental ones. The statement about the impossibility of the simultaneous theoretical description of the experimental findings had been declared by independent experiment [60], in which the results of [58] were confirmed. In later experiments with $Cu_{48}Ni_{52}/Nb/Cu_{48}Ni_{52}$ trilayers [61], a dependence $T_c(\alpha)$ on the misalignment angle $\alpha$ between magnetic moments of the CuNi alloy layers was measured showing standard SSV effect of 3–7 mK amplitude. Calculations in the same work, utilizing self-consistent numerical solution of Bogoliubov–de Gennes equations, have given the SSV effect two orders in magnitude stronger compared with the experiment.

One of the causes for the nonsatisfactory results of the fittings, as expected in [59], could be neglect of the electron spin-flip scattering. Indeed, in the work [62], the estimations for frequencies of the spin–orbit and paramagnetic scatterings ($\tau_{so}^{-1}$ and $\tau_{m}^{-1}$, respectively) in $Cu_{0.47}Ni_{0.53}$/Nb system have been obtained based on the modeling of temperature dependencies of the critical current. It had been found that, at least, the paramagnetic scattering processes could make a significant contribution to the characteristics of the structure (of the order of the exchange interaction energy $E_{ex}$). In [63], the SSV effect for the structures with thin S-layers ($d_S \approx \xi_S$) has been investigated depending on $\tau_{so}^{-1}$, $\tau_{m}^{-1}$, $\gamma_b$ ($T \approx (1 + \gamma_b)^{-1}$ [64, 65]), as well as on the pair-breaking parameters. In accordance with [62, 63], and utilizing the experimental data given in [58, 59], the data from [60] can be consistently explained in a quantitative level.

One of the significant reasons of the small *P–AP* SSV effect could be nonuniformity of the layer thicknesses, which affects the effective interface transparency [64, 65]. Indeed, the experiment with the same structure $Cu_{0.47}Ni_{0.53}$/Nb/$Cu_{0.47}Ni_{0.53}$ [66], as was used by the authors of [58] (the same $d_S$, and the $d_F$ twice thicker), but with a much higher quality of the SF interfaces, gives the SSV effect of $\Delta T_c = 30$ mK value (see inset in Fig. 12 in [66]). Apparently, for F/S/F structures with weak ferromagnets, it is infrequent observation of the well-pronounced SSV effect (see also [67]).

The most consistent viewpoint on the discrepancy between the theoretically predicted and the measured SSV effect has given in [68] (the main task of the work was to investigate the "re-entrance" effects in the two-layered structure Nb/$Cu_{0.41}Ni_{0.59}$). In accordance with [68], especially noteworthy that the minimum on the $T_c(d_F)$ is shallow for the F/S/F structures with thick S-layer (see Fig. 4 in [57]). Therefore, this dependence does not correspond to the conspicuous SSV effect (see [49, 50]), so that the measured values $\Delta T_{c,max} = 6$ mK (at $d_S = 18$ nm) and $\Delta T_{c,max} = 3.5$ mK (at $d_S = 19$ nm) are quite plausible. The experimental observation of the pronounced switching effect requires samples, which have a sufficiently high critical temperature and, on the other hand, thinner S-layer. For example, the samples of Nb/$Cu_{0.41}Ni_{0.59}$ bilayers fabricated by the authors of [68] are characterized by a high quality, which is evident from the value of the critical S-layer thickness, $d_{S,cr} \approx 6$ nm $\approx \xi_S = 6.2$–$6.8$ nm (for the F/S/F trilayers, $d_{S,cr} \sim 12$ nm). Hence, in this case, we can find a relatively wide range of the layer thicknesses, corresponding to the ideal or almost ideal switching effect. This range was estimated for the "hypothetical" F/S/F trilayer structure with material parameters that have been identified by fitting the experimental data of the "pilot" series of samples in [68]. As a result, the optimal thickness of Nb-layer amounts to 12–16 nm, the thickness of CuNi-layers belongs to the interval 3.5–5 nm, and the forecasted critical temperature is $T_{AP} \sim 1$ K. Given the typical values of the roughness of interfaces (of the order of 0.4 nm), the range of acceptable thickness values is relatively wide.

Thus, the SSV effect in the elementary structure with a weak ferromagnet can be treated as a "subtle," and its detection requires a preliminary detailed study of the "strong" effects [39, 69–72].

## 4 Elementary Spin Valve with Strong Ferromagnets

It was reasonable to expect a significant improvement in the parameters of SSV based on strong ferromagnets since they have high spin polarization. This simple motivation had the following implications: (a) observation of the normal and inverse SSV effects and (b) the numerous investigations of the effects of domain structure of strong ferromagnets. In addition, the problem of understanding the processes of the spin transport through the SF interface on the quantitative level had sharply actualized.

### *4.1 Normal and Inverse Spin Valve Effects in the Elementary Structures*

First experimental results, which seem to agree with the theory of SSV, had been got for symmetrical structures AF/Ni(7)/Nb($d_S$)/Ni(7) and AF/Py(8)/Nb($d_S$)/Py(8) (in parentheses are the thicknesses of the layers in nanometers) [73, 74]. The $\Delta T_c(T_c)$ characteristics were measured in full $T_c$ range, that is, from $T_c(d_{S,cr})$ to the asymptotic values of the $T_c(d_S)$ dependences. For the both structures, the function $\Delta T_c(T_c)$ is monotonically decreasing, with the highest values $\Delta T_{c,\max} \approx +41$ mK (for Ni/Nb/Ni) and $\Delta T_{c,\max} \approx 20$ mK (for Py/Nb/Py) at $T_c \sim 0.5$ K. In this case, the *P–AP* effect was small a priori, since the experimental thicknesses $d_F$ are much larger than the characteristic length of the decay and the oscillations of the order parameter, $\zeta_F < 1$ nm (with estimations for Ni: $\zeta_F \sim 0.7$ nm [73] and $\zeta_F \sim 0.88$ nm in [75], see Fig. 7). It should be noted that the coincidence of the theoretical curve $\Delta T_c(d_S)$, calculated in [74], Fig. 4, by the exact method [55], with experimental characteristics may not be a rigorous proof of the quantitative agreement between the experiment and the theory. Indeed, in certain cases, a number of theoretical curves can fit the experimental dependence $T_c(d_S)$ or $T_c(d_F)$ [76–78].

Later on, the comparable result, $\Delta T_{c,\max} \approx +30$ mK at $T_c \approx 1.1$ K, was obtained on the epitaxial structure AF/Fe(6)/V(40)/Fe(6) in [79]. In this case, the high quality of samples, low quantum-mechanical transparency of the V/Fe interface (characterized by $\gamma_b \sim 180$ according to [80], see definitions there as well), and strong suppression of the critical temperature due to the proximity effect have led to the well-defined but weak SSV effect.

Meanwhile, the opposite result, namely the *inverse spin valve effect*, has been obtained in F1/S/F2 trilayers belonging to Nb/Py system [81, 82]. In this case, the magnetoresistive measurements had been carried out on the asymmetrical samples Py(50 nm)/Nb(25)/Py(20 nm). The strong dependence of the coercive field on the Py-film thickness made it possible to control the relative orientation of the magnetizations of the F1- and F2-layers by weak magnetic fields without using antiferromagnetic exchange biasing. Besides, the large difference between Py coercive fields ($H_{co}$(50 nm) ~ 15 Oe and $H_{co}$(20 nm) ~ 95 Oe) ensured the well-defined segments of *AP*-

states on the hysteresis loop. However, the asymmetry of the structure with respect to superconducting condensate is not so obvious since the both F-layers are semi-infinite. The distinction between F-layers arises due to the drift not only $H_{co}$, but also the material parameters of F-film that define the superconducting state of the structure [76]. Therefore, the inverse SSV effect ($\Delta T_c$ = –30 mK at $T_c \approx 3.7$ K [81, 82]) and the normal one do not contradict each other, but, in general, point to a fact of inapplicability of the diffusive limit theory to S/F nanostructures with strong ferromagnets. To interpret the inverse SSV effect, the accumulation of spin [83] in S-layer was proposed in the works [81, 82, 84] (the latter deals with F/HTSC/F structure utilizing $YBa_2Cu_3O_7$ and $La_{0.7}Ca_{0.3}MnO_3$ as a superconductor and a ferromagnet, respectively). In a number of experimental works (see, e.g., [85–87]), other causes of the inverse effect had been called, in particular the influence of stray fields of a ferromagnet.

## 4.2 *Superconducting Spin Valve Effect and the Domain Structures of Ferromagnets*

In [88], the stray field in F1/S/F2 structure had been considered as a main factor of superconducting critical temperature variations associated with the inverse *P–AP* SSV effect. This standpoint has been based on the following experimental results [88]:

First, the minimum of the resistance $R(H)$ and, accordingly, the maximum on the $T_c(H)$ dependence, measured for the Fe/Nb(27.5)/Co structure, were observed for the *P*-state, in which the stray field is practically absent (see Fig. 6 in [88] and Fig. 5 in this chapter), since the magnetizations of the F-layers reach saturation (here, $H$ is a magnitude of the external magnetic field).

Second, for the value of $H$ close to the coercive field of Co, $H_{co,Co} \approx 150$ Oe, which corresponds to strongest expected stray fields, there is a sharp drop in the critical temperature $T_c$ (see Fig. 6 in [88] and Fig. 5 in this chapter). Indeed, the amplitude of the perpendicular component of the stray field can reach several kOe at the distance of 10 nm from the surface, as it is shown in [88]. Such a field induces the "spontaneous vortex phase" in the superconducting layer, the flow of which due to the transport current leads to suppression of superconductivity [42, 89–92].

Third, the $\Delta T_c$ value disappears for the exchange-biased structure CoO/Co/Nb/Fe with S-layer thickness of 30 nm (CoO is an antiferromagnet). Due to the presence of antiferromagnetic CoO, in this case, the hysteresis loop contains a wide segment of *AP*-state, which corresponds to a weak stray field. At this segment, the dependence $T_c(H)$ acquires the local maximum, which is only slightly lower than the maximum corresponding to the *P*-state (see Fig. 7 in [88]). At the same time, as for the structure without the antiferromagnetic biasing layer, there is a downward cusp in $T_c$ for the external field, equal to the coercive field of Fe-layer.

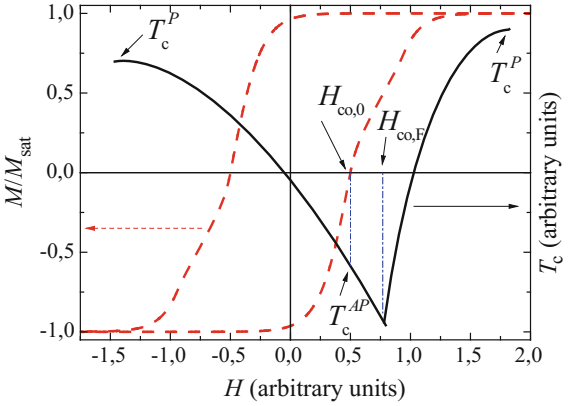


**Fig. 5** Illustration to stray field effect on the critical temperature of an F1/S/F2 structure with different F1 and F2 ferromagnets. The hysteresis loop (dashed red line and left scale) has invented on the base of the simplest formula. The dependence of the critical temperature versus the magnitude of the external magnetic field (freehand drawing and right scale) is a typical for experiments mentioned in the text. Farther, $M_{\text{sat}}$ is the saturation magnetization, $H_{\text{co},0}$ and $H_{\text{co,F}}$ are the coercive fields the F1/S/F2 structure and one of its F-layers, respectively

Therefore, it was concluded that the observed $\Delta T_c$ effect can be interpreted in terms of stray fields originating from domain configurations in ferromagnetic layers. The relationship between the proximity *P–AP* and the stray field effects still remained unquantified.

In experiments of [93, 94] on symmetric Py/Nb/Py structures, a positive effect ($\Delta T_c > 0$) had been measured quite clearly; moreover, it was shown that the largest change in the critical temperature (suppression of $T_c$) is observed in the multidomain (D) state. In this regard, it was proposed that negative *P–AP* effect can be due to "unaccounted" stray fields of the F-layers that were present in the state of remanent magnetization. Indeed, the experiments on S/F, S/I/F bilayers and F/S/F trilayers with amorphous materials show that vortex nucleation, induced by stray fields in certain conditions, may have much stronger influence on superconductivity than the SF proximity at interfaces upon reversal of magnetic moments of the F-layers [95]. The amorphous ferromagnetic material ($a$-$Gd_{19}Ni_{81}$) has a very high saturation magnetization and very low coercive field, and the amorphous superconductor ($a$-$Mo_{2.7}Ge$) is characterized by a very weak vortex pinning force. The *giant* magnetoresistive effect taking place in such F/S/F structure (at $H \approx \pm H_{co}$) was considered arising from the coupling between the F-layers by means of stray fields of the Bloch-type domain walls (see also [96]). The relationship between different magnetoresistive effects was analyzed in [97] from measurements on Nb/Py and Py($d_{F,1}$)/Nb/Py($d_{F,2}$) sandwiches. The transition of the domain structure in thin permalloy films with increasing the thickness $d_{\text{F}}$ from Neél type to Bloch type at $d_F \approx 30$ nm [98] was realized. It turned out that effect of the positive magnetoresistance at $T < T_c$ occurs regardless

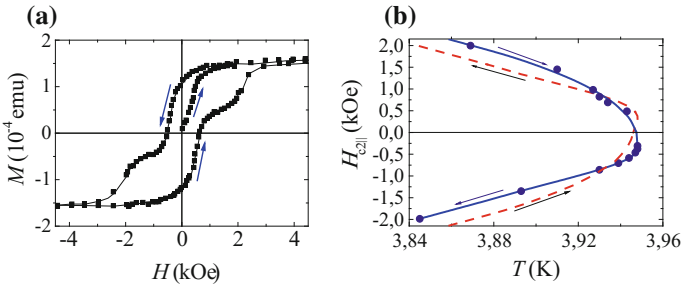


**Fig. 6** **a** Hysteresis loop and **b** the upper parallel critical field for Ni(1.8)/V(44)/Ni(4) structure (adopted from [101]). Adapted Figs. 2b and 4 from the article by P.V. Leksin, R.I. Salikhov, I.A. Garifullin, H. Vinzelberg, V. Kataev, R. Klingeler, L.R. Tagirov, and B. Büchner originally published in Journal of Experimental and Theoretical Physics Letters (JETP Letters) **90**, 59 (2009) with permission of Pleiades Publishing, Ltd

of the magnitude of stray fields. Perhaps, the results of [95] can be regarded as a "contrary instance" with respect to [88].

The enhancement of superconductivity due to the multidomain structure of the F-layer is possible at a condition that the sizes of domain walls are of the order of $\xi_S$ [99, 100]. This effect had been observed for the first time in experiments with a bilayer structure Nb/Py [101]. The thickness of Py(20 nm) in this structure satisfies conditions of the Neél-type domain wall formation. It was found that the resistance, measured at a temperature slightly above $T_c$, falls sharply in a very narrow neighborhood of the external parallel field $H = H_{co}$ (corresponds to the multidomain state of the F-layer). In accordance with, the critical temperature $T_c$ at $H = H_{co}$ is above the critical temperature in zero magnetic field. The rise of $T_c$ is small (~10 mK) but of the order of the *P–AP* effect value. The interplay between these two effects is very pronounced in the experiment with Ni($d_{F1}$)/V($d_S$)/Ni($d_{F2}$) structures [102]. The thickness of the S-layer ($d_S = 44$ nm ~ $4.5\xi_S$) means *a fortiori* small variations of the critical temperature under reversal of one of the magnetic moments as well as a little significance of stray fields in the formation of critical and supercritical state of superconductivity. The F-layer thicknesses ($d_{F1} = 1.8$ nm and $d_{F2} = 4$ nm) ensured large difference between coercive fields ($H_{co,1} = 2.2$ kOe and $H_{co2} = 0.44$ kOe). This means that in the experimental range of $H$, from +2 kOe to −2 kOe, the layer F1 can be considered in a monodomain phase. As a result, the "evolution" of the magnetic state of the structure has reflected in the characteristic $H_{c2||}(T)$ quite clearly (Fig. 6).

Figure 6 shows that the highest critical temperature is reached at field $H \approx -H_{co,2}$, that is, when the layer of Ni(4) is demagnetized. Therefore, in this case (as well as in [101]), the domain walls of the Néel type enhance superconductivity. In the region of $|H| > |H_{co}| \approx 0.7$ kOe, when the magnetization directions of F-layers are well defined, there is inverse *P–AP* effect (see Fig. 1 in [102]). At last, measurements of the critical currents in the trilayer $Cu_{0.43}Ni_{0.57}$/Nb/$Cu_{0.43}Ni_{0.57}$ have shown some indications of superconductivity enhancement by Néel domain walls [103].

### 4.3 Theory of Spin Valve in the Clean Limit

Experiments with SF heterostructures, where F-material is strong and clean ferromagnet (like metallic iron, cobalt, or nickel), have addressed problem of calculating the superconducting properties of the systems including clean ferromagnets. Halterman and Valls developed an approach to the SF proximity effect, utilizing self-consistent solution of the Bogoliubov–de Gennes equations [104]. They applied their technique to clean F/S/F spin valves [105–107] (see also [108]) and found that the *AP* geometry favors superconductivity. Later on, they extended the approach on the F/F/S-type spin valves [109] focusing their attention mainly on the triplet correlation in the structure. The issue of the inverse SSV ($\Delta T_c < 0$) remained beyond the discussion.

Though being pretty informative and detailed, the above approach requires deep involvement into numerical methods and supercomputer facilities hardly available as a routine interaction with an experiment. So, the complementary approaches utilizing the quasiclassical Eilenberger theory formalism [110] were tried to develop. The key problem along the way is angular anisotropy of the equations formulated for quasiclassical trajectories crossing (or reflected by) the S/F interface at a particular incidence angle. A case of weak proximity was considered by Linder et al. in [111] at which the spatial depletion of the superconducting order parameter near the S/F interface was neglected and employs quasione-dimensional approximation to the transport through S/F interface taking into account only normal-incidence trajectories. Within these restrictions, the theory grants access to the crossover regime from ballistic to diffusive regimes of the proximity effect in F/S/F-type spin valves, predicting positive $\Delta T_c$ in the investigated range of parameters.

Last to the authors' knowledge attempt to study the SSV effect in F1/S/F2 structures with strong ferromagnets had been made in [112] within the formalism of Eilenberger equations. In the case of thin S-layer, $d_S \sim \xi_S$, the analytical expressions for the quasiclassical anomalous Green's functions had been found that have given the following results:

(1) For F/S/F structures with identical F-layers, the inequality $T_{AP} > T_P$ always holds.
(2) In the diffusive limit, the inequality $T_{AP} > T_P$ holds for F1/S/F2 structures with arbitrary layer thicknesses.
(3) The critical temperatures $T_{AP}$ and $T_P$ as well as their difference are oscillating functions of the F-layer thicknesses (see Fig. 7).

Structures with layers of atomic thickness were considered in [113–115] and predicted both direct and inverse SSV effects depending on the system parameters.

To conclude, there is a step-by-step movement to noticeable correlation between the theoretical results and the experimental data for SF heterostructures with F-metal being strong and clean elemental ferromagnet.

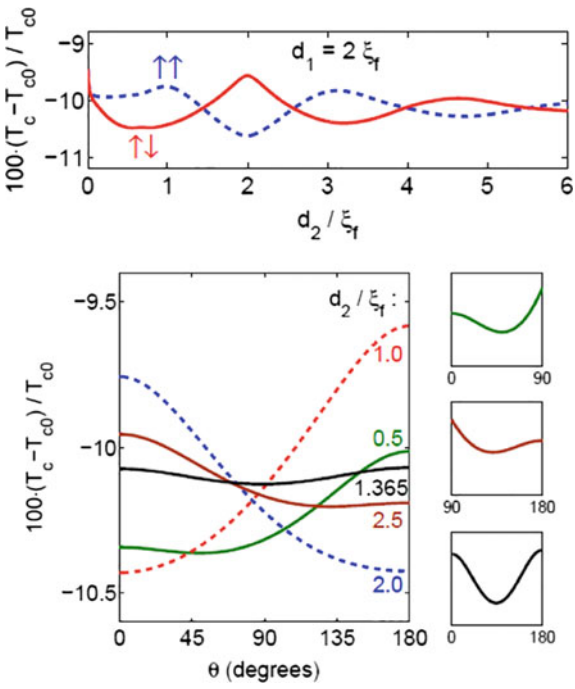


**Fig. 7** Normalized critical temperature of an F1/S/F2 trilayer versus thickness of the F2-layer (upper panel) and as a function of angle between magnetic moments of the F1- and F2-layers (lower panel) in the clean limit of microscopic theory of superconductivity. Reprinted Figs. 2b and 4 from [S.V. Mironov, A. Buzdin, Phys. Rev. B **89**, 144505 (2014)] with permission by the American Physical Society. Copyright APS 2014

## *4.4 Parametric Spin Valve*

In this section, we discuss two of unusual results of an experiment on the observation of *P–AP* and triplet pairing effect in epitaxial Ho($d_0$)/Nb/Ho($d_F$) structures [116]. They are as follows:

(1) quasi-S/N behavior of the experimental $T_{cP}(d_F)$, $T_{cAP}(d_F)$ dependences (see below);
(2) large *P–AP* effect, namely $\Delta T_c \approx 400$ mK at $d_0 = 10$ nm and $d_F = 40$ nm.

The treatment of these results has given in [78]; here, we present short comments and refinements of the main issues.

(1) Notwithstanding the fact that the value of $\Delta T_c$ is an order of magnitude higher than that obtained for other F1/S/F2 structures (moreover, a "SSV spiral effect" of ~700 mK was measured on the same samples), we analyze the first issue. The term "quasi-S/N behavior" means no $T_c(d_F)$ oscillations and the decay length of the dependence $T_c(d_F)$ like in S/N structures. Formally, it is of the order of smallest of ($\xi_F$, $\zeta_F$) (where $\zeta_F = \xi_F\sqrt{2\pi T_S/E_{ex}}$, where $T_S$ is the critical temperature of a stand-alone superconductor); however, almost all experimentally studied S/F structures satisfy the condition $\zeta_F \ll \xi_F$ ($E_{ex} \gg 2\pi T_S$). Therefore, quasi-S/N behavior of an S/F structure is possible, at the first glance, only provided that $E_{ex} \to 2\pi T$. Indeed, in the case under consideration, the fitting

procedure based on Usadel equations has given a value of $E_{ex} \sim 10$ K and the coherence length $\xi_F \sim 30$ nm [116] (for comparison, the coherence lengths for Nb/Cu system are $\xi_N \sim 35$ nm [117, 118]). In addition, unusually high value of $\xi_S \sim 30$ nm for niobium appears in the fitting procedure as a factor for a suppression of the critical temperature at the small $E_{ex}$ (the typical values for niobium are $\xi_S \sim 6$–$11$ nm [77, 117–119]). The measured saturation in-plane magnetization $M_s$ and the residual magnetization $M_r$ were 2500 G and 2100 G, respectively [116], or approximately 20–30% lower than the maximum $M_{s;m} \sim$ 3100–3400 G obtained in the bulk along the easy axis of magnetization [120]. Therefore, it is hard to expect a mechanism leading to the almost complete concealing of the exchange field compared to bulk holmium.

The contradiction could be resolved in a following way. In the formalism of Usadel equations, used in [116], an S/F system is characterized by the parameters $T_S, E_{ex}, \xi_S, \xi_F, \mathcal{T}$ and the ratio $p = \rho_S/\rho_F$ of the normal state low-temperature resistivities of the S- and F-layers (or $\gamma = p\xi_S/\xi_F$ [66]). Three of them can be estimated from independent measurements. Namely, $T_S$ is determined from the asymptotic behavior of $T_c(d_S -> \infty)$ measured for a series of Nb($d_S$)/Ho(12) samples [121] and from the data of [116]. The possible values of $p$ lie in a wide neighborhood of $p \sim 0.05$, according to the data of [116, 121–123], while for the interface transparency coefficient $\mathcal{T}$ we have an upper bound of $\mathcal{T} \sim 0.5$. Moreover, the upper bound of the admitted values for $\xi_S, \xi_F < 20$ nm was imposed. A reliable evaluation of the all parameters requires simultaneous fit of $T_c(d_S)$ and $T_c(d_F)$ dependences [77]. As usual, a scatter is expected since fabrication conditions for the two series are not completely identical. Indeed, the fitting with the exact solution of the Usadel equations (see [119, 124]) has led to the following conclusions:

(a) For any given value of $E_{ex}$ in the interval (50—$3 \times 10^3$K), there exists a region in the parameter space ($\xi_S, \xi_F, p, \mathcal{T}$) which reproduces the experimental dependences with the same accuracy. The quantity $E_{ex} \sim \times 10^3$ K determines the upper bound of applicability of the diffusion (Usadel) approximation;
(b) The consequence from (a) is that the thicknesses of the S- and F-layers exceed the respective coherence lengths, which is a necessary condition of the parametric degeneracy of the $T_c(d_S)$ characteristics [77, 117, 118].

The statement (a) is illustrated in Fig. 8.

The above results suggest an alternative to the explanations of S/N behavior of the characteristic $T_c(d_F)$ by small values of $E_{ex}$ and large coherence lengths. In the experiment [116], the $T_c(d_F)$ dependence was measured in a wide range of $d_F =$ 10–70 nm. In this case, the mean free path $\ell_F$ and the low-temperature resistivity $\rho_F \sim 1/\ell_F$ vary as a function of thickness [125], which have an effect on the critical temperature [126]. The magnitude of this effect can be estimated from measurements of the resistivity of Nb and $Pd_{81}Ni_{19}$ films [127]. Namely, the resistivity of the $Pd_{81}Ni_{19}$ film decreases 3.3 times when the thickness increases from 10 to 70 nm (see Fig. 3 in [127]); consequently, the parameter $p(d_F)$ of the SF interface increases by the same factor for a fixed value of $d_S$. We calculate $T_{cP}(d_F)$ and $T_{cAP}(d_F)$ for

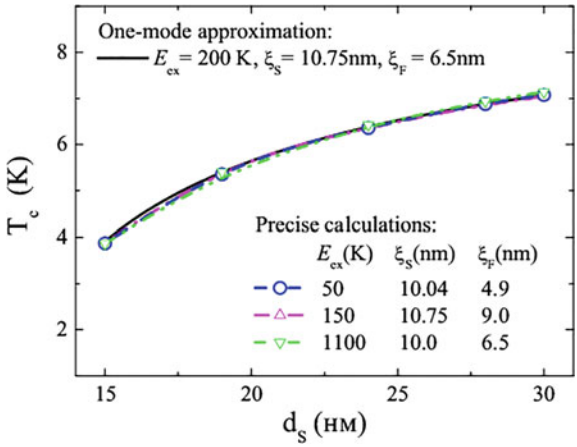


**Fig. 8** Critical temperature of a Nb($d_S$)/Ho(12) structure that we calculated with parameters quoted at panel

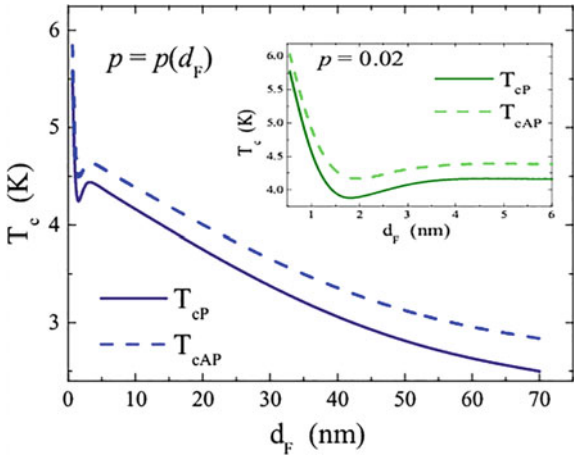


**Fig. 9** Critical temperatures of the F($d_0$)/S/F($d_F$) structure calculated for *P* and *AP* magnetic states taking into account the drift in the parameters. Inset: The same but without taking into account the drift of the parameters of the structure

the structure Ho(10)/Nb(20)/Ho($d_F$) using $p(d_F)$ dependence from [125–127], and other parameters were given from considerations of closeness of the theoretical and experimental curves. The result of the calculation with one of sets of parameters ($E_{ex}$ = 2000 K, $p(10) = 0.021$, $\mathcal{T} = 0.5$, $T_S = 9.2$ K, $\xi_S = 13$ nm and $\xi_F = 9.2$ nm.) is shown in Fig. 9. The $T_{cP}(d_F)$ and $T_{cAP}(d_F)$ dependences calculated neglecting drift in the resistivity of the F-layer (i.e., at $p = 0.065$) are also shown in Fig. 9 (inset), which show typical behavior for S/F structures with a strong ferromagnet. Moreover, the oscillation effect is well expressed on the characteristics with drifting asymptotics. We note also that Fig. 9 forecasts increase of the spin valve effect magnitude with increasing the thickness of the F-layer (look at a divergence of the solid and dash lines).

(2) The variation of the critical temperature $T_c(d_F)$ is accompanied by transformations of distribution of the superconducting condensate in the structure. In

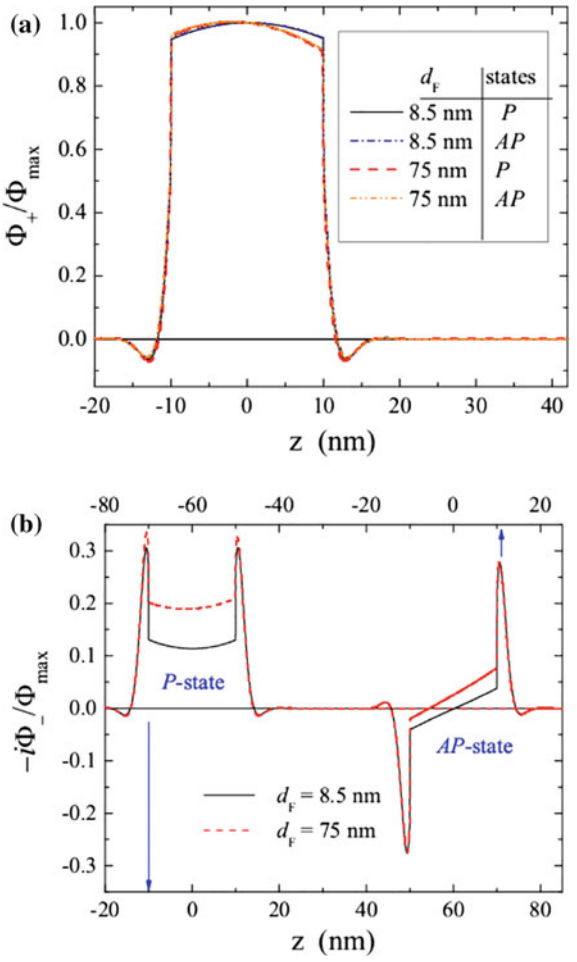


**Fig. 10** Singlet (+) and $s_{10}$-triplet (−) components of the state function of the superconducting condensate in the F0(10)/S(20)/F($d_F$) structure in *P* and *AP* magnetic states. The variations of the state functions with increasing $d_F$ are due solely to the drift of the parameter $p$

the single-mode approximation, the superconductivity of a system can have characterized by the only two components of the state-vector function, namely $\mathbf{\Phi}(z) = \Phi_+(z) \oplus \Phi_-(z)$ [119, 124]. Here, the functions $\Phi_+(z)$ and $\Phi_-(z)$ describe the singlet ($s_0$) and $s_{10}$-triplet components of the condensate, respectively; the indices in symbol $s_{10}$ mean spin 1 and zero spin projection. We calculated the state function $\mathbf{\Phi}(z)$ for a structure of the same geometry as the experimental one, Ho(10)/Nb(20)/Ho($d_F$) [116], taking into account the drift of the parameter $p$ (assuming that the length $\zeta_F$ is independent on $l_F$). The result for several values of $d_F$ is quoted in [78]. Here, we calculate the state function for the small and very large F-layer thicknesses ($d_F$, $\delta$, $\xi_F$, and $d_F$ in the asymptotic range of $p(d_F)$ dependence) to focus the attention on the following property of the *P*- and *AP*-states of the structure under consideration (Fig. 10):

Firstly, the shape of the singlet component of the state function is indifferent to the inversions of the magnetizations and is weakly sensitive to the variations of the parameter $p$. Secondly, the amplitude of triplet component in S-layer distinctly rises with $p$ increasing; the variations of triplet component in the $P$-state are substantially greater than those in the $AP$-state. The shape of the state functions does not change fundamentally if we include the drift in $\zeta_F \sim \ell_F^{1/2}$.

The calculation results show that the quasi-S/N behavior of $T_c(d_F)$ in the Nb/Ho system can be obtained utilizing: (1) drift of the system parameters at increasing the F-layer thickness; (2) high exchange energy; (3) high resistivity of holmium and low transparency of the SF interface.

Due to the high exchange energy, the superconducting condensate penetrates into a small depth of F-layer determined by $\zeta_F$, so that the pairing functions rapidly approach their asymptotic values as the thickness of the F-layer is increased (Fig. 10). Hence, each value of $T_c$ measured for $d_F \gg \zeta_F$ is asymptotic in this sense, but it does drift because of the increased intensity of the electron pair diffusion through the SF interface owing to gradual reduction in the resistivity $\rho_F$. The experiment [116] may represent an example of the dependence of critical temperature and magnitude of the SSV effect on the parameter that determines the intensity of diffusion through the SF interface.

## 5 Superconducting Spin Valve Effect in the S/F1/N/F2 Structures

In the above, the more intense studies of the FSF-type SSV [49, 50] were reviewed; however earlier, an SFF type of SSV was proposed theoretically by Oh, Youm, and Beasley [128] based on the calculation of the Usadel functions and suppression of the singlet pairing wave functions in the $P$- and $AP$-states. To the authors' knowledge, this idea found its implementation starting from the work by Westerholt et al. [129], where $\Delta T_c$ as large as 100 mK was observed in superconducting 16-nm-thick vanadium layer attached to the $[Fe(2ML)V(11ML)]_{20}$ superlattice (ML means monolayers, while subscript "20" beyond the square brackets means number of the bilayer repetitions in the superlattice) upon going from $AP$ to $P$ alignment in the latter. With further optimization of the structure, the same group has reached $\Delta T_c \sim 200$ mK in Pd(5 nm)/V(24 nm)/$[Fe(3ML)/V(12ML)]_{25}$ combination. Further on, the $[Fe/V]_n$ superlattice was replaced by Fe/V($d_{V2}$)/Fe/CoO magnetic control unit [130]; however, the SSV effect appeared to be smaller, with $\Delta T_c \sim 35$mK received for the 21-nm-thick basic V-layer and $d_{V2} = 2.1$ nm for the vanadium interlayer in the control unit.

A pulse to deeper elaboration of the SFF type of SSV was given by a work [131] where simplified S/F1/F2 structure was analyzed within the dirty limit of the quasiclassical theory of superconductivity and for a particular case of $d_{F2} \to \infty$ and $\mathcal{T} = 1$. The calculations have shown that in the SFF structure, both standard and inverse

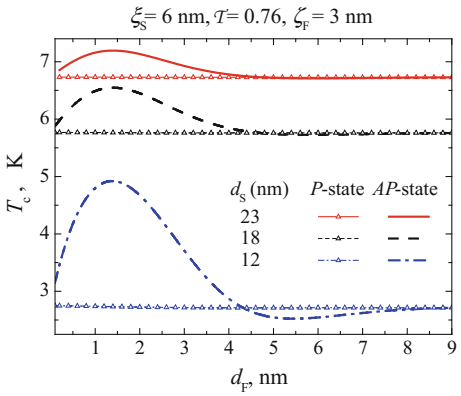


**Fig. 11** Critical temperature versus F-layer thickness for *P* and *AP* magnetic states of the S/F/F0 structure with different S-layer thicknesses $d_S$. The parameters of the structure are the same as for F0/S/F, represented by the characteristics in Fig. 3

*P–AP* SSV effects are possible depending on parameters of the layers. Namely, the standard one is realized for thicknesses $d_{F1} < (3\pi/8)\zeta_F$, and the inverse effect takes place when $(3\pi/8)\zeta_F < d_{F1} < (7\pi/8)\zeta_F$. Figure 11 shows the dependencies $T_{cP}(d_F)$ and $T_{cAP}(d_F)$ calculated for the structure S/F/F0 that differs from the previously considered F0/S/F (see Fig. 3) only by permutation of the layers. As can be seen from Fig. 11, the values of $d_F$ at the $T_{cP}(d_F)$–$T_{cAP}(d_F)$ crossover points correlate with those derived in [131].

If magnetizations of the F-layers are not collinear, the spin-projection one triplet components $s_{11}$ of the superconducting pairing come into play, and dependence of the critical temperature $T_c(\theta)$ on the angle $\theta$ between $\boldsymbol{M}_1$ and $\boldsymbol{M}_2$ can be nonmonotonic as it is shown in Fig. 12 (see in more detail in the chapter "Superconducting Triplet Proximity and Josephson Spin Valves"). Considered in correlation with the similar analysis of the $T_c(\theta)$ dependence in F1/S/F2 [55], this allows to conclude that due to more tight proximity of the ferromagnetic layers in the adjacent SFF-type SSV, compared with the interleaved FSF type, the amplitude of the triplet components as well as their impact on the superconducting properties of the structures is more strong and diverse (see [132]) in SFF-type superconducting spin valves.

The predictions of the dirty limit quasiclassical theory were re-analyzed in the clean limit by self-consistent numerical solutions of Bogoliubov–de Gennes equations [133]. The calculations had been performed for relatively wide range of thicknesses for the outer layer (F2 in our notations, up to $0.6\xi_S$) and thin inner F-layer (F1 in our notations, typically the thickness up to $0.1\xi_S$), and for the values of the exchange energy corresponding to moderate and strong ferromagnets ($E_{ex}$ up to $0.15\varepsilon_F$, $\varepsilon_F$ being the Fermi energy). It turned out that all features obtained in the dirty limit were confirmed even with enhanced magnitude of the SSV effects. This indicates that the superconducting properties of the critical state of S/F1/F2 structures have universal character that distinguishes them from F1/S/F2 structures.

Experimentally, Leksin et al. studied P–AP SSV effect in Fe/Cu/Fe/In [134–136] and Fe/Cu/Fe/Pb heterostructures [137–139] prepared by an UHV electron beam evaporation technique. In the first experiment [134], the small but pure *P–AP* effect

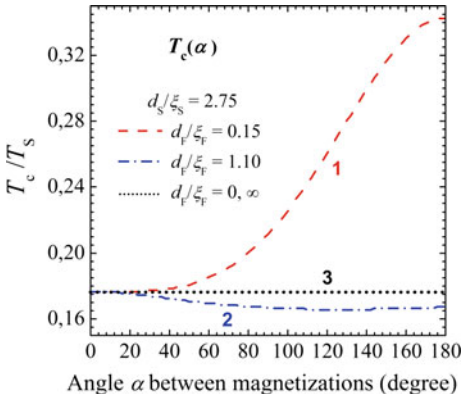


**Fig. 12** Critical temperature $T_c$ versus the misalignment angle $\alpha$ for various thicknesses of the Fl-layer. Curves *1* and *2* correspond to the standard and inverse SSV effects, respectively. $d_{F1} = 0$ case is equivalent to S/F bilayer; therefore, the superconducting $T_c$ does not depend on angle (dot line 3). At $\alpha = 0$, all the curves coincide, since in this case the F part of the system is physically equivalent to a single half-infinite F-layer. Adapted Fig. 3 from the article by Ya.V. Fominov, A.A. Golubov, T.Yu. Karminskaya, M.Yu. Kupriyanov, R.G. Deminov, and L.R. Tagirov originally published in Journ. Exp. Theor. Phys. Letters (JETP Letters) **91**, 308 (2010) with permission of Pleiades Publishing, Ltd

was measured on the structure $CoO_x$/Fe(2.4 nm)/Cu(4 nm)/Fe(0.5 nm)/In(230 nm) (the difference $\Delta T_c = +19$ mK is larger than the width of the resistive transition, $\delta T_c = 7$ mK) [134]. One of the reasons that the pure effect could be observed is the sharp SF interface due to the mutual immiscibility of iron and indium and the large superconducting coherence length of the latter. As a result, full switching of the structure between the normal state-resistance and zero-resistance superconducting state had been achieved.

Further detailed studies have shown that $\Delta T_c(d_{F2})$ can be positive and negative as well, showing standard and inverse SSV effects in accordance with the theory [131]. The oscillatory behavior of $\Delta T_c(d_{F2})$ was also observed in the $CoO_x$(4 nm)/Fe(2.5 nm)/Cu(4 nm)/Fe($d_{Fe2}$)/Pb(35 nm) heterostructures [137–139]. For the both systems, a standard SSV effect holds at values $d_{F2} < 1$ nm, and it turns into the inverse *P–AP* effect at the interval 1 nm $< d_{F2} <$ 2 nm ($\Delta T_{c,max} \sim 20$ mK and 40 mK, $\Delta T_{c,min} \sim -32$ mK and $-14$ mK for structures with In and Pb, respectively). At the same time, one could assume a better agreement between the above experimental data and the theory in the clean limit, since metallic iron used as a material for the F-layers is certainly very strong and clean ferromagnet. Indeed, the length $L_F$ in the range of around 1 nm looks quite reasonable as a measure of the $\Delta T_c$ oscillations half-period, since it is an expected oscillations length of the $s_0$ singlet and $s_{10}$-triplet pairing functions in clean and strong elemental ferromagnets, like iron and cobalt, deposited in ultra-high vacuum conditions.

Similar results for $T_c(\theta)$, with maximal P–AP SSV effect of about 8 mK, were obtained in [140] for the structure of CoO/Co/Cu/Co/Nb(17) (with variable thickness

of the cobalt and copper layers). A fit within the numerical solution of the clean-limit Bogoliubov–de Gennes equations has shown satisfactory agreement using reasonable conduction-band exchange splitting energy ~$0.15\varepsilon_F$.

The Au(6)/Nb(50)/Co(1.6)/Nb(3)/Co(0.8)/IrMn(4)/Co(3)/Ta(7.5)/Si(sub) structure (the numbers indicate thickness of the layers in nm) was studied by Flokstra et al. [141]. Compared to the previous work, the superconducting Nb-layer is much thicker (50 nm against 17 nm); therefore, only the long-range $s_{11}$ pairing is expected to permeate across the 50-nm-thick niobium being responsible for the observed resistance changes and variations of $T_c$ with the angle between magnetic moments of the ferromagnetic layers. Indeed, the P–AP SSV is pretty small (2–3 mK) but detectable, and $T_{c\mathrm{AP}}$ is always higher than $T_{c\mathrm{P}}$.

In [142], a Co/Cu/NiFe(Py)/Cu/Nb superconducting pseudo-spin valves were studied, where the magnetically hard cobalt and magnetically soft permalloy (NiFe(Py)) were used to create well-distinguished magnetic configurations upon rotating the sample with respect to an initial in-plane saturation field of 3 kOe along the hard axis of the Py-layer. At every rotation step, a 50 Oe in-plane magnetic field was applied, sufficient to align and saturate the Py magnetic moment without affecting much harder Co-layer staying at the remanent state. The P–AP configurations difference of about 10 mK (see Fig. 3b of the paper, the sample Cu(5)/Co(6)/Cu(5)/Py(4)/Cu(5)/Nb(21)—numbers in nm units) had been achieved representing the inverse SSV effect.

Finally, the F1/N/F2/S structure of the "mixed" type was prepared to observe the triplet spin valve effect [143, 144]; namely, for a magnetically hard layer F1, the strong ferromagnet (Co) has used, while for a magnetically soft layer F2—weak ferromagnetic alloy $Cu_{41}Ni_{59}$, and thin (6 nm < $d_{S,\,cr}$, N-layer) Nb magnetically decoupled the Co- and $Cu_{41}Ni_{59}$-layers to allow them rotate independently. A few nanometers thick $Cu_{41}Ni_{59}$ is known a perpendicular anisotropy material [145] with the magnetic easy axis normal to the film plane. This feature was utilized to cover three characteristic alignments when remagnetizing the sample in a magnetic field applied in-plane: parallel at complete saturation, orthogonal at a coercive field of the soft layer, and antiparallel at saturation of the soft layer. The scenario was realized cooling down the sample from room temperature to 10 K in an in-plane magnetic field of about 1T and then circulating along the major magnetic hysteresis loop in the range (−5, +5) kOe. The P–AP SSV effect in 3–5 mK range was observed in the experiments.

More complicated heterostructures, comprising several superconducting and ferromagnetic layers, were considered theoretically in [146–152], albeit hitherto remain unexplored experimentally.

## 6 Discussion and Conclusion

The main goal of this review chapter is to analyze to date status in experimental studies of the superconducting spin valves—a class of superconducting spintronic

devices. Intentionally, the heterostructure devices can be switched between normal-conducting state and superconducting state applying a pulse of weak (from several to dozens Oersted) magnetic field which re-magnetizes magnetically soft ferromagnetic layer parallel and antiparallel to a magnetically hard, reference ferromagnetic layer. The superconducting state critical temperature $T_c$ changes synchronously with the switching of the magnetic state. It is a SSV effect quantified in a $T_c$ difference between the AP and P magnetic configurations, $\Delta T_c = T_c^{AP} - T_c^{P}$, which can be either positive (standard or direct SSV effect) or negative (inverse SSV effect). Though the theory for the elementary FSF- and FFS-core structures forecasts the size of the SSV effect measured in a portion of $T_S$, the transition temperature of a superconducting material itself, the experimentally measured SSV in vast majority of cases lies within 100 mK. The effect pretty easy to measure, however, is hard to imagine in applications. There are several obstacles on a way to realize an SSV switching device:

(1) Weak alloy ferromagnets (like CuNi alloy with the Ni content in the range 52–60%) provide longer coherence length because of smaller exchange splitting of the conduction band; however, intrinsic magnetic inhomogeneity of the alloy and possible clustering destroy superconducting pairing, thus negating advantages of the alloy ferromagnet utilization. In the absence of stoichiometric low-temperature weak ferromagnets, the iron-group–palladium alloys (PdFe, e.g., [153]) can be viewed as a dilute ferromagnetic material for superconductor–ferromagnet hybrids. Palladium and platinum are enhanced paramagnets close to the Stoner criterion of paramagnet–ferromagnet transition, so small doping with iron or nickel (of around 1 at.%) causes these alloys to be ferromagnets with low Curie temperature of the order of 15–50 K [154]. More homogeneous ferromagnetism with lower spin-flip scattering is expected for dilute Pd alloys, though possible clustering of iron is anticipated according to [155] in $Pd_{1-x}Fe_x$ alloy with $x = 0.01$. An additional advantage of the Pd (or Pt)-based alloys is a temporal stability of the material against deterioration;
(2) Strong ferromagnets like iron, cobalt, and nickel have large exchange splitting of the conduction band and hence short coherence length of the order of 1 nm. Therefore, extremely thin layers must be used (also of the order of 1 nm), and it is hard to provide flatness of the film and low roughness of the interfaces (the best one in the range of 0.3–0.5 nm turns out comparable with a film thickness);
(3) At 1–10 nm range of thickness, mesoscopic dimensional effects start to manifest themselves; for example, physical properties and parameters, like electron mean free paths, of materials are determined mostly by interfaces but not the bulk. This has to be controlled in experiment by preceding material studies on pilot samples and also properly treated in a theory to make predictive calculations;
(4) Large desired SSV effect ($\Delta T_c$ up to 1 K) alone is necessary but not sufficient condition, and it must be larger than the superconducting transition width $\delta T_c$: $\Delta T_c \gg \delta T_c$, to provide full switching between the normal-conducting and zero-resistance superconducting states;

(5) There is no routinely applicable theory for SSVs based on strong and clean ferromagnets (like iron, cobalt, and nickel prepared at UHV conditions). The case intermediate between the clean and the dirty limits, which may be necessary to correctly treat permalloy, for example, is *terra incognita* yet; the only known fact is that in this case the decay length and the spatial oscillation period of the superconducting correlations in F-layer may exhibit a nonmonotonic dependence as a function of its exchange field or its electron mean free path [156];
(6) Remagnetization should be done by an in-plane uniaxial magnetic field upon which domain structures may superimpose their stray fields influence onto proximity physics. This domain structure issue, however, can be relaxed in micro- and nanostructured samples with lateral dimensions below the equilibrium magnetic domain size;
(7) It is desirable that both idle states, between which the switching occurs, would not require retaining field;
(8) There is a still poorly explored issue of multilayer structures in superconducting spintronics. Indeed, the *spectral* character of superconductivity in multilayer S/F structures to possess multiple superconducting states determines their fundamental properties and promises perspectives in superconducting spintronics.

Both experimentalists' and theorists' efforts are expected to optimize the material choice and design of superconducting spin valves to realize a kind of proximity effect spintronic device physics. At the same time, clear understanding of microscopic processes behind the S/F device physics and development of the mathematical apparatus to calculate basic thermodynamic characteristics of the complicated S/F heterostructures have obviously extended generality and applications to other kinds of superconducting heterostructures.

**Acknowledgements** The authors gratefully acknowledge a long-term cooperation with C. Attanasio, I. Garifullin, S. Gsell, S. Horn, J.-M. Kehrle, D. Lenk, H.-A. Krug von Nidda, J. Lindner, C. Müller, J. Moosburger-Will, R. Morari, A. Prepelitsa, E. Antropov, E. Nold, G. Obermeier, V. Oboznov, S.L. Prischepa, C. Cirillo, J. Aarts, N. Pugach, V.V. Ryazanov, M. Schreck, R. Tidecks, H. Zabel, V.I. Zdravkov. Authors are grateful to A.I. Buzdin and J.Y. Gu for the permission to use the materials from their articles. Special thanks to A.v. Humboldt Foundation (Karlsruhe-INT/Kishinev-IIEN Institutspartnerschaften-Project), to DFG (Grant No. HO 955/9-1), to the Russian Science Foundation (M.Yu.K, Grant No 17-12-01079) and Ministry of Education of the Republic Belarus. L.R.T. acknowledges partial support from RFBR (grant No 16-02-01171_a) and Institute for Advanced Studies, Tatarstan Academy of Sciences. A.S.S. acknowledges support from STCU (grant No 6329) and the Moldova Academy of Sciences research project "Nonuniform superconductivity as the base for superconducting spintronics."

## References

1. S.A. Wolf, D. Treger, IEEE Trans. Magn. **36**, 2748 (2000)
2. S.A. Wolf, D.D. Awschalom, R.A. Buhrman, J.M. Daughton, S. von Molnar, M.L. Roukes, A.Y. Chtchelkanova, D.M. Treger, Science **294**, 1488 (2001)

3. M.N. Baibich, J.M. Broto, A. Fert, F. Nguen van Dau, F. Petroff, P. Etienne, G. Creuzet, A. Friederich, J. Chazelas, Phys. Rev. Lett. **61**, 2472 (1988)
4. G. Binasch, P. Grünberg, F. Saurenbach, W. Zinn, Phys. Rev. B **39**, 4828 (1989)
5. I. Žutić, J. Fabian, S. Das Sarma, Rev. Mod. Phys. **76**, 323 (2004)
6. A. Fert, Uspekhi Fizicheskih Nauk **178**, 1136 (2008) [Physics-Uspekhi (Advances in Physics Sciences) **178**, 1136 (2008)]
7. N.F. Mott, Proc. R. Soc. Lond. A **156**, 368 (1936)
8. H. Zabel, Superlatt. Microstruct. **46**, 541 (2009)
9. E.Y. Tsymbal, D.G. Pettifor, Perspectives of giant magnetoresistance. Solid State Phys. **56**, in ed. by H. Ehrenreich, F. Spaepen (Academic Press, 2001), p. 113
10. P.A. Grünberg, Physics-Uspekhi (Adv. Phys. Sci.) **178**, 1349 (2008) [Uspekhi Fizicheskih Nauk **178**, 1349 (2008)]
11. E.Y. Tsymbal, I. Žutić, *Handbook of Spin Transport and Magnetism* (CRC Press, Taylor and Francis Group, 2012), p. 808
12. P.G. de Gennes, Phys. Lett. **23**, 10 (1966)
13. A.I. Buzdin, Rev. Mod. Phys. **77**, 935 (2005)
14. G. Deutscher, F. Meunier, Phys. Rev. Lett. **22**, 395 (1969)
15. J.J. Hauser, Phys. Rev. Lett. **23**, 374 (1969)
16. J. Evetts, *Concise Encyclopedia of Magnetic and Superconducting Materials* (Pergamon, 1992)
17. M.L. Kulić, M. Endres, Phys. Rev. B **62**, 11846 (2000)
18. A. Millis, D. Rainer, J.A. Sauls, Phys. Rev. B **38**, 4504 (1988)
19. T. Tokuyasu, J.A. Sauls, D. Rainer, Phys. Rev. B **38**, 8823 (1988)
20. A. Cottet, W. Belzig, Phys. Rev. B **72**, 180503(R) (2005)
21. M. Eschrig, Rep. Progr. Phys. **78**, 104501 (2015)
22. A. Cottet, Phys. Rev. B **76**, 224505 (2007)
23. B. Li, N. Roschewsky, B.A. Assaf, M. Eich, M. Epstein-Martin, D. Heiman, M. Münzenberg, J.S. Moodera, Phys. Rev. Lett. **110**, 097001 (2013)
24. D. Lenk, R. Morari, V.I. Zdravkov, A. Ullrich, G. Obermeier, C. Müller, A.S. Sidorenko, H.-A. Krug von Nidda, S. Horn, L.R. Tagirov, R. Tidecks, Phys. Rev. B **96**, 184521 (2017) (Appendix A)
25. Y. Zhu, A. Pal, M.G. Blamire, Z.H. Barber, Nat. Mater. **16**, 195 (2017)
26. A.A. Golubov, M.Yu. Kupriyanov, Nat. Mater. **16**, 156 (2017)
27. B.I. Kochelaev, L.R. Tagirov, and M.G. Khusainov, Sov. Phys. JETP **49**, 291 (1979) [Zh. Eksp. Teor. Fiz. **76**, 578 (1979); **79**, 333E (1980)]
28. B.I. Kochelaev, L.R. Tagirov, Solid State Commun. **53**, 961 (1995)
29. B.I. Kochelaev, L.R. Tagirov, Sov. Phys. JETP **62,** 787 (1985) [Zh. Eksp. Teor. Fiz. **89**, 1358 (1985)]
30. L.R. Tagirov, IEEE Trans. Magn. **23**, 2230 (1987)
31. V.L. Ginzburg, Sov. Phys. JETP **4**, 153 (1957) [Zh. Eksp. Teor. Fiz. **31**, 202 (1956)]
32. P. Fulde, R. Ferrell, Phys. Rev. **135**, A550 (1964)
33. A.I. Larkin, Yu.N. Ovchinnikov, JETP **47**, 1136 (1964)
34. P. Fulde, Adv. Phys. **22**, 667 (1973), Fig. 22
35. P.G. de Gennes, E. Guyon, Phys. Lett. **3**, 168 (1963)
36. N.R. Werthamer, Phys. Rev. **132**, 2440 (1963)
37. P.G. de Gennes, Rev. Mod. Phys. **36**, 225 (1964)
38. B.Y. Jin, J.B. Ketterson, Adv. Phys. **38**, 189 (1989)
39. A.S. Sidorenko, Low Temp. Phys. **43**(7), 366–371 (2017)
40. C.L. Chien, D.H. Reich, J. Magn. Magn. Mater. **200**, 83 (1999)
41. Yu.A. Izyumov, Yu.N. Proshin, M.G. Khusainov, Usp. Fiz. Nauk **172**, 113 (2002) [Physics-Uspekhi **45**, 109 (2002)] (see also comment by Ya.V. Fominov, M.Yu. Kupriyanov, and M.V. Feĭgel'man, Physics-Uspekhi **46**, 105 (2003))
42. A.A. Golubov, M.Yu. Kupriyanov, E. Il'ichev, Rev. Mod. Phys. **76**, 411 (2004)
43. I.F. Lyuksyutov, V.L. Pokrovsky, Adv. Phys. **54**, 67 (2005)

44. K.B. Efetov, I.A. Garifullin, A.F. Volkov, K. Westerholt, in *Magnetic Heterostructures. Advances and Perspectives in Spinstructures and Spintransport*. Springer Tracts in Modern Physics, vol. 227 ed. by H. Zabel, S.D. Bader (Springer, Berlin, Heidelberg, 2008), Chap. 5, pp. 251–289
45. F.S. Bergeret, A.F. Volkov, K.B. Efetov, Rev. Mod. Phys. **77**, 1321 (2005)
46. M. Eschrig, Phys. Today **64**, 43 (2011)
47. M.G. Blamire, J.W.A. Robinson, J. Phys.: Condens. Matter **26**, 453201 (2014)
48. J. Linder, J.W.A. Robinson, Nat. Phys. **11**, 307 (2015)
49. L.R. Tagirov, Phys. Rev. Lett. **83**, 2058 (1999)
50. A.I. Buzdin, A.V. Vedyayev, N.V. Ryzhanova, Europhys. Lett. **48**, 686 (1999)
51. B. Dieny, V.S. Speriosu, S.S.P. Parkin, B.A. Gurney, D.R. Wilhoit, D. Mauri, Phys. Rev. B **43**, R1297 (1991)
52. K.D. Usadel, Phys. Rev. Lett. **25**, 507 (1970)
53. M.G. Khusainov, Yu.N. Proshin, Phys. Rev. B **56**, R14283 (1997). Erratum: Phys. Rev. B **62**, 6832E (2000)
54. L.R. Tagirov, Physica C **307**, 145 (1998)
55. Ya.V. Fominov, A.A. Golubov, M.Yu. Kupriyanov, JETP Lett. **77**, 510 (2003) [Pis'ma v ZhETF **77**, 609 (2003)]
56. I. Baladié, A. Buzdin, Phys. Rev. B **67**, 014523 (2003)
57. S. Tollis, Phys. Rev. B **69**, 104532 (2004)
58. J.Y. Gu, C.-Y. You, J.S. Jiang, J. Pearson, Ya.B. Bazaliy, S.D. Bader, Phys. Rev. Lett. **89**, 267001 (2002)
59. C.-Y. You, Ya.B. Bazaliy, J.Y. Gu, S.-J. Oh, L.M. Litvak, S.D. Bader, Phys. Rev. B **70**, 014505 (2004)
60. A. Potenza, C.H. Marrows, Phys. Rev. B **71**, 180503(R) (2005)
61. J. Zhu, I.N. Krivorotov, K. Halterman, O.T. Valls, Phys. Rev. Lett. **105**, 207002 (2010)
62. M. Fauré, A.I. Buzdin, A.A. Golubov, M.Yu. Kupriyanov, Phys. Rev. B **73**, 064505 (2006)
63. M. Fauré, A.I. Buzdin, D. Gusakova, Physica C **454**, 61 (2007)
64. M.Yu. Kuprianov, V.F. Lukichev, Sov. Phys. JETP **67**, 1163 (1988) [Zh. Eksp. Teor. Phys. **94**, 139 (1988)]
65. L.R. Tagirov, N. Garcia, Superlatt. and Microstr. **41**, 152 (2007)
66. J. Aarts, C. Attanasio, C. Bell, C. Cirillo, M. Flokstra, J.M. v. d. Knaap, *Nanoscience and Engineering in Superconductivity* (Springer, Berlin, Heidelberg, 2010), p. 323
67. Y. Luo, K. Samwer, Eur. Phys. Lett. **91**, 37003 (2010)
68. V.I. Zdravkov, J. Kehrle, G. Obermeier, S. Gsell, M. Schreck, C. Müller, H.-A. Krug von Nidda, J. Lindner, J. Moosburger-Will, E. Nold, R. Morari, V.V. Ryazanov, A.S. Sidorenko, S. Horn, R. Tidecks, L.R. Tagirov, Phys. Rev B **82**, 054517 (2010)
69. V.I. Zdravkov, J. Kehrle, G. Obermeier, A. Ullrich, S. Gsell, D. Lenk, C. Müller, R. Morari, A.S. Sidorenko, V.V. Ryazanov, L.R. Tagirov, R. Tidecks, S. Horn, Supercond. Sci. Technol. **24**, 095004 (2011)
70. V.I. Zdravkov, J. Kehrle, D. Lenk, G. Obermeier, A. Ullrich, C. Müller, H.A. Krug von Nidda, R. Morari, A.S. Sidorenko, L.R. Tagirov, S. Horn, R. Tidecks, J. Appl. Phys. **114**, 033903 (2013)
71. V.I. Zdravkov, D. Lenk, R. Morari, A. Ullrich, G. Obermeier, C. Müller, H.-A. Krug von Nidda, A.S. Sidorenko, S. Horn, R. Tidecks, L.R. Tagirov, Appl. Phys. Lett. **103**, 062604 (2013)
72. E. Antropov, M. Kalenkov, A. Zaikin, J. Kehrle, V. Zdravkov, R. Morari, A. Socrovisciuc, C. Müller, G. Obermeier, S. Horn, L.R. Tagirov, A. Sidorenko, H. Hahn, R. Tidecks, Supercond. Sci. Technol. **26**, 085003 (2013)
73. I.C. Moraru, W.P. Pratt Jr., N.O. Birge, Phys. Rev. Lett. **96**, 037004 (2006)
74. I.C. Moraru, W.P. Pratt Jr., N.O. Birge, Phys. Rev. B **74**, 220507(R) (2006)
75. A.S. Sidorenko, V.I. Zdravkov, A. Prepelitsa, C. Helbig, Y. Luo, S. Gsell, M. Schreck, S. Klimm, S. Horn, L.R. Tagirov, R. Tidecks, Annalen der Physik (Leipzig-Berlin) **12**, 37–50 (2003)

76. V.N. Kushnir, S.L. Prischepa, C. Cirillo, C. Attanasio, Eur. Phys. J. B **52**, 9 (2006)
77. D. Mancusi, E.A. Ilyina, V.N. Kushnir, S.L. Prischepa, C. Cirillo, C. Attanasio, J. Appl. Phys. **110**, 113904 (2011)
78. V.N. Kushnir, M.Yu. Kupriyanov, Low Temp. Phys. **42**, 900 (2016) [Fiz. Nizk. Temp. **42**, 1148 (2016)]
79. G.-X. Miao, A.V. Ramos, J.S. Moodera, Phys. Rev. Lett. **101**, 137001 (2008)
80. J. Aarts, J.M.E. Geers, E. Brück, A.A. Golubov, R. Coehoorn, Phys. Rev. B. **56**, 2779 (1997)
81. A.Yu. Rusanov, S. Habraken, J. Aarts, Phys. Rev. B. **73**, 060505(R) (2006)
82. J. Aarts, A.Yu. Rusanov, Comptes rendus—Physique **7**, 99 (2006)
83. S. Takahashi, H. Imamura, S. Maekawa, Phys. Rev. Lett. **82**, 3911 (1999)
84. V. Peña, Z. Sefrioui, D. Arias, C. Leon, J. Santamaria, J.L. Martinez, S.G.E. te Velthuis, A. Hoffmann, Phys. Rev. Lett. **94**, 057002 (2005)
85. D. Stamopoulos, E. Manios, M. Pissas, Phys. Rev. B **75**, 014501. (2007)
86. M.G. Blamire, M. Ali, C.-W. Leung, C.H. Marrows, B.J. Hickey, Phys. Rev. Lett. **98**, 217202 (2007)
87. D. Stamopoulos, E. Aristomenopoulou, A. Lagogiannis, Supercond. Sci. Technol. **27**, 095008 (2014)
88. R. Steiner, P. Ziemann, Phys. Rev. B **74**, 094504 (2006)
89. E.B. Sonin, Sov. Tech. Phys. Lett. **14**, 714 (1988). [Pis'ma Zh. Tekh. Fiz. **14**, 1640 (1988)]
90. E.B. Sonin, Phys. Rev. B **66**, 100504R (2002)
91. V.V. Ryazanov, V.A. Oboznov, A.S. Prokof'ev, S.V. Dubonos, JETP Lett. **77**, 39 (2003) [Pis'ma v ZhETF **77**, 43 (2003)]
92. I.S. Burmistrov, N.M. Chtchelkatchev, Phys. Rev. B **72**, 144520 (2005)
93. D.H. Kim, T.J. Hwang, Physica C **455**, 58 (2007)
94. J. Zhu, X. Cheng, C. Boone, I.N. Krivorotov, Phys. Rev. Lett. **103**, 027004 (2009)
95. C. Bell, S. Turşucu, J. Aarts, Phys. Rev. B **74**, 214520 (2006)
96. M. Flokstra, J. M. van der Knaap, J. Aarts, Phys. Rev. B **82**, 184523 (2010)
97. A.Yu. Rusanov, T.E. Golikova, S.V. Egorov, JETP Lett. **87**, 175 (2008) [Pis'ma v ZhETF **87**, 204 (2008)]
98. T. Trunk, M. Redjdal, A. Kákay, M.F. Ruane, F.B. Humphrey, J. Appl. Phys. **89**, 7606 (2001)
99. M. Houzet, A.I. Buzdin, Phys. Rev. B **74**, 214507 (2006)
100. T. Champel, M. Eschrig, Phys. Rev. B **71**, 220506 (2005); **72**, 054523 (2005)
101. A.Yu. Rusanov, M. Hesselberth, J. Aarts, A.I. Buzdin, Phys. Rev. Lett. **93**, 057002 (2004)
102. P.V. Leksin, R.I. Salikhov, I.A. Garifullin, H. Vinzelberg, V. Kataev, R. Klingeler, L.R. Tagirov, and B. Büchner, JETP Lett. **90**, 59 (2009). [Pis'ma v ZhETF **90**, 64 (2009)]
103. M. Flokstra, J. Aarts, Phys. Rev. B **80**, 144513 (2009)
104. K. Halterman, O.T. Valls, Phys. Rev. B **65**, 014509 (2001)
105. K. Halterman, O.T. Valls, Phys. Rev. B **72**, 060514(R) (2005)
106. K. Halterman, P.H. Barsic, O.T. Valls, Phys. Rev. Lett. **99**, 127002 (2007)
107. K. Halterman, O.T. Valls, P.H. Barsic, Phys. Rev. B. **77**, 174511 (2008)
108. M. Božović, Z. Radović, Europhys. Lett. **70**, 513 (2005)
109. C.-T. Wu, O.T. Valls, K. Halterman, Phys. Rev. B **86**, 014523 (2012)
110. G. Eilenberger, Z. Phys. **214**, 195 (1968)
111. J. Linder, M. Zareyan, A. Sudbø, Phys. Rev. B **79**, 064514 (2009)
112. S.V. Mironov, A. Buzdin, Phys. Rev. B **89**, 144505 (2014)
113. A. Buzdin, M. Daumens, Europhys. Lett. **64**, 510 (2003)
114. S. Tollis, M. Daumens, A. Buzdin, Phys. Rev. B **71**, 024510 (2005)
115. X. Montiel, D. Gusakova, M. Daumens, A. Buzdin, Europhys. Lett. **86**, 67002 (2009)
116. J.Y. Gu, G.B. Halász, J.W.A. Robinson, M.G. Blamire, Phys. Rev. Lett. **115**, 067201 (2015)
117. V.N. Kushnir, E.A. Ilyina, S.L. Prischepa, C. Cirillo, C. Attanasio, Superlattices Microstruct. **43**, 86 (2008)
118. V.N. Kushnir, S.L. Prischepa, C. Cirillo, C. Attanasio, J. Appl. Phys. **106**, 113917 (2009)
119. V.N. Kushnir, S.L. Prischepa, C. Cirillo, A. Vecchione, C. Attanasio, M.Yu. Kupriyanov, J. Aarts, Phys. Rev. B **84**, 214512 (2011)

120. J. Jensen, A.R. Mackintosh, *Rare Earth Magnetism. Structures and Excitations* (Clarendon Press, Oxford, 1991)
121. J.Y. Gu, J.W.A. Robinson, M. Bianchetti, N.A. Stelmashenko, D. Astill, F.M. Grosche, J.L. MacManus-Driscoll, M.G. Blamire, APL Mater. **2**, 046103 (2014)
122. A. Tesauro, A. Aurigemma, C. Cirillo, S.L. Prischepa, M. Salvato, C. Attanasio, Supercond. Sci. Technol. **18**, 1 (2005)
123. I. Sosnin, H. Cho, V.T. Petrashov, A.F. Volkov, Phys. Rev. Lett. **96**, 157002 (2006)
124. V.N. Kushnir, M.Yu. Kupriyanov, Pis'ma Zh. Exp. Teor. Fiz **93**, 597 (2011) [JETP Lett. **93**, 539 (2011)]
125. D. Movshovitz, N. Wiser, Phys. Rev. B **41**, 10503 (1990)
126. G. Brammertz, A.A. Golubov, P. Verhoeve, R. den Hartog, T. Peacock, H. Rogalla, Appl. Phys. Lett. **80**, 2955 (2002)
127. V.N. Kushnir, S.L. Prischepa, Dokl. NAN Belarusi **56**, 60 (2012)
128. S. Oh, D. Youm, M.R. Beasley, Appl. Phys. Lett. **71**, 2376 (1997)
129. K. Westerholt, D. Sprungmann, H. Zabel, R. Brucas, B. Hjörvarsson, D.A. Tikhonov, I.A. Garifullin, Phys. Rev. Lett. **95**, 097003 (2005)
130. G. Nowak, K. Westerholt, H. Zabel, Supercond. Sci. Technol. **26**, 025004 (2013)
131. Ya.V. Fominov, A.A. Golubov, T.Yu. Karminskaya, M.Yu. Kupriyanov, R.G. Deminov, L.R. Tagirov, JETP Lett. **91**, 308 (2010). [Pis'ma v Zh. Exp. Teor. Fiz **91**, 329 (2010)]
132. T.Yu. Karminskaya, A.A. Golubov, M.Yu. Kupriyanov, Phys. Rev. B. **84**, 064531 (2011)
133. C.-T. Wu, O.T. Valls, K. Halterman, Phys. Rev. B **86**, 014523 (2012)
134. P.V. Leksin, N.N. Garif'yanov, I.A. Garifullin, J. Schumann, H. Vinzelberg, V. Kataev, R. Klingeler, O.G. Schmidt, and B. Büchner, Appl. Phys. Lett. **97**, 102505 (2010)
135. P.V. Leksin, N.N. Garif'yanov, I.A. Garifullin, J. Schumann, V. Kataev, O.G. Schmidt, B. Büchner, Phys. Rev. Lett. **106**, 067005 (2011)
136. P.V. Leksin, N.N. Garif'yanov, I.A. Garifullin, J. Schumann, V. Kataev, O.G. Schmidt, B. Büchner, Phys. Rev. B **85**, 024502 (2012)
137. P.V. Leksin, N.N. Garif'yanov, I.A. Garifullin, J. Schumann, V. Kataev, O.G. Schmidt, B. Büchner, Phys. Rev. Lett. **109**, 057005 (2012)
138. P.V. Leksin, A.A. Kamashev, N.N. Garif'yanov, I.A. Garifullin, Ya.V. Fominov, J. Schumann, C. Hess, V. Kataev, B. Buchner, JETP Lett. **97**, 478 (2013) [Pis'ma v ZhETF **97**, 549 (2013)]
139. P.V. Leksin, N.N. Garif'yanov, A.A. Kamashev, Ya.V. Fominov, J. Schumann, C. Hess, V. Kataev, B. Büchner, I.A. Garifullin, Phys. Rev. B **91**, 214508 (2015)
140. A.A. Jara, C. Safranski, I.N. Krivorotov, C.-T. Wu, A.N. Malmi-Kakkada, O.T. Valls, K. Halterman, Phys. Rev. B **89**, 184502 (2014)
141. M.G. Flokstra, T.C. Cunningham, J. Kim, N. Satchell, G. Burnell, S.J. Bending, P.J. Curran, S.J. Langridge, C. Kinane, J.F.K. Cooper, N. Pugach, M. Eschrig, S.L. Lee, Phys. Rev. B **91**, 060501(R) (2015)
142. X.L. Wang, A. Di Bernardo, N. Banerjee, A. Wells, F.S. Bergeret, M.G. Blamire, J.W.A. Robinson, Phys. Rev. B **89**, 140508(R) (2014)
143. V.I. Zdravkov, J. Kehrle, G. Obermeier, D. Lenk, H.-A. Krug von Nidda, C. Müller, M.Yu. Kupriyanov, A.S. Sidorenko, S. Horn, R. Tidecks, L.R. Tagirov, Phys. Rev. B **87**, 144507 (2013)
144. D. Lenk, V.I. Zdravkov, J.-M. Kehrle, G. Obermeier, A. Ullrich, R. Morari, H.-A. Krug von Nidda, C. Müller, M.Yu. Kupriyanov, A.S. Sidorenko, S. Horn, R.G. Deminov, L.R. Tagirov, R. Tidecks, Beilstein J. Nanotechnol. **7**, 957 (2016)
145. A. Ruotolo, C. Bell, C.W. Leung, M.G. Blamire, J. Appl. Phys. **96**, 512 (2004)
146. Yu.N. Proshin, Yu.A. Izyumov, M.G. Khusainov, Phys. Rev. B **64**, 064522 (2001)
147. K. Halterman, O.T. Valls, Phys. Rev. B **69**, 014517 (2004)
148. K. Halterman, O.T. Valls, Phys. Rev. B **70**, 104516 (2004)
149. Y.N. Proshin, A. Zimin, N.G. Fazleev, M.G. Khusainov, Phys. Rev. B **73**, 184514 (2006)
150. P.H. Barsic, O.T. Valls, K. Halterman, Phys. Rev. B **75**, 104502 (2007)
151. V.N. Kushnir, M.Yu. Kupriyanov, JETP Lett. **93**, 539 (2011)

152. V.N. Kushnir, S.L. Prischepa, C. Cirillo, A. Vecchione, C. Attanasio, M.Yu. Kupriyanov, J. Aarts, Phys. Rev. B **84**, 214512 (2011)
153. I.A. Golovchanskiy, V.V. Bolginov, N.N. Abramov, V.S. Stolyarov, A. Ben Hamida, V.I. Chichkov, D. Roditchev, V.V. Ryazanov, Journ. Appl. Phys. **120**, 163902 (2016)
154. M.Yu. Kupriyahov, A.A. Golubov, M. Siegel, Proc. SPIE **6260**, 62600S (2006)
155. L.S. Uspenskaya, A.L. Rakhmanov, L.A. Dorosinskii, A.A. Chugunov, V.S. Stolyarov, O.V. Skryabina, S.V. Egorov, JETP Lett. **97**, 155 (2013)
156. N.G. Pugach, M.Yu. Kupriyanov, E. Goldobin, R. Kleiner, D. Koelle, Phys. Rev. B **84**, 144513 (2011)

# Superconducting Triplet Proximity and Josephson Spin Valves


**L. R. Tagirov, M. Yu. Kupriyanov, V. N. Kushnir and Anatolie Sidorenko**

**Abstract** A heterostructure comprising several ferromagnetic and superconducting layers acquires functionality of managing the superconducting properties of a system applying external magnetic field. At non-collinear magnetic configurations of the ferromagnetic layers, spin-triplet pairings can be induced in these heterostructures. The triplet pairing channel brings additional degrees of freedom to manage superconducting transition temperature in proximity effect superconducting spin valves. Applied to Josephson junctions' physics, a robust long-range pairing in ferromagnetic weak links produces spin-polarized Josephson currents available for manipulations with magnetic fields and currents. The unique features of the spin-triplet pairings in superconductor–ferromagnet heterostructures make them promising for superconducting spintronics (supertronics).

L. R. Tagirov
Zavoisky Physical-Technical Institute of Russian Academy of Sciences, Kazan 420029, Russia
e-mail: ltagirov@mail.ru

L. R. Tagirov
Universität Augsburg, Universitätsstraße 1, 86159 Augsburg, Germany

L. R. Tagirov · M. Yu. Kupriyanov
Kazan Federal University, Kazan 420008, Russia
e-mail: mkupr@pn.sinp.msu.ru

M. Yu. Kupriyanov
Skobeltsyn Institute of Nuclear Physics, Moscow State University, Moscow 119992, Russia

V. N. Kushnir
Belarus State University of Informatics and Radioelectronics, 220013 Minsk, Belarus
e-mail: vnkushnir@gmail.com

V. N. Kushnir
Physics Faculty, Belarus State University, 220000 Minsk, Belarus

A. Sidorenko (✉)
Institute of Electronic Engineering and Nanotechnologies, Academy of Sciences of Moldova, 2028 Chisinau, Moldova
e-mail: anatoli.sidorenko@kit.edu



A. Sidorenko (ed.), *Functional Nanostructures and Metamaterials for Superconducting Spintronics*, NanoScience and Technology,
https://doi.org/10.1007/978-3-319-90481-8_2

## 1 Introduction

Usually, superconductivity and ferromagnetism are considered as antagonistic long-range orders, which cannot coexist in a homogeneous medium [1]. Indeed, ferromagnetism is expected to suppress singlet s-wave superconductivity, because the presence of an exchange splitting of the conduction band breaks the time reversal symmetry of a Cooper pair. Fulde-Ferrell and Larkin-Ovchinnikov (FFLO) [2, 3] have shown that, nevertheless, superconductivity may survive in the presence of the magnetic background, however, restricted to an extremely narrow range of parameters [4]. The idea was that the Cooper pair keeping zero total spin acquires nonzero pairing momentum. There are very few examples of compounds that can be considered as showing indications of the FFLO state (see, for example, [5–8]). The idea became much more applicable for systems in which superconductivity and ferromagnetism (or, more generally, some kind of strong magnetism, like antiferromagnetism) are separated in space either because of chemical structure of a unit cell, see, for example, reviews on coexistence and interaction of superconductivity and magnetism in Chevrel phases and ternary rhodium borides [9], borocarbides [10] and ruthenates [11, 12]. From the latter, $Sr_2RuO_4$ is commonly believed to realize triplet (equal-spin pairing) superconductivity with at least p-wave pairing to fulfill symmetry requirements. There are experimental indications of the triplet superconductivity in heavy fermion compounds and low-dimensional organic salts (see, for example, a review [13] and references therein).

The artificially layered systems are ultra-thin film heterostructures in which superconductivity (S) and ferromagnetism (F) locate at different adjoining or closely lying layers but strongly interact via interfaces. These *proximity*-coupled systems exhibit a lot of unconventional features because of competition and mutual adjustment of the two long-range orders (see chapter "Basic Superconducting Spin Valves" by V.N. Kushnir et al.). Special attention has been drawn to nonzero spin pairing that could be realized in SF heterostructures atop the ferromagnetic background. Indeed, it was shown by Bergeret et al. [14] that the spin-triplet s-wave pairing can be induced by a conventional superconductor in proximity with the ferromagnetic subsystem containing non-collinear magnetizations. This pairing is non-oscillating and extraordinary long-range that makes it promising mediator of the spin-polarized Josephson current.

The theory of the triplet s-wave superconductivity had been developed in a numerous works within the diffusive limit [14–48], on the base of quasiclassical Eilenberger approximation [21, 34, 36, 49–58], in the framework of the Bogoluibov-de Gennes equations formalism [46, 48, 59–70] and reviewed in detail in [71–74]. The manifestations of the triplet pairing on the main thermodynamic characteristics (Josephson critical current, the local density of states, the critical temperature) have been investigated for the following SF systems:

(a) SF structures with domain walls [14–16, 21–23, 25, 26, 31, 34, 40, 46] (in the classical works [14–16], the choice of such structure for consideration is moti-

vated, particularly, by the observed anomalous conductivity of the ferromagnet wire contacting with superconductor [75, 76]);

(b) SF structures with a conical ferromagnets [16, 17, 23, 27, 28, 33, 38, 40, 43, 67, 68];

(c) multilayers with a non-collinear magnetizations of the F layers [18–20, 24, 29, 30, 32, 35, 37, 39, 41, 42, 44, 45, 48, 53–59, 62, 63, 66, 69, 70, 77];

(d) SF structures with a half-metal as F layer [21, 35, 49–52, 60, 61, 64, 65], firstly considered by M. Eschrig et al. [49].

The basic (primal) problem of superconducting spintronics, namely the control of the superconducting state by variations of the magnetic state, has the simplest practical solution for spin valves based on SF structures of type c [78]. The intention of this short review is to describe manifestations of this long-range equal-spin s-wave pairing in superconducting spin-valve heterostructures.

The outline of the chapter is as follows: First, we describe basic structures to control superconductivity by proximity with two metallic ferromagnet layers. Then, we give short overview of experimental works aimed to observed effects predicted by theory. Finally, we present a short description of weak superconductivity control in Josephson junctions.

## 2 Superconductor–Ferromagnet Proximity Spin Valves

In 1997, Oh et al. [79] proposed an S/F switching structure that they called superconductive magnetoresistive memory element (see Fig. 1a). The structure consists of a superconducting film S deposited onto a conventional Dieny spin valve [80]. The latter one comprises two ferromagnetic metal (FM) layers, separated by a very thin non-magnetic metal spacer, and an auxiliary insulating antiferromagnetic layer to pin the magnetic moment of the adjacent ferromagnet FM2. The FM1 layer is considered magnetically soft to rotate its magnetic moment by an external (pulsed) magnetic field. The ultra-thin non-magnetic spacer NM is necessary in real experiments to decouple exchange interaction between the neighboring FM1 and FM2 ferromagnetic layers. Thus, the resulting heterostructure is composed from superconducting and magnetic sub-systems joined via a common interface. We will call it the adjacent design (FFS-type superconducting spin valve).

Calculations within the dirty-limit quasiclassical Usadel theory [81] of superconductivity and single-mode solution of the resulting equations for superconductivity have shown that the pairing function in the S layer is suppressed stronger (this means that the superconducting transition temperature $T_c$ is lower) if the magnetic moments of the FM layers are aligned parallel [79]. With a proper choice of parameters, the $S$ layer can be switched between the normal conducting state at P alignment and the superconducting state at $AP$ alignment, i.e., serve as a superconductive memory cell. This condition $T_c^{AP} > T_c^P$ was coined as standard switching or standard supercon-

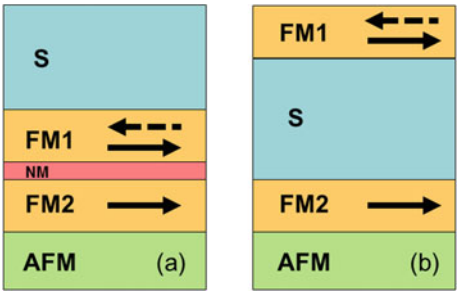


**Fig. 1** Two designs of the proximity effect superconducting spin valves: **a** FFS—adjacent, and **b** FSF—interleaved. Solid arrows show parallel (P) alignment of magnetizations (in the film plane), while the dash arrows indicate reversed magnetic moment of the FM1 layer at the antiparallel (AP) alignment of the magnetizations. AFM is an auxiliary antiferromagnetic insulator layer, and NM is very thin non-magnetic metal spacer

ducting spin-valve (SSV) effect. Naturally, in 1997 no spin-triplet pairing had been considered upon calculations by Oh et al. [79].

Later on, in [82, 83], another design of a superconducting spin valve was proposed (see Fig. 1b) in which the superconducting layer was placed in between of the ferromagnetic metal layers (FSF-type superconducting spin valve) and served simultaneously to decouple exchange interaction between the ferromagnets. Calculations within the single-mode dirty-limit quasiclassical Usadel theory have shown that similar to the adjacent FFS spin valves, the interleaved SSV exhibits $T_c^{AP} > T_c^P$, i.e, the standard SSV effect (for the full angular dependence $T_c(\alpha)$ between P and *AP* alignments see [84]). Spin-triplet pairing had not been considered upon these calculations too.

In 2003, Fominov et al. [20] re-examined the analysis of [82–84] for F/S/F SSV taking into account in addition to the singlet ($s_0$), a complete set of Matsubara odd frequency triplet component (projections zero, $s_{10}$, and $\pm 1 - s_{1,\pm 1}$) [14–19, 71–74] and applying asymptotically exact multimode solution [85] of resulting superconductivity equations. Since the $s_{1,\pm 1}$ superconducting pairing components penetrate into the ferromagnet over a distance of the order of $\xi_N \gg \xi_F$, the analog control device with the structure FM1/S/FM2 as a core is not a trivial generalization of *P*–A*P* SSV since it is based on a new effect. Nevertheless, the exact solution of the diffusive limit equations for a symmetric F/S/F structure with in-plane-magnetized layers led to a monotonically varying function $T_c(\alpha)$ [20], so that for arbitrary $\alpha$, the inequalities $T_c^P(d_F) \leq T_c(d_F, \alpha) \leq T_c^{\mathrm{AP}}(d_\mathrm{F})$ hold, and therefore, the SSV effect is standard. They have found differences of about 15% from calculations of [84] along the angular dependence of superconducting $T_c$.

The main results of [20] have also been extended on asymmetric structures FM1/S/FM2 [29, 86]. The monotony of the function $T_c(\alpha)$ had been confirmed in the experiment with the structure $Cu_{48}Ni_{52}(d_F)$/Nb(18)/$Cu_{48}Ni_{52}(d_F)$ [87]. The maximum effect, 7 mK, practically coincided with the value of $\Delta T_c$ given in [88] for an almost identical Nb/CuNi system. Quantitative analysis of the data had car-

ried out within the framework of the Bogoliubov—de Gennes equations formalism, taking into account electron scattering processes at the S–F interfaces. The agreement between the theoretical and experimental dependences of $T_c(d_F)$, and between the scaled dependences $\Delta T_c(\alpha;d_F)$ was surprisingly good (the value of the fitting parameter of the theory, $I = 0.032$, or $E_{ex} \sim 10^3$ K, is reasonable in the sense that it compensates for the absence of mean free paths in the theory of the clean limit). However, the calculated absolute values of $\Delta T_c$ were about two orders of magnitude larger, similar to the earlier studies in [88].

The dependences $T_c(\alpha)$ for the structures F1/S/F2, which satisfy the conditions of the clean limit, have a completely different character. Namely in conformity with the *P–AP* effect, they can be monotonically increasing, decreasing, and non-monotonic (see Fig. 2 adapted from [58]). Indeed, in the experiment with the Co/Nb/Co structure, oscillations were measured on the $R(\alpha)$ dependence described by a simple formula $R(\alpha) \approx R_{\min} + \Delta R\sqrt{\sin\alpha}$ [89]. The triplet SSV has also been realized based on the structure FM1/S/FM2 with the collinear vectors $\boldsymbol{M}_1$ and $\boldsymbol{M}_2$ in the case of the spin-active S–F interface (see [21] and references therein). The results of experimental investigation of such structures had been reported in [90]. The parent structure was Py/Nb/Py, for which, as in [91, 92], a weak standard switching effect had been observed. When inserting Ho interlayers between Py- and Nb-induced triplet components with spin projections $\pm 1$, the standard SSV had transformed into the inverse effect with increase in the Ho thickness to 8 nm. The critical temperature remained very high (6–7 K), which is possible only if there is a "long-range" triplet component in the condensate. Almost full switching between the normal conducting and superconducting states has been obtained in [93] in the Co/CoOx/$Cu_{41}Ni_{59}$/Nb/$Cu_{41}Ni_{59}$ core structure. By detailed matching the magnetic configurations of the ferromagnetic layers of the structure, the observed features in magnetoresistance were ascribed to generation of the triplet pairings in the system. Apparently, the works [87, 89, 90, 93] cited in this section exhaust the experimental studies of the triplet effect in the FSF-type structures.

## 3 Superconducting Spin-Valve Effect in the S/F1/N/F2 Structures

With the triplet pairing in SF heterostructures [71–74], getting more and more evidences to exist, the Oh, Youm, and Beasley FFS-valve theory was re-examined by Fominov et al. [39] to take explicitly into account the triplet pairings, zero $s_{10}$, and $\pm 1$ projection $s_{1,\pm1}$, on superconducting $T_c$ at the arbitrary misalignment angle $\alpha$ between the magnetic moments of the FM layers and under constraints $d_{F2} \to \infty$ and $T = 1$ ($T$ is a transparency of S–F interfaces).

The analysis performed within the dirty-limit quasiclassical Usadel formalism has shown that three regimes of switching can be realized in the SFF-type structure when the triplet pairings are treated in an equal footing with the singlet one (see

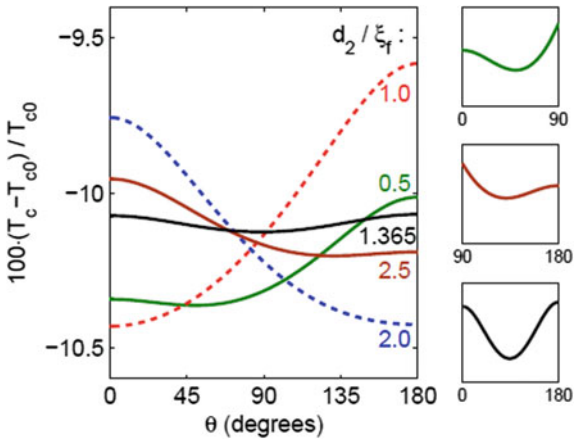


**Fig. 2** Dependences of the normalized critical temperature of the clean FM1/S/FM2 core structure on the angle $\alpha$ between the magnetic moments of the FM layers. Reprinted Fig. 4 from [S.V. Mironov, A. Buzdin, Phys. Rev. B **89**, 144505 (2014)] with permission by the American Physical Society. Copyright APS 2014

Fig. 3): The first regime was described before, and it corresponds to $T_c^{AP} > T_c^P$ and coined as *standard* switching regime (curve 1 in Fig. 3); in the second regime, the *AP* alignment transition temperature is lower than for the P alignment, $T_c^{AP} < T_c^P$, and it is *inverse* switching regime (curve 2 in Fig. 3); at last, the *triplet* switching regime (curve 3 in Fig. 3) is characterized by a pronounced concave angular dependence of $T_c(\alpha)$ with an absolute minimum at $T_c^{NC} < \{T_c^P, T_c^{AP}\}$ (NC means non-collinear magnetizations). At the same time, the unusual behavior of $T_c(\alpha)$ in the triplet switching regime could serve as indirect evidence of the triplet pairing generation in the SFF-type heterostructures. Moreover, for the triplet switching regime, the dependence $T_c(\alpha)$ shows the effect of the disappearance and reentrance of superconductivity as soon as the thickness of the S-layer becomes less than the threshold value [39]. The suppression in the critical temperature for the deviation of the vector $\boldsymbol{M}_1$ from the direction of $\boldsymbol{M}_2$ is just due to the induction of the triplet component of the superconducting condensate. The relationships between the singlet and triplet components of the superconductivity state functions of the S/F1/F2 structure have been obtained in [42] for more general case, namely for arbitrary transparencies of interfaces. It is unusual that the triplet component, unlike at such in the F1/S/F2 structure, may be the largest not in the neighborhood of $\alpha = \pi/2$, but, for example, at a slight violation of the collinearity of $\boldsymbol{M}_1$ and $\boldsymbol{M}_2$ [42]. Further, it turned out that the natural assumption of full transparency of the F1–F2 interface as a condition for the maximum of the triplet component turns out to be too strong. This fact testifies in favor of S/F1/F2 structures, because all experimental systems include N-spacer between F1 and F2 layers, so that the full transparency of F1–F2 interface is impossible (in [42], N-interlayer is taken into account by the free parameter $T_{F1F2}$). In this regard, we note that if the S material is a buffer layer (this is convenient from a technological point of view), then it could play an active role in the formation of the superconducting condensate distribution.

The analytical properties of the function $T_c(\alpha)$ and the patterns of distribution of the singlet and triplet components of the order parameter were investigated also

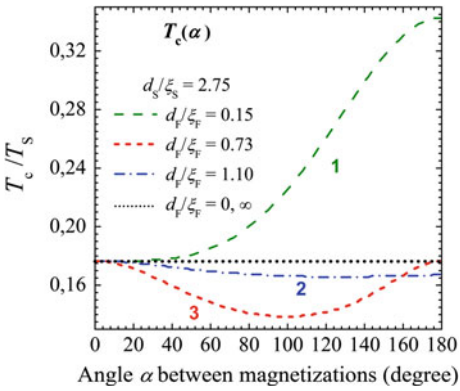


**Fig. 3** Critical temperature $T_c$ versus the misalignment angle $\alpha$ for various thicknesses of the Fl layer. For details of the parameters see [39]. Horizontal dot line is drawn for the FM1 layer thickness equal to zero, then, obviously, $T_c$ does not depend on $\alpha$. Curves *1* and *2* correspond to the standard and inverse switching effects, respectively. Curve *3* demonstrates the triplet spin-valve effect. Adapted Fig. 3 from the article by Ya.V. Fominov, A.A. Golubov, T. Yu. Karminskaya, M. Yu. Kupriyanov, R.G. Deminov, L.R. Tagirov originally published in J. Exp. Theor. Phys. Lett. (JETP Lett.) **91**, 308 (2010) with permission of Pleiades Publishing, Ltd

in the clean limit within the numeric solution of Bogoluibov-de Gennes equations [66]. The calculations were performed for the thickness of the inner F layer up to 1 nm and for the values of the exchange energy corresponding to moderate and strong ferromagnets ($E_{ex} \geq 1000$ K). As it turned out, the behavior of the obtained dependences is in fact the same as in cases (a, b) of diffusive limit (the critical temperatures and the magnitude of the SSV effects in the clean limit are higher, as it obvious). This indicates that the properties of the critical state of the structures S/F1/F2 have a universal character, which distinguishes them the structures from F1/S/F2.

The paper [39] has triggered extensive studies of adjacent SFF-type spin valves by several groups. Leksin et al. published the results of systematic experimental triplet SSV effect studies on the systems Fe/Cu/Fe/In and Fe/Cu/Fe/Pb [94–99]. The advantage of the selected materials were in sharp S-F interface due to the mutual insolubility of the selected superconducting transition (In, Pb) and ferromagnetic (Fe) materials and in narrow width of superconducting transition $\delta T_c$ of In, Pb, which is well below the $T_c$ variation $\Delta T_c$ due to SSV effect. The main result of the series of experiments with Fe($d_{F1}$)/Cu/Fe($d_{F2}$)/In system is observation of both standard and inverse SSV effects when varying the thickness $d_{F2}$. [94, 95]. The oscillatory behavior of the $\Delta T_c(d_{F2})$ dependence was observed also for Fe($d_{F1}$)/Cu/Fe($d_{F2}$)/Pb structures [96, 97]. For the both systems, a standard SSV effect holds at values $d_{F2} < 1$ nm, and it turns into the inverse *P–AP* effect at the interval 1 nm$< d_{F2} <$2 nm ($\Delta T_{c,\max}$ ~20 and 50 mK, $\Delta T_{c,\min} \sim -30$ and $-15$ mK for structures with In and Pb, respectively). This result follows directly from the theory in the diffusive limit [39],

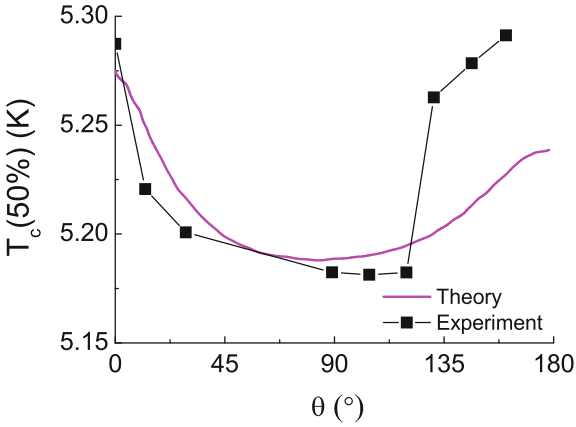


**Fig. 4** Dependences of the critical temperature of the Cu/Co/Cu/Py/Cu/Nb structure on the angle between the magnetic moments of the Co and Py layers. Reprinted Fig. 3d from [X.L. Wang, A. Di Bernardo, N. Banerjee, A. Wells, F.S. Bergeret, M.G. Blamire, and J.W.A. Robinson, Phys. Rev. B **89**, 140508(R) (2014)] with permission by the American Physical Society. Copyright APS 2014

as shown by the fit of the characteristics $\Delta T_c(d_{F2})$ (see Fig. 4 in [94] and Fig. 2 in [96]).

At the same time, one can assume better agreement between the experimental data and the theory in the clean limit, keeping in mind the curves in Fig. 2 calculated for F1/S/F2 systems in [58]. The length of $\zeta_F < 1$ nm as a measure of the oscillations of $\Delta T_c$ is completely natural, since it is also a measure of the oscillations of the order parameter in the usual bilayer S/F structure. At last, a triplet effect has investigated on the Fe1/Cu/Fe2/Cu/Pb structure [96]. The measured characteristics $T_c(\alpha)$ have a minimum in the neighborhood of $\alpha = \pi/2$ (i.e., almost for the orthogonal vectors $\boldsymbol{M}_1$ and $\boldsymbol{M}_2$) in the full compliance with the theory. The greatest depth of this minimum, of order of 60 mK below $T_{AP}$, had achieved at an internal F layer thickness of about 0.6 nm, which is close to the result of the theory in the diffusion approximation [39].

Similar characteristics $T_c(\alpha)$, with the maximal effect of about 20 mK, were obtained in [100] for the structure of Co/Cu/Co(0.6)/Nb(17) (the angle range of the measurements was from $-180°$ to $180°$). Again, a good fit based on of formulae for the clean limit of microscopic theory gives strong reasons to assume the triplet effect in F1/F2/S systems to be stable against perturbations. At last, is worth noting the interesting fact, that the scaled angular dependence of the averaged triplet component, at least for $\alpha > \pi/6$, practically merges with the curve $\Delta T_c(\alpha)$, measured in this experiment.

Almost the same structure on the base of Co, but with Nb spacer, thick Nb layer (50 nm) and the inner Co layer of 1.6 nm thickness were used in the already mentioned experiment by Flokstra et al. [89]. In these conditions, the long-range triplet SSV effect was approximately the same as in [100], $\Delta T_c(\pi/2) \approx 15$ mK. The indication of presence of the long-range triplet component in the superconducting condensate is the well-expressed dependence $R(\alpha) \approx R_{min} + \Delta R\sqrt{\sin\alpha}$, measured for an external magnetic field close to the saturation field.

In [101], the problem of increasing the triplet SSV effect in S/F1/N/F2 structures has been substantially developed due to two factors. First, the magnetic hard (Co)

and magnetically soft (Py) materials were taken as external and internal F layers, respectively. The second factor is the controlled magnetic state of the structure, since directions of the easy and hard magnetization axes of the layer F1 (perpendicular and parallel to the magnetic moment of the layer F2, respectively) could be given. As a result, a well-pronounced triplet effect (with a minimum of the function $T_c(\alpha)$ at the point $\alpha_m \approx \pi/2$) was obtained (see Fig. 4).

Attention has been drawn to dependence of the magnitude of the effect on the thickness of the S layer. Namely, for the Cu/Co(6)/Cu/Py/Cu/Nb(21) structure, the triplet effect was about 20 mK, while for a structure with the cobalt thickness of 3 nm and a thickness of niobium of 20 nm, the 0.12 K SSV effect was observed and called "giant." Another feature is the high critical temperatures (about 5.6 K in the first case, and 5.2–5.3 K in the second), due, among other things, to very high quality of the superconducting material. Let us pay attention to the fact that strong increase in the effect is associated with a decrease in the thickness of the niobium layer by only one nanometer. It is associated with the fact that the thicknesses of the S layers of the investigated samples are close to the critical value, $d_{S,cr}$. It seems that fabrication of another sample with a thickness $d_S$ slightly less than 20 nm would make it possible to observe the effect of reentrant superconductivity on the $T_c(\alpha)$ dependence. Further on, a role of the Cu buffer layer between the superconductor and the ferromagnet is interesting. Its addition suppresses superconductivity in the structure (although not so much, due to the small transparency of the Nb–Cu interface), and therefore, the $T_c(d_S)$ characteristic of the structure becomes more shallow at small $d_S$. This probably gave an opportunity for a more confident observation of the effect.

Along with the term "giant" [101], the term "colossal" appeared in [102] regarding the triplet SSV effect of the ~ 800 mK size. The experimental feature of the work [102] was ferromagnetic semi-metal $CrO_2$ taken as the outer layer of the structure, whereas for the F2 layer, an ordinary ferromagnetic Ni had been used. Moreover, the rotation of the magnetic moment of the F1 layer occurred in a plane orthogonal to the plane of the layers. Since the rotation of the magnetic moment is carried out by an external magnetic field $H_0$ (0.25 T or 0.5 T), the dependence $T_c(\alpha; H = H_0)$ is formally measured. The spin-triplet effect was determined empirically by subtracting the quantity $\delta T_{c0} = (T_c(0; H_0)) - T_c(\alpha; H_0))$, measured either for a planar sample of a superconductor of thickness $d_S$, or for a segment of the structure S/F1/N (they are approximately the same layer by layer), from the value of $\delta T_c$, measured for sample S/F1/N/F2.

In [103], the structure F1/N/F2/S of the "mixed" type was used to observe the triplet effect. In it a strong ferromagnetic (Co) with a fixed direction of magnetization was separated from a weak ferromagnet $Cu_{41}Ni_{59}$, by the Nb "spacer" which had the thickness $d_N < d_{S,cr}$. The equilibrium magnetization axes of Co and CuNi were oriented parallel and perpendicular to the plane of the layers, respectively (the "out-of-plane" switching principle, as well as in [102]). The effect was detected by measuring the $T_c(H)$ dependence for a field varying in the range (+2, −2) kOe. At field values in a small neighborhood of $H \approx -20$ Oe, when the magnetizations of the layers were orthogonal to one another, a sharp drop in the critical temperature

was detected, which was regarded as an influence, among other factors, of the triplet components.

Finally, we describe another experimental study that demonstrates the possibility of the maximum achievable *P–AP* SSV effect by improving the quality of the structure and managing transparency of the interface. The Bochum group performed an experiment on a $V(d_{V1})$/Fe($d_F$)/$V(d_{V2})$/Fe($d_F$) structure with single-crystalline vanadium layers and high quality of interfaces [104]. The outer layer of vanadium had a thickness very close to the coherence length $\xi_S$ ($d_{V1} = 24$ nm for three samples and $d_{V1} = 21$ nm for the fourth sample; $d_{V1}/\xi_S = 1.23 - 1.03$). Thicknesses of the Fe layers were from 0.43 to 0.9 nm, which is close to the optimum value $\xi_F/2$. As a result, a relatively large effect of 24 mK at $T_c = 2.67$ K was achieved on one of the samples with an $S$ layer thickness of 24 nm. However, the largest difference, $\Delta T_c = 35$ mK, was obtained on a sample with the thinnest outer vanadium layer, $d_{V1} = 21$ nm ($d_{V1,cr} = 17$ nm). The critical temperature in this case turned out to be quite high, $T_c \sim 2.5$ K. We also draw attention to the fact that in the fourth sample, the $Fe_{0.35}V_{0.65}$ alloy was used as a ferromagnet, and in this case, as mentioned above, the transparency of the S–F interface increases. Apparently, optimization of the V content in F layers of this structure can lead to stronger triplet effect.

## 4 Josephson Spin Valves with Ferromagnetic Weak Links

Josephson junctions with ferromagnetic films in the weak link region are considered now as promising memory elements for superconducting memory [105]. In their first implementations, such memory elements contained two or three ferromagnetic layers [71–74, 106, 107]. It was shown that the magnitude and sign of the critical current, $I_C$, of such Josephson junctions can depend both on the magnitude of the exchange energy, $E_{ex}$, of the ferromagnets and on the mutual orientation, $\alpha$, of the vectors of their magnetization.

To understand physical reasons that lead to the dependence of $I_C(E_{ex}, \alpha)$, it is sufficient to consider a SFIFS junction consisting of two SF electrodes separated by a dielectric layer I with tunnel-type conductivity [108–110]. In particular, in [108–110] it was shown that in the limit of small thickness of the F layers, $d_F << \xi_F \min\{1, (\pi T_C/E_{ex})^{1/2}\}$, and relatively small transparency of the S–F interface, the anomalous Green's functions $F_F$, which described superconducting correlations in F films, has the form

$$F_F = \frac{\pi T_c \Delta G}{\omega \gamma_{BM}} \left( \frac{|\omega|}{\omega^2 + E_{ex}^2} - i \frac{E_{ex} \mathrm{sign}(\omega)}{\omega^2 + E_{ex}^2} \right). \quad (1)$$

Here, $\Delta$ is a complex order parameter in the S electrode, $\omega = \pi T(2n+1)$ are Matsubara frequencies, $G = \Delta/(\omega^2 + \Delta^2)^{1/2}$, and $\gamma_{BM} >> T_C/T$ is the suppression parameter inversely proportional to the transparency of the F–S interface.

The first, even in frequency term in (1) determines the magnitude of the singlet superconducting correlations, while the second term is odd in frequency and determines the short-range triplet superconductivity arising in the F layer. It is seen that there is $\pi/2$ shift between the singlet and the triplet correlations. It can be demonstrated [71–74] that this $\pi/2$ phase shift is the general property of proximity effect in SF multilayers, which is independent on the geometric features of the considered structures.

Substitution of (1) into standard expression for the supercurrent across SFIFS junctions results in sinusoidal current-phase relation with the critical current

$$\frac{eR_nI_c}{\pi T} = \sum_{\omega}\left(\frac{\pi T_c \Delta G}{\omega \gamma_{BM}}\right)^2 \left(\frac{\omega^2 - E_{\mathrm{exR}}E_{\mathrm{exL}}}{\left(\omega^2 + E_{\mathrm{exR}}^2\right)\left(\omega^2 + E_{\mathrm{exL}}^2\right)}\right). \tag{2}$$

Here, $E_{\mathrm{exR}}$, $E_{\mathrm{exL}}$ are the exchange energies in right (FS) and left (SF) electrodes of SFIFS junction, respectively, and $R_{\mathrm{n}}$ is junction's resistance. Expression (2) is valid for parallel ($\alpha = 0$) or antiparallel ($\alpha = \pi$) alignment of the F films' magnetizations. It says that the supercurrent across SFIFS junction consists of two parts. The first is always positive. It specifies a superconducting current, which is carried by singlet superconducting correlations. It is seen that this contribution to the supercurrent monotonically decreases with increase of $E_{\mathrm{exR}}$ and $E_{\mathrm{exL}}$. The second item in (2) is a part of the supercurrent carried by triplet superconducting correlations. For $\alpha = 0$ the exchange energies, $E_{\mathrm{exR}}$, $E_{\mathrm{exL}}$, have the same sign, so that the triplet supercurrent flows in direction opposite to the singlet one. In this case, increase of the exchange energy results in suppression of the supercurrent to zero and even to change the direction of the net current flow. It is transformation from 0- to so-called π-junction. Contrary to that, for $\alpha = \pi$, the exchange energies $E_{\mathrm{exR}}$, $E_{\mathrm{exL}}$ have the opposite sign. In this geometry, the triplet supercurrent flows in the same direction as the singlet one. The net supercurrent increases with increasing of an exchange energy achieving maximum exactly at the point at which the crossover from 0- to $\pi$-junction takes place for $\alpha = 0$ and starts to decrease with $E_{\mathrm{exR}}$, $E_{\mathrm{exL}}$ for larger exchange energies.

The simple example given above shows that a change in the mutual orientation of the magnetization vectors can indeed lead to control of the supercurrent across the Josephson junction, substantially changing its magnitude and even sign. This fact had been confirmed experimentally in SFNFS and SFF'FS Josephson pseudo spin valves [111–125].

The use of spin valves in superconductor memory devices is limited for a number of reasons. The experimental data [111–125] have shown that the typical magnitudes of characteristic voltage, $V_{\mathrm{C}} = I_C R_n$, across the valves, containing two or more F films in the weak link region, lie in the microvolt and nanovolt ranges, respectively. These values are several orders of magnitude lower than $V_{\mathrm{C}}$ of the junctions used in RSFQ circuits. Strong suppression of $I_C$ has a simple physical nature. To accomplish the control effect, one has to remagnetize one of the F layers without changing the direction of magnetization in the other F film. This can be only done if the weak link is a combination of "strong" and "weak" ferromagnets, i.e., the materials with

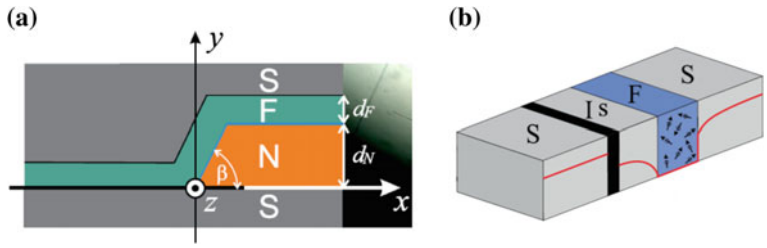


**Fig. 5** Josephson structures with one ferromagnetic layer and a more complex weak link region: **a**—rotary spin valve [126], **b**—SIsFS tunnel junction with IsF containing insulator I, thin superconducting film s and F layer inside the weak link [128–135]. Figure 5a is reproduced from [I.I. Soloviev, N.V. Klenov, S.V. Bakurskiy, V.V. Bol'ginov, V.V. Ryazanov, M.Yu. Kupriyanov, A.A. Golubov. Appl. Phys. Lett. **105,** 242601 (2014), http://dx.doi.org/10.1063/1.4904012]; Fig. 5b is reproduced from [S.V. Bakurskiy, N.V. Klenov, I.I. Soloviev, V.V. Bol'ginov, V.V. Ryazanov, I.I. Vernik, O.A. Mukhanov, M. Yu. Kupriyanov, A.A. Golubov, Appl. Phys. Lett. **102**, 192603 (2013), http://dx.doi.org/10.1063/1.4805032] with permissions of AIP Publishing

considerably different exchange energies $E_{ex}$ and/or thicknesses of F layers. As a result, $I_C$ is manipulated against the background of its considerable suppression by the strong ferromagnet. It should also be noted that the characteristic time of magnetization reversal of ferromagnetic films is of the order of inverse frequency of ferromagnetic resonance and by approximately three orders of magnitude exceeds the characteristic time scale of the Josephson structures.

The solution of these problems can be found in a transition to structures with one ferromagnetic layer, but with more complex weak link region [126–135]. Two examples of these structures are presented in Fig. 5.

Figure 5a shows the sketch of rotary spin valve [126, 127]. It consists of superconducting electrodes separated by a ferromagnetic interlayer with the thickness $d_F$ or by a sandwich containing the same F layer and a normal metal (N) layer with the thickness $d_N$. The magnitude of the critical current in this structure is determined by the orientation of the magnetization vector of the ferromagnetic film with respect to the direction separating the SFS and SNFS segments of the SF–NFS junction (the $z$ axis in Fig. 5). Such a spin valve can appear in two states with substantially different critical currents. These states correspond to mutually orthogonal directions of the magnetization vector $\boldsymbol{M}$, which allows switching the valve by applying mutually orthogonal external magnetic fields. Maintenance of these states does not require external energy sources.

Figure 5a shows a sketch of SIsFS junctions studied in [128–135]. They consist of two superconducting electrodes S separated by a tunnel barrier I, an intermediate thin superconducting films, and a ferromagnetic layer F.

It was demonstrated that there are several modes of operation of these junctions. For the s layer in the superconducting state, they are S-I-sfS or SIs-F-S devices with the weak place located at the insulator (mode 1a) or at the F layer (mode 1b), respectively. For a small s layer thickness, its intrinsic superconductivity is completely suppressed, resulting in formation of an InF weak place (mode 2). These modes are

distinguished by the shape of the current-phase relation (CPR) that is the relation between supercurrent across the SIsFS junction, $J_S$, and phase difference, $\varphi$, of order parameters in S banks.

For mode 1, the current-phase relation (CPR) can substantially differ from the sinusoidal even in vicinity of $T_c$. The deviations are largest when the structure is close to the crossover between modes 1a and 1b. This effect results in kinks in dependencies of the critical current $J_C$ on temperature, as well as on thickness of the layers $d_F$,$d_S$ and the exchange energy $E_{ex}$. The calculations [131] have shown that in mode 1a, nearly 10% change in the exchange energy can cause a 0-$\pi$ transition, i.e., changing the sign of the product $J_C R_N$, while maintaining its absolute value. This unique feature can be implemented in mode 1a, since changes of the exchange energy determine only the presence or absence of a $\pi$-shift between the s and S electrodes and do not affect the magnitude of the critical current of the SIs part of the SIsFS junction.

The transformation of the CPR is even more important at low temperatures. For $T$ smaller than $0.25T_C$, a sharp 0-$\pi$ transition can be realized induced by a small temperature variation [131]. More detailed analysis of the CPR shape [132] in a vicinity of 0-$\pi$ transition has shown that the CPR in the SIsFS structures is qualitatively different from that in regular SFS junctions. The classification of the various CPR types requires the use of two indices. One of them, $k$, indicates the number of the existing ground states, while the other, m, defines the number of current leaps occurring during variation of the phase difference $\varphi$ in each of these ground states from 0 to $2\pi$. The values of these indices depend on the ratio between the amplitudes of the first, $A$, and the second, $B$, harmonics in CPR of sFS part of SIsFS junction. In [135], the areas in the A-B plane, corresponding to all possible combinations of pairs of these indices, as well as the typical shapes of the CPR for each of these areas have been identified. It was shown that some of the found states are protected. It means that the SIsFS structure can stay either in 0 or in $\pi$ ground state, with only slight difference between the magnitudes of its energy $E(\varphi)$ at $\varphi = 0$ and $\varphi = \pi$. Furthermore, a transition from one ground state to another is not possible by a continuous adiabatic variation of the phase $\varphi$. The analysis has done in the frame of resistively shunted junction model and confirmed that this property is conserved even in dynamic regime, despite there is a voltage drop across the SIsFS junction and $\varphi$ is time dependent. To switch SIsFS junction between the 0- and $\pi$-states, one should increase a bias current across the junction to a value larger than the critical current of the sFS part of the structure.

In mode 2, a sinusoidal CPR is realized. Despite that, the distribution of the phase difference $\chi(x)$ in the IsF weak place may have a complex structure, which depends on the thickness of the s and F layers. These effects should influence the dynamics of a junction in its AC state and deserve further study.

To conclude, spin-triplet pairing in superconductor–ferromagnet heterostructures appeared to be not an exotic phenomenon like triplet superconductivity in compounds and low-dimensional organic salts. During the course of the studies, it turned out that the spin-triplet pairing is inevitable property of superconductor–ferromagnet heterostructures, which has diverse manifestations. Is seems that this unconventional

pairing is not a basic physics property, which can be reliably detected, but it may also provide device physics utilized in superconducting spintronics [75, 78, 107].

**Acknowledgements** The authors gratefully acknowledge a long-term cooperation with C. Attanasio, I. Garifullin, S. Gsell, S. Horn, J.-M. Kehrle, D. Lenk, H.-A. Krug von Nidda, J. Lindner, C. Müller, J. Moosburger-Will, R. Morari, A. Prepelitsa, E. Antropov, E. Nold, G. Obermeier, V. Oboznov, S.L. Prischepa, C. Cirillo, J. Aarts, N. Pugach, V.V. Ryazanov, M. Schreck, R. Tidecks, H. Zabel, and V.I. Zdravkov. Special thanks to A.v. Humboldt Foundation (Karlsruhe-INT/Kishinev-IIEN Institutspartnerschaften-Project), to DFG (Grant No. HO 955/9-1), Russian Science Foundation (M.Yu.K, Grant No 17-12-01079) and Ministry of Education of the Republic Belarus. L.R.T. acknowledges partial support from RFBR (grant No 16-02-01171_a) and Academy of Sciences of the Republic of Tatarstan (Institute for Advanced Studies ASRT). A.S.S. acknowledges support from STCU (grant No 6329), and the Moldova Academy of Sciences research project "Nonuniform superconductivity as the base for superconducting spintronics."

## References

1. V.L. Ginzburg, Sov. Phys. JETP **4**, 153 (1957) [Zh. Eksp. Teor. Fiz. **31**, 202 (1956)]
2. P. Fulde, R. Ferrell, Phys. Rev. **135**, A550 (1964)
3. A.I. Larkin, Yu.N. Ovchinnikov, JETP **47**, 1136 (1964)
4. P. Fulde, Adv. Phys. **22**, 667 (1973), Fig. 22
5. A. Bianchi, R. Movshovich, C. Capan, P.G. Pagliuso, J.L. Sarrao, Phys. Rev. Lett. **91**, 187004 (2003)
6. R. Lortz, Z. Wang, A. Demuer, P.H.M. Boettger, B. Bergk, G. Zwicknagl, Z. Nakazawa, J. Wosnitza, Phys. Rev. Lett. **99**, 187002 (2007)
7. M. Kenzelmann, Th. Strässle, C. Niedermayer, M. Sigrist, B. Padmanabhan, M. Zolliker, A.D. Bianchi, R. Movshovich, E.D. Bauer, J.L. Sarrao, J.D. Thompson, Science **321**, 1652 (2008)
8. B. Bergk, A. Deumer, I. Sheikin, Y. Wang, J. Wosnitza, Y. Nakazawa, R. Lortz, Phys. Rev. B **83**, 064506 (2011)
9. M.B. Maple, Ø. Fischer, *Superconductivity in Ternary Compounds* (Springer, 1982), 283 pp
10. K.-H. Müller, V.N. Narozhnyi, Rep. Prog. Phys. **64**, 943 (2001)
11. A.P. Mackenzie, Y. Maeno, Rev. Mod. Phys. **75**, 657 (2003)
12. V.P.S. Awana, in *Frontiers in Magnetic Materials*, ed. by A.V. Narlikar (Springer, 2005), p. 531
13. M.B. Maple, E.D. Bauer, V.S. Zapf, J. Wosnitza, Unconventional superconductivity in novel materials, in *Superconductivity. Conventional and Unconventional Superconductors*, ed. by K.H. Bennemann, J.B. Ketterson, vol. I. (Springer, Berlin, Heidelberg, 2008), p. 639
14. F.S. Bergeret, A.F. Volkov, K.B. Efetov, Phys. Rev. Lett. **86**, 4096 (2001)
15. A. Kadigrobov, R.I. Shekhter, M. Jonson, Europhys. Lett. **54**, 394 (2001)
16. F.S. Bergeret, V.V. Pavlovskii, A.F. Volkov, K.B. Efetov, Int. J. Mod. Phys. B **16**, 1459 (2002)
17. F.S. Bergeret, A.F. Volkov, K.B. Efetov, Phys. Rev. B **64**, 134506 (2001)
18. A.F. Volkov, F.S. Bergeret, K.B. Efetov, Phys. Rev. Lett. **90**, 117006 (2003)
19. F.S. Bergeret, A.F. Volkov, K.B. Efetov, Phys. Rev. B **68**, 064513 (2003)
20. Ya.V. Fominov, A.A. Golubov, M.Yu. Kupriyanov, JETP Lett. **77**, 510 (2003) [Pis'ma v ZhETF **77**, 609 (2003).]
21. M. Eschrig, J. Kopu, A. Konstandin, J.C. Cuevas, M. Fogelström, G. Schön, *Advances in Solid State Physics*, vol. 44 (book series), ed. by B. Kramer (Springer, Berlin, Heidelberg, 2004), pp. 533–546
22. T. Champel, M. Eschrig, Phys. Rev. B **71**, 220506(R) (2005)
23. T. Champel, M. Eschrig, Phys. Rev. B **72**(11), 054523 (2005)

24. T. Löfwander, T. Champel, J. Durst, M. Eschrig, Phys. Rev. Lett. **95**, 187003 (2005)
25. A. Konstandin, J. Kopu, M. Eschrig, Phys. Rev. B **72**, 140501(R) (2005)
26. A.F. Volkov, Ya.V. Fominov, K.B. Efetov, Phys. Rev. B **72**, 184504 (2005)
27. A.F. Volkov, A. Anishchanka, K.B. Efetov, Phys. Rev. B **73**, 104412 (2006)
28. D.A. Ivanov, Y.V. Fominov, Phys. Rev. B **73**, 214524 (2006)
29. T. Löfwander, T. Champel, M. Eschrig, Phys. Rev. B **75**, 014512 (2007)
30. B. Crouzy, S. Tollis, D.A. Ivanov, Phys. Rev. B **75**, 054503(8) (2007)
31. Ya.V. Fominov, A.F. Volkov, K.B. Efetov, Phys. Rev. B **75**, 104509 (2007)
32. M. Houzet, A.I. Buzdin, Phys. Rev. B **76**, 060504(R) (2007)
33. T. Champel, T. L.ofwander, and M. Eschrig. Phys. Rev. Lett. **100**, 077003 (2008)
34. A.F. Volkov, K.B. Efetov, Phys. Rev. B **78**, 024519 (2008)
35. I.B. Sperstad, J. Linder, A. Sudbø, Phys. Rev. B **78**, 104509 (2008)
36. M. Eschrig, T. Löfwander, Nat. Phys. **4**, 138 (2008)
37. T.Yu. Karminskaya, M.Yu. Kupriyanov, A.A. Golubov, JETP Lett. **87**, 570 (2008) [Pis'ma v ZhETF **87**, 657 (2008)]
38. G.B. Halasz, J.W.A. Robinson, J.F. Annett, M.G. Blamire, Phys. Rev. B **79**, 224505 (2009)
39. Ya.V. Fominov, A.A. Golubov, T.Yu. Karminskaya, M.Yu. Kupriyanov, R.G. Deminov, L.R. Tagirov, JETP Lett. **91**, 308 (2010). [Pis'ma Zh. Exp. Teor. Fiz **91**, 329 (2010)]
40. M. Alidoust, J. Linder, G. Rashedi, T. Yokoyama, A. Sudbø, Phys. Rev. B **81**, 014512 (2010)
41. A.F. Volkov, K.B. Efetov, Phys. Rev. B **81**, 144522 (2010)
42. T.Yu. Karminskaya, A.A. Golubov, M.Yu. Kupriyanov, Phys. Rev. B **84**, 064531 (2011)
43. M. Alidoust, K. Halterman, J. Linder, Phys. Rev. B **88**, 075435(5) (2013)
44. M. Alidoust, K. Halterman, J. Linder, Phys. Rev. B **89**, 054508 (2014)
45. M. Alidoust, K. Halterman, Phys. Rev. B **89**, 195111(11) (2014)
46. J. Linder, K. Halterman, Phys. Rev. B **90**, 104502 (2014)
47. M.V. Avdeev, Yu.N. Proshin, Supercond. Sci. Technol. **27**, 035006 (2014)
48. M. Alidoust, K. Halterman, O.T. Valls, Phys. Rev. B **92**, 014508 (2015)
49. M. Eschrig, J. Kopu, J.C. Cuevas, and Gerd Schön, Phys. Rev. Lett. **90**, 137003 (2003)
50. M. Eschrig, T. Löfwander, T. Champel, J.C. Cuevas, J. Kopu, G. Schön, J. Low Temp. Phys. **147**, 457 (2007)
51. A.V. Galaktionov, M.S. Kalenkov, A.D. Zaikin, Phys. Rev. B **77**, 094520 (2008)
52. J.N. Kupferschmidt, P.W. Brouwer, Phys. Rev. B **84**, 014512(14) (2011)
53. V. Braude, Yu.V. Nazarov, Phys. Rev. Lett. **98**, 077003 (2007)
54. L. Trifunovic, Z. Radović, Phys. Rev. B **82**, 020505(R) (2010)
55. L. Trifunovic, Phys. Rev. Lett. **107**, 047001 (2011)
56. L. Trifunovic, Z. Popović, Z. Radović, Phys. Rev. B **84**, 064511 (2011)
57. M. Knežević, L. Trifunovic, Z. Radović, Phys. Rev. B **85**, 094517(7) (2012)
58. S.V. Mironov, A. Buzdin, Phys. Rev. B **89**, 144505 (2014)
59. Z. Pajović, M. Božović, Z. Radović, J. Cayssol, A. Buzdin, Phys. Rev. B **74**, 184509 (2006)
60. Y. Asano, Y. Tanaka, A.A. Golubov, Phys. Rev. Lett. **98**, 107002 (2007)
61. Y. Asano, Y. Sawa, Y. Tanaka, A.A. Golubov, Phys. Rev. B **76**, 224525 (2007)
62. K. Halterman, P.H. Barsic, O.T. Valls, Phys. Rev. Lett. **99**, 127002 (2007)
63. K. Halterman, O.T. Valls, P.H. Barsic, Phys. Rev. B **77**, 174511 (2008)
64. B. Béri, J.N. Kupferschmidt, C.W.J. Beenakker, P.W. Brouwer, Phys. Rev. B **79**, 024517 (2009)
65. K. Halterman, O.T. Valls, Phys. Rev. B **80**, 104502 (2009)
66. C.-T. Wu, O.T. Valls, K. Halterman, Phys. Rev. B **86**, 014523 (2012)
67. C.-T. Wu, O.T. Valls, K. Halterman, Phys. Rev. Lett. **108**, 117005 (2012)
68. C.-T. Wu, O.T. Valls, K. Halterman, Phys. Rev. B **86**, 184517 (2012)
69. C.-T. Wu, O.T. Valls, K. Halterman, Phys. Rev. B **90**, 054523 (2014)
70. K. Halterman, O.T. Valls, C.-T. Wu, Phys. Rev. B **92**, 174516 (2015)
71. F.S. Bergeret, A.F. Volkov, K.B. Efetov, Rev. Mod. Phys. **77**, 1321 (2005)

72. K.B. Efetov, I.A. Garifullin, A.F. Volkov, K. Westerholt, *Magnetic Heterostructures. Advances and Perspectives in Spinstructures and Spintransport*, ed. by H. Zabel, S.D. Bader. Book series: Springer Tracts in Modern Physics, vol. 227. (Springer, Berlin/Heidelberg, 2007). Chap. 5, pp. 251–290
73. F.S. Bergeret, A.F. Volkov, K.B. Efetov, Appl. Phys. A **89**, 599 (2007)
74. M. Eschrig, Rep. Progr. Phys. **78**, 104501 (2015)
75. M. Giroud, H. Courtois, K. Hasselbach, D. Mailly, B. Pannetier, Phys. Rev. B **58**, R11872 (1998)
76. V.T. Petrashov, I.A Sosnin, I. Cox, A. Parsons, C. Troadec, Phys. Rev. Lett. **83**, 3281 (1999)
77. A. Moor, A.F. Volkov, K.B. Efetov, Phys. Rev. B **93**, 104525 (2016)
78. J. Linder, J.W.A. Robinson, Nat. Phys. **11**, 307 (2015)
79. S. Oh, D. Youm, M.R. Beasley, Appl. Phys. Lett. **71**, 2376 (1997)
80. B. Dieny, V.S. Speriosu, S.S.P. Parkin, B.A. Gurney, D.R. Wilhoit, D. Mauri, Phys. Rev. B **43**, R1297 (1991)
81. K.D. Usadel, Phys. Rev. Lett. **25**, 507 (1970)
82. L.R. Tagirov, Phys. Rev. Lett. **83**, 2058 (1999)
83. A.I. Buzdin, A.V. Vedyayev, N.V. Ryzhanova, Europhys. Lett. **48**, 686 (1999)
84. I. Baladié, A. Buzdin, N. Ryzhanova, A. Vedyayev, Phys. Rev. B **63**, 054518 (2001)
85. Ya.V. Fominov, N.M. Chtchelkatchev, A.A. Golubov, Phys. Rev. B **66**, 014507 (2002)
86. P. Cadden-Zimansky, Ya.B. Bazaliy, L.M. Litvak, J.S. Jiang, J. Pearson, J.Y. Gu, C.-Y. You, M.R. Beasley, S.D. Bader, Phys. Rev. B **77**, 184501 (2008)
87. J. Zhu, I.N. Krivorotov, K. Halterman, O.T. Valls, Phys. Rev. Lett. **105**, 207002 (2010)
88. J.Y. Gu, C.-Y. You, J.S. Jiang, J. Pearson, Ya.B. Bazaliy, S.D. Bader, Phys. Rev. Lett. **89**, 267001 (2002)
89. M.G. Flokstra, T.C. Cunningham, J. Kim, N. Satchell, G. Burnell, S.J. Bending, P.J. Curran, S.J. Langridge, C. Kinane, J.F.K. Cooper, N. Pugach, M. Eschrig, S.L. Lee, Phys. Rev. B **91**, 060501(R) (2015)
90. N. Banerjee, C.B. Smiet, R.G.J. Smits, A. Ozaeta, F.S. Bergeret, M.G. Blamire, J.W.A. Robinson, Nat. Commun. **5**, 1 (2014)
91. I.C. Moraru, W.P. Pratt Jr., N.O. Birge, Phys. Rev. Lett. **96**, 037004 (2006)
92. I.C. Moraru, W.P. Pratt Jr., N.O. Birge, Phys. Rev. B **74**, 220507(R) (2006)
93. V.I. Zdravkov, D. Lenk, R. Morari, A. Ullrich, G. Obermeier, C. Müller, H.A. Krug von Nidda, A.S. Sidorenko, S. Horn, R. Tidecks, L.R. Tagirov, Appl. Phys. Lett. **103**, 062604 (2013)
94. P.V. Leksin, N.N. Garif'yanov, I.A. Garifullin, J. Schumann, V. Kataev, O.G. Schmidt, B. Büchner, Phys. Rev. Lett. **106**, 067005 (2011)
95. P.V. Leksin, N.N. Garif'yanov, I.A. Garifullin, J. Schumann, V. Kataev, O.G. Schmidt, B. Büchner, Phys. Rev. B **85**, 024502 (2012)
96. P.V. Leksin, N.N. Garif'yanov, I.A. Garifullin, J. Schumann, V. Kataev, O.G. Schmidt, B. Büchner, Phys. Rev. Lett. **109**, 057005 (2012)
97. P.V. Leksin, A.A. Kamashev, N.N. Garif'yanov, I.A. Garifullin, Ya.V. Fominov, J. Schumann, C. Hess, V. Kataev, and B. Buchner, JETP Lett. **97**, 478 (2013) [Pis'ma v ZhETF **97**, 549 (2013)]
98. P.V. Leksin, N.N. Garif'yanov, A.A. Kamashev, Ya.V. Fominov, J. Schumann, C. Hess, V. Kataev, B. Büchner, I.A. Garifullin, Phys. Rev. B **91**, 214508 (2015)
99. P.V. Leksin, N.N. Garif'yanov, A.A. Kamashev, A.A. Validov, Ya.V. Fominov, J. Schumann, V. Kataev, J. Thomas, B. Büchner, I.A. Garifullin, Phys. Rev. B **93**, 100502(R) (2016)
100. A.A. Jara, C. Safranski, I.N. Krivorotov, C.-T. Wu, A.N. Malmi-Kakkada, O.T. Valls, K. Halterman, Phys. Rev. B **89**, 184502 (2014)
101. X.L. Wang, A. Di Bernardo, N. Banerjee, A. Wells, F.S. Bergeret, M.G. Blamire, J.W.A. Robinson, Phys. Rev. B **89**, 140508(R) (2014)
102. A. Singh, S. Voltan, K. Lahabi, J. Aarts, Phys. Rev. X **5**, 021019 (2015)
103. V.I. Zdravkov, J. Kehrle, G. Obermeier, D. Lenk, H.-A. Krug von Nidda, C. Müller, M.Yu. Kupriyanov, A.S. Sidorenko, S. Horn, R. Tidecks, L.R. Tagirov, Phys. Rev. B **87**, 144507 (2013)

104. G. Nowak, K. Westerholt, H. Zabel, Supercond. Sci. Technol. **26**, 025004 (2013)
105. J.W. Lu, E. Chen. M. Kabir, M.R. Stan and S.A. Wolf, Int. Mater. Rev. **61**, 456 (2016)
106. A.A. Golubov, M.Yu. Kupriyanov, E. Il'ichev, Rev. Mod. Phys. **76**, 411 (2004)
107. M.G. Blamire, J.W.A. Robinson, J. Phys.: Cond. Matter **26**, 453201 (2014)
108. V.N. Krivoruchko, E.A. Koshina, Phys. Rev. B **63**, 224515 (2001)
109. V.N. Krivoruchko, E.A. Koshina, Phys. Rev. B **64**, 172511 (2001)
110. A.A. Golubov, M.Yu. Kupriyanov, Ya.V. Fominov, Pis'ma Zh. Eksp. Teor. Fiz. **75**, 223 (2002) [JETP Lett. **75**, 190 (2002)]
111. C. Bell, G. Burnell, C.W. Leung, E.J. Tarte, D.-J. Kang, M.G. Blamire, Appl. Phys. Lett. **84**, 1153 (2004)
112. M.A.E. Qader, R.K. Singh, S. Galvin, L. Yu, J.M. Rowell, N. Newman, Appl. Phys. Lett. **104**, 022602 (2014)
113. B. Baek, W.H. Rippard, S.P. Benz, S.E. Russek, P.D. Dresselhaus, Nat. Commun. **5**, 3888 (2014)
114. B. Baek, W.H. Rippard, M.R. Pufall, S.P. Benz, S.E. Russek, H. Rogalla, P.D. Dresselhaus, Phys. Rev. Appl. **3**, 011001 (2015)
115. J.W.A. Robinson, G.B. Halasz, A.I. Buzdin, M.G. Blamire, Phys. Rev. Lett. **104**, 207001 (2010)
116. J.W.A. Robinson, J.D.S. Witt, M.G. Blamire, Science **329**, 59 (2010)
117. A. Iovan, T. Golod, V.M. Krasnov, Phys. Rev. B **90**, 134514 (2014)
118. D. Sprungmann, K. Westerholt, H. Zabel, M. Weides, H. Kohlstedt, Phys. Rev. B **82**, 060505 (2010)
119. B.M. Niedzielski, S.G. Diesch, E.C. Gingrich, Y. Wang, R. Loloee, W.P. Pratt Jr., N.O. Birge, I.E.E.E. Tran, Appl. Supercond. **24**, 1800307 (2014)
120. E.C. Gingrich, B.M. Niedzielski, J.A. Glick, Y. Wang, D.L. Miller, R. Loloee, W.P. Pratt Jr., N.O. Birge, Nat. Phys. **12**, 564 (2016)
121. W.M. Martinez, W.P. Pratt, N.O. Birge, Phys. Rev. Lett. **116**, 077001 (2016)
122. T.S. Khaire, M.A. Khasawneh, W.P. Pratt Jr., N.O. Birge, Phys. Rev. Lett. **104**, 137002 (2010)
123. M.A. Khasawneh, W.P. Pratt Jr., N.O. Birge, Phys. Rev. B **80**, 020506(R) (2009)
124. C. Klose, T.S. Khaire, Y. Wang, W.P. Pratt Jr., N.O. Birge, B.J. McMorran, T.P. Ginley, J.A. Borchers, B.J. Kirby, B.B. Maranville, J. Unguris, Phys. Rev. Lett. **108**, 127002 (2012)
125. N. Banerjee, J.W.A. Robinson, M.G. Blamire, Nat. Commun. **5**, 4771 (2014)
126. I.I. Soloviev, N.V. Klenov, S.V. Bakurskiy, V.V. Bol'ginov, V.V. Ryazanov, M. Yu Kupriyanov, A.A. Golubov, Appl. Phys. Lett. **105**, 242601 (2014)
127. I.I. Soloviev, N.V. Klenov, S.V. Bakursky, M.Yu. Kupriyanov, A.A. Golubov, Pis'ma JETP **101**, 258 (2015) [JETP Lett. **101**, 240 (2015)]
128. T.I. Larkin, V.V. Bol'ginov, V.S. Stolyarov, V.V. Ryazanov, I.V. Vernik, S.K. Tolpygo, O.A. Mukhanov, Appl. Phys. Lett. **100**, 222601 (2012)
129. I.V. Vernik, V.V. Bol'ginov, S.V. Bakurskiy, A.A. Golubov, M.Yu. Kupriyanov, V.V. Ryazanov, O.A. Mukhanov, IEEE Trans. Appl. Supercon. **23**, 1701208 (2013)
130. S.V. Bakurskiy, N.V. Klenov, I.I. Soloviev, V.V. Bol'ginov, V.V. Ryazanov, I.I. Vernik, O.A. Mukhanov, M.Yu. Kupriyanov, A.A. Golubov, Appl. Phys. Lett. **102**, 192603 (2013)
131. S.V. Bakurskiy, N.V. Klenov, I.I. Soloviev, M.Yu. Kupriyanov, A.A. Golubov, Phys. Rev. B **88**, 144519 (2013)
132. I.I. Soloviev, N.V. Klenov, S.V. Bakurskiy, V.V. Bol'ginov, V.V. Ryazanov, M.Yu. Kupriyanov, A.A. Golubov, Appl. Phys. Lett. **105**, 242601 (2014)
133. N. Ruppelt, H. Sickinger, R. Menditto, E. Goldobin, D. Koelle, R. Kleiner, O. Vavra, H. Kohlstedt, Appl. Phys. Lett. **106**, 022602 (2015)
134. S.V. Bakurskiy, N.V. Klenov, I.I. Soloviev, M. Yu Kupriyanov, A.A. Golubov, Appl. Phys. Lett. **108**, 042602 (2016)
135. S.V. Bakurskiy, V.I. Filippov, V.I. Ruzhickiy, N.V. Klenov, I.I. Soloviev, M.Yu. Kupriyanov, A.A. Golubov, Current-phase relations in SIsFS junctions in the vicinity of 0-$\pi$ transition. Phys. Rev. B **95**, 094522 (2017)

# Compact Josephson $\varphi$-Junctions


**S. V. Bakurskiy, N. V. Klenov, I. I. Soloviev, Anatolie Sidorenko, M. Yu. Kupriyanov and A. A. Golubov**

**Abstract** This chapter is devoted to the study of controllable proximity effects in superconductors (S), in terms of both fundamental aspects and applications. As a

S. V. Bakurskiy · N. V. Klenov (✉) · I. I. Soloviev · M. Yu. Kupriyanov · A. A. Golubov
Lomonosov Moscow State University, Skobeltsyn Institute of Nuclear Physics,
119991 Moscow, Russia
e-mail: nvklenov@mail.ru

S. V. Bakurskiy
e-mail: r3zz@mail.ru

I. I. Soloviev
e-mail: igor.soloviev@gmail.com

M. Yu. Kupriyanov
e-mail: mkupr@pn.sinp.msu.ru

A. A. Golubov
e-mail: A.A.Golubov@tnw.utwente.nl

S. V. Bakurskiy · N. V. Klenov · I. I. Soloviev · M. Yu. Kupriyanov
Moscow Institute of Physics and Technology, State University,
Dolgoprudniy, Moscow region, Russia

N. V. Klenov
Physics Faculty, Lomonosov Moscow State University, 119991 Moscow, Russia

N. V. Klenov
N. L. Dukhov All-Russia Research Institute of Automatics, 127055 Moscow, Russia

A. Sidorenko
Institute of Electronic Engineering and Nanotechnologies, Academy of Sciences of Moldova,
2028 Chisinau, Moldova
e-mail: anatoli.sidorenko@kit.edu
URL: http://nano.asm.md

A. Sidorenko
Institut für Physik, Universität Augsburg, 86159 Augsburg, Germany

A. A. Golubov
Faculty of Science and Technology and MESA + Institute for Nanotechnology,
University of Twente, 7500 AE Enschede, The Netherlands



A. Sidorenko (ed.), *Functional Nanostructures and Metamaterials for Superconducting Spintronics*, NanoScience and Technology,
https://doi.org/10.1007/978-3-319-90481-8_3

part of the work, theoretical description was suggested for a number of structures with superconducting electrodes and multiple interlayers with new physics related to the proximity effect and nanoscale $\varphi$-junctions. They are Josephson structures with the phase of the ground state $\varphi_g$, $0 < \varphi_g < \pi$ $\varphi$-junctions can be created on the basis of longitudinally oriented normal metal (N) and ferromagnetics (F) layers between superconducting electrodes. Under certain conditions, the amplitude of the first harmonic in the current-phase relation (CPR) is relatively small due to F layer. The coupling across N layer provides negative sign of the second harmonic. To derive quantitative criteria for realization of a $\varphi$-junction, we have solved two-dimensional boundary-value problem in the frame of Usadel equations for overlap and ramp geometries of different structures with NF bilayer. This chapter is focused on different geometries of nanoscale $\varphi$-structures of the size much less than Josephson penetration depth $\lambda_J$. At the same time, $\varphi$-state cannot be realized in conventional SNS and SFS sandwiches. Proximity effect between N and F layers limits minimal possible size of $\varphi$-junction. In the case of smaller junctions, NF bilayer becomes almost homogeneous, $\varphi$-state is prohibited, and junction exists in 0- or $\pi$-state. The conditions for realization of $\varphi$-junctions in ramp-type S–NF–S, overlap-type SFN–FN–NFS, and RTO-type SN–FN–NS geometries are discussed in the chapter. It is shown that RTO-type SN–FN–NS geometry is most suitable for practical realization. It is also shown in this chapter that the parameter range of $\varphi$-state existence can be sufficiently broadened. It allows to realize Josephson $\varphi$-junctions using up-to-date technology. By varying the temperature, we can slightly shift the region of 0-$\pi$ transition and, consequently, we can control the mentioned phase of the ground state. Furthermore, sensitivity of the ground state to an electron distribution function permits applications of $\varphi$-junctions as small-scale self-biasing single-photon detectors. Moreover, these junctions are controllable and have degenerate ground states $+\varphi$ and $-\varphi$, providing necessary condition for the so-called silent quantum bits.

## 1 Introduction

In recent years, the development of superconducting (S) electronics is rapidly growing field [1]. Energy efficiency and high characteristic frequencies of superconductive devices may potentially provide significant benefit compared to other proposals of future electronic circuits. The main direction of this field is the development of controllable superconducting devices and memory elements. One of the possible ways to control properties of superconducting structures is the implementation of ferromagnetic layers in Josephson junctions [2–12]. There are a lot of different proposals and concepts in this field.

It took a long time before the first experimental observation of coupling even through single ferromagnet (F) layer [13]. This problem was solved with the help of soft magnetic CuNi alloys. Shortly after, the experiments provided the evidence of junctions with negative critical current ($\pi$-shift of the current-phase relation, CPR) through phase-sensitive experiments [14] and demonstrated temperature-induced

transition to this $\pi$-state [15]. At the same time, other challenges appeared in the field.

One of the main problems of superconductive electronics is the creation of $\varphi$-junction, the structure with nontrivial phase $\varphi$ in the ground state. Implementation of these structures in conventional schemes rapid single flux quantum logic (RSFQ-logic) can reduce the size of the circuits and increase their speed [16–18]. Another possibility is the development of quantum bits using $\varphi$-contacts. It would mean down-sizing and decreased sensitivity to external noise [19–22]. However, the development of $\varphi$-junction reveals the problem of miniaturization. Most of earlier proposals are addressed to complex structures in the long Josephson junction regime ($W > \lambda_J$) [23–28].

The relation between supercurrent $I_S$ across a heterostructure and its Josephson phase $\varphi$ plays an important role for various superconducting devices. In standard structures, superconductor–insulator–superconductor (SIS) with tunnel type of conductivity, the CPR has the sinusoidal form $I_s(\varphi) = A\sin(\varphi)$. In SNS or SINIS junctions (N is for normal metal here) with metallic type of conductivity in the weak link area, the decrease in the temperature $T$ increases the deviations from the $\sin(\varphi)$ form and $I_S(\varphi)$ achieves its maximum at $\pi/2 \leq \varphi \leq \pi$. In SIS junctions, the amplitude $B$ of the second harmonic in CPR, $B\sin(2\varphi)$, is the value of the second order of smallness (with respect to the probability of tunneling through the barrier) and is negligibly small for all $T$. In sandwiches with normal metal in the vicinity of critical temperature $T_C$, $A \sim (T_C - T)$, but the second harmonic amplitude in CPR is also small here. At low temperatures, $A$ and $B$ have comparable magnitudes, thus giving rise to qualitative modifications of CPR shape.

Nota bene: In all discussed types of structures, the ground state corresponds to phase $\varphi = 0$, since at $\varphi = \pi$ a junction is at nonequilibrium state.

New opportunities open up in Josephson junctions involving ferromagnets as weak link materials. The so-called $\pi$-state in SFS Josephson junctions (with $\pi$-shift of the CPR) was predicted in the 1970s and observed in experiments at the beginning of this century [29–32]. Contrary to SIS or SNS junctions, in SFS devices one can have to have the ground state $\varphi_g = \pi$. It was proven experimentally [33] that such $\pi$-junctions can be used as on-chip $\pi$-phase batteries for self-biasing in various quantum and classical circuits in order to decouple quantum circuits from environment or to replace conventional inductance and strongly reduce the size of an elementary cell [34].

But for some purposes (e.g., for fast memory cells), on-chip $\varphi$-batteries are even more attractive. The so-called $\varphi$-junctions with Josephson phase $\varphi_g = \varphi$, ($0 < |\varphi| < \pi$) in the ground zero-current state were predicted by Mints [35] for the case of randomly distributed alternating 0- and $\pi$-facets along grain boundaries in high-$T_c$ superconductors (e.g., cuprates) with d-wave symmetry of the order parameter. It can be shown that $\varphi$-junctions can be realized on the base of 0- and $\pi$-segments in an inhomogeneous structure SFS structure [36]. Depending on the weights of the segments, the state with an "average" phase $\varphi_g$ can be generated if the mismatch between the segments is relatively small, $-\pi \leq \varphi_g \leq \pi$. Remarkable progress was

recently achieved on the implementation of $\varphi$-junctions within competing concepts [37–42].

In order to create a $\varphi$-junction, one needs a Josephson structure with nonsinusoidal CPR. In the simplest case, this CPR is written as follows

$$I_S(\varphi) = A\sin(\varphi) + B\sin(2\varphi), \tag{1}$$

where the following amplitudes of the CPR harmonics, $A$, and, $B$, are needed

$$|B| > |A|/2, B < 0. \tag{2}$$

In SIS and SFS structures, the requirements (2) cannot be met. In SFS junctions in the vicinity of 0 to $\pi$ transition, the amplitude of the first harmonic in CPR is close to zero, thus opening an opportunity for creating a $\varphi$-battery, if $B$ is negative. But in both the SFS and the SIFS structures with high transparencies of SF interfaces, decay length for superconducting correlations induced into F layer is complex: $\xi_H = \xi_1 + i\xi_2$. Here $A \approx \exp\{-L/\xi_1\}\cos(L/\xi_2)$, $B \approx -\exp\{-2L/\xi_1\}\cos(2L/\xi_2)$, and for $L = (\pi/2)\xi_2$ corresponding to the first 0–$\pi$ transition, the second harmonic amplitude $B$ is always positive.

The way forward is possible here due to the idea of the so-called current-in-plane SFS devices [43, 44] with NF or FNF multilayers in the weak link region consisting and with the supercurrent flowing parallel to FN interfaces. In these structures, superconductivity is induced from the S electrodes into the normal (N) film, while F films serve as a source of spin-polarized electrons and provide an effective control for exchange field. The reduction of effective exchange energy here permits to increase the decay length from the scale of the order of 1 nm up to 100 nm. But the approaches developed during the analysis of such structures cannot help us: The calculations performed did not go beyond linear approximation; hence, the amplitude of the second harmonic in the CPR is considered small.

The purpose of this chapter is to demonstrate that the mentioned concept of the current-in-plane devices (see Fig. 1) can be used as effective $\varphi$-shifters. The structure of the paper is the following. In Sect. 2, we formulate quantitative model in terms of Usadel equations with Kupriyanov–Lukichev boundary conditions. In Sect. 3, the criteria of zero-current $\varphi$-state existence are derived for different types of S–FN–S structure. Finally in Sect. 4, we consider properties of real materials and estimate the possibility to realize $\varphi$-junctions using up-to-date technology.

## 2 Model

We consider here different types of symmetric multilayered structures (see sketches on Fig. 1). The structures consist of superconducting electrodes contacting either the end wall of a FN bilayer (ramp-type structures) or the surface of F or N films (overlap-type geometry with thickness $d_F$ and $d_N$, respectively. The conditions of a dirty limit

are fulfilled for all metals; effective electron–phonon coupling constant is zero in $F$ and $N$ films. We assume that the parameters $\gamma_{BN}$ and $\gamma_{BF}$ for the transparencies of NS and FS interfaces are large enough

$$\gamma_{BN} = \frac{R_{BN}\mathcal{A}_{BN}}{\rho_N \xi_N} \gg \frac{\rho_S \xi_S}{\rho_N \xi_N},$$
$$\gamma_{BF} = \frac{R_{BF}\mathcal{A}_{BF}}{\rho_F \xi_F} \gg \frac{\rho_S \xi_S}{\rho_F \xi_F}, \tag{3}$$

in order to neglect suppression of superconductivity in S banks. Here $R_{BN}$, $R_{BF}$ and $\mathcal{A}_{BN}$, $\mathcal{A}_{BF}$ are the resistances and areas of the SN and SF interfaces, $\xi_S$, $\xi_N$, and $\xi_F$; $\rho_S$, $\rho_N$, and $\rho_F$ are the decay lengths and resistivities for the corresponding materials.

Under the above conditions, the problem of calculation of the supercurrent in the structures reduces to solution of the set of Usadel equations [45]

$$\frac{\xi^2}{G_\omega}\partial\left[G_\omega^2 \partial \Phi_\omega\right] - \frac{\tilde{\omega}}{\pi T_C}\Phi_\omega = 0, \; G_\omega = \frac{\tilde{\omega}}{\sqrt{\tilde{\omega}^2 + \Phi_\omega \Phi^*_{-\omega}}}, \tag{4}$$

where $\Phi_\omega$ and $G_\omega$ are Usadel Green's functions in $\Phi$ parametrization. They are $\Phi_{\omega,N}$ and $G_{\omega,N}$ or $\Phi_{\omega,F}$ and $G_{\omega,F}$ in N and F films correspondingly, $\omega = \pi T(2m+1)$ are Matsubara frequencies (m = 0,1,2,…). Here, we use $\tilde{\omega} = \omega + iH$, and $H$ is the exchange field in ferromagnetic material, $\xi^2 = \xi^2_{N,F} = D_{N,F}/2\pi T_C$ for $N$ and $F$ layers, respectively, $D_{N,F}$ are diffusion coefficients, and $\partial = (\partial/\partial x, \partial/\partial z)$ is 2D gradient operator. To write (4), we have chosen the $z$ and $x$ axes in the directions, respectively, perpendicular and parallel to the plane of N film. We always set the origin in the middle of the junction at the free interface of $F$ film (see Fig. 1).

We calculate the supercurrent $I_S(\varphi)$ by integrating the standard expressions for the current density $j_{N,F}(\varphi, z)$ over the junction cross section:

$$\frac{2ej_{N,F}(\varphi,z)}{\pi T} = \sum_{\omega=-\infty}^{\infty} \frac{iG^2_\omega}{\rho_{N,F}\tilde{\omega}^2_{N,F}}\left[\Phi_\omega \frac{\partial \Phi^*_{-\omega}}{\partial x} - \Phi^*_{-\omega}\frac{\partial \Phi_\omega}{\partial x}\right],$$
$$I_S(\varphi) = W\int_0^{d_F} j_F(\varphi,z)dz + W\int_{d_F}^{d_F+d_N} j_N(\varphi,z)W dz, \tag{5}$$

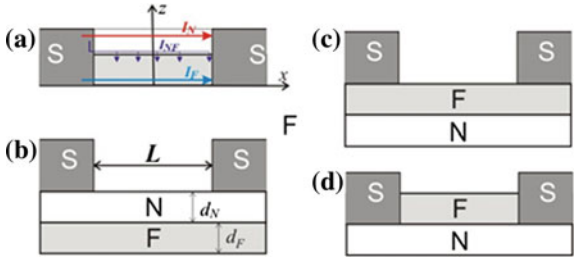


**Fig. 1** **a** S–NF–S junction, **b** the SNF–NF–FNS junction, **c** the SFN–FN–NFS junction, and **d** the SN–FN–NS junction

where $W$ is the width of the structures, which is supposed to be small compared to Josephson penetration depth. It is convenient to perform the integration in (5) in F and N layers separately along the line located at $x = 0$; $z$-component of supercurrent vanishes from considerations of symmetry.

Equation (5) must be supplemented by the boundary conditions. Since these conditions link the Usadel Green's functions corresponding to the same Matsubara frequency $\omega$, we may simplify the notations by omitting the subscript $\omega$. At the NF interface, the boundary conditions have the form:

$$\begin{aligned}\gamma_{BFN}\xi_F\frac{\partial\Phi_F}{\partial z} &= -\frac{G_N}{G_F}\left(\Phi_F - \frac{\tilde{\omega}}{\omega}\Phi_N\right),\\ \gamma_{BNF}\xi_N\frac{\partial\Phi_N}{\partial z} &= \frac{G_F}{G_N}\left(\Phi_N - \frac{\omega}{\tilde{\omega}}\Phi_F\right),\end{aligned} \tag{6}$$

$$\gamma_{BFN} = \frac{R_{BFN}\mathcal{A}_{BFN}}{\rho_F\xi_F} = \gamma_{BNF}\frac{\rho_F\xi_F}{\rho_N\xi_N},$$

where $R_{BFN}$ and $\mathcal{A}_{BFN}$ are the resistance and area of the NF interface.

The conditions at free interfaces are

$$\frac{\partial\Phi_N}{\partial n} = 0,\ \frac{\partial\Phi_F}{\partial n} = 0. \tag{7}$$

The partial derivatives in (7) are taken in the direction, which is normal to the boundary, so that $n$ can be either $z$ or $x$ depending on the particular geometry of the junction.

We have ignored the suppression of superconductivity in S banks, and hence, we have:

$$\Phi_S(\pm L/2) = \Delta\exp(\pm i\varphi/2),\ G_S = \frac{\omega}{\sqrt{\omega^2+\Delta^2}}, \tag{8}$$

where $\Delta$ is magnitude of the order parameter here. Therefore for NS and FS interfaces, we have:

$$\begin{aligned}\gamma_{BN}\xi_N\frac{\partial\Phi_N}{\partial n} &= \frac{G_S}{G_N}(\Phi_N - \Phi_S(\pm L/2)),\\ \gamma_{BF}\xi_F\frac{\partial\Phi_F}{\partial n} &= \frac{G_S}{G_F}\left(\Phi_F - \frac{\tilde{\omega}}{\omega}\Phi_S(\pm L/2)\right).\end{aligned} \tag{9a}$$

$$\begin{aligned}\gamma_{BN}\xi_N\frac{\partial\Phi_N}{\partial n} &= \frac{G_S}{G_N}(\Phi_N - \Phi_S(\pm L/2)),\\ \gamma_{BF}\xi_F\frac{\partial\Phi_F}{\partial n} &= \frac{G_S}{G_F}\left(\Phi_F - \frac{\tilde{\omega}}{\omega}\Phi_S(\pm L/2)\right).\end{aligned} \tag{9b}$$

As in (7), $n$ in (9a) and (9b) is a normal vector directed into material mentioned in derivative.

For the structure presented at Fig. 1a, the boundary-value problem (4)–(9b) was solved analytically in the linear approximation [44], when

$$G_N \equiv sgn(\omega), G_F \equiv sgn(\omega). \tag{10}$$

In the following sections, we will go beyond the linear approximation in order to find new properties of CPR of the structures under consideration.

## 3 Ramp- and Overlap-Type Geometries

The ramp-type Josephson consists of the NF bilayer, laterally connected with S banks (see Fig. 1a and insets at Fig. 2).

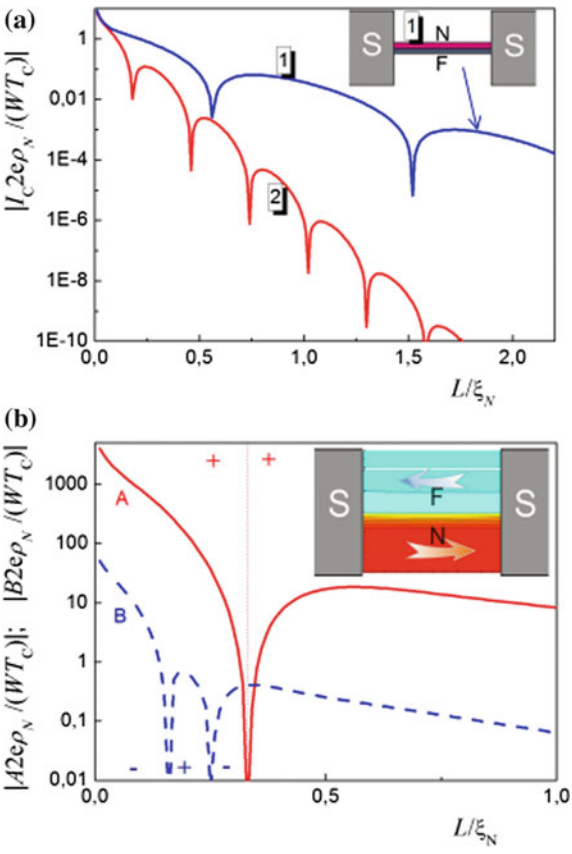


**Fig. 2** **a** Normalized critical current $I_C$ versus normalized spacing $L$ between S electrodes for SFS structure (2) and for heterostructures with thin NF bilayer (1). **b** CPR harmonic amplitudes $A$ (solid line) and $B$ (dashed line) for S–NF–S structure versus spacing $L$ for heterostructures with thick NF bilayer. Inset presents current distribution calculated for the case of $\varphi$-junction existence ($L = 0.33\xi_N$). The colors in the inset correspond to the intensity and sign of the current density concentration in the horizontal ($x$) direction

Properties of the considered structure are significantly different in the two opposite limits: in the limits of thin (1)/thick (2) N and F films. In the first case (thin films), the properties resemble the properties of the SFS junction with slightly enlarged coherence length (see Fig. 2a). For the second case (thick films), the weak link region may be divided into domains with the supercurrent flowing in the opposite directions. The current density map along S–NF–S two-dimensional junction is shown in the inset at Fig. 2b. Hence, the first harmonic amplitudes in the CPR, $A$, may be equal to zero due to cancelation of the current contributions from F and N channels in $\pi$- and in 0-state, respectively. For certain parameters of NF bilayer (mainly for $d_N$ and $d_F$), one can obtain stable $\varphi$-state due to the strongly nonsinusoidal CPR with negative amplitude of the second harmonic, $B$.

In general case, there are three characteristic scales for the decay of superconducting correlations: $\xi_N$, $\xi_H = \xi_1 + i\xi_2$, $\zeta = \zeta_1 + i\zeta_2$ [46]. The first two scales determine decay and oscillations of superconducting correlations far from FN interface, while the last one, $\zeta$, describes their behavior in its vicinity. Similar length scale $\zeta$ occurs near a domain wall in ferromagnets [47]. Here, the exchange field is averaged out for antiparallel directions of magnetizations, and the decay length of superconducting correlations tends to $\xi_N$. At FN interface, the flow of spin-polarized electrons from F to N metal and reverse flow of unpolarized electrons from N to F suppress the exchange field, thus providing the existence of $\zeta$. Under certain set of parameters, these scales, $\zeta_1$ and $\zeta_2$, can be comparable with $\xi_N$, which is typically much larger than $\xi_1$ and $\xi_2$ ($\xi_F\sqrt{\pi T_C/H}$ for $H \gg \pi T_C$).

The existence of three decay scales, $\xi_N$, $\zeta$, and $\xi_H$, should lead to appearance of three contributions to total supercurrent, $I_N$, $I_{FN}$, and $I_F$, respectively. The main contribution to "normal" component $I_N$ comes from the supercurrent, which is uniformly distributed in the N film. In accordance with the mentioned above qualitative analysis [48], it is the only current component which leads to a negative value of the amplitude of the second harmonic $B$ in the CPR. The smaller is the distance between the S electrodes, $L$, the larger is this contribution to the total supercurrent. To create a $\varphi$-contact, one needs to compensate the amplitude of the first harmonic, $A$, in a total current to a value that satisfies the conditions (2). Contribution to this amplitude $A$ from $I_N$ also increases with decreasing spacing $L$. Obviously, it is difficult to suppress the coefficient $A$ due to the "boundary" contribution $I_{FN}$ only, since $I_{FN}$ flows through thin near-boundary layer. Therefore, strong reduction of $A$ can be obtained as a result of competition between $I_N$ and $I_F$ currents flowing in opposite directions in N and F films far from FN interface. Note that the oscillatory behavior of the $I_F(L)$ dependence allows to meet conditions (2) in a certain range of $L$. The role of "boundary" contribution $I_{FN}$ in the required balance between $I_N$ and $I_F$ can be understood by solving the boundary-value problem (4)–(9b) which admits an analytic solution in some interesting cases.

***Spacing L is small***. Solution of the boundary-value problem (4)–(9b) can be simplified in the limit of small distance between superconducting electrodes:

$$L << \min\{\xi_1, \xi_N\}. \tag{11}$$

In this case, we decide to neglect nongradient terms in (4). Hence, the contributions to the total current resulting from the redistribution of currents near the FN interface cancel each other, leading to $I_{FN} = 0$ [48]. As a result, the total current $I_S(\varphi)$ is a sum of the following two terms

$$I_S(\varphi) = I_N(\varphi) + I_F(\varphi),$$

$$\frac{2eI_N(\varphi)}{\pi T W d_N} = \frac{1}{\gamma_{BN}\xi_N\rho_N}\sum_{\omega=-\infty}^{\infty}\frac{\Delta^2 G_N G_S \sin(\varphi)}{\omega^2} \tag{12}$$

$$\frac{2eI_F(\varphi)}{\pi T W d_F} = \frac{1}{\gamma_{BF}\xi_F\rho_F}\sum_{\omega=-\infty}^{\infty}\frac{\Delta^2 G_N G_S \sin(\varphi)}{\omega^2} \tag{13}$$

where $G_N = \frac{\omega}{\sqrt{\omega^2+\Delta^2\cos^2\left(\frac{\varphi}{2}\right)}}$. The "normal" and "ferromagnet" currents $I_N(\varphi)$ and $I_F(\varphi)$ flow independently across the corresponding parts of the weak link. The $I_{N,F}(\varphi)$ dependencies coincide with those calculated previously for double-barrier junctions [49] when value $L$ lies within the interval from the inequalities (11).

It follows from (12) and (13) that in this case the amplitude of the first harmonic for "ferromagnet" component $I_F(\varphi)$ is always positive and the condition (2) cannot be met.

***Spacing L is intermediate***. In this limit, we have

$$\xi_1 = L = \xi_N \tag{14}$$

and for the values of suppression parameters at SN and SF interfaces satisfying the conditions (3), the boundary problem (4)–(9b) can be solved analytically for sufficiently large magnitude of suppression parameter $\gamma_{BFN}$. It was shown in [48] that under these restrictions in the first approximation we can neglect the suppression of superconductivity in the N film due to proximity with the F layer:

$$\Phi_N = \Delta\cos\left(\frac{\varphi}{2}\right) + i\frac{\Delta G_S \sin\left(\frac{\varphi}{2}\right)}{\gamma_{BN} G_N}\frac{x}{\xi_N}, G_N = \frac{\omega}{\sqrt{\omega^2 + \Delta^2\cos^2\left(\frac{\varphi}{2}\right)}}, \tag{15}$$

while spatial distribution of $\Phi_F(x, z)$ includes three terms.

The first two terms in (15) describe the influence of the N film, while the last one has the form well known for SFS junctions. Expression (5) allows us to represent the total supercurrent in the form:

$$I_S(\varphi) = I_N(\varphi) + I_F(\varphi) + I_{FN}(\varphi). \tag{16}$$

Here $I_N(\varphi)$ is given by the expression (12). The second term in (16) in the limit of small transparencies of SF interfaces is as follows:

$$\frac{2eI_F(\varphi)}{\pi T W d_F} = \frac{\Delta^2 \sin(\varphi)}{\gamma_{BF}^2 \xi_F \rho_F} \sum_{\omega=-\infty}^{\infty} \frac{G_S^2}{\omega^2 \sqrt{\tilde{\Omega}} \sinh(2q_L)}, \tag{17}$$

where $q_L = L\sqrt{\tilde{\Omega}}/2\xi_F$, $\tilde{\Omega} = |\Omega| + iH\mathrm{sgn}(\Omega)/\pi T_C$, $\Omega = \omega/\pi T_C$.

The last contribution contains three components

$$I_{FN}(\varphi) = I_{FN1}(\varphi) + I_{FN2}(\varphi) + I_{FN3}(\varphi). \tag{18}$$

with additional smallness parameters $\gamma_{BFN}^{-1}$ and $\gamma_{BFN}^{-1}\xi_F/\xi_N$ in comparison with the "ferromagnet" component $I_F(\varphi)$. Nevertheless, these terms should be taken into account in the analysis because they decay significantly slower than $I_F(\varphi)$ with increasing spacing $L$.

***Stable zero-current φ-state.*** Here, we need relatively large absolute value for the amplitude of the second harmonic (and hence we need low temperatures). But in the limit $T = T_C$, we can go from summation to integration over $\omega$ in (12), (17). Thus

$$\frac{2eI_N(\varphi)}{W d_N} = \frac{\Delta}{\gamma_{BN}\xi_N \rho_N} K\left(\sin\frac{\varphi}{2}\right)\sin(\varphi), \tag{19}$$

where $K(x)$ is the complete elliptic integral of the first kind. We expanded the obtained expression (19) in the Fourier series:

$$A_N = Q_0 \frac{8}{\pi} \int_0^1 x^2\sqrt{1-x^2}K(x)dx = \mathrm{Y}_A Q_0, \tag{20}$$

$$B_N = 2A_N - \frac{32}{\pi} Q_0 \int_0^1 x^4\sqrt{1-x^2}K(x)dx = \mathrm{Y}_B Q_0, \tag{21}$$

where $Q_0 = \Delta W d_N/e\gamma_{BN}\xi_N\rho_N$. $A_N$, $B_N$ are the first and the second harmonic amplitudes of $I_N(\varphi)$,

$$\mathrm{Y}_A = \frac{2\pi^2}{\Gamma^2\left(-\frac{1}{4}\right)\Gamma^2\left(\frac{7}{4}\right)}; 0.973,$$

$$\mathrm{Y}_B = 2\mathrm{Y}_A - \frac{\pi}{2}{}_3F_2\left(\tfrac{1}{2}, \tfrac{1}{2}, \tfrac{5}{2}; 1, 4; 1\right); -0.146,$$

where $\Gamma(z)$ is the well-known Gamma function and ${}_pF_q$ is generalized hypergeometric function.

Evaluation of the sums in (17) can be done for $H >> \pi T_C$ and $T = T_C$ resulting in sinusoidal "ferromagnet" component $I_F(\varphi) = A_F \sin(\varphi)$ with

$$A_F = P_0 \frac{2}{\sqrt{h}} \exp(-\kappa L)\cos\left(\kappa L + \frac{\pi}{4}\right), \tag{22}$$

$\kappa = \sqrt{h}/\sqrt{2}\xi_F$, $h = H/\pi T_C$, and $P_0 = \Delta W d_F/e\gamma_{BF}^2\xi_F\rho_F$. Substitution of (20), (21) into the inequalities (2) gives analytical form of the $\varphi$-state conditions for the ramp-type structure:

$$\left|\mathrm{Y}_A + \frac{1}{\varepsilon}\Psi(L)\right| < 2|\mathrm{Y}_B|, \varepsilon = \frac{\sqrt{h}\gamma_{BF}^2}{2\gamma_{BN}}\frac{d_N\xi_F\rho_F}{d_F\xi_N\rho_N},$$
$$\Psi(L) = \exp(-\kappa L)\cos\left(\kappa L + \frac{\pi}{4}\right). \tag{23}$$

These expressions give us the limitation on geometrical and material parameters of the considered junctions, providing the existence of stable zero-current $\varphi$-state. Function $\Psi(L)$ has the first minimum at $\kappa L = \pi/2$, $\Psi(\pi/2\kappa) \approx -0.147$. For large enough values of $\varepsilon$, inequality (23) cannot be fulfilled at any spacing $L$. Thus, solutions exist only in the area with upper limit

$$\varepsilon < \frac{-\Psi(\pi/2\kappa)}{\mathrm{Y}_A - 2|\mathrm{Y}_B|} \approx 0.216. \tag{24}$$

At $\varepsilon \approx 0.216$, the left-hand side of inequality (23) equals to its right-hand part, providing the nucleation of an interval of $\kappa L$ in which we can expect the creation of a $\varphi$-structure. This interval increases with decrease in $\varepsilon$ and achieves its maximum length

$$1.00 \lesssim \kappa L \lesssim 2.52, \tag{25}$$

at $\varepsilon = \frac{-\Psi(\pi/2\kappa)}{\mathrm{Y}_A+2|\mathrm{Y}_B|} \approx 0.116$. Nota bene: At $\varepsilon = -\Psi(\pi/2\kappa)/\mathrm{Y}_A \approx 0.151$, there is a transformation of the left-hand side local minimum in (23), which occurs at $\kappa L = \pi/2$, into local maximum; so that at $\varepsilon \approx 0.116$, the both sides of (23) become equal to each other, and the interval (25) of $\varphi$-contact existence subdivides into two parts. With a further decrease in $\varepsilon$, these parts are transformed into bands, which are localized in the vicinity of the $0-\pi$ transition point ($A_N + A_F = 0$). These narrow valleys of required parameters take place at $\kappa L = \pi/4$ and $\kappa L = 5\pi/4$. The width of the mentioned bands decreases with decrease in $\varepsilon$.

Thus, our analysis has shown that for

$$0.12 \le \varepsilon \le 0.2 \tag{26}$$

we can expect the creation of $\varphi$-structure in a sufficiently wide range $\Delta L$ of spacing between the S electrodes. One can determine the value $\Delta L$ from (23).

Let us take into account the impact of the interface term $I_{FN}(\varphi)$. In the considered case, we have [48] the following contributions:

$$I_{FN1}(\varphi) = \frac{2U_0\xi_F\exp\left(-\frac{\kappa L}{2}\right)\cos\left(\frac{\kappa L}{2} - \frac{\pi}{4}\right)}{\gamma_{BF}\gamma_{BN1}\xi_N h^{3/2}}\sin(\varphi) \tag{27}$$

$$I_{FN2}(\varphi) = -\frac{\sqrt{2}U_0\xi_F}{4h^{3/2}\gamma_{BF}\gamma_{BN1}\xi_N}\sin(\varphi)K\sin\left(\frac{\varphi}{2}\right) \tag{28}$$

$$I_{FN3}(\varphi) = -\frac{2U_0\xi_F\exp\left(-\frac{\kappa L}{2}\right)\sin\left(\frac{\kappa L}{2}\right)}{h\gamma_{BF}}\sin(\varphi)K\sin\left(\frac{\varphi}{2}\right) \tag{29}$$

where $U_0 = \Delta W/e\gamma_{BFN}\rho_F$. In the range of spacings $\pi/4 < \kappa L < 5\pi/4$, the currents $I_{FN2}(\varphi)$ and $I_{FN3}(\varphi)$ are less than zero. These contributions have the same form of CPR as it was for the "normal" $I_N(\varphi)$ term, and due to negative sign, suppress the magnitude of supercurrent across the junction, thus making the inequality (23) easier to perform. The requirement $B < 0$ imposes additional restriction on the value of the suppression parameter $\gamma_{BFN}$

$$\gamma_{BFN} > \frac{\rho_N\xi_N}{hd_N\rho_F}\left(\frac{\xi_F}{\xi_N\gamma_{BFN}h^{1/2}} + \frac{\gamma_{BN}}{\gamma_{BF}}\right). \tag{30}$$

In order to obtain this inequality, we have used the fact that in the range of distances between the electrodes $\pi/4 < \kappa L < 5\pi/4$ depending on $\kappa L$ factor in (29) is of the order of unity. It follows from (30) that for a fixed value of $\gamma_{BFN}$ domain of $\varphi$-structure existence extends with increase in thickness of N film $d_N$. Stable zero-current state is impossible if $d_N$ becomes smaller than the critical value, $d_{NC}$,

$$d_{NC} = \frac{\rho_N\xi_N}{h\rho_F\gamma_{BFN}}\left(\frac{\xi_F}{\xi_N\gamma_{BFN}h^{1/2}} + \frac{\gamma_{BN}}{\gamma_{BF}}\right). \tag{31}$$

The existence of the critical thickness $d_{NC}$ follows from the fact that the amplitude $B$ in "normal" component $I_N$ is proportional to $d_N$, while in $I_{FN}$ term $B$ is independent on $d_N$. The sign of $I_{FN1}(\varphi)$ term is positive for $\pi/4 < \kappa L < 3\pi/4$ and negative for $3\pi/4 < \kappa L < 5\pi/4$, thus providing an advantage for a $\varphi$-structure realization for the spacings which correspond to the second interval.

Figure 4b illustrates our analytical results. The solid line at the figure is the absolute value of the first harmonic amplitude versus spacing $L$ between S banks. It is the sum of two components, which were calculated from expressions (17) (dash-dotted line) and (12) (dashed line). The dash-dot-dotted line at Fig. 4b is the amplitude of the second harmonic in "normal" component (12). The dotted line is the $I_{FN}(L)$ dependence calculated from (18). We made all calculations for the following set of parameters, which is close to those in real experiment: $d_N = 0.1\xi_N$, $d_F = 0.65\xi_N$, $\gamma_{BN} = 0.1$, $\gamma_{BF} = 1$, $\gamma_{BNF} = 10$, $\xi_F = 0.1\xi_N$, $\rho_N = \rho_F$, $T = 0.7T_C$, $H = 10T_C$. All the amplitudes in CPRs were normalized using factor $(2e\rho_N/(WT_C))^{-1}$. There is an interval of spacings $L$, when the currents in N and F layers flow in opposite directions and the points of $0-\pi$ transitions for both dependencies become closer to each other. In the entire region between these points, the conditions (2) are fulfilled. This is exactly the required "$L$–interval," inside which a zero-current stable $\varphi$-state can be achieved. The contribution of $I_{FN}$ term into the total supercurrent in accordance with our analysis is really small.

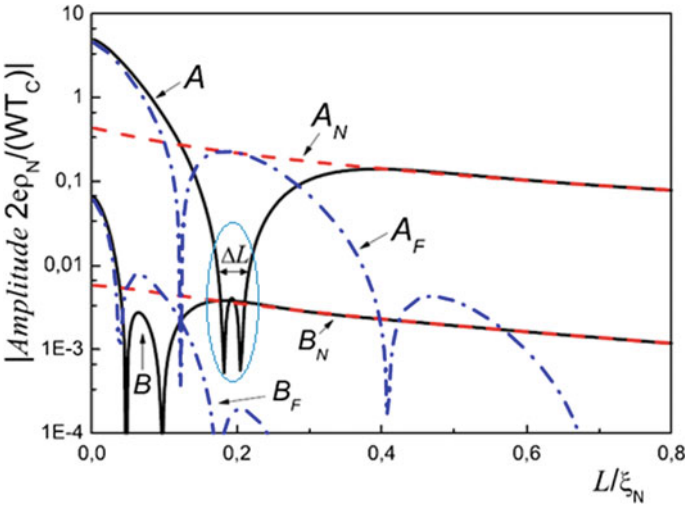


**Fig. 3** Numerical results for the amplitudes *A and B* in the CPR of the ramp-type S–NF–S structure ($d_N = 0.1\xi_N$; $d_F = 1.06\xi_N$) and their components $A_N$, $A_F$, $B_N$, $B_F$ versus spacing $L$ at $T = 0.7T_C$. Parameters are chosen to form enhanced $\varphi$-state interval marked by "$\Delta L$"

To confirm the obtained findings, we have solved the boundary problem (4)–(9a, 9b) for the same set of parameters of the structure except $d_F$. The results of calculations for two values of F-layer thickness ($d_F = 1.06\xi_N$ and $d_F = 1.4\xi_N$) are presented at Figs. 3 and 4a. The solid lines in Fig. 3 correspond to the absolute values of the amplitudes of the first, $A$, and the second, $B$, harmonics in CPR. The dashed and dash-dotted curves demonstrate the contributions to these amplitudes from the supercurrents, respectively, in N and F layers. The main difference between analytical solutions presented in Fig. 4b and the results of numerical calculations belong to the limit of small spacings $L$. The amplitudes of the first and the second harmonics of the supercurrent in the normal layer decrease with increasing spacing. The points of $0 - \pi$ transition of the first harmonic amplitude of the supercurrent in the ferromagnetic are shifted to the right, toward larger distances between superconducting electrodes. The amplitude of the second harmonic here, $B_F$, in the vicinity of $L \approx 0.2\xi_N$ is negligibly small in comparison with the magnitude of $B_N$. As a result, the shapes of $A(L)$ curves in Figs. 3 and 4b are nearly the same, with a little bit larger interval of stable zero-current $\varphi$-state for the curve representing numerical results.

In Fig. 4a, we demonstrate the same dependencies $A(L)$ and $B(L)$ as in Fig. 3 (solid and dashed lines) together with similar curves calculated for the case $d_F = 1.4\xi_N$ (dash-dotted and dotted lines for $A$ and $B$). For larger values of $d_F$, we get out of the interval (26) and instead of relatively large zone $\Delta L_1$ have to deal with two very narrow intervals $\Delta L_2$ and $\Delta L_3$ located in the vicinity of $0 - \pi$ transitions of the first harmonic amplitude $A$.

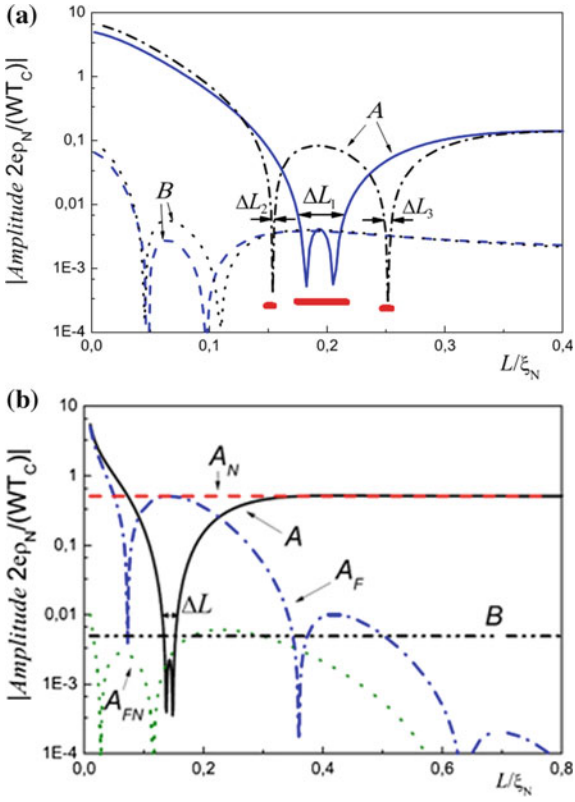


**Fig. 4** **a** Numerically calculated CPR amplitudes $A$ and $B$ versus electrode spacing $L$ for S–FN–S structures with $d_F = 1.06\xi_N$ (solid and dashed lines, respectively). Enhanced $\varphi$-interval $\Delta L_1$ is much larger than the sum of "standard" $\varphi$ -intervals $\Delta L_2$ and $\Delta L_3$ (see dashed lines for $d_F = 1.4\xi_N$). **b** Analytically calculated amplitudes $A$ and $B$ in the CPR of the ramp S–NF–S structure ($d_N = 0.1\xi_N$, $d_F = 0.65\xi_N$) and their components $A_N, A_F, A_{FN}$ versus spacing $L$ at temperature $T = 0.7\ T_C$. Interval of $\varphi$-state existence, $\Delta L$, is marked

***Overlap-type geometry***. From technological point of view, the overlap-type geometry (with the overlap length much larger $\xi_N$, see Fig. 1b) looks more reliable than the ramp-type one. We have shown in our numerical calculations that in the case of thin layers and large transparency of FN interface it does not matter, whether the film of normal metal lays above or behind the F layer (see Fig. 5a).

At arbitrary layer thickness in SFN–FN–NFS junctions (Fig. 5b), the large difference between values $\xi_N$ and $\xi_F$ results in the formation of two (SFS and SFNFS) competing parallel current channels. In SNF–NF–FNS structures, the current through long SNFNS channel is always much smaller than the current through SNS pathway. In SFN–FN–NFS structures, the signs of the critical current $I_C$ and harmonic amplitudes in the SFS channel are controlled by the distance $L$ between S banks. The sign of the SFNFS contribution to the total supercurrent is a function of ferromagnetic layer thickness, $d_F$. In Fig. 6a, we represent the phase diagram of the CPR harmonic amplitudes in $(L, d_F)$ plane: The proper choice of the F-film topology allows

(1) to suppress the amplitude of the first harmonic in CPR;
(2) to make the necessary sign for zero-current $\varphi$-state existence for the amplitude $B$ of the second one (see Fig. 6b).

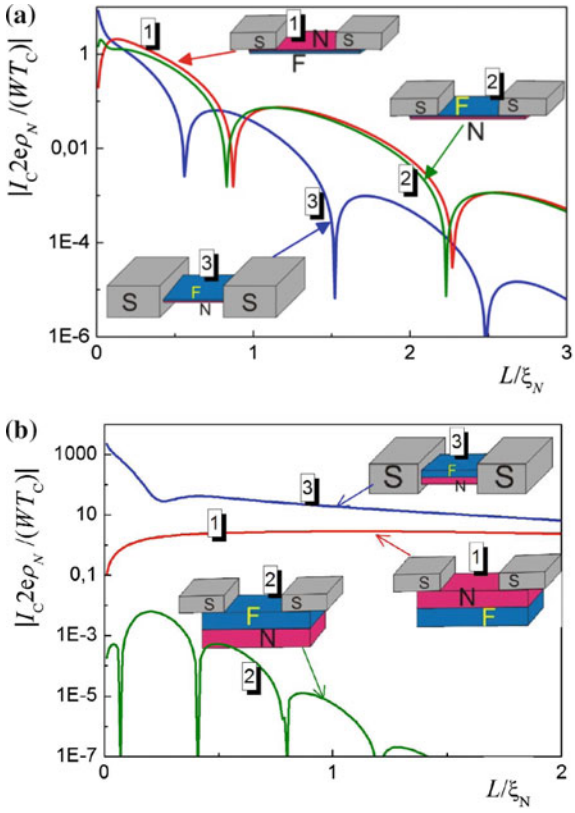


**Fig. 5** Numerically calculated normalized critical current $I_C$ versus spacing $L$ for (1) SNF–NF–FNS, (2) SFN–FN–NFS and (3) the ramp-type S-NF-S junctions in the case of **a** thin, $d_N = d_F = 0.01\xi_N$, and **b** thick, $d_N = d_F = 3\xi_N$, layers

***Combined ramp-type-overlap (RTO) junctions.*** It will be somewhat easier to fulfill the conditions for the $\varphi$-structure existence due to slight modifications of junction topology. We need here a combination of the ramp-type and the overlap-type configurations, as it is shown in Fig. 1. Figure 7a demonstrates numerical calculations of spatial distribution of supercurrent in RTO $\varphi$-structure at Josephson phase $\varphi = \pi/2$.

The supercurrent density is represented through the color saturation. The amplitude of the first harmonic is relatively small here due to opposite current directions in N and F layers. The main feature of the ramp-type-overlap geometry is seen to be specific current distribution in the normal metal layer, leading to another CPR shape with dependence on thickness $d_N$. Further, the current $I_N$ should saturate as a function of $d_N$, since normal film regions located at distances larger than $\xi_N$ from SN interface are practically excluded from the process of supercurrent transfer due to exponential decay of proximity-induced superconducting correlations. The RTO structure was analyzed in the most interesting practical case of thin layer of normal metal

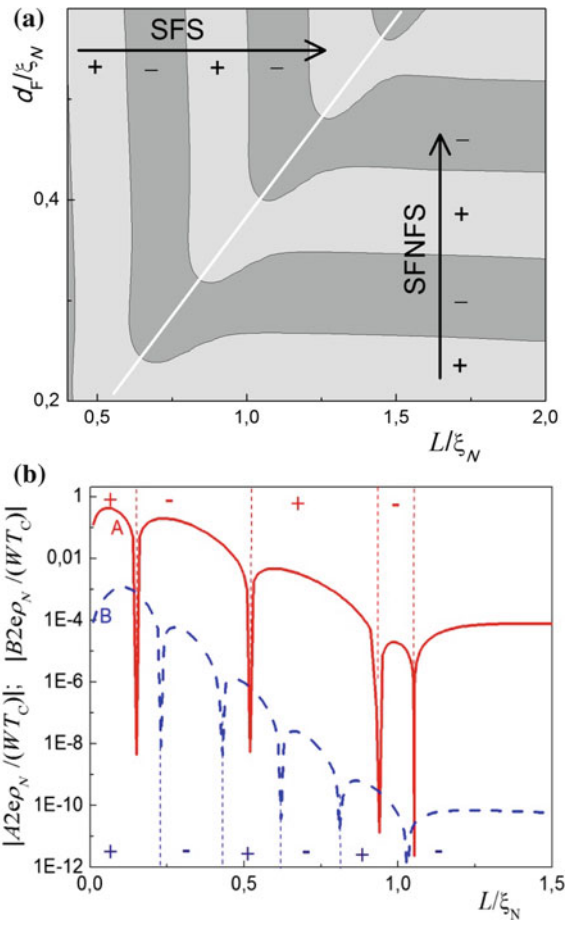


**Fig. 6** **a** ($L$, $dF$) phase diagram in SFN–FN–NFS structure with alternating 0- and $\pi$-state areas. **b** Harmonic amplitudes $A$ (solid) and $B$ (dashed line) in the CPR for SFN–FN–NFS structure versus spacing $L$ for heterostructures with thick FN bilayer

$$d_N = \xi_N \tag{32}$$

$$L = \xi_N, \tag{33}$$

and sufficiently large characteristic of boundary transparency $\gamma_{BFN}$, providing negligibly small suppression of superconductivity in N film due to proximity with F layer. Under these conditions, we can at the first stage consider the Josephson effect in overlap SN-N-NS structure. Then, at the second stage we will use the obtained solutions to calculate supercurrent flowing across the ferromagnetic pathway in the RTO structure [48]. Once again we represent the supercurrent in the following form:

$$I_S(\varphi) = I_N(\varphi) + I_F(\varphi) + I_{FN}(\varphi). \tag{34}$$

Expression for the $I_N$ component has the form

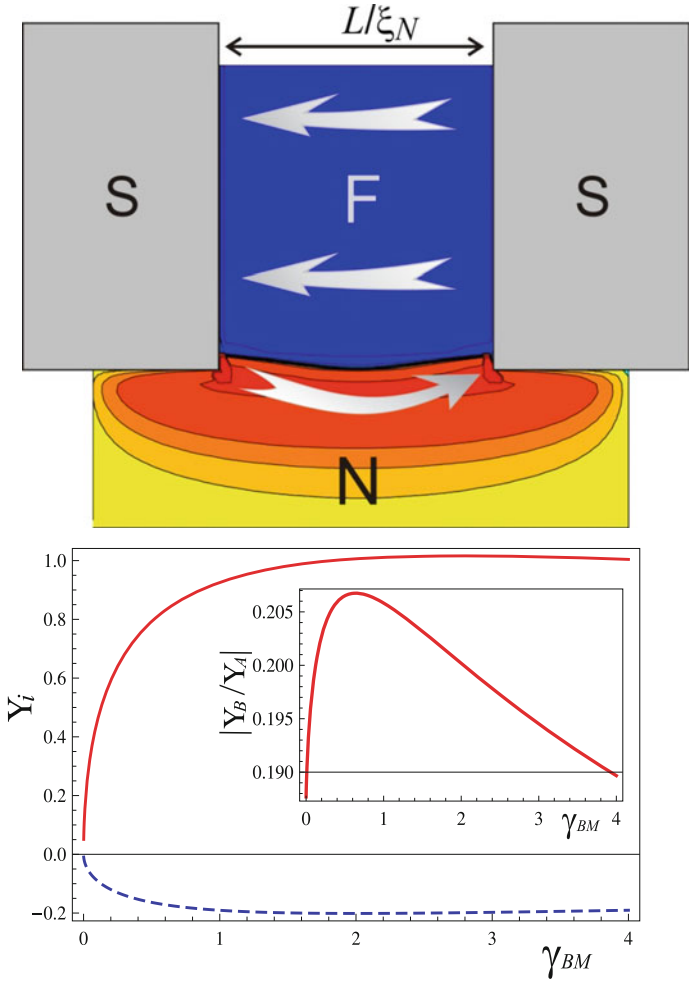


**Fig. 7** **a** Current distribution along the RTO-type SN–FN–NS structure at $L = 0.63\xi_N$, $d_N = \xi_N$, $d_F = 2\xi_N$, and $T = 0.7T_C$. The intensity of color corresponds to the supercurrent density in directions indicated by arrows. **b** The amplitudes of the first harmonic $Y_A$ (solid line) and the second one $Y_B$ (dashed line) normalized on $2W\Delta/e\rho N_{BN}$ versus reduced thickness $Y_{BM}$. Inset shows the ratio of harmonics $|Y_B/Y_A|$ versus $Y_{BM}$

$$\frac{2eI_N(\varphi)}{\pi TWd_N} = \frac{2}{\rho_N\xi_N\sqrt{\gamma_{BM}}}\sum_{\omega=-\infty}^{\infty}\frac{r^2\delta^2\sin\varphi\sqrt{(\Omega\gamma_{BM}+G_S)}}{\sqrt{2\Omega\mu^2\left(\sqrt{\Omega^2+r^2\delta^2}+\mu\right)}}, \tag{35}$$

where $r = G_S/(\Omega\gamma_{BM} + G_S)$, $\gamma_{BM} = \gamma_{BN}d_N/\xi_N$, and $\mu = \sqrt{\Omega^2 + r^2\delta^2\cos^2(\varphi/2)}$, $\delta = \Delta/\pi T_C$.

The "ferromagnetic" term $I_F(\varphi)$ in (34) is the supercurrent through one-dimensional double-barrier SFS structure defined by (17), while the FN-interface term $I_{FN}(\varphi)$ was discussed before.

The larger the relative amplitude of the second harmonic (or the lower is the temperature of a junction compare to $T_C$), the better we meet the conditions for the implementation of a zero-current $\varphi$-state. At high temperature $T = T_C$, we can transform summation into integration over $\omega$ in (35) and calculate numerically the dependencies $A$ and $B$:

$$A_N = \frac{2W\Delta}{e\rho_N\gamma_{BN}}\mathrm{Y}_A, \tag{36}$$

$$B_N = \frac{2W\Delta}{e\rho_N\gamma_{BN}}\mathrm{Y}_B \tag{37}$$

on suppression parameter $\gamma_{BM}$. The results of our calculations $\mathrm{Y}_A(\gamma_{BM})$ and $|\mathrm{Y}_B|(\gamma_{BM})$ are presented in Fig. 7b. Both $\mathrm{Y}_A$ and $|\mathrm{Y}_B|$ increase with increasing of $\gamma_{BM}$ and saturate at $\gamma_{BM} \approx 1$. Inset in Fig. 7b shows the ratio of the harmonics $|\mathrm{Y}_B/\mathrm{Y}_A|$ as a function of $\gamma_{BM}$. It achieves maximum at $\gamma_{BM} \approx 0.64$, and thus, it determines the optimal values of normalized amplitudes of the first $\mathrm{Y}_A \approx 0.844$ and the second $\mathrm{Y}_B \approx -0.175$ harmonics of the current in the film of normal metal. It is seen from the inset in Fig. 7b that the ratio $|\mathrm{Y}_B/\mathrm{Y}_A|$ is slowly decreasing function of $\gamma_{BM}$. Therefore, the estimates given below for $\gamma_{BM} = 0.64$ are applicable in a wide range of parameters: $0.5 \le \gamma_{BM} \le 10$.

Hence, we can write down the condition of zero-current $\varphi$-state existence similar to (23)

$$\left|\mathrm{Y}_A + \frac{1}{\varepsilon}\Psi(L)\right| \le 2|\mathrm{Y}_B|,\ \varepsilon = \frac{\sqrt{h}\gamma_{BF}^2}{\gamma_{BN}}\frac{\xi_F\rho_F}{d_F\rho_N},$$
$$\Psi(L) = \exp(-\kappa L)\cos\left(\kappa L + \frac{\pi}{4}\right), \tag{38}$$

with modified dimensionless parameter $\varepsilon$. The wide region of $\varphi$-state existence still can be found if $\varepsilon$ is within the interval

$$0.123 \le \varepsilon \le 0.298. \tag{39}$$

$\kappa L$ value here satisfies the condition (38). As follows from (38), interval of $\kappa L$ product gains its maximum length

$$0.94 \le \kappa L \le 2.72, \tag{40}$$

at $\varepsilon = 0.123$. These intervals are slightly larger than those given by (25) for the ramp-type junction topology.

Figure 8 represents our main results for the interval of $\varphi$-state existence, $\Delta L$, in the ideal case of $T = T_C$, $\gamma_{BM} = 0.64$, and $\varepsilon = 0.123$. The corresponding set of

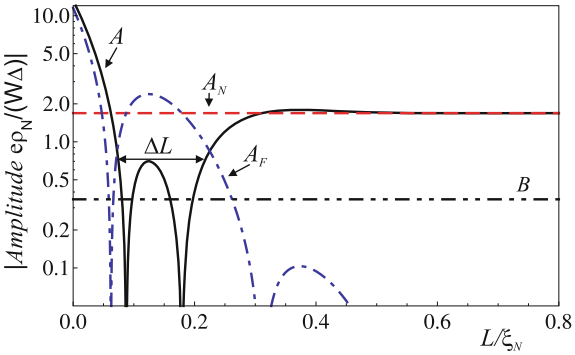


**Fig. 8** Amplitudes $A$, $A_N$, $A_F$, $B$ of the CPR harmonics versus spacing $L$ for the RTO junction at small temperature $T << T_C$, $\gamma_{BM} = 0{:}64$ and $\varepsilon = 0.123$. The mark "$\Delta L$" shows enhanced $\varphi$-state interval

parameters $d_N = 0.64\xi_N$, $d_F = 1.45\xi_N$, $\gamma_{BN} = 1$, $\gamma_{BF} = 1$, $\xi_F = 0.1\xi_N$, $\rho_N = \rho_F$, and $H = 10T_C$ was substituted in (17), (35). The solid line is an absolute value of the first harmonic amplitude; its normal, $A_N$, and ferromagnetic, $A_F$, components are shown by dashed and dash-dotted lines, respectively. The second harmonic amplitude is shown as dash-dot-dotted curve. It is clear that $|A|$ is small enough in the wide region $\Delta L$ and reaches the value of $|2B|$ only at local maximum. The increased width of $\Delta L$ is provided by geometric attributes of RTO-type structure.

Let us illustrate the range of nontrivial ground phase $\varphi_g$ with the help of Fig. 9. Here, the total supercurrent $I_S$ is shown as a function of Josephson phase $\varphi$ and spacing $L$. It means that each $L$-section of this 3D graph is a single CPR. Thick red lines mark the ground-state phases at each value of $L$. In the range of small and large spacing $L$ ground phase is located at $\varphi_g = 0$. However, in the $\Delta L$-interval the CPRs become significantly nonsinusoidal and demands ground phase $\varphi_g$ to split and go to $\pi$ from both sides; then, $\pi$-state is realized at $\kappa L = \pi/2$. Clearly, for $\varepsilon \geq 0.123$ the value $\varphi_g = \pi$ cannot be reached (see Fig. 9a), while in the case of $\varepsilon \leq 0.123$ the prolonged $\pi$-state region is formed (see Fig. 9c).

## 4 Discussion and Conclusion

We have shown that zero-current stable $\varphi$-state

- cannot be achieved in conventional SIS, SNS, and SFS structures;
- can be realized in S–NF–S structures with longitudinally oriented NF bilayers. We have discussed the conditions for the creation of $\varphi$-junctions in the ramp-type S–NF–S, in the overlap-type SFN–FN–NFS, and in the combined RTO-type SN–FN–NS geometries. The most favorable suggestions for experimental realization of $\varphi$-structure are based on using copper as a normal film

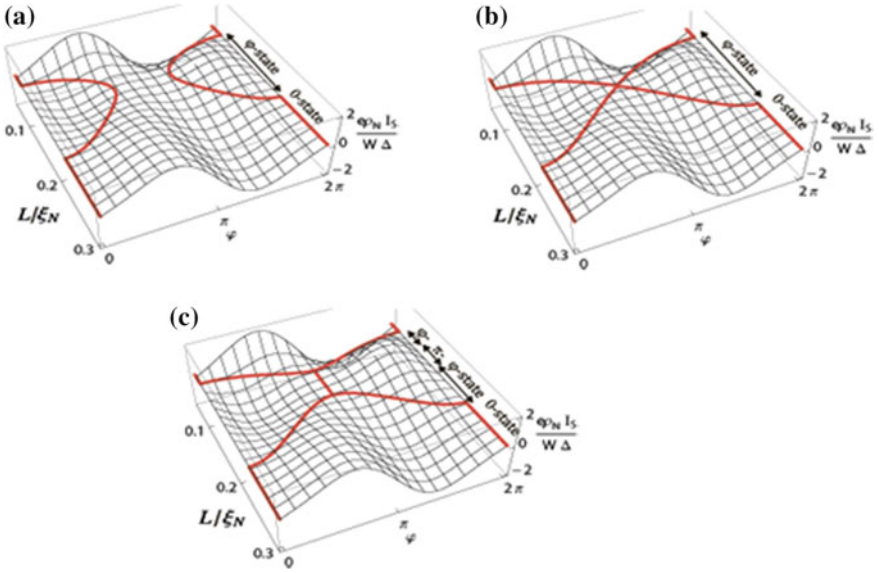


**Fig. 9** Total supercurrent $I_S$ versus Josephson phase $\varphi$ and spacing $L$ for the optimal RTO structure at $T << T_C$; $\Upsilon_{BM} = 0.64$ and at different F-layer thickness parameters **a** $\varepsilon = 0.137$, **b** $\varepsilon = 0.123$, **c** $\varepsilon = 0.111$. The lines mark the ground-state phase $\varphi_g$ [48]

($\xi_N \approx 100\,\text{nm}$ and $\rho = 5 * 10^{-8}\Omega\text{m}$) and strongly diluted ferromagnet like FePd or CuNi alloy ($\xi_F \approx 10\,\text{nm}$, $H \approx 10T_C$) as the F layer. We would like to choose Nb ($T_C \approx 9K$) as a material for S electrodes since it is widely used in superconducting applications. We also propose to use sufficiently thick normal layer (above the saturation threshold) when N-layer thickness has almost no effect. After substitution of relevant values into (39) and (40), we came to fairly broad geometrical margins, within which there is a possibility for the creation of $\varphi$-structures.

$$\begin{aligned} &d_N \geq 50\,\text{nm}, \\ &60\,\text{nm} \leq d_F \leq 150\,\text{nm}, \\ &7\,\text{nm} \quad \leq L \leq 22\,\text{nm}. \end{aligned} \tag{41}$$

Finally, the width: The last out-of-plane characteristic geometrical scale can be put equal to $W = 140\,\text{nm}$. This allows to maximize "available" supercurrent and conserves the scale of structure in a range of 100 nm. The magnitude of the critical current in the $\varphi$-state is determined by the second harmonic amplitude $B$

$$I_C \sim B_N = \frac{2W\Delta}{e\rho_N\gamma_{BN}}\Upsilon_B \approx 1\text{mA}. \tag{42}$$

The spreads of geometric scales for the creation of $\varphi$-junction as well as the magnitude of its critical current are large enough for practical realization of the considered compact structure.

By creating $\varphi$-state in a Josephson junction, one can fix certain value of ground phase $\varphi_g$. Temperature variation slightly shifts the interval of relevant $0 - \pi$ transition and permits one to tune the desired ground-state phase. The prospects for the practical use of such structures are related to the possibility of obtaining bistable logic or memory elements on their basis. The characteristic time for the read and, of particularly importance, the write operations here is determined by the Josephson processes and, as a consequence, in many orders of magnitude less than this value in typical cryogenic magnetic-memory cells. Additional superconducting layer in the region of the weak link will increase here the characteristic voltage and frequency to the values that are close to typical for tunnel junctions [50]. Moreover, for the $\varphi$-state of the junction the double-well potential is formed at the degeneracy point without any additional fields and ground-state splitting provides necessary condition for quantum bits and quantum detectors. To summarize, Josephson $\varphi$-structures can be realized using up-to-date technology as a novel basic element for superconducting electronics.

**Acknowledgements** S.B., I.S., N.K., and M.K. carried out research on current transport for the structures with complex weak link region (bilayer) with support of the RSF grant No. 17-12-01079. This work was also supported in part by the Ministry of Education and Science of the Russian Federation, Grant SC 8168.2016.2, and by RFBR, Grant 16-29-09515-ofi-m.

## References

1. S.K. Tolpygo, Low Temp. Phys. **42**, 463 (2016)
2. A.A. Golubov, M.Yu. Kupriyanov, E. Il'ichev, Rev. Mod. Phys. **76**, 411 (2004)
3. A.I. Buzdin, M.Yu. Kupriyanov, Pis'ma Zh. Exp. Teor. Fiz. **52**, 1089 (1990) [JETP Lett. **52**, 487 (1990)]
4. L.R. Tagirov, Physica C **307**, 145 (1998)
5. T. Kontos, M. Aprili, J. Lesueur, X. Grison, Phys. Rev. Lett. **86**(2), 304 (2001)
6. C. Bell, R. Loloee, G. Burnell, M.G. Blamire, Phys. Rev. B **71**, 180501 (R) (2005)
7. M. Weides, M. Kemmler, E. Goldobin, H. Kohlstedt, R. Waser, D. Koelle, R. Kleiner, Phys. Rev. Lett. **97**, 247001 (2006)
8. A.V. Ustinov, V.K. Kaplunenko, J. Appl. Phys. **94**, 5405 (2003)
9. Ya.M. Blanter, F.W.J. Hekking, Phys. Rev. B **69**, 024525 (2004)
10. I.B. Sperstad, J. Linder, A. Sodbo, Phys. Rev. B **78**, 104509 (2008)
11. M.G. Blamire, J.W.A. Robinson, J. Phys.: Condens. Matter **26**, 453201 (2014)
12. M. Eschrig, Rep. Prog. Phys. **78**, 104501 (2015)
13. V.V. Ryazanov, V.A. Oboznov, A.V. Veretennikov, A.Yu. Rusanov, Phys. Rev. B **65**, 02051(R) (2001)
14. S.M. Frolov, D.J. Van Harlingen, V.A. Oboznov, V.V. Bolginov, V.V. Ryazanov, Phys. Rev. B. **70**, 144505 (2004)
15. V.V. Ryazanov, V.A. Oboznov, A.Yu. Rusanov, A.V. Veretennikov, A.A. Golubov, J. Aarts, Phys. Rev. Lett. **86**(11), 2427 (2001)
16. P. Bunyk, K. Likharev, and D. Zinoviev, Int. J. High Speed Electron. Syst. **11**, 1, 257, (2001)

17. T. Ortlepp, Ariando, O. Mielke, C.J.M. Verwijs, K.F.K. Foo, H. Rogalla, F.H. Uhlmann, H. Hilgenkamp, Science **312**, 1495 (2006)
18. O. Wetzstein, T. Ortlepp, R. Stolz, J. Kunert, H.-G. Meyer, H. Toepfer, IEEE Trans. Appl. Supercon. **21**, 814 (2011)
19. M.H.S. Amin, A.Yu. Smirnov, A.M. Zagoskin, T. Lindstrom, S.A. Charlebois, T. Claeson, A. Ya. Tzalenchuk, Phys. Rev. B **73**, 064516-1-5 (2005)
20. N.V. Klenov, V.K. Kornev, N.F. Pedersen, Physica C **435**, 114 (2006)
21. N.V. Klenov, N.G. Pugach, A.V. Sharafiev, S.V. Bakurskiy, V.K. Kornev, Phys. Solid State **52**, 2246 (2010)
22. I. Askerzade, Low Temp. Phys. **41**, 241 (2015)
23. A. Buzdin, A.E. Koshelev, Phys. Rev. B **67**, 220504(R) (2003)
24. N.G. Pugach, E. Goldobin, R. Kleiner, D. Koelle, Phys. Rev. B. **81**(10), 104513 (2010)
25. H. Sickinger, A. Lipman, M. Weides, R.G. Mints, H. Kohlstedt, D. Koelle, R. Kleiner, E. Goldobin, Phys. Rev. Lett. **109**, 107002 (2012)
26. E. Goldobin, H. Sickinger, M. Weides, N. Ruppelt, H. Kohlstedt, R. Kleiner, D. Koelle, Appl. Phys. Lett. **102**, 242602 (2013)
27. A. Lipman, R.G. Mints, R. Kleiner, D. Koelle, E. Goldobin, Phys. Rev. B. **90**(18), 184502 (2014)
28. R. Menditto, H. Sickinger, M. Weides, H. Kohlstedt, M. Zonda, T. Novotny, D. Koelle, R. Kleiner, E. Goldobin, Phys. Rev. B. **93**, 174506 (2016)
29. J.W.A. Robinson, S. Piano, G. Burnell, C. Bell, M.G. Blamire, Phys. Rev. Lett. **97**, 177003 (2006)
30. S. Piano, J.W.A. Robinson, G. Burnell, M.G. Blamire The, Eur. Phys. J. B **58**, 123 (2007)
31. R.S. Keizer, S.T.B. Goennenwein, T.M. Klapwijk, G. Miao, G. Xiao, A. Gupta, Nature **439**, 825 (2006)
32. M.S. Anwar, M. Veldhorst, A. Brinkman, J. Aarts, Appl. Phys. Lett. **100**, 052602 (2012)
33. V. Shelukhin, A. Tsukernik, M. Karpovski, Y. Blum, K.B. Efetov, A.F. Volkov, T. Champel, M. Eschrig, T. Lofwander, G. Schon, A. Palevski, Phys. Rev. B. **73**, 174506 (2006)
34. A.K. Feofanov, V.A. Oboznov, V.V. Bol'ginov et al., Nat. Phys. **6**, 593 (2010)
35. R.G. Mints, Phys. Rev. B **57**, R3221 (1998)
36. J. Pfeiffer, M. Kemmler, D. Koelle, R. Kleiner, E. Goldobin, M. Weides, A.K. Feofanov, J. Lisenfeld, A.V. Ustinov, Phys. Rev. B. **77**, 214506 (2008)
37. T. Golod, A. Iovan, V.M. Krasnov, Nat. Commun. **6**, 8628 (2015)
38. I.V. Vernik, V.V. Bol'ginov, S.V. Bakurskiy, A.A. Golubov, M.Yu. Kupriyanov, V.V. Ryazanov, O.A. Mukhanov, IEEE Trans. Appl. Supercon. **23** (3), 1701208 (2013)
39. S.V. Bakurskiy, N.V. Klenov, I.I. Soloviev, V.V. Bol'ginov, V.V. Ryazanov, I.I. Vernik, O.A. Mukhanov, M.Yu. Kupriyanov, A.A. Golubov, Appl. Phys. Lett. **102**, 192603 (2013)
40. S.V. Bakurskiy, N.V. Klenov, I.I. Soloviev, M.Yu. Kupriyanov, A.A. Golubov, Phys. Rev. B **88**, 144519 (2013)
41. I.I. Soloviev, N.V. Klenov, S.V. Bakurskiy, V.V. Bol'ginov, V.V. Ryazanov, M.Y. Kupriyanov, A.A. Golubov, Appl. Phys. Lett. **105**, 242601 (2014)
42. N.V. Klenov, V.I. Ruzhickiy, I.I. Soloviev, Moscow Univ. Phys. Bull. **70**, 404 (2015)
43. T.Yu. Karminskaya, M.Yu. Kupriyanov, Pis'ma Zh. Eksp. Teor. Fiz. **85**, 343 (2007) [JETP Lett. **85**, 286 (2007)]
44. T.Yu. Karminskaya, A.A. Golubov, M.Yu. Kupriyanov, A.S. Sidorenko, Phys. Rev. B **81**, 214518 (2010)
45. F. Born, M. Siegel, E.K. Hollmann, H. Braak, A.A. Golubov, D.Yu. Gusakova, M.Yu. Kupriyanov, Phys. Rev. B. **74**, 140501 (2006)
46. A.A. Golubov, M.Yu. Kupriyanov, Ya.V. Fominov, JETP Lett. **75**, 709 (2002) [Pisma v ZhETF **75**, 588 (2002)]
47. I.S. Burmistrov, N.M. Chtchelkatchev, Phys. Rev. B **72**, 144520 (2005)
48. S.V. Bakurskiy, N.V. Klenov, T.Yu. Karminskaya, M.Yu. Kupriyanov, A.A. Golubov, Supercond. Sci. Technol. **26**, 015005 (2013)

49. R.S. Keizer, S.T.B. Goennenwein, T.M. Klapwijk, G. Miao, G. Xiao, A. Gupta, Nature **439**, 825 (2006)
50. S.V. Bakurskiy, N.V. Klenov, I.I. Soloviev, M.Yu. Kupriyanov, A.A. Golubov, Appl. Phys. Lett. **108**, 042602 (2016)
51. M. Houzet, V. Vinokur, F. Pistolesi, Phys. Rev. B **72**, 220506 (2005)
52. F.S. Bergeret, A.F. Volkov, K.B. Efetov, Phys. Rev. Lett. **86**, 3140 (2001)

# Magnetic Proximity Effect and Superconducting Triplet Correlations at the Heterostructure of Cuprate Superconductor and Oxide Spin Valve


**K. Y. Constantinian, G. A. Ovsyannikov, V. V. Demidov and Yu. N. Khaydukov**

**Abstract** We report on studies of heterostructure made of a cuprate superconductor $YBa_2Cu_3O_{7-d}$, a ruthenate/manganite ($SrRuO_3/La_{0.7}Sr_{0.3}MnO_3$) spin valve, and thin gold film (Au). It is shown that a magnetic moment is excited in the cuprate superconductor due to magnetic proximity effect, at the same time magnetic moment is suppressed in the ruthenate/manganite part. The measurements showed that magnetic moment penetration depth significantly exceeds the coherence length of the cuprate superconductor. The induced magnetic moment could be attributed to coupling of the Cu and Mn atoms by a covalent chemical bond resulting in a strong hybridization and orbital reconstruction. The mesa-structures with micrometer sizes were prepared by adding superconducting niobium film (Nb) adjacent to the gold, forming a second superconducting electrode. The DC superconducting current flowing across the mesa-structure was observed even in the case when interlayer thicknesses were much greater than the coherence lengths of the ferromagnets in heterostructure. The maximum of the critical current took place when the thicknesses of ferromagnetic films in spin valve were near to the coherence lengths of the ferromagnets. Obtained data agree with the theoretical predictions for occurrence of the spin-triplet pairing. We measured superconducting current when applied magnetic field was by two orders

K. Y. Constantinian (✉) · G. A. Ovsyannikov · V. V. Demidov
Kotelnikov Institute of Radio Engineering and Electronics RAS, Mokhovaya 11, bld.7, Moscow 125009, Russia
e-mail: karen@hitech.cplire.ru

G. A. Ovsyannikov
e-mail: gena@hitech.cplire.ru

V. V. Demidov
e-mail: demidov@cplire.ru

Yu. N. Khaydukov
Max-Planck Institute for Solid State Research, 70569 Stuttgart, Germany
e-mail: Yury.Khaydukov@frm2.tum.de



A. Sidorenko (ed.), *Functional Nanostructures and Metamaterials for Superconducting Spintronics*, NanoScience and Technology,
https://doi.org/10.1007/978-3-319-90481-8_4

greater than the field level required for one magnetic flux quantum nucleation in the mesa-structure. Although theory for long-range spin-triplet pairing predicts a dominance of the second harmonic, our estimation of the second harmonic amplitude in the current-phase relation of superconducting current did not exceed 50% of the first one.

## 1 Introduction

In a contact of a superconductor (S) with a normal (non-superconducting) metal (N), superconducting correlations penetrate at the distance which is much grater than the interatomic one [1]. This phenomenon is known as a proximity effect, and first was discussed in detail by de Gennes [2, 3]. Along with the penetration of superconducting correlations into the normal metal, there is a change in superconducting order parameter due to a "leakage of Cooper pairs" at the interface. Earlier it was assumed that due to the "antagonism" between superconductivity and magnetism, there is no proximity effect at the superconductor (S) and ferromagnet (F) interface. Larkin and Ovchinnikov [4], and Fulde and Ferrell [5] predicted an occurrence of inhomogeneous superconducting correlations (LOFF state) in an S/F structure. The presence of LOFF states in the junction was manifest by oscillations of the superconducting critical current with temperature and F-interlayer thickness [6, 7].

In 2001, it was theoretically demonstrated that the triplet superconducting correlations (TSC) with nonzero spin projection together with the usual (singlet) one at the S/F interface occur [8, 9]. A distinctive feature of TSC is the fact that they are insensitive to the exchange field and penetrate into the ferromagnet at distances that are typical for a non-magnetic metal. Experimentally the occurrence of TSC was recorded by the presence of a superconducting current in structures composed of two superconductors with singlet superconductivity coupled by a ferromagnetic interlayer with spiral magnetization [10] as well as for ferromagnetic film with non-uniform magnetization [11]. TSCs in superconducting structures with a ferromagnetic interlayer made of two ferromagnets ($S/F_L/F_R/S$) were theoretically predicted for ballistic electron transport [12] and for diffuse scattering [13]. It was theoretically demonstrated that a second harmonic in the current-phase relation (CPR) of a superconducting current dominates [10, 12–14].

In oxide structures such as a cuprate superconductor–manganite ferromagnet, the transparency of the interface is determined by a work function and can be low [15]. It limits the proximity effect. The reports about the excitation of triplet correlations at the cuprate superconductor and manganite ferromagnet interface are rather contradictory [16–21]. It should be noted that the manganites $La_{0.7}Sr_{0.3}MnO_3$ (LSMO) and $La_{0.7}Ca_{0.3}MnO_3$ (LCMO) used in the experiment are ferromagnets having 100% carrier polarization (magnetic half-metal) at low temperatures. The appearance of singlet excitations at the ferromagnet boundary is suppressed that does not exclude the excitation of spin-triplet correlations.

The ferromagnetic correlations from the ferromagnet at F/N interface penetrate into the N-metal at a small interatomic distance due to the locality of the exchange interaction [22, 23]. It was theoretically demonstrated that at the S/F interface, there is a change in the density of states due to its difference for electrons with spin-up and spin-down ones [24–27]. The sign and magnitude of the magnetic moment occurring in the superconductor strongly depend on the parameters of the S/F interface, such as transparency, impurities, and layer thickness [28–31]. An experimental study of the magnetic proximity effect in S/F structures based on ferromagnets and metal superconductors that was performed using a variety of methods (ferromagnetic resonance, muon scattering, neutron scattering, etc.) generally confirmed the conclusions of the theory [32–35].

The presence of a magnetic moment in cuprate superconductor in $YBa_2Cu_3O_7/La_{2/3}Ca_{1/3}MnO_3]_n$ ($[YBCO/LCMO]_n$) superlattices was revealed [36–40]. An induced magnetic moment of the Cu atoms oriented antiparallel to the magnetic moment of Mn atoms was detected at interface using X-ray dichroism technique [38–40]. It was shown that the Cu and Mn atoms were connected through the interface by a covalent chemical bond, resulting in a strong hybridization and orbital reconstruction. The typical lengths of the orbital reconstruction greatly exceed the interatomic distances and are equal to 8–10 nm [41, 42].

Here we present results on experimental investigation of the changes of magnetic moment in the heterostructure containing the cuprate superconductor and ferromagnetic spin valve. Measurements of the heterostructure's magnetic moment were carried out by SQUID magnetometer and ferromagnetic resonance (FMR) technique. Analysis of data obtained allowed us to determine the magnitude of the magnetic moment induced in the superconductor, as well as the change of magnetic moment in the ferromagnetic spin valve.

Then the results of experimental studies of superconducting and quasiparticle currents in micrometer size mesa-structures Nb/Au/LSMO/SRO/YBCO with a top electrode made of Nb are presented as well. We evaluated characteristic parameters, such as the depth of the penetration of superconducting correlations into a ferromagnet and the transparency of the cuprate superconductor–ruthenate ferromagnet interface. The contribution of the second harmonic of the superconducting current-phase relation was experimentally determined. Based on the experimental data, we concluded that the contribution of the triplet superconducting correlations to the transport of superconducting carriers in mesa-structures is dominant.

## 2 Experimental

We studied epitaxial thin-film heterostructures consisting of a cuprate superconductor $YBa_2Cu_3O_{7-\delta}$ and two ferromagnetic layers $SrRuO_3$ (SRO) and $La_{0.7}Sr_{0.3}MnO_3$ prepared by laser ablation at temperatures of 700–800 ºC and oxygen pressure of 0.3–0.6 mbar. The thickness of the superconductor was in the range of 80–200 nm, whereas the thickness of the ferromagnetic layers varied from 5 to 20 nm (see Table 1).

**Table 1** Composition and thickness of the test heterostructures, as well as the experimentally determined changes of magnetic moment of the heterostructures. $d_S$ is the thickness of the YBCO film, $d_{SRO}$ is the thickness of the SRO film, $d_{LSMO}$ is the thickness of the LSMO film, and $\Delta m$ is the change of magnetic moment

| N | Substrate | $d_S$, nm | $d_{SRO}$, nm | $d_{LSMO}$, nm | $\Delta m$, $10^{-6}$ emu |
|---|---|---|---|---|---|
| 1 | (001)$LaAlO_3$ | 80 | 20 | 14 | 10 |
| 2 | (110)$NdGaO_3$ | 80 | 17 | 7 | $(5 \pm 1.5)$ |
| 3 | (110)$NdGaO_3$ | 180 | 0 | 20 | $\leq(1 \pm 2)$ |
| 4 | (001)LSAT | 150 | 13 | 25 | 2.5 |
| 5 | (110)$NdGaO_3$ | 0 | 14 | 40 | – |
| 6 | (110)$NdGaO_3$ | 0 | 0 | 50 | – |

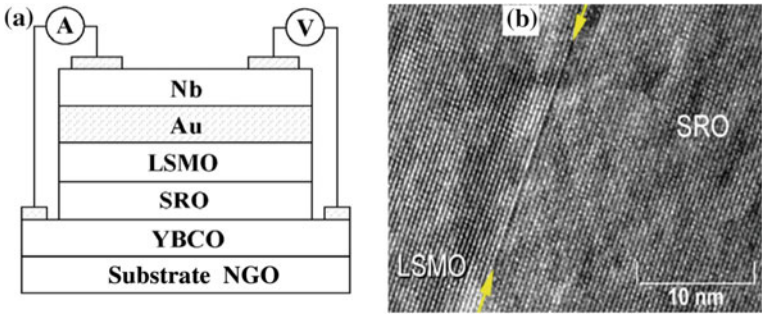


**Fig. 1** **a** Cross section of a mesa-structure and the measurement circuit, **b** an image of the interface between SRO and LSMO, obtained by transmission electron microscope JEM-2100 with the $8 \times 10^5$ zoom. The interface is marked by arrows

The heterostructures were covered by thin (20 nm) layer of gold on top. We used substrates with the dimensions $5 \times 5$ mm made of (110)$NdGaO_3$ (NGO). The magnetization vector of the LSMO film deposited on a (110)NGO substrate (or YBCO film) is generally lays in the plane of the substrate [43, 44] whereas for SRO film is outside of the plane of the substrates used [45]. LSMO with a uniaxial magnetic anisotropy of 20–30 mT at the room temperature and exchange energy of 2.3 meV [49] and SRO with a magnetic anisotropy of about 1 T and exchange energy of 13 meV [50] were used. The surface properties were tested for film satellites on an atomic-force microscope, and fairly sharp boundaries between the SRO/LSMO layers were observed by transmission electron microscope (Fig. 1b).

We investigated mesa-structures with an Au-Nb bilayer served as the top superconducting electrode. The bilayer was deposited by magnetron sputtering [43].

## 3 Magnetic Proximity Effect

*Magnetic moment in heterostructures.* A detailed study of the field and temperature dependences of magnetization in the separate films and heterostructures was conducted using a SQUID magnetometer MPMS-3 [46]. The plane of the substrate was set relative to the direction of the magnetic field within 1°–2°. Table 1 shows used substrate and thicknesses of the heterostructure films, as well as the changes of the magnetic moments of the heterostructure, $\Delta m$.

The values of $\Delta m$ for samples N2 and N3 are obtained from FMR measurements and correspond to the changes in magnetization of the SRO layer for heterostructures No. 2 and the LSMO film for heterostructure No.3; the rest of the measurements were carried out for changes in magnetization of the entire structure. In the sample No. 4, we used a $(LaAlO_3)_{0.3}(Sr_2AlTaO_6)_{0.7}$ (LSAT) substrate, onto which we deposited the epitaxial film made out of a calcium-doped cuprate superconductor $Y_{0.7}Ca_{0.3}Ba_2Cu_3O_x$.

Figure 2 shows a family of temperature dependences for the magnetic moment parallel to the substrate plane $m_{\|}$, for heterostructure No. 1. These dependences are obtained using the SQUID magnetometer during cooling in a magnetic field (FC mode). The external magnetic field was located in the substrate plane and was directed along one of its edges. Detailed measurements of the magnetic anisotropy have shown that the substrate edges form an angle of 40º–50º relative to the easy axis of the LSMO magnetic anisotropy. For the temperatures $T<T_{SRO}$ (the Curie temperature of the SRO film $T_{SRO} \approx 150$ K for the given heterostructure), $m_{\|}$ is determined by the sum of the LSMO film magnetic moment and the projections of the SRO film magnetic moment on the direction of the magnetic field. Under the influence of a magnetic field magnetic moment, $m_{\|}$ changes due to the rotation of the LSMO and SRO film magnetic moments. As a result, magnetic moments of LSMO and SRO films give smaller total magnetic moment of the spin valve at low fields than that of the LSMO film at the same temperature, whereas at $H > 1$ kOe it is larger. The results of measuring the field dependence of magnetic moment $m$ of the Au/LSMO/SRO/YBCO heterostructure (see No. 1 in Table 1) are shown in the inset of Fig. 2a for a magnetic field directed along the substrate edge at the temperature $T = 100$ K, which is higher than the critical temperature of the superconductor ($T_C$). The position of the magnetization easy axis of the SRO film is close to the normal to the substrate plane. The non-collinearity of the magnetization vectors of the ferromagnetic films contributes to the generation of superconducting triplet correlations having a nonzero spin projection of superconducting carriers, in the ferromagnetic interlayer [43, 49, 50].

At $T \approx T_C$ when magnetic field is parallel to the substrate plane, there is a sharp increase in the magnetic moment of the heterostructure (Fig. 2a). The thickness of the YBCO film $d_S = 80$ nm is less than the London penetration depth of the magnetic field. The magnetic field that is directed along the plane of the film completely penetrates the superconductor, and the diamagnetic response is not observed as expected due to the Meissner effect.

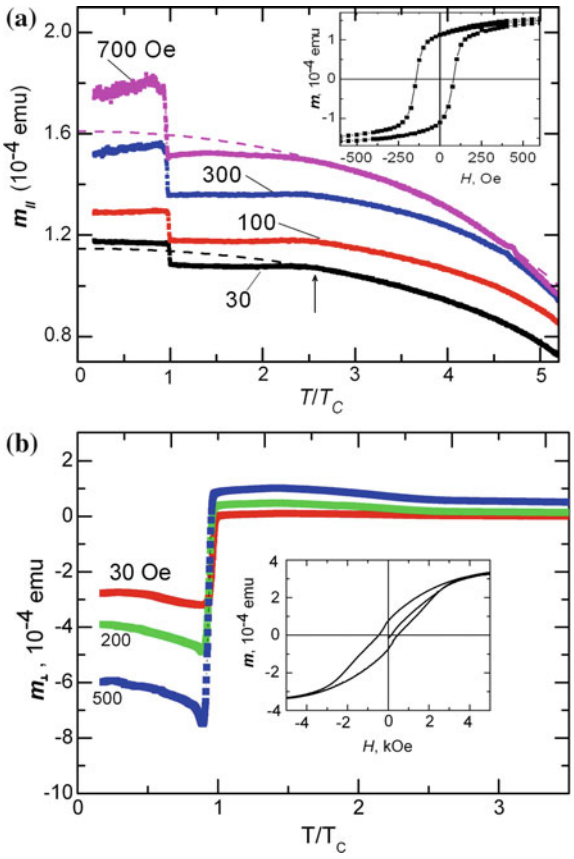


**Fig. 2** Temperature dependences of magnetic moment of Au/LSMO/SRO/YBCO heterostructure in FC mode, 1 kOe, for magnetic field directed in parallel to the substrate plane (**a**) and in perpendicular (**b**). The transition of SRO to ferromagnetic state is observed at $T/T_C = 2.5$. Insets show the hysteresis loops for the corresponding magnetic field direction

The occurrence of a magnetic moment in a cuprate superconductor contacting manganite was theoretically considered in [42]. It was demonstrated that as a result of the antiferromagnetic interaction of the spins $x^2 - y^2$ of Cu electrons with e.g. electrons of Mn, an induced negative spin polarization in the cuprate superconductor occurs. The impact of this process on the properties of the superconductor is much stronger than injecting the spin-polarized electrons of the ferromagnet. It was determined this mechanism is responsible for induced magnetic moment in the $[YBCO/LCMO]_n$ superlattice [17]. The magnetic moment of the Cu atom induced in the superconductor is equal to 0.23 $\mu_B$/Cu and is directed against the magnetic moment of Mn. Assuming that the change in the magnetic moment of our heterostructure occurs due to copper atoms located in a 10 nm thick layer, we obtain $\Delta m \sim 10^{-5}$ emu in sample No. 1 (see Fig. 2a) and the induced magnetic moment

~0.25 $\mu_B$/Cu. The change to the direction of the copper magnetic moment in the YBCO/SRO contacts, observed both in [51] and in our case, can be caused by the negative magnetization of the SRO film [27, 45].

If the magnetic field is directed perpendicularly to the plane of the superconducting film, then the shielding currents occur in the layer $\lambda_\perp = \lambda_L^2/d_S \approx 0.3$ μm on the edge of the film. The magnetic field gets pushed out of the superconducting film and a diamagnetic response is observed (Meissner effect). This can be seen on the dependence of the magnetic moment $m_\perp(T)$ of the heterostructure, measured in the direction of the magnetic field that is perpendicular to the plane of the substrate (see Fig. 2b). It is easy to determine the superconductor critical temperature $T_C$ in the heterostructure using the dependence $m_\perp(T)$. Note that the form of the dependences of perpendicular $m_\perp(T)$ does not change if we change measurement modes (FC or ZFC).

*Ferromagnetic resonance in the heterostructure.* The heterostructures were also studied using a Bruker ER 200 magnetic resonance spectrometer, operating in the frequency $\omega/2\pi = 9.7$ GHz. We measured ferromagnetic resonance spectra over a wide range of temperatures: 20–300 K. The FMR spectra of the LSMO film in the heterostructures were obtained by cooling the sample in the field of the Earth. Upon reaching the given temperature, we scanned the magnetic field from 0 to 4 kOe. The FMR spectrum from the SRO film does not measured at our experimental conditions due to the large value of the magnetic anisotropy field of the SRO film.

During the measurement of the ferromagnetic resonance spectrum, the magnetic component of the microwave field was perpendicular to the plane of the substrate. The external magnetic field $H$ was always located in the plane of the substrate (parallel orientation) whereas in experiments with sample cooling, it was put along the magnetization easy axis of the induced uniaxial anisotropy of the LSMO film. The direction of this axis was predetermined from the angular dependences of the resonance field $H_{CF}$, taken at different temperatures under the conditions of magnetic field rotations around the normal to the substrate plane in a parallel orientation [44]. The angular dependences of the FMR spectrum of thin ferromagnetic film in the presence of uniaxial and biaxial anisotropy are described by the following equation [44]:

$$\left(\frac{\omega}{\gamma}\right)^2 = (H_0 + H_u \cos 2\varphi_u + H_c \cos 4\varphi_c)\left(4\pi M_0 + H_0 + H_u \cos^2 \varphi_u + H_c \frac{1 + \cos^2 2\varphi_c}{2}\right) \quad (1)$$

wherein $\gamma$ is the gyromagnetic ratio, $H_u = 2K_u/M_0$, $H_c = 2K_c/M_0$, $K_u$ and $K_c$ are uniaxial anisotropy and cubic anisotropy constants correspondingly, the $M_0$ parameter is equal to the equilibrium magnetization in the absence of adjacent ferromagnetic layers, and $\varphi_u$ and $\varphi_c$ are angles at which the uniaxial and cubic anisotropy easy axes of magnetization are directed, relative to the external magnetic field, respectively. As a result of fitting the experimental data (Fig. 3) using (1), we were able to determine the following ferromagnetic parameters: $K_u$, $K_c$, $M_0$, as well as the direction of both the uniaxial and cubic anisotropy easy axes (see inset in Fig. 3). As noted previously, the processing of the angular dependences of the FMR spectra according

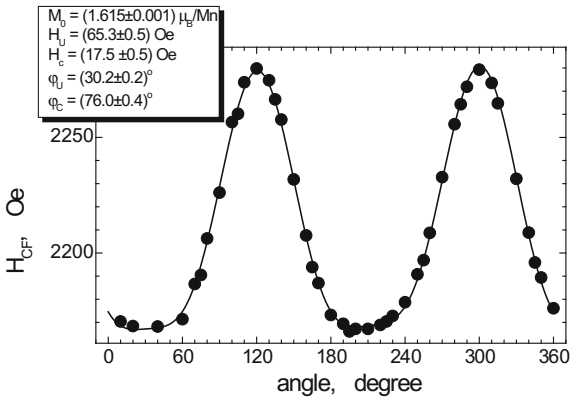


**Fig. 3** Angular dependence of the resonant magnetic field at $T$ = 295 K, heterostructure Au/LSMO/SRO/YBCO. The solid line was obtained using (1) with fitting parameters shown in the inset

to (1) allows us to determine the $M_0$ parameter and the directions of the easy axes in the LSMO films of the heterostructures.

The interlayer exchange between two ferromagnets must be considered at lower temperatures, because it leads to a resonance relation that differs from the (1). The temperature dependences of FMR spectra of the LSMO film in the heterostructure No. 2 have been measured. At $T \leq T_C$, when the YBCO film is in the superconducting state, a huge signal of non-resonant absorption was recorded at low magnetic fields having a hysteresis in the magnetic field. As a result, the FMR signals were recorded with an increase in the error of resonant field $H_{CF}$ at $T < T_C$, but allow us to determine the superconducting transition temperature $T_C$ of YBCO films. At $T > T_C$, the values of $H_{CF}$ are determined much more accurately.

Figure 4 shows the temperature dependences of the resonant field $H_{CF}$ for FMR signals from LSMO films in Au/LSMO/SRO/YBCO (N5) and Au/LSMO/YBCO (N6) heterostructures in vicinity of $T_C$ of superconducting films. In all cases, the external magnetic field was directed along the easy magnetization axis. It is evident that for the Au/LSMO/SRO/YBCO heterostructure, there is a sharp change in the resonant field in the superconducting transition range.

Since in the Au/LSMO/SRO/YBCO heterostructure the LSMO film is separated from the superconducting YBCO film by the ferromagnetic SRO film, the jump of the resonance field $H_{CF}$ of the LSMO layer could be associated with the change in magnetization of the SRO film. So, one must take into account the interlayer exchange interaction between LSMO and SRO which occurs through the magnetically ordered boundary layer with a high conductivity [52–55]. Using the procedure outlined in [56, 57], we obtained an expression that describes the relationship between the frequency and the resonance field for the LSMO layer in the LSMO/SRO heterostructure. The expression is similar to (1) but its value for the resonant field should be replaced with this combination

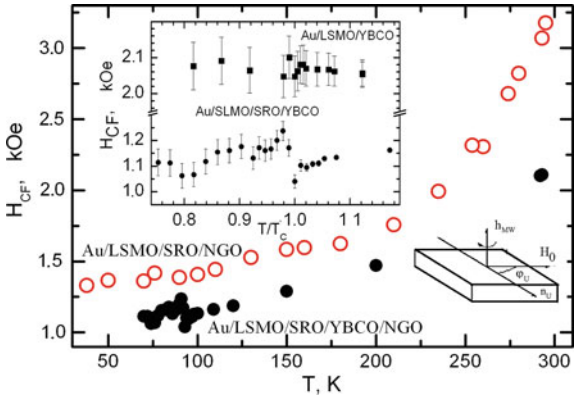


**Fig. 4** Temperature dependence of the resonance field in the LSMO film for two heterostructures: Au/LSMO/YBCO and Au/LSMO/SRO/YBCO. The top inset shows the temperature dependence of the resonance field of these heterostructures in the vicinity of $T_C$. The bottom inset shows the geometry of FMR spectrum measurements

$$H_{CF} + \frac{H_{J1}^{\mathrm{LSMO}}\left(H_{CF} + H_{J1}^{\mathrm{SRO}}\right)}{H_{\mathrm{SRO}} - 4\pi M_{\mathrm{SRO}} - H_{J2}^{\mathrm{SRO}}}. \tag{2}$$

Here $H_{\mathrm{SRO}}$ and $M_{\mathrm{SRO}}$ represent the field of the uniaxial magnetic anisotropy and the magnetization of the SRO film correspondingly, $H_{J1}^{\mathrm{LSMO,SRO}}$ and $H_{J2}^{\mathrm{SRO}}$ are the effective fields of bilinear and biquadratic interlayer exchanges, respectively. For the corresponding layers, the magnitudes of these fields are inversely proportional to the magnetization of the corresponding layers [56, 57]. In order to fulfill the resonance ratio, it is required that the combination in (2) was constant on both sides of the magnetization jump. It allows us to obtain the relation between the changes of the resonant field $\delta H_{CF}$ in the LMSO film and the magnetization of the SRO film $\delta H_{CF}$:

$$\frac{\delta M_{\mathrm{SRO}}}{M_{\mathrm{SRO}}} \approx \frac{\delta H_{CF}}{H_{CF}} \frac{H_{\mathrm{SRO}}}{4\pi M_{\mathrm{SRO}}} \tag{3}$$

An assessment of $\delta H_{CF}$ performed in accordance with (3) shows that change in magnetization of the SRO film during the YBCO transition to the superconducting state is about ~$0.5M_{\mathrm{SRO}}$. Taking into account the contribution of the SRO film ($m_{\mathrm{SRO}}$ ~ $10^{-5}$ emu) to the total magnetic moment $m\|$ of the heterostructure (Fig. 2a), we find that the change of magnetic moment of the composite ferromagnet is smaller than the magnetic moment induced in the superconductor. Note that the positive sign of $\delta M_{\mathrm{SRO}}$ indicates that the magnetization of the SRO film decreases, since in this layer the magnetization has a negative sign (see also [27]). According to Fig. 4, we can also see that in the Au/LSMO/YBCO heterostructure, in which the ferromagnetic LSMO film is in contact with the YBCO film, a remarkable change in the magnetization of LSMO at $T \approx T_C$ is not detected. This difference in the

Au/LSMO/YBCO heterostructure can be explained by the absence of excitation of the triplet component of the superconducting current in the ferromagnetic interlayer [22, 27, 49, 50, 58] and low transparency of the YBCO/LSMO interface [50]. This leads to a negligibly small penetration of the superconducting order parameter from YBCO into the LSMO film and therefore, to a negligibly small change in the magnetic moment of the LSMO film in the heterostructure.

## 4 Superconducting Triplet Correlations

*Electron transport in mesa-structures.* Micrometer-sized mesa-structures in which the two superconductors YBCO and the Au-Nb bilayer are separated by a magnetic spin-valve SRO/SLMO were used. Five square-shaped mesa-structures with linear dimensions in the plane $L$ = 0, 20, 30, 40, and 50 μm were prepared on a substrate (hereinafter referred to as "chip") using ion beam etching, and photolithography. A $SiO_2$ film with a thickness of 40 nm was used to isolate the contact at the edges of the mesa-structure. The scheme of measurements and the cross section of the mesa-structure are shown in Fig. 1a. The resistive characteristics of the satellite film and current–voltage characteristics (I-V curve) of mesa-structures were measured using four-point probe (see Fig. 1a) over the temperature range 4.2 K < $T$ < 300 K, magnetic fields $H$ of up to 2 kOe, and microwave monochromatic signal at frequencies $f_e$ = 1–3 GHz and 36–45 GHz. Microwaves at frequency band of 1–3 GHz were applied to the sample by a coaxial cable. To reduce the influence of external electromagnetic fields, the measurements were conducted in a shielded box with filter on leads in. By varying the thickness of the interlayer, it was possible to estimate the penetration depth of superconducting correlations into the ferromagnetic layer.

On temperature dependence of mesa-structure resistance *R(T)* (Fig. 5), there are two highlighted regions of resistance reduction which correspond to the transition of YBCO and Au-Nb bilayer films to the superconducting state correspondingly. Above the critical temperature YBCO $T_C$ the dependence $R(T)$ has a linear metal-type dependence, which is typical for the temperature dependence of a YBCO electrode. At $T < T_C$, the value of $R$ decreases rapidly while features of interlayer ferromagnetic films are not observed. This behavior is explained by the fact that below the critical temperature of YBCO, the contribution from LSMO and SRO films into the value $R_N A$ (area $A = L^2$) is inferior to the contribution from the interface resistance of mesa-structure. Additional measurements showed that the resistance of Au-Nb bilayer film in normal state is also small [59]. As a result, in the temperature range $T < T_C$ the resistance of the mesa-structure is combined with the resistance of the interfaces between the boundaries between materials YBCO/SRO, SRO/LSMO, LSMO/Au:

$$R_{\mathrm{MS}} = R_{\mathrm{YBCO/SRO}} + R_{\mathrm{SRO/LSMO}} + R_{\mathrm{LSMO/Au}}.$$

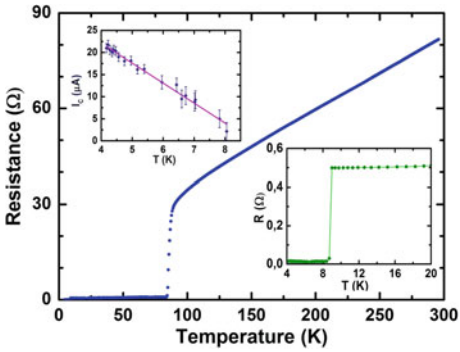


**Fig. 5** Temperature dependence of the mesa-structure resistance $R(T)$. The bottom inset shows an enlarged area of $R(T)$ at low temperatures, whereas the top inset shows the temperature dependence of the critical current

In order to clarify the contribution from each of the interfaces that define the resistance of the composite layer mesa-structure, we also prepared mesa-structures with a single ferromagnetic interlayer. For mesa-structures with an SRO interlayer, the value $R_N A$ is almost three orders of magnitude lower than for a structure with an LSMO interlayer. If we assume that the resistance of the LSMO/Au border does not exceed the value of 1 $\mu\Omega$ cm$^2$ [60], then the resistance of the YBCO/LSMO/Au mesa-structure (100 $\mu\Omega$ cm$^2$) can be explained by the dominance of the YBCO/LSMO interface resistance. Using the data from [60], we find that the resistance of the SRO/Au interface can be estimated to be 0.05 $\mu\Omega$ cm$^2$, whereas the resistance of the YBCO/SRO border is about 0.1 $\mu\Omega$ cm$^2$, which is consistent with the data in [61]. Consequently, the value of $R_N A$ of the mesa-structure is determined mainly by the sum of the resistances of $R_{\mathrm{LSMO/Au}}$ and $R_{\mathrm{YBCO/SRO}}$ [50].

*The critical current of a mesa-structure.* Superconducting current was observed for the most of the mesa-structures under investigation having interlayer thickness up to 50 nm. The critical current $I_C$ decreases linearly as the temperature increases (inset in Fig. 5) over the temperatures $4.2\mathrm{K} < T < T_C^{Au-Nb}$. For comparison, in mesa-structures with one ferromagnetic interlayer (LSMO or SRO), the superconducting current is absent at interlayer thicknesses exceeding 5 nm, which is about equal to the coherence length $\xi_F$. At smaller interlayer thicknesses, the superconducting current found on some samples was caused by pinholes. The presence of a critical current decline for the spin-valve thicknesses greater than 5 nm is an indication of the spin-triplet superconducting correlation transport via the spin valve [13, 62].

Outlines of the experimental values for the critical current density $j_C$ for LSMO and SRO film thicknesses between 0 and 20 nm are shown in Fig. 6. We can see a peak for critical current density at layer thicknesses $d_{\mathrm{LSMO}} \approx 6$ nm and $d_{\mathrm{SRO}} \approx 8$ nm. Note that the critical current maximum in superconducting structures with a two-layer composite ferromagnetic interlayer is predicted at thicknesses that are about equal to the coherence length [63]. Since the mean free path $l$ in oxide materials

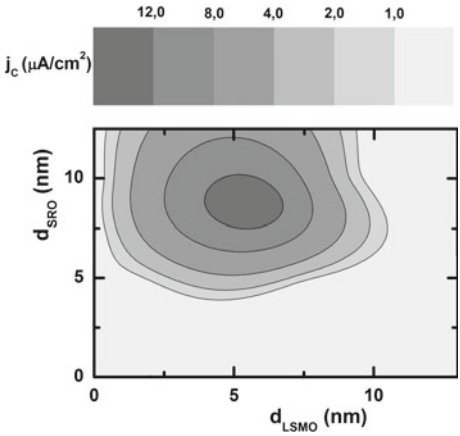


**Fig. 6** Outlined regions of critical current density as a function of the plane thickness of spin-valve ferromagnetic layers at $T = 4.2$ K

(SRO and LSMO) is sufficiently small [64, 65], we can assume that the electron transport is diffusive in nature.

*Magnetic field dependences.* For the Josephson junction with a uniform critical current distribution, the critical current as the function of the magnetic field is described by the Fraunhofer relationship

$$I_C(H) = I_C(0)\left|\frac{\sin(\pi\Phi/\Phi_0)}{\pi\Phi/\Phi_0}\right| \tag{4}$$

where $\Phi_0 = 2.06783461 \times 10^{-15}$ Wb is the magnetic flux quantum and $\Phi = \mu_0 H S_{eff}$ is the magnetic flux of the external field in the mesa-structure [66, 67]. The zeros of the Fraunhofer dependence are observed when the external field through a cross section of the mesa-structure is equal to the magnetic flux quantum $\Phi \approx \Phi_0$. The measured magnetic field dependences of critical currents of mesa-structures were markedly different from the (4). Changing the direction of the magnetic field sweep (from ascending to descending, and vice versa), a hysteresis is observed caused by ferromagnetic nature of the interlayer materials [43]. Moreover, the critical current was observed at considerably high levels of magnetic field up to 2 kOe (see Fig. 7a). Therefore, at $H = 1.3$ kOe the value $I_C = 16.5$ μA which composes 94% of the $I_C(H = 0)$ and 0.7 of the maximum measured at $H = -6.5$ Oe. Note that in YBCO/Au/Nb structures without magnetic interlayer [68] or with an antiferromagnetic $Ca_{0.7}Sr_{0.3}CuO_2$ interlayer [69], the critical current dropped sharply with an increasing of magnetic field. While it even increased in the mesa-structures at fields greater than 1 kOe. This unusual behavior of the critical current in the structures with a metallic ferromagnetic interlayer was mentioned also in [70].

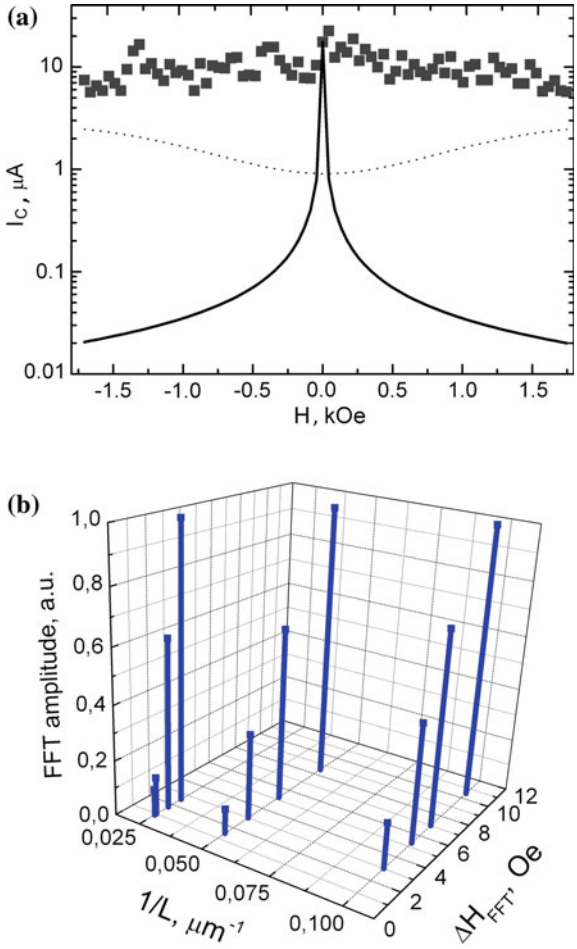


**Fig. 7** Dependence of the critical current on the magnetic field over a wide range of magnetic fields for the mesa-structure with $d_{SRO}$ = 8.5 nm, $d_{LSMO}$ = 3 nm, $L$ = 10 μm. The solid line shows the expected decline of the maxima of the values $I_C$ of the Fraunhofer oscillatory dependence (4). The dotted line shows the level of noise that limits our ability to measure the critical current (**a**). The periods $\Delta H_{FFT}$ and amplitudes of the Fourier components as a function of parameter 1/$L$ for magneto-field dependences of the critical current of three mesa-structures with $L$ = 10, 20, 40 μm, arranged on a chip (**b**)

There are several mechanisms that determine the critical current versus magnetic field dependence as follows: the penetration of the magnetic flux quanta (Josephson vortices) which creates the "Fraunhofer" oscillation, the emergence of a domain structure in the ferromagnetic interlayer, and the rotation of the layer magnetization under the influence of external magnetic field. Note that in the absence of triplet correlation, the superconducting current according to (4) must be significantly sup-

pressed in the magnetic field at $\Phi \gg \Phi_0$. Several quanta of magnetic flux penetrate into the transition since the maxima of the Fraunhofer dependence fall at a rate of $1/\Phi$ (see Fig. 7a).

In assessing the effective area of penetration of the magnetic field directed along the plane of the transition $S_{\text{eff}} = Ld'$, the magnetic permeability of the layers must be taken into account $d' = \mu_1 d_{\text{LSMO}} + \mu_2 d_{\text{SRO}} + \lambda_{\text{Nb}} + \lambda_{\text{YBCO}}$ where $\lambda_{Nb} = 90$ nm and $\lambda_{\text{YBCO}} = 150$ nm are the London penetration depths of the magnetic field for Nb and YBCO, respectively, and $\mu_{1,2}$ is the magnetic permeability for the spin valve. For the Josephson junctions with the ferromagnetic interlayer, the effective thickness increases by $\mu = 1 + \chi$ times [67, 71] where $\chi$ is the magnetic susceptibility. The values $\mu_1 = 12$, $\mu = 3$ were obtained from the magnetic field dependences of the spin-valve interlayer magnetic moment of a mesa-structure with $d_{\text{LSMO}} = 6$ nm and $d_{\text{SRO}} = 8.5$ nm and $L = 10$ nm. Substituting these values of the critical current minima for the mesa-structure should be located at $\Delta H = 6$ Oe due to the penetration of the Josephson vortices. This value is slightly different from the experimental value of $\Delta H \approx 10$ Oe which is the distance between the minima for $I_C(H)$. During the calculation of $\chi$, we used data from the measurement of the magnetic moment $M(H)$ for a direction of the external magnetic filed coinciding with the hard axis [49]. Fourier analysis of the oscillatory dependences $I_C(H)$ for three mesa-structures with the identical thickness $d'$ shows the presence of at least two periods $\Delta H_{FFT}$ with significant FFT amplitudes (see Fig. 7b). At the same time, there is an increase in $\Delta H_{FFT}$ proportional to $1/L$. It is known that the domain structure in the ferromagnetic interlayer could have a dramatic effect on the electron transport mechanism [72, 73]. The domain generated non-uniformities of magnetization in the LSMO films could lead to an additional modulations of the $I_C(H)$ dependences. However, based on the data in Fig. 7b we can see that the oscillations $I_C(H)$ are not caused by the domain structure. The effective area of the magnetic field penetration $S_{\text{eff}} = d_{\text{dom}} d'$ must correspond to much greater periods of critical current oscillations due to magnetic field, than the values $\Delta H_{FFT}$ in the figure. The presence of the Fourier transform components with fractional periods $\Delta H_{FFT}$ is most likely indicative of superconducting current-phase relation (CPR) deviation from the sinusoidal form [49, 50].

*Microwave dynamics of mesa-structures.* A study of the high-frequency dynamics of Shapiro steps on the I-V curve when microwave radiation is applied proves the absence of pinholes ("short-circuiting") between superconducting electrodes. This is confirmed by the presence of Shapiro step oscillations in response to microwave power. The amplitudes of steps are in good agreement with the resistively shunted junction model (RSJ) [59]. The absence of pinholes is ensured by thick interlayers. The roughness of the layers is smaller than the thickness of LSMO and SRO films. A comparison of the experimental Shapiro steps with those calculated according to the modified RSJ model [59] allows us to determine the CPR of superconducting current. Measurements of CPR were carried out in a zero magnetic field and during cooling the mesa-structures in a constant magnetic field (100–200 Oe). A family of I-V curves obtained under microwave radiation at frequency of 41 GHz is shown in Fig. 8a. Since the frequency of the microwave signal $f_e$ is greater than the characteristic frequency of the mesa-structure $f_e >> f_C = \frac{2e}{h} I_C R_N$, McCumber

parameter $\beta_C = \frac{2\pi}{\Phi_0} I_C R_N^2 C << 1$ the impact of capacitance of the mesa-structure could be ignored. Under these conditions, the appearance of fractional Shapiro steps on the I-V curve (see Fig. 8a) clearly points on non-sinusoidal nature of the CPR [59]. Figure 8b shows the experimental and theoretical dependences of the critical current $I_C$ and the first Shapiro step $I_1$ versus normalized microwave current $x = I_{RF}/I_C\omega$ where $I_{RF}$ is the amplitude of the microwave current and $\omega = f_e/f_C$. The ratio of the amplitude of the second harmonic in CPR to the first one $q = I_{C2}/I_{C1}$ was determined according to the numerical approximation of the critical current and Shapiro step amplitudes as functions of the microwave power [49, 50]. Due to the influence of the second harmonic in CPR, the critical current and the first Shapiro step have nonzero local minima (see Fig. 8b). Since it was assumed that $I_{C1} \approx I_C$ (valid for $q < 1$), then the values of $q$ determined by this method are underestimated. According to the theoretical study in [13] during the excitation of spin-triplet correlations in the junction with bilayer interlayer, the second harmonic dominates in CPR increasing with the disorientation angle of interlayer magnetization reaching a maximum at angles close to $\pi/2$. According to the measurements obtained using the SQUID magnetometer at low fields, the magnetization projection of the SRO film is directed in the direction opposite to the magnetization of LSMO that determines the magnetization direction angle for the LSMO film. At fields greater than the values of the anisotropy field (200–300 Oe), the magnetization of the LSMO layer is directed along the field. Therefore, we should observe the growth of the second harmonic in CPR in small fields. However, in the microwave experiment on five mesa-structures, we did not observe an increase of the second harmonic in range of magnetic fields 20–50 Oe as predicted in [12–14] and the ratio of amplitude of second harmonic to the critical current did not exceed the value of $q = 0.5$.

## 5 Conclusion

The manifestation of an induced magnetic moment in the superconductor is experimentally observed in the heterostructure based on the cuprate superconductor with the ferromagnetic spin valve. The magnetic moment occurring in the superconductor coincides with the calculations for the magnetic moment of Cu atoms induced due to the orbital reconstruction at the S/F interface. The typical penetration depth of the magnetic moment into the superconductor is significantly greater than the coherence length of the cuprate superconductor. It is experimentally shown that in superconducting mesa-structures with the spin valve LSMO/SRO interlayer, the superconducting current is observed when the total layer thickness is up to 50 nm. This thickness of the interlayer is significantly greater than the coherence length. The maximum value of the critical current density is observed at interlayer thicknesses that are close to the coherence length of the ferromagnetic films. The oscillations of periods of magnetic field critical current dependence arise due to the deviation of the superconducting current-phase relation from the sinusoidal form. This feature is confirmed by microwave measurements of the Shapiro step heights as functions of

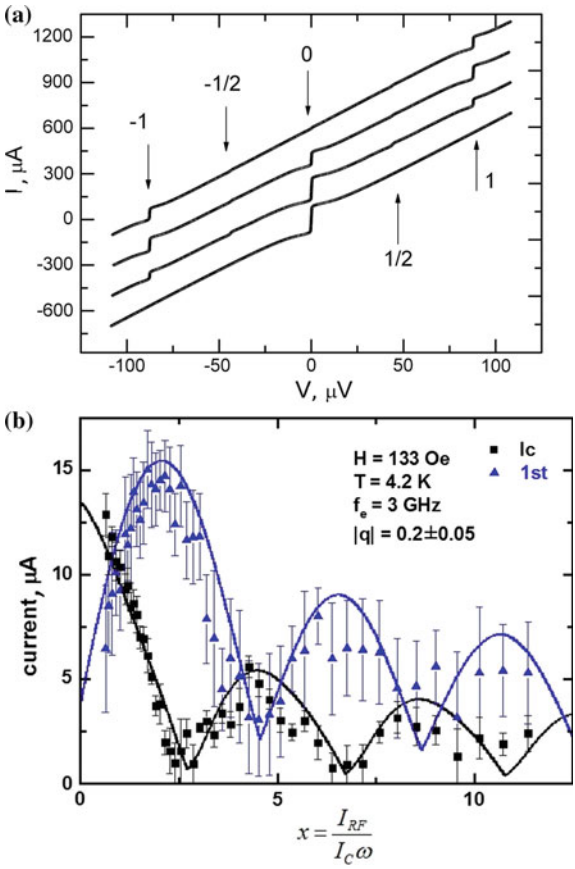


**Fig. 8** A set of I-V curves for the mesa-structure with $d_{SRO}$ = 8.5 nm, $d_{LSMO}$ = 6 nm, $L$ = 10 μm when subjected to electromagnetic radiation with a frequency $fe$=41 GHz. The arrows indicate the number n of the Shapiro steps on the voltage axis, $n$ = 0 corresponds to the critical current $I_C$ (**a**). The dependence of the critical current amplitude and the first Shapiro step for the mesa-structure with $d_{SRO}$ = 5.6 nm, $d_{LSMO}$ = 15 nm, $L$ = 50 μm, $f_e$ = 3 GHz (**b**)

applied microwave power. The large value of the second harmonic in CPR up to 50% of the critical current was evaluated. Another factor which may affect magnetic field dependence of the critical current is the impact of magnetic domains in the interlayer.

**Acknowledgements** The authors wish to thank V.A. Atsarkin, I.V. Borisenko, A.F. Volkov, A.V. Zaitsev, B. Keimer, A.I. Kalabukhov, Yu.V. Kislinskiy, G. Logvenov, A.M. Petrzihk, A.V. Shadrin, A.E. Sheyerman, and D. Winkler for their assistance in conducting these experiments and the useful discussions.

## References

1. A.I. Buzdin, Rev. Mod. Phys. **77** (2005)
2. G. Deutscher, P.G. de Gennes, Proximity effects, in *Superconductivity*, ed. by R.D. Parks (Dekker, NewYork, 1969), pp. 1005–1034
3. P.G. de Gennes, Phys. Lett. **23**, 10–11 (1966)

4. A.I. Larkin, Yu.N. Ovchinnikov, JETP **47**, 1136 (1964)
5. P. Fulde, R. Ferrell, Phys. Rev. **135**, A550 (1964)
6. A.I. Buzdin, L.N. Bulayevskiy, S.V. Panyukov, JETP Lett. **35**, 147 (1982)
7. V.V. Ryazanov, V.A. Oboznov, AYu. Rusanov, A.V. Veretennikov, A.A. Golubov, J. Aarts, Phys. Rev. Lett. **86**, 2427 (2001)
8. F.S. Bergeret, A.F. Volkov, K.B. Efetov, Phys. Rev. Lett. **86**, 4096 (2001)
9. A. Kadigrobov, R.I. Shekhter, M. Jonson, Europhys. Lett. **54**, 394 (2001)
10. J.W.A. Robinson, J.D.S. Witt, M.G. Blamire, Science **329**, 59 (2010)
11. M.S. Anwar, F. Czeschka, M. Hesselberth, M. Porcu, J. Aarts, Phys. Rev. B **82**, 100501 (2010)
12. L. Trifunovic, Z. Popovíc, Z. Radovíc, Phys. Rev. B **84**, 064511 (2011)
13. C. Richard, M. Houzet, J.S. Meyer, Phys. Rev. Lett. **110**, 217004 (2013)
14. L. Trifunovic, Phys. Rev. Lett. **107**, 047001 (2011)
15. S. Yunoki, A. Moreo, E. Dagotto, S. Okamoto, S.S. Kancharla, Phys. Rev. B **76**, 064532 (2007)
16. C. Visani, Z. Sefrioui, J. Tornos et al., Nat. Phys. **2318**, 1 (2012)
17. T. Hu, H. Xiao, C. Visani, Z. Sefrioui, J. Santamaria, C.C. Almasan, Phys. Rev. B **80**, 060506R (2009)
18. Y. Kalcheim, T. Kirzhner, G. Koren, O. Millo, Phys. Rev. B **83**, 064510 (2011)
19. T. Golod, A. Rydh, V.M. Krasnov, I. Marozau, M.A. Uribe-Laverde, D.K. Satapathy, Th. Wagner, C. Bernhard, Phys. Rev. B **87**, 134520 (2013)
20. M. van Zalk, A. Brinkman, J. Aarts, H. Hilgenkamp, Phys. Rev. B **82**, 134513 (2010)
21. A.M. Petrzhik, G.A. Ovsyannikov, A.V. Shadrin, K.Y. Constantinian, A.V. Zaitsev, V.V. Demidov, Yu.V. Kislinskiy, JETP **139**, 1190 (2011)
22. H. Zabel, S. D. Bader (eds.), *Magnetic Heterostructures, Advances and Perspectives in Spinstructures and Spintransport*. Springer Tracts in Modern Physics, vol. 227 (Springer, Berlin, Heidelberg, 2008), pp. 251–289
23. W.L. Lim, N. Ebrahim-Zadeh, J.C. Owens et al., Appl. Phys. Let. **102**, 162404 (2013)
24. K. Halterman, O.T. Valls, Phys. Rev. B **66**, 224516 (2002)
25. R. Fazio, C. Lucheroni, Europhys. Lett. **45**, 707 (1999)
26. V.N. Krivoruchko, E.A. Koshina, Phys. Rev. B **66**, 0145621 (2002)
27. F.S. Bergeret, A.F. Volkov, K.B. Efetov, Phys. Rev. B **69**, 174504 (2004)
28. F.S. Bergeret, A.L. Yeyati, A. Martin-Rodero, Phys. Rev. B **72**, 064524 (2005)
29. M.Yu. Kharitonov, A.F. Volkov, K.B. Efetov, Phys. Rev. B **73**, 054511 (2006)
30. R. Grein, T. Löfwander, M. Eschrig, Phys. Rev. **88**, 054502 (2013)
31. M. Alidoust, K. Halterman, J. Linder, Phys. Rev. B **89**, 054508 (2014)
32. I.A. Garifullin, D.A. Tikhonov, N.N. Garif'yanov, et al., Appl. Magn. Reson. **22**, 439 (2002)
33. M.G. Flokstra, S.J. Ray, S.J. Lister et al., Phys. Rev. B. **89**, 054510 (2014)
34. J. Xia, V. Shelukhin, M. Karpovski et al., Phys. Rev. Lett. **102**, 087004 (2009)
35. R.I. Salikhov, I.A. Garifullin, N.N. Garif'yanov, et al., Phys. Rev. Lett. **102**, 087003 (2009)
36. J. Stahn, J. Chakhalian, Ch. Niedermayer, et al., Phys. Rev. B **71**, 1405098 (R) (2005)
37. D.K. Satapathy, M.A. Uribe-Laverde, I. Marozau et al., Phys. Rev. Lett. **108**, 197201 (2012)
38. J. Chakhalian, J.W. Freeland, G. Srajer et al., Nat. Phys. **2**, 244 (2006)
39. J. Chakhalian, J.W. Freeland, H.-U. Habermeier et al., Science **318**, 1114 (2007)
40. H.-U. Habermeier, J. Phys.: Conf. Ser. **108**, 012039 (2008)
41. J. Santamaria, J. Garcia-Barriocanal, Z. Sefrioul, C. Leon, Int. J. Modern Phys. B **27**(19) (2013)
42. J. Salafranca, S. Okamoto, Phys. Rev. Lett. **105**, 256804 (2010)
43. G.A. Ovsyannikov, A.E. Sheyerman, A.V. Shadrin, Yu.V. Kislinskii, K.Y. Constantinian, A. Kalabykhov, JETP Lett. **97**, 145 (2013)
44. V.V. Demidov, I.V. Borisenko, A.A. Klimov, G.A. Ovsyannikov, A.M. Petrzhik, S.A. Nikitov, Zh Eksp, Teor. Fiz. **139**, 943 (2011)
45. G. Koster, L. Klein, W. Siemons et al., Rev. Mod. Phys. **84**, 253 (2012)
46. https://www.qdusa.com/products/mpms3.html
47. B.F. Woodfield, M.L. Wilson, J.M. Byers, Phys. Rev. Lett. **78**, 3201 (1997)
48. I. Asulin, O. Yuli, G. Koren, O. Millo, Phys. Rev. B **79**, 174524 (2009)
49. Yu.N. Khaydukov, G.A. Ovsyannikov, A.E. Sheyerman et al., Phys. Rev. B **90**, 035130 (2014)

50. A.E. Sheyerman, K.Y. Constantinian, G.A. Ovsyannikov, Yu.V. Kislinskii, A.V. Shadrin, A.V. Kalabukhov, Yu.N. Khaydukov, JETP **120**, 1024 (2015)
51. H.-U. Habermeier, G. Cristiani. Physica C **408–410**, 864 (2004)
52. P. Padhan, W. Prellier, R.C. Budhani, Appl. Phys. Lett. **88**, 192509 (2006)
53. M. Ziese, I. Vrejoiu, E. Pippel et al., Phys. Rev. Lett. **104**, 167203 (2010)
54. A.Y. Borisevich, A.R. Lupini, J. He et al., Phys. Rev. B **86**, 140102(R) (2012)
55. M. Ziese, F. Bern, A. Setzer et al., Eur. Phys. J. B **86**, 42 (2013)
56. V.N. Menshov, V.V. Tygyshev, JETP **125**, 136 (2004)
57. N.M. Kreines, FNT **28**, 807 (2002) [Low Temp. Phys. **28**, 581 (2002)]
58. N. Pugach, A.I. Buzdin, Appl. Phys. Lett. **101**, 242602 (2012)
59. P. Komissinskiy, G.A. Ovsyannikov, K.Y. Constantinian, Y.V. Kislinski, I.V. Borisenko, I.I. Soloviev, V.K. Kornev, E. Goldobin, D. Winkler, Phys. Rev. B **78**, 024501 (2008)
60. L. Mieville, D. Worledge, T.H. Geballe, R. Contreras, K. Char, Appl. Phys. Lett. **73**, 1736 (1998)
61. M. van Zalk, A. Brinkman, J. Aarts, H. Hilgenkamp, Phys. Rev. B **82**, 134513 (2010)
62. M.A. Khasawneh, T.S. Khaire, C. Klose, W.P. Pratt Jr., N.O. Birge, Supercond. Sci. Technol. **24**, 024005 (2011)
63. A.F. Volkov, K.B. Efetov, Phys. Rev. B **81**, 144522 (2010)
64. J.L. Cohn, J.J. Neumeier, C.P. Popoviciu, K.J. McClellan, Th. Leventouri, Phys. Rev. B **56**, R8495 (1997)
65. P. Kostic, Y. Okada, N.C. Collins, Z. Schlesinger J.W. Reiner, L. Klein, A. Kapitulnik, T.H. Geballe, M.R. Beasley, Phys. Rev. Lett. **81**, 2498 (1998)
66. A. Barone, J. Paterno, *Josephson Effect* (Physics and Application (Mir, Moscow, 1984)
67. A. Pal, Z.H. Barber, J.W.A. Robinson, M.G. Blamire, Nat. Commun. **5**, 3340–3344 (2014)
68. F.V. Komissinskiy, G.A. Ovsyannikov, Z.G. Ivanov, FTT **43**, 769 (2000)
69. Yu.V. Kislinkii, K.Y. Konstantinian, G.A. Ovsyannikov, F.V. Komissinskiy, I.V. Borisenko, A.V. Shadrin, JETP **106**, 800 (2008)
70. C. Klose, T.S. Khaire, Y. Wang, W.P. Pratt Jr., N.O. Birge, B.J. McMorran, T.P. Ginley, J.A. Borchers, B.J. Kirby, B.B. Maranville, J. Unguris, Phys. Rev. Lett. **108**, 127002 (2012)
71. G. Wild, C. Probst, A. Marx, R. Gross, Eur. Phys. J. B **78**, 509 (2010)
72. A.F. Volkov, K.B. Efetov, Phys. Rev. Lett. **102**, 077002 (2009)
73. A.I. Buzdin, A.S. Mel'nikov, N.G. Pugach, Phys. Rev. **B83**, 144515 (2011)

# Nanodevices with Normal Metal—Insulator—Superconductor Tunnel Junctions


**M. Tarasov and V. Edelman**

**Abstract** Normal metal–insulator–superconductor (NIS) tunnel junctions, as well as SIS junctions, are the main building blocks for superconducting electronics. Single NIS junctions and arrays are used in microwave bolometers, cryogenic thermometers, electron coolers, radiation detector. In such devices, junctions should fit different parameters for area, transparency, material properties and thermal characteristics. This leads to various fabrication methods and technique for measurements. Estimations made for equilibrium measurement conditions can be controversial in the case of microwave bolometers, ultra-low temperature thermometers, electron coolers. In terahertz bolometers, as well as in electron coolers, the energy distribution of electrons becomes different from Fermi distribution. In bolometers illuminated with terahertz radiation, the density of electrons will increase at higher energies, and in electron coolers, the distribution will be with reduced density at higher energies. Andreev reflection and proximity effect at the superconductor-normal metal interface induce changes in IV curve compared to simple SIN model. In this review, we present two levels of description for practical applications; first approximation is conventional with single-electron tunneling and equilibrium electron energy distribution, and the second taking into account non-Fermi distribution, Andreev currents, high-energy phonon creation and phonon escape.

M. Tarasov (✉)
V.Kotelnikov Institute of Radio Engineering and Electronics, Russian Academy of Sciences, Moscow, Russia
e-mail: tarasov@hitech.cplire.ru

V. Edelman
P.Kapitza Institute for Physical Problems, Russian Academy of Sciences, Moscow, Russia
e-mail: edelman@kapitza.ras.ru



A. Sidorenko (ed.), *Functional Nanostructures and Metamaterials for Superconducting Spintronics*, NanoScience and Technology,
https://doi.org/10.1007/978-3-319-90481-8_5

## 1 Introduction: The NIS Junction at a Glance

DC current across NIS tunnel junction in the first approximation is described by single-electron tunneling from the normal metal to the superconductor $\Gamma_{ns}(E)$ and in the opposite direction $\Gamma_{sn}(E)$. The net current is the difference of these rates [1]

$$I(V, T_e) = -e \int [\Gamma_{ns}(E) - \Gamma_{sn}(E)] \mathrm{d}E$$

For the normal metal, the Fermi function is expected as normalized density of states $n(E, T) = 1/[\exp(E/T) + 1]$. In such simplified case, the IV curve is given by

$$I(V, T_n) = \frac{1}{eR_n} \int_{-\infty}^{\infty} \frac{|E|\theta\left(E^2 - \Delta^2(T_S)\right)}{\sqrt{E^2 - \Delta^2(T_S)}} [f_N(E - eV, T_N) - f_S(E, T_S)] \mathrm{d}E$$

where $R_N$ is the normal-state resistance, $T_N$ is the electron temperature in the normal electrode. At temperatures much below the critical temperature of the superconductor, the integral can be approximated by asymptotic solutions for voltages $V < (\Delta - \mathrm{k}T)/e$. The ideal SIN tunnel junction IV curve can be fitted as

$$I(V, T) = \frac{1}{eR_n} \sqrt{2k\pi\, T_e e V_\Delta} \exp\left(-\frac{eV_\Delta}{kT_e}\right) \sinh\left(\frac{eV}{kT_e}\right) \tag{1}$$

in which $T$ is electron temperature, $T_c$ is critical temperature of superconductor, $e$—electron charge, $k$—Boltzmann constant, $V$—voltage. A simple figure of merit for the normal-metal electrode temperature is the ratio of dynamic resistance at zero bias to asymptotic resistance of NIS junction

$$r_d = \frac{R(0)}{R_n} = \sqrt{\frac{2k_bT}{\pi e V_\Delta}} \frac{\exp\left(\frac{eV_\Delta}{k_bT}\right)}{\cosh\left(\frac{eV}{k_bT}\right)} \tag{2}$$

This formula can give correct estimation for electron temperature in Al-based NIS junctions in the range 0.2–1 K if superconducting electrode is rather big and hot quasiparticles do not overheat the superconductor and do not tunnel back to normal electrode.

The actual dynamics in SINIS bolometers is more complicated due to electron cooling, Andreev reflection, nonequilibrium, non-Fermi energy distribution of electrons. When the superconductor temperature is raised, or athermal phonons due to quasiparticle recombination are absorbed in the normal-metal, bolometer and refrigerator performance will be degraded. In reality, the shape of IV curve is not as sharp as in simple model. For fitting, some authors use a semi-empirical Dynes parameter in density of states [2]

$$f(E) = \left| Re \frac{\frac{E}{\Delta} - i\gamma}{\sqrt{\left(\frac{E}{\Delta} - i\gamma\right)^2 - 1}} \right| \quad (3)$$

The source of the additional tunneling that leads to use $\gamma$ is not well understood and may vary based on junction materials, quality of barrier, shape, and proximity to normal metal leads, environment conditions like external thermal radiation. Proximity effect can change transition temperature of adjacent part of superconductor, its energy gap, and density of states. As a result instead of a single value of energy gap and sharp density dependence, we have a combination of density dependencies that in total leads to smearing of NIS IV curve. In general, it is necessary to solve differential equation to calculate quasiparticle density vs position in a superconductor. Alternative to empirical Dynes model can be explanation taking into account Andreev reflection using Hekking–Nazarov model, which is presented in the last section of this article.

## 2 Fabrication Technology

Conventional SINIS bolometers (Fig. 1a) are fabricated on Si substrates, and absorber is deposited directly on the substrate. Reducing heat losses in absorber can be obtained in traditional way by using SiN membrane and metal thin-film beams using rather complicated technology [3]. In such a design, the volume and thermal capacity of absorber together with membrane is reduced compared to the case of absorber on a thick silicon substrate [4]. Further improvement can be achieved if the absorber is suspended without any supporting membrane or substrate. For electron that absorbs photon at 350 GHz, the electron–phonon and electron–electron scattering time is about 0.2 ns and 1 ns, respectively. The excited electron creates a high-energy phonon that can easily escape from the absorber if it is placed on a substrate, or connected to electrodes of the same material [5]. Using absorber material different from that of electrodes can improve thermal insulation further due to a high acoustic-impedance mismatch and increased Kapitza resistance between the absorber and electrode. Earlier bolometers (Fig. 1a) with the absorber made of a non-superconducting Al thin film [6] leaks heat both into the substrate and electrodes. As an example of suspended bridges, we can mention experiments where a suspended copper nanowire $10 \times 0.3 \times 0.03\ \mu m^3$ on a SiN membrane demonstrated a better electron cooling compared to the non-suspended device [7]. Another example is a suspended AuPd beam 50 nm thick [8]. There is also suspended single-electron transistors [9] fabricated with help of reactive ion etching of Si substrate under 100 nm thick islands. A different technique was employed in [10] in which the suspended bridge was achieved by dry etching of the underlying organic polymer in oxygen plasma. Finally, we mention the successful chemical etching of 100-nm-thick aluminum layer under 100 nm thick layer of Cu [11]. As alternative to NbN membrane technique, we can also mention suspended parts supported from below by a silicon oxide layer left after

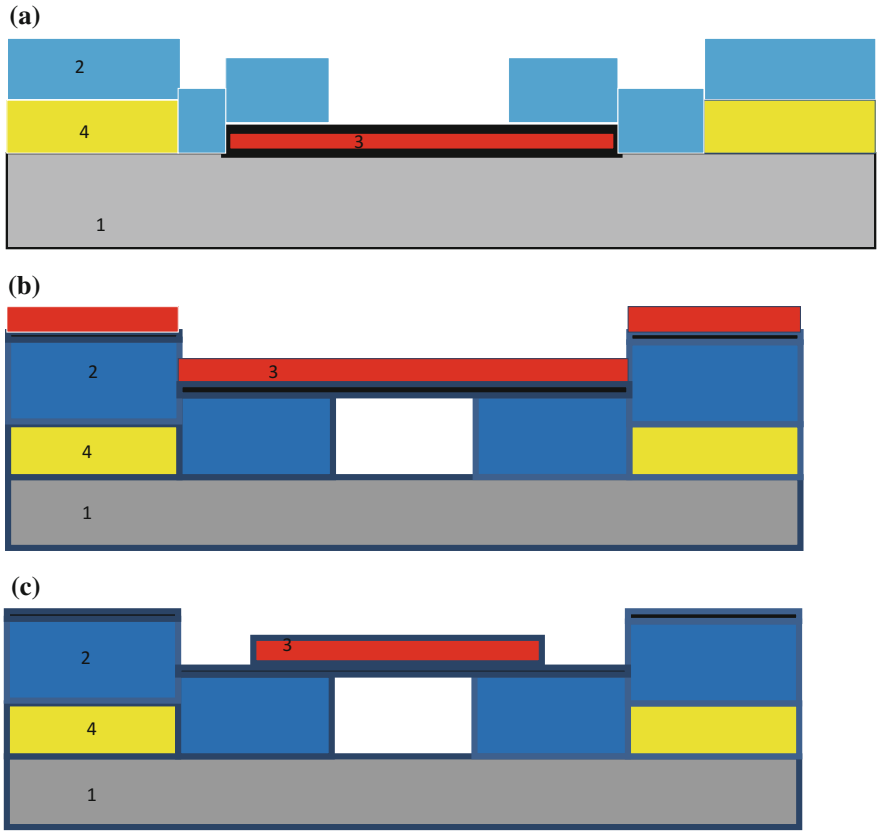


**Fig. 1** Conventional SINIS bolometer with absorber on the substrate (**a**), suspended bolometer with proximity to Au wiring (**b**), and suspended bolometer with reduced proximity (**c**). Samples fabricated on Si substrates (1, gray), superconducting Al electrodes (2, blue). Absorber (3, red) in (**a**) is oxidized to form a tunnel barrier to superconducting electrode, and in (**b**), (**c**) superconducting electrode is oxidized to make a tunnel barrier

backside etching in $SF_6$ plasma [12]. The above examples use relatively thick copper or gold thin films. For bolometer applications though it is advantageous to reduce volume of the absorber and increase its electrical resistance for better matching to the planar-antenna impedance.

Here we describe in more detail a novel design of SINIS bolometers [13, 14]. Compared to conventional SINIS bolometers (Fig. 1a), in the new design normal-metal absorber is placed above the tunnel junctions in a suspended position (Fig. 1b, c). The fabrication process is simpler compared to the previously used shadow evaporation technique. Films can be deposited by several methods such as thermal evaporation, electron beam evaporation, and magnetron sputtering. Patterning of both layers can be done by simple liftoff process. Figure 1b shows a schematic view of the simplest version of proposed structure. First, we deposit a trilayer of Ti (~10 nm)

Au (~50 nm) Pd (~10 nm). This trilayer is patterned for antenna, wiring, and contact pads (yellow). The next step is evaporation of SIN structure. Superconducting Al (~100 nm) is deposited and oxidized about 10 min in an atmosphere of pure oxygen at a pressure of 20 mbar. On top of oxide, the absorber normal-metal layer (20–30 nm of Pd, Hf, or Cu) is deposited. To form the suspended absorber bridge, we selectively etch Al layer under the absorber in the region defined by a window in the resist. Aluminum under the bridge region is completely removed by etching in a weak base (Microposit MF CD 26 developer diluted 1:1). The results of etching are clearly visible in scanning electron microscope (Fig. 3) and even in an optical microscope. Etching in conventional acid mixture (80% $H_3PO_4$, 5% $HNO_3$, 5% $CH_3COOH$) was neither controllable nor reproducible.

At the beginning, the suspended absorbers were made of Cu. It was observed that Cu thin films are soft and have a tendency to sag down to the substrate. Besides that, Cu is a good conductor at cryogenic temperatures and forms relatively low resistivity bridges even at thicknesses approaching 20 nm. This restricts such devices impedance matching with quasioptical antennas having impedances around 50 Ω. An absorber of Cu (~20 nm) with a thin (~3 nm) layer of Cr was instead used to create rigid suspended bridges. While Cr + Cu is a robust thin film, care needs to be taken during subsequent fabrication steps involving resist development and liftoff. Each of these steps need to be terminated using a critical point drying step in liquid $CO_2$ to prevent the collapse of already-formed bridges. Rinsing in acetone, ethanol, or methanol instead of water and blow-dry with nitrogen can be alternative to critical point dryer for hard and thick Pd and Hf suspended bridges.

To investigate the influence of proximity effect on superconductivity in S electrode of NIS junction, we added in fabrication a one more step of chemical etching of Cu in diluted 1:50 $HNO_3$. By this, we were able to vary the distance from golden wiring film (4, yellow) to S electrode of SIN junction (see Fig. 1c). SEM images of fabricated samples are presented in Figs. 2 and 3.

## 3 Terahertz Band Conventional SINIS Bolometer

In SINIS bolometer, the absorbed THz radiation raises the electron temperature that is seen by an increase of the tunneling current. For estimations of sensitivity, it is usually expected that absorption of radiation is equivalent to the DC heating at the same applied power. It is assumed that the electron system is overheated to some enhanced electron temperature $T_e$. In the case of rather high photon energy $hf >> k_B T_e$, the energy distribution of electrons is affected by the electron–electron, electron–phonon, phonon–electron, phonon–phonon interactions and tunneling of the excited electrons in SIN junction. Here h is the Planck constant, f is the frequency of incident radiation, $k_B$ is the Boltzmann constant, and $T_e$ is the temperature of the electron system in the normal metal. The distribution function of electrons can be substantially different from the Fermi distribution function. If the heat leakage to the substrate and electrodes via phonons is reduced by decoupling the absorber from

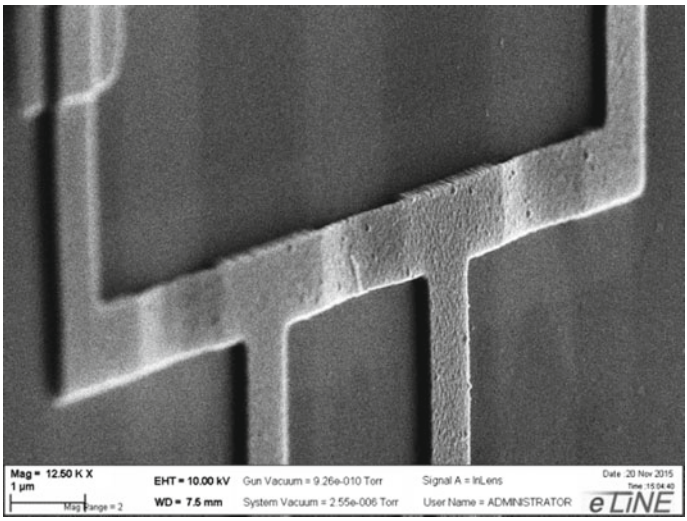


**Fig. 2** SEM image of fabricated sample according to schematics Fig. 1 top, test structure with three suspended bridges and four SIN junctions

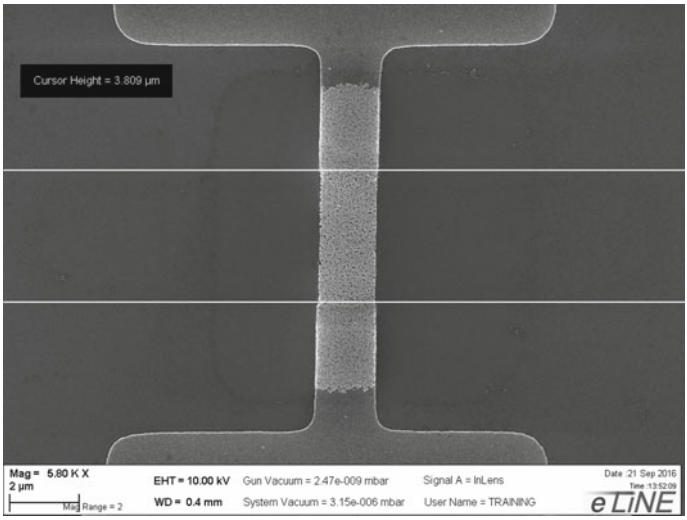


**Fig. 3** SEM image of the SINIS device according to schematics Fig. 1c. In this layout, the distance from SIN junction to normal-metal wiring can be varied from 0.5 to 3 µm

the substrate phonon bath, the detector response would be improved by a factor of $hf/k_{\mathrm{B}}T_e$ through the multiplication of excited electrons.

Combination of two NIS junctions and common normal-metal absorber makes SINIS bolometer that can be used in Terahertz frequency band. In such bolometer,

NIS junctions have several functions: temperature sensing, electron cooling, capacitive signal matching to the antenna [15, 16]. Under microwave irradiation, excited electrons with excess energy lead to increase in tunneling current and/or decrease of DC voltage and such response is dependent on applied power and frequency. Usually for theoretical estimations, it is assumed that microwave radiation is equivalent to DC heating at the same absorbed power. In such process, the electron temperature of absorber is increased over the phonon temperature.

However, in normal metal for Terahertz radiation at frequency $f \gg kT/h$ occurs quantum absorption of photons with energy $E = hf \gg kT$ by single electrons [17–20]. In this case, the distribution of electrons on energy is determined by a balance of processes of photon quantum absorption, electron-electron, electron–phonon, phonon—electron, phonon escape processes, and tunneling of excited electrons in a SIN junction [17, 18]. This distribution function is significantly different from equilibrium Fermi distribution. Microscopic calculations of tunneling current in clean limit [17, 18] for electron–electron and electron–phonon collision integrals show that increase of response is dependent on multiplication of excited electrons with energies $\varepsilon > kT$ due to electron–electron interactions and reabsorption of nonequilibrium phonons that did not escape from absorber. Multiplication of nonequilibrium electrons leads to increase of current response $\delta I(P)$, in which $P$—absorbed power that leads to increase in current $\delta I$ for voltage bias mode. In such case, current response $\delta I$ of SINIS detector can exceed the photon counter limit of e/hf, but still being below the bolometric response limit of $e/kT$. Studies and optimization of energy relaxation in electron system at low temperatures can help to improve the practical optical response of SINIS detectors.

In experiments [21, 22] ,voltage response $\delta V(I) = V_{I,\,P=0} - V_{I,P}$ shows no thermal equilibrium in electron system. Here we present detail analysis of experimental data on IV curves, dynamic resistance, optical response to show absence of equilibrium in electron system and significant tunnel current due to electrons with excess energy.

Bolometers containing SINIS structures were integrated in twin-slot antennas. Bottom layer of conventional bolometer was made of normal-metal Al absorber 10 nm thick in which superconductivity was suppressed by underlayer of 1-nm-thick Fe film [23]. For microwave signal, such bolometers were connected in parallel by means of capacitive connection. Dimensions of elements: area of tunnel junctions 0.25 $\mu m^2$, length, width and thickness of normal-metal strip between tunnel junctions $1 \times 0.1 \times 0.01$ $\mu m^3$, DC resistance of single absorber ~200 Ω. Parallel connection for microwave signal makes optimal antenna load of 60 Ω. Tunnel junctions parameters were similar to [7, 8]. When cooling down to $T < 0.1$ K, the resistance ratio $R_d(V = 0)/R_n$ (see (2)) approached $R_d/R_n = 15000$, and total resistance of array at 0.1 K approached $R_{d(V=0)} = 300$–$400$ MΩ.

Samples were measured in dilution cryostat equipped with a pulse tube refrigerator [24]. Additional recondensing stage with liquefying of He gas in 0.125 l container allows to keep temperature below 0.1 K during 4–6 h with compressor shut down. Chip with SINIS receiver was mounted inside copper radiation shield at temperature 0.4–0.45 K, in which inner wall was painted with black absorber containing Stycast® 2850FT.

Silicon chip 0.35 mm thick was attached to sapphire hyperhemisphere lens 10 mm in diameter that collect radiation to the planar antenna. Lens itself was glued with Stycast® 1266 in copper holder screwed to the dilution chamber. Measurements with $RuO_2$ thermometer glued to Si plate instead of detector show that its temperature at 0.1 K differs by less than 2–3 mK from mixing chamber temperature measured by LakeShore® thermometer with absolute error below 5 mK.

In front of lens in the bottom of radiation shield, it was a hole 5 mm in diameter, which was covered with planar bandpass filters [25] for middle frequency of 330 GHz and total passband of 50 GHz. Spectral transmission within 10% accuracy is described by product of two Lorentz lines with halfwidth of 70 GHz. Transmission of filter in the maximum was over 90%. Distance from lens to filter is 2–3 mm, between filters 2 mm, from filter to black body source 2–3 mm.

Radiation source is a black body made of Si wafer covered with NiCr film of square resistance of 300 Ω. Wafer was mounted on heat insulating legs to 1 K pot. Temperature of radiation source was monitored by resistance of calibrated $RuO_2$ chip resistor and varied by current through the NiCr film in the range of 0.9–15 K. Dissipated power was up to few milliwatts, time constant for heating/cooling of the order of 0.1 s.

Power received by antenna was calculated using Planck formula for single mode

$$P_{\text{incident}} = \int \mathrm{d}f \frac{hf}{\exp\left(\frac{hf}{kT_R}\right) - 1} * K1 * K2 * K3 \tag{4}$$

in which $T_R$—radiation source temperature, coefficients $K1$ and $K2$ accounted for transmission of filters and spectral matching of antenna. For antenna, we take Lorentz line with halfwidth of 100 GHz and maximum at 330 GHz. Influence of $K2$ was rather small, below 20%. Coefficient $K3 = 0.82$ takes into account reflection of sapphire-vacuum interface.

Electron temperature in normal metal absorber was deduced from dependencies of dynamic resistance $R_d = \mathrm{d}V/\mathrm{d}I$ and comparison with dV/dI dependence of ideal SIN junction at some effective electron temperature. In Fig. 4a, b presented IV curves for two temperatures and calculation according to simple analytic relation (1). IV curve of ideal SIN junction for voltages below the gap of superconductor $V_\Delta = \Delta/e$ (in which Δ—energy gap of superconductor.), for single junction, can be presented as (1) see [26]. In our case, we have six junctions connected in series, so measured values of $R_n$ and $V$ are divided by six to fit with model curve. Voltage derivative of current brings dynamic conductivity and inverse value is dynamic resistance. In experimental curves, measured voltage corresponds to $6V_{\text{sin}}$ in which $V_{\text{SIN}}$—voltage across the single SIN junction.

Gap voltage $V_\Delta$ in (2) according to BCS theory corresponds to $eV_\Delta = \Delta(0) = 1.76 \times \mathrm{kT}_c$ in which $T_c$—critical temperature. It can be determined from the dependence, $R_d(T, V = 0)$ which in the temperature range ~0.3–0.5 K has exponential shape. At higher temperatures, it should be accounted also the temperature dependence $\Delta(T)$, and at temperatures below 0.2 K dynamic resistance $R_d$, approaches

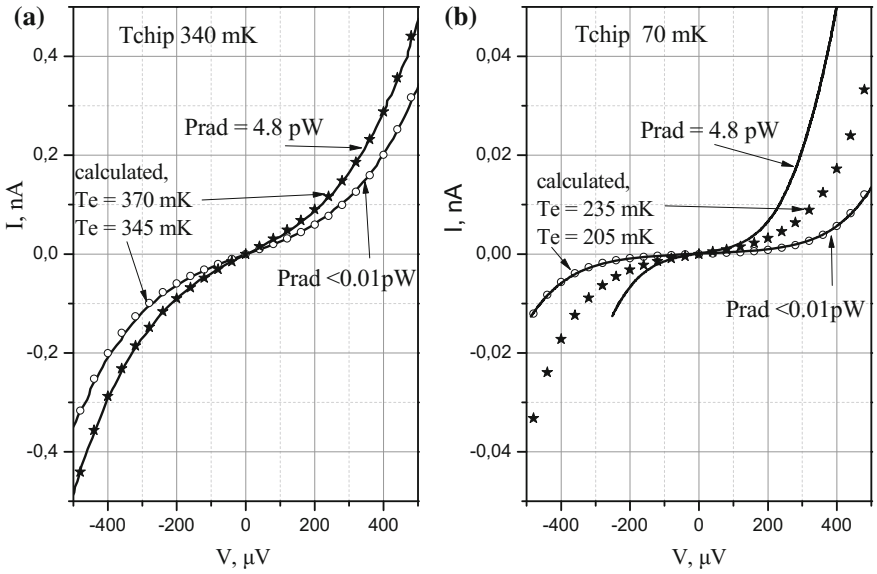


**Fig. 4** IV curves of SINIS bolometer at bath temperature 340 mK (**a**) and 70 mK (**b**). Solid lines correspond to experimental data obtained at two radiation power levels of 4.8 pW and below 10 fW. Stars and circles—calculated curves for 370 mK and 345 mK (**a**), and 235 mK and 205 mK (**b**)

constant value that is explained by overheating of electron system by external radiation. Value of equivalent $T_e$ can be estimated by fitting with (2). In our case, using $\Delta = k \times 2.45$ K, we obtained good correspondence of experimental calculated curves in all figures. Small difference can be observed at $V > 0.4$–$0.5$ mV, where resistance is higher compared to calculated one due to electron cooling. In our fitting, we use value of $\Delta$ that corresponds to $T_c$ ~1.4 K. In measurements at $T = 1.5$ K IV, curve is linear and at 1.3 K nonlinearity is clearly visible, so $T_c$ is within this range.

If electron system is excited by microwave radiation, then the dependence is different from heating of sample, see Fig. 5. There is no more correspondence with the simple thermal model. If we take $T_e$ for which $R_d(V = 0)$ is the same as in model, then at higher bias current the difference in resistance can be more than 10 times. One can see that power response and temperature response are different at 70 mK and coincide at 340 mK.

Dependencies of responsivity dV/dP on phonon and equivalent electron temperature are presented in Fig. 6a, b for radiation power levels 0.22, 1.35, 2.95, 4.95 pW. When plotted in dependence on electron temperature (b) the shape of dependence is more natural and shows that responsivity is dependent on nonequilibrium electron temperature. When irradiated at 5 pW load, the responsivity is reduced by an order of magnitude compared to 0.2 pW power load. When bath is heated to 0.34 K, these responsivities become equal for all power loads which means that in this range detector becomes linear, dV/dP is independent on power, and is determined by tem-

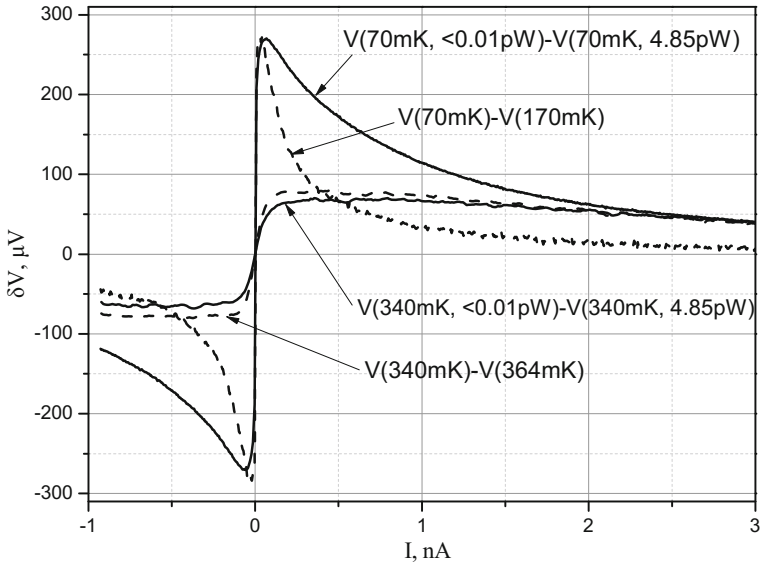


**Fig. 5** Voltage response dependence on DC voltage for temperatures 70 and 340 mK. Solid lines under 4.85 pW irradiation, dashed response to equivalent increase in temperature without irradiation

perature. In this case, electron and phonon temperatures are equal. It means that increase in bath temperature leads to increase of relaxation processes and thermalization of electron system.

Losses in bolometer can roughly be estimated from power to current transfer ratio, or current responsivity. Compare a number of incoming quanta $I_Q = 5 \times 10^8$ $s^{-1}$ for 0.1 pW at frequency 330 GHz and number of excited electrons that tunnel due to irradiation $I_S = 6 \times 10^8$ $s^{-1}$ (current increase at this power load). Quantum efficiency $\eta = I_S/I_Q = 1.2$ is close to unity, which means that one quantum produce just one electron, that is a photon counter mode. There is no multiplication of excited electrons number which was predicted in [17–19] for bolometric mode of operation. If energy did not escape from electron system, then the number of excited electrons with energies in the range ~(0.2–1)$\Delta$ should be 30 times more. Bolometers with suspended absorber are intended for improving quantum response over these values.

## 4 Mechanisms of Energy Relaxation and Time Scale

According to estimations [27], the difference of calculated and experimental curves proves the absence of equilibrium in electron system when energy distribution for electrons with energy above the Fermi energy and holes with energy below it does not correspond to Fermi distribution with equivalent electron temperature. These

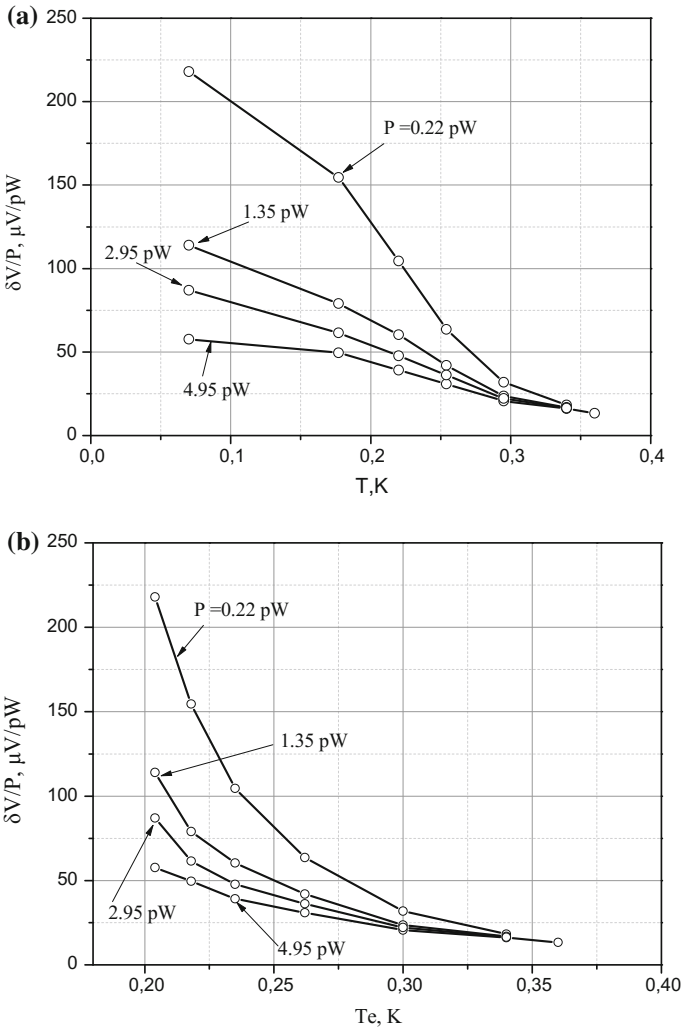


**Fig. 6** Responsivity dependence on bath temperature (**a**) and on equivalent electron temperature (**b**) for radiation power levels 0.22, 1.35, 2.95, 4.95 pW

excited electrons can be viewed in two groups: thermalized and athermal. Impact of thermalized electrons can be estimated assuming that their temperature corresponds to calculated for the case when calculated curve tangenting experimental at $V = 0$, and dynamic resistance of both are equal. In Fig. 4b, such assumption leads to the electron temperature under irradiation estimation of 235 mK. The impact from athermal electrons can be estimated as a difference between measured and calculated and can be up to 70% of the total response. When temperature increase, the relaxation processes speed-up, and at 0.34 K, the impact from athermal electrons is

much less. At the same time impact from thermalized electrons increase, they prevail in tunneling current. As a result, the voltage dependence of response approaches the calculated one.

Radiation power is collected in a normal-metal absorber with dimensions much less compared to the wavelength, so it can be considered as a lumped element. When absorbing the radiation quantum energy $hf/k$ = 16 K, all this energy is transferred to electron, it forms electron-hole pair with energies from 0 to hf above/below the Fermi energy. The average energy of excited electron and hole is 8 K.

Excited electrons and holes diffuse toward the area of tunnel junctions with diffusion time $\tau_{\text{diff}}$, after that transfer into superconducting electrode with time constant $\tau_{\text{sin}}$. During this period, energy is redistributed due to electron–phonon, phonon—electron, electron–electron, phonon–phonon, and phonon escape processes. As a result, energy of excited electrons is reduced, their number can increase, some power escape into substrate and superconducting electrodes. Additional tunneling current under irradiation depends on ratio of time constants of these processes. Since all time constants are strongly dependent on excitation energy, the dynamics become very complicated, especially taking into account transition from two-dimensional to three-dimensional cases when changing temperature and power. Processes in superconducting electrode will be also ignored; we assume it as a thermal sink.

Microscopic model described in [28] assumes that as the result of electron–electron interaction, primary electron after each inelastic collision will produce three new quasiparticles: two electrons and one hole. Each of them has hf/6 of initial energy. Absorption of one phonon will produce two quasiparticles: one electron and one hole, similar to photon absorption. Spontaneous emission of phonons preserves the number of quasiparticles. Rate of electron–electron collisions that are necessary for multiplication of electrons is an order of magnitude slower compared to electron–phonon relaxation which reduce excitation energy and do not lead to multiplication of quasiparticles. The phonon–electron process can slightly increase bolometer response above the photon counter limit.

Model of thermalization in normal metal is also discussed in [29]. According to this model, the most probable process for energy relaxation of electron from energy level of $E = \Delta$ is down to $\Delta/4$ and emerging of phonon with energy $3\Delta/4$. This energy is much higher compared to thermal phonons, and we obtain a nonthermal distribution for both phonons and electrons.

First, we estimate the diffusion constant for electrons in normal metal:

$$D = \frac{1}{e^2 N \rho} \tag{5}$$

in which $\rho = 0.07\ \Omega \times \mu\text{m}$, $N = 2.3 \times 10^{10}\ \mu\text{m}^{-3}\ \text{eV}^{-1}$ is electron density at Fermi level, this brings $D = 0.004\ \text{m}^2/\text{s}$. Diffusion time for electrons to travel the distance about 1 μm from the middle of absorber to tunnel junction area is $T_{\text{diff}} = 0.25$ ns.

Relation of diffusion constant $D$ with speed $v$ and mean free path $l$ is $D = lv/3$. Taking Fermi velocity $v_F = 2 \times 10^6$ m/s, one can get the mean free path in absorber

l = 6 nm. Thickness of absorber in our samples is 10 nm, which is comparable to mean free path. Diffusion time through the thickness of absorber is 0.025 ps.

One more important parameter is characteristic time for tunneling in SIN junction. Time constant for electrons to escape from normal metal to superconducting electrode is determined by time of many attempts providing close to unity probability to tunnel through the barrier. Transparency of barrier is related to normal resistance of junction. According to [17, 26], if in the bias point, differential resistance is close to normal resistance $R_n$, then tunneling time constant for junction of area $S$ and film thickness $t$ is

$$\tau_{\text{sin}} = N(0)e^2 R_n S t \tag{6}$$

Opposite process of phonon-electron interaction is rather fast, according to [6, 28]:

$$\tau_{pe} = \frac{234\, N_A\, n_d\, k^3}{6\, \Sigma\, \Theta_D^3\, E^2} \tag{7}$$

in which $N_A \times n_d$—atomic density that is for aluminum $6 \times 1022$ cm$^{-3}$, $\Theta_D$ = 428 K—Debye temperature. If we take the distribution of energy from electron with initial energy 8 K to electron and phonon with the ratio 1:3, this corresponds to $\tau_{pe}$(6 K) = 5 ps.

The dynamics is quite different for electrons in the region of tunnel junctions. For acoustic waves both normal and superconducting electrodes separated by barrier below 2 nm thick is the same material and phonons can escape from normal into superconductor metal in few picoseconds without returning energy to electrons in absorber. Such process is a loss channel for energy that irreversibly escapes to superconductor or substrate. Characteristic time for such escape through the thickness of absorber $t_{\text{abs}}$ is $\tau_{\text{escape}} = t_{\text{abs}}/v_{\text{sound}}$ = 2 ps.

Phonon relaxation time can be estimated in the case of scattering at boundaries by dividing the characteristic length of our sample about $l_{\text{abs}}$ = 3 μm by sound speed $\tau_{\text{pp}} = l_{\text{abs}}/v_{\text{sound}}$ = 600 ps.

Redistribution of energy among electrons is governed mainly by electron–electron interaction. Equation for calculating of such time constant $\tau_{\text{ee}}$ for two-dimensional case corresponding to thin normal absorber taken from [26, 28]:

$$\tau_{ee} = \frac{hE_F}{\pi^2 E^2 \ln\left(\frac{E_F}{E}\right)} \tag{8}$$

in which $E_F$ = 11.6 eV—is Fermi energy. At electron temperature of 8 K, this time is $\tau_{\text{ee}}$ = 1 ns, that exceeds $\tau_{\text{ep}}$ = 0.2 ns for the same electron energy. For three-dimensional case, $\tau_{\text{ee}}$ is over order of magnitude as much compared to two-dimensional. Value of $\tau_{\text{ee}}$ becomes equal to $\tau_{\text{sin}}$ for temperatures in the range 1–1.3 K. Value of $\tau_{\text{ep}}$ becomes equal to $\tau_{\text{sin}}$ for electron temperatures ~2 K.

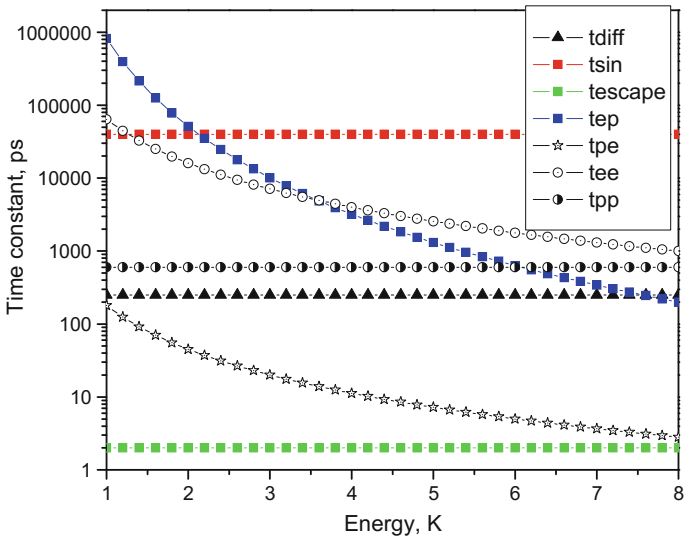


**Fig. 7** Time constant dependencies on excitation energy plotted in Kelvins, i.e., E/k

From the above estimations, it is clear that due to complicated combination of electron–electron, electron–phonon, phonon–electron interactions which vary with signal frequency and power, the energy distribution of electrons is much different from simple Fermi distribution. A nonequilibrium property of system is mainly determined by ratio of escape time for electrons due to tunneling $\tau_{sin}$ to electron–electron and electron–phonon time constant. Finally, we can pick out two groups of time constants, first is energy independent, it is diffusion time $\tau_{dif} = 0.25$ ns, tunneling time $\tau_{sin} = 40$ ns, phonon escape time $\tau_{esc} = 2$ ps, and phonon-phonon time $\tau_{pp} = 0.6$ ns. Energy-dependent time constants are second-order dependent $1/E^2$ electron–electron time $\tau_{ee}$ and $\tau_{pe}$, and also a fourth-order dependent $1/E^4$ electron–phonon constant $\tau_{ep}$. Dependencies are presented in Fig. 7.

Electron–electron and electron–phonon time constants become equal at energy around 3.7 K, and for lower energies electron–phonon interaction get slower, so electron–electron interaction can become dominating. To increase bolometer efficiency, the length of absorber should be increased providing diffusion time $\tau_{dif}$ longer compared to $\tau_{ee}$ and $\tau_{ep}$, value of $\tau_{ep}$ should be increased by using absorber material with lower electron–phonon parameter sigma; resistivity, density, and acoustic impedance of absorber material should be increased as well. According to [17], the optimal resistance of SIN junction should be around 10 kΩ.

For SINIS detectors, nonequilibrium in electron system plays the main role in optical response performance. Ultimate parameters can be achieved for maximum multiplication of electrons in absorber due to electron–electron interactions and absorption of nonequilibrium phonons. Time of electron–electron collisions is relatively big at the beginning of such process, and this factor diminishes multiplication.

Nonequilibrium of phonon system is determined by freedom of phonon escaping to superconducting electrode that is fabricated from the same aluminum as absorber. The natural way to increase multiplication and response of detector is using material with lower $\tau_{ee}$, higher $\tau_{ep}$, and higher acoustic mismatch with aluminum, which can be Hafnium. Inversion of sequence of layers with placing absorber above superconductor can also reduce phonon escape to substrate.

## 5 Electron Cooling of Absorber and Overheating of Superconductor

When biasing SIN junction slightly below the energy gap voltage, the junction removes high-energy electrons from the normal metal to the superconductor. At this optimal bias, the SIN junction keeps the electron temperature in the absorber $T_e$ below the phonon temperature making the absorber more thermally sensitive even at higher substrate temperatures.

Accurate relation for electron cooling is rather complicated integral equation, but for bias voltages close to the energy gap, it can be presented by a simplified analytic expression [1]

$$P_{\text{cool}}(\tau, V) = \frac{\sqrt{2\pi\,\Delta k_b T_e}}{2eR_N}\left(\frac{\Delta}{e} - V\right)\exp\left(-\frac{\Delta - eV}{k_b T_e}\right) \tag{9}$$

The effective electron temperature $\tau$ can be determined in first approximation from (10)

$$\left(T_{ph}^5 - T_e^5\right)\Sigma v = P_{\text{cool}}(T_e) - P_{\text{bgn}} - \frac{V^2}{R_s} \tag{10}$$

in which $T_{\text{ph}}$ is phonon temperature, $V$ is DC bias voltage, $R_s$ is shunting resistance, $P_{\text{bgn}} = 0.5hf\,\Delta f = 6 \times 10^{-14}$ W background power load, $\Sigma = 3 \times 10^9$ W/m$^3$ K$^5$ is material parameter, $v = 1.8 \times 10^{-19}$ m$^3$ is absorber volume.

Experiment with electron cooling in the test structure with 4 SIN junctions shows the best cooling drop by about 200 mK [30, 31], see Fig. 8.

Efficient electron cooling was realized due to the improved geometry of the cooling tunnel junctions and additional Au traps for hot quasiparticles just near junctions. Normal-metal traps are expected to reduce returning of hot quasiparticles after removing them from normal metal and absorbing phonons produced by quasiparticle recombination. Later (see Fig. 9), we made separate experiment to investigate the influence of such traps on electron cooling, energy gap smearing, and suppression. Minimum in resistance corresponds to the energy gap edge where density of states in superconductor sharply increases.

In Fig. 9, we present three dependencies for dynamic resistance of samples with 4 SIN junctions and distance from N wiring to S electrode of 1, 2, and 3 μm.

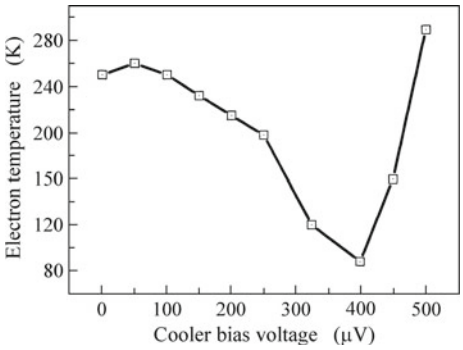


**Fig. 8** Electron temperature dependence on bias voltage for bath temperature 280 mK

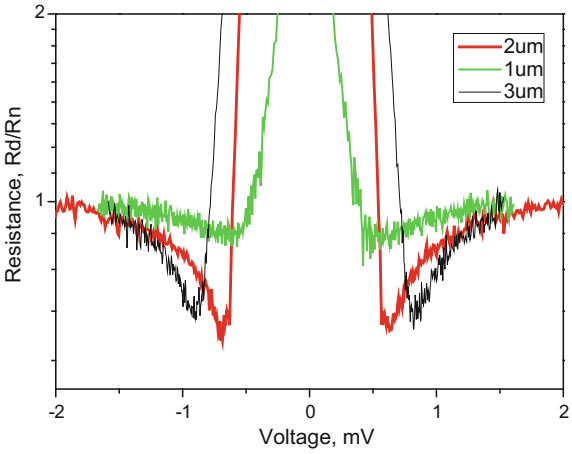


**Fig. 9** Dynamic resistance of four SIN junctions connected in series with corresponding single energy gap of 0.1, 0.155, and 0.2 mV for samples with distance from normal-metal trap to superconducting electrode of 1, 2, and 3 μm measured at 300 mK

The corresponding energy gap for one SIN is 0.1, 0.155, and 0.2 mV. From these dependencies, we can conclude that such direct N-traps do not help much for cooling of S electrode but can significantly suppress the energy gap. Reducing of gap can be explained by overheating of superconductor at high bias current around the energy gap. Taking the relation for temperature dependence of the energy gap as

$$\Delta(T) = \Delta_0 \sqrt{\frac{2\pi kT}{\Delta_0}} \exp\left(-\frac{\Delta_0}{kT}\right) \text{ or } \Delta(T) = \Delta(0)\sqrt{Cos\left(\frac{\pi T}{2T_c}\right)},$$

we can estimate the temperature of overheated superconducting aluminum with energy gap at 100 μV as 0.85 K, that is much higher compared to bath temperature of 280 mK. Improved cooling in [30, 31] with Au traps close to SIN junctions is possible due to the specific feature of Au–Al interface that is actually an intermetallic compound that can be treated as tunnel barrier with relatively high transparency. Detail studies of optimal barrier for N-trap is performed in [37] where they discovered that for NIS junction barrier the oxidation doze is 1.3 mbar 300 s and for NIS

trap barrier it is 0.18 mbar 1 s, that is about three orders lower. We assume that Al–Au interface makes comparable barrier.

For presented electron cooling temperatures below 150 mK, the estimated value of temperature is not exactly corresponding to the case with Fermi energy distribution of electrons. Actual distribution is nonequilibrium and non-Fermi and the estimated value can be accepted only as a rough qualitative estimation of the electron cooling. In the case of SINIS bolometer, the electron cooling leads to fast removing of hot electrons that did not share energy and not thermalize, so the quantum efficiency is low.

## 6 NIS Thermometer

The current through a NIS tunnel junction is proportional to the difference in the tunneling rates between tunneling from the normal metal to the superconductor, and tunneling from the superconductor to the normal metal integrated over all energies. For estimation of the actual electron temperature, the natural way is to fit IV curve of a real junction by ideal NIS tunnel junction IV curve that can be approximated as (1). A subgap leakage current and Andreev current can affect both shape of IV curve and electron temperature of the bolometer. Such subgap residual conductivity can be due to imperfectness of the tunnel barrier, normal inclusions in superconductor, etc. Another mechanism of subgap conductivity is two-electron tunneling when two normal electrons can be converted into a Cooper pair, which is usually mentioned as Andreev current [32]. Under subgap conditions, the Andreev current is found to dominate the single-particle tunnel current [33]. The phase-coherent Andreev current introduces a significant dissipation in the normal-metal absorber and corresponding overheating. The heat balance equation should be written as $2P_{\text{cool}} + P_{\text{eph}} + I_A V = 0$.

This effect dominates at temperatures below 200 mK; the electron temperature in a small-volume bolometer saturates with phonon cooling. For samples with big volume of normal metal that are intended for temperature sensing, such overheating is smaller and SIN thermometer can operate down to 25 mK (Fig. 10). At very low temperature, the electron temperature first increases with the bias due to Andreev current heating before decreasing due to tunnel current-based cooling effect. Contrary to ballistic regime, this current is not vanishing due to quasiparticles confinement in the vicinity of the interface. Although the Andreev current $I_A$ is a small effect in terms of charge current, it is much more important if one consider the heat current. Andreev current contributes fully to heating as a Joule power $I_A V$, while the tunnel current cools with a moderate efficiency of $T_e/2T_c$, which is below 5% at 100 mK electron temperature (Fig. 11).

The dependencies from Fig. 10 are typical for single NIS junction connected to a relatively big volume of normal metal that function as a trap for hot quasiparticles. The important aspect of this device is using the Al film with suppressed by ferromagnetic $CrO_2$ or Fe superconductivity as N electrode. In this case, Andreev currents are suppressed and we get IV curves more close to the perfect NIS junction as in (1, 2).

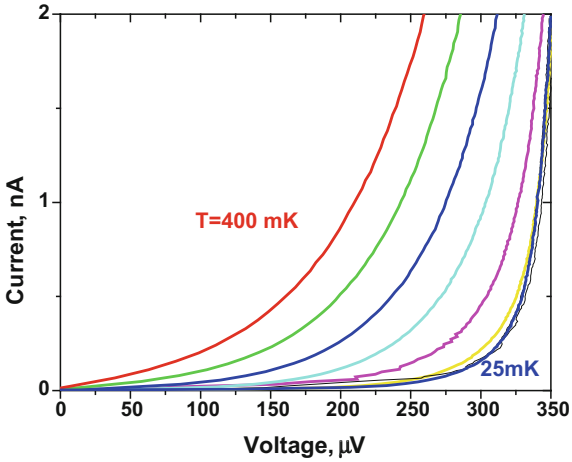


**Fig. 10** IV curves of CEB thermometer with large N electrode taken at temperatures from 25 to 400 mK

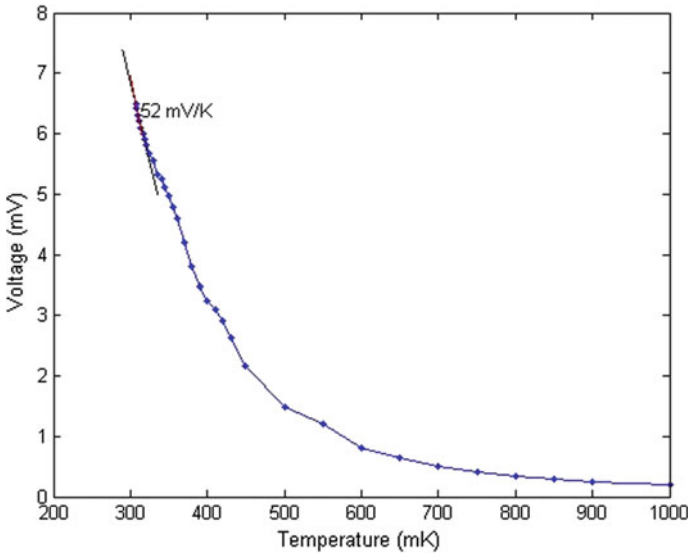


**Fig. 11** Voltage versus temperature dependence for 100 junctions $2 \times 2\ \mu m^2$ area

For an array of 100 junctions, a temperature resolution of 5 μK has been achieved which is better than the result of 30 μK for 10 junctions. Increasing the number of junctions in series allow us to achieve higher sensitivity, which enables use of NIS tunnel junctions fabricated in direct-write technology for thermometry application [34].

## 7 Andreev Current and Hot Electron Traps

Andreev reflection that describes mechanism of current and heat conductivity in NS contact is usually not taken into account in tunnel NIS junctions due to much larger single-particle tunneling. In the case of long mean free path for electrons, the probability for electron to tunnel with Andreev reflection is very low. But at temperatures much below $T_c$ and bias voltages much below the energy gap $V_{\Delta,}$ the single-electron current drops down exponentially and Andreev current can become dominating. The additional factor for increase of Andreev current is that in thin-film structures, the electron-hole pair can drop many times at the NS border that will proportionally increase the probability of tunneling. According to [32], the Andreev subgap current contains two terms $I_n$ and $I_s$ related to electron transport in $N$ and $S$ electrodes.

$$I_{\text{subgap}}(U,T) = I_n + I_s = \frac{\hbar}{e^3 R_n^2 S \nu_n d_n} \tanh(eU + 2kT) + \frac{\hbar}{e^3 R_n^2 S \nu_s d_s 2\pi} \frac{eU/\Delta_c}{\sqrt{1 - eU/\Delta_c}} \quad (11)$$

In this equation, $\nu_n$, $\nu_s$—electron densities in $N$ and $S$ electrodes, $d_n$, $d_s$, and $S$ thickness of electrodes and area, $R_n$ asymptotic resistance of junction, U bias voltage. At temperatures below 200 mK, such excess subgap current is clearly observed in IV curves of NIS junctions with Cu normal electrode (Fig. 12). In junctions with ferromagnetic $CrO_2$ or Fe underlayer, it is not so clearly visible, but still presented. Magnetic field leads to dephasing in Cooper pairs and suppression of Andreev current (Fig. 13).

Single-particle tunneling is dramatically sensitive to normal magnetic field, and the Andreev current is sensitive to the applied in-plane external magnetic field. We measured magnetic field dependencies in tangential and normal direction of external magnetic field, see Fig. 13.

With ferromagnetic layer, Andreev current dependence is not as clear as for pure Cu absorber, nevertheless it is impossible to describe IV curve in the model of simple NIS junction (Fig. 14). Taking into account smaller area of junctions with Fe, the values of $I_n$ and $I_s$ are in the same range as for Cu samples. Explanation of discrepancy from simple model using Dynes parameter (Fig. 15) gives worse fitting. So we can assume that instead of unclear empirical Dynes parameter, it is more reasonable to use Hekking–Nazarov model.

The important issue of SINIS bolometer and electron cooler development is a proper cooling of superconducting electrode. The natural way is to increase the thickness and volume of S electrode that will help to spread injected hot quasiparticles in a large volume, and finally this energy will be transferred to phonons and sink in the substrate. Another popular method is using a normal-metal trap. One of pioneering experimental works [35] shows some improvement in cooling of thin 18 nm Al with 28 nm Cu film deposited above Al over oxide barrier. They observed improvement

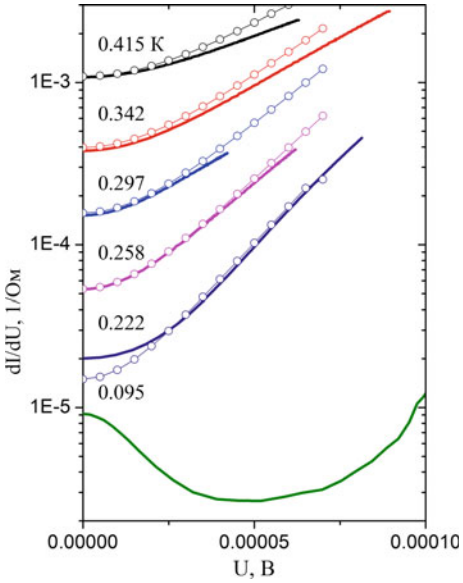


**Fig. 12** Measured NIS conductivity (lines) and calculated according to (1,2) circles for temperatures from 95 to 415 mK

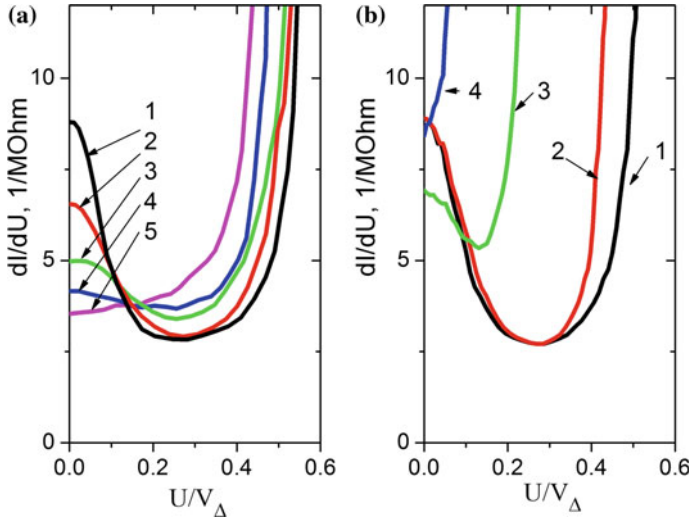


**Fig. 13** Conductivity of NIS junction for in-plane magnetic field 0; 95; 140; 180; 235 G (**a**), and normal to the substrate direction 0; 19; 29; 34 G (**b**), both at temperature 90 mK

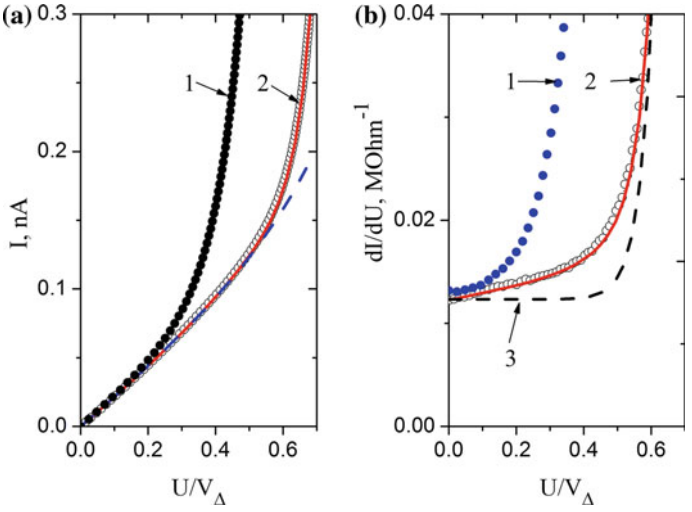


**Fig. 14** IV curve (**a**) and dynamic conductivity (**b**) for NIS with Fe underlayer, (1) measured at 130 mK, (2) at 80 mK. Dashed in A calculated current, line (2) in B calculated full conductivity, (3) calculated conductivity assuming absence of Andreev conductivity and shunting of junction by 80 MΩ

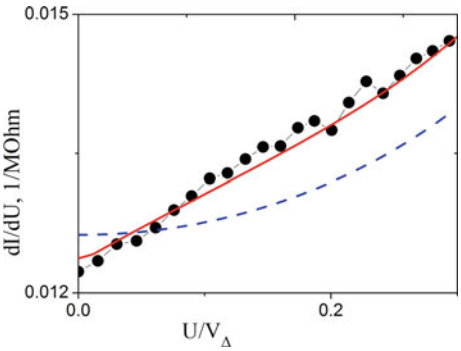


**Fig. 15** Measured conductivity of NIS with Fe (black dots), approximation with Hekking–Nazarov model (line) and using Dynes model (dash)

when reduced distance from junction to Cu film from 8 to 0.2 μm. Another option is using direct contact of normal-metal trap [36] in which the measured trapping efficiency, that is the ratio of absorbed to incident power, was about 10% near 100 mK.

In our earlier paper [31], see figure above, the normal-metal traps were made of Au film 60 nm thick, above that 65 nm of Al makes superconducting electrode. Actually contact between Au and Al is a sort of resistive intermetallic compound with not very high transparency. In some sense, such contact can be viewed as a sort of tunnel junction, similar to [35]. In the case of Fig. 1b, c, we have Pd at the top of TiAuPd trilayer and the top Pd makes perfect contact to Al. As a result, when Pd is ultimately close to Al, as in Fig. 1b, we have visible suppression of superconductivity

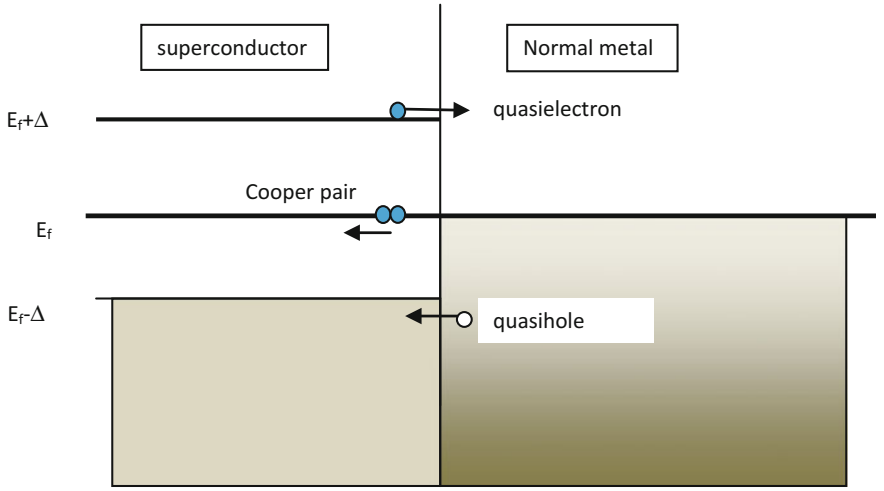


**Fig. 16** Energy diagram illustrating how hot quasiparticle (red) with energy above the gap crossing the SN border and resulting in moving back of Cooper pair (two blue circles) hot quasi-hole (red) from N electrode. This provides the conservation of charge and energy. Finally, no energy escapes from superconductor, similar to NS process of conventional Andreev reflection

and no strong evidence of electron cooling. When introducing a separation of 1–2 μm as in Fig. 1c, we return back to the original value of a double energy gap of Al that is about 380 μV. Cooling of superconductor by normal-metal trap with direct NS contact seems to be not as effective as with NIS junction with relatively high transparency. This assumption can be illustrated with energy diagram (Fig. 16). Similar to N-S transport, in the case of S-N transport the hot quasi-electron transfer from S to N is accompanied with transfer in the opposite direction of Cooper pair and a quasi-hole. In this case, we satisfy to charge, energy, and pulse conservation. It can be described using equation [38] for heat transfer from S to N:

$$P(T) = \frac{f_0}{2} S * \left(\frac{2p_0}{h}\right)^2 \frac{k^2}{h} T\sqrt{\pi T \Delta}\exp\left(-\frac{\Delta}{kT}\right) = w_0 S T\sqrt{T\Delta}\exp\left(-\frac{\Delta}{kT}\right) \tag{12}$$

with $p_0$—Fermi pulse, $f_0$ constant of the order of unity, $S$ junction area. For the temperature difference $\delta T$, the resulting thermal flux for low temperatures

$$Q = A\sqrt{\frac{\Delta^3}{T}}\exp\left(-\frac{\Delta}{kT}\right) * \delta T \tag{13}$$

The temperature drop $\delta T$ determined by this equation occurs at each of the boundaries between the S and N electrodes. According to this equation, the additional thermal resistance increases by 5 orders of magnitude when cooling down to $0.1T_c$.

## 8 Current Response, Quantum Efficiency, and Thermalization

In our earlier experiments with conventional bolometers directly placed on silicon substrate, we measure voltage response, as in Sect. 3 of this article. If we study instead a current response, it can bring a clear description of quantum efficiency of bolometer that is the number of tunneling electrons induced by a single photon of radiation $\eta = n_e/n_p$.

For conventional bolometers, it was about $\eta$ = 1.2–1.5 instead of expected $\eta = hf/kT = 50$ as it is predicted in theory for bolometric response [39], contrary to the photon counter limit with $\eta = 1$. In the case of our suspended bolometer with current response as in Fig. 17 of 0.7 nA at the incident power of 0.06 pW, the current responsivity is $1.1 \times 10^4$ A/W. Such current of 0.7 nA corresponds to $4.3 \times 10^9$ electrons per second and radiation power 0.06 pW at 350 GHz corresponds to $2.8 \times 10^8$ photons per second. As a result, we have quantum efficiency over 15 electrons per photon. This is direct proof of our initial design idea to disconnect absorber from direct contact to substrate for improving of thermal insulation and increasing of bolometer response.

The important feature of our suspended bolometer is similar shape of IV curve and dynamic resistance to thermal and optical heating (see Fig. 18). This is clear proving that in such bolometers, we can obtain thermalization of radiation heated electrons, which in turn provide better quantum efficiency. In conventional bolometers with absorber on substrate, we observed nonthermal optical response [27], see also Fig. 5, that is reflection of nonequilibrium energy distribution that is different from Fermi distribution. By means of suspending absorber disconnected from substrate, we managed better thermalization of energy in the electron system, and as a result, obtained higher quantum gain.

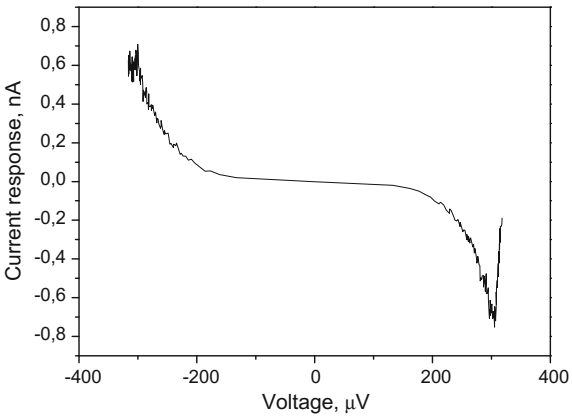


**Fig. 17** Current response of suspended bolometer 0.7 nA corresponding to quantum efficiency over 15 electrons per single photon at 350 GHz

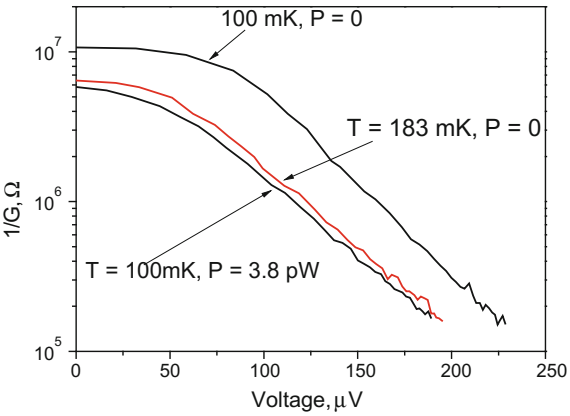


**Fig. 18** Dynamic resistance for phonon temperatures 100 and 183 mK without radiation, and for 100 mK with 3.8 pW optical power load

## 9 Conclusion

We develop a robust and simple technology for fabricating a new type of bolometer with a suspended normal-metal (N) thin-film bridges between superconducting (S) aluminum electrodes with tunnel barriers (I) forming a SINIS structure. The bridges represent effective bolometer absorbers with reduced heat losses to substrates. Such SINIS bolometers integrated with planar antennas are intended for operation in the THz-range of radiation. Samples with different absorber materials like Pd, Cr, and Cu were fabricated, and current–voltage characteristics were measured at 50–350 mK bath temperatures. NIS junctions with Al superconductor and suspended Cu absorbers demonstrate low leakage at zero bias and a high subgap resistance that makes them competitive to conventional SINIS detectors with absorber directly placed on Si substrate. The electrical responsivity of over $10^9$ V/W was measured by heating the absorber through additional contacts. Optical response of such bolometers measured at 300 GHz and 100 mK bath temperature was over $3 \times 10^8$ V/W. Current responsivity of $1.1 \times 10^4$ A/W and quantum efficiency over 15 electrons per 350 GHz photon was measured in such samples. Dependence of subgap resistance on in-plane magnetic fields up to 30 mT shows zero-bias conductivity minimum which could be explained by Andreev reflections in such structures. Contrary to that in the normal magnetic field, the zero-bias conductivity increase due to Abrikosov vortices in Al thin film that is a type 2 superconductor in the case of thin film. We investigated the influence of a normal-metal trap on the performance of NIS junction and came to the conclusion that such trap does not bring significant cooling for S electrode but suppress superconducting gap in close region of NIS junction. Improvement in S cooling can be achieved by diluting hot quasiparticles in a big volume of superconducting electrodes and by means of large area normal-metal trap and sink made of high transparency NIS junctions.

**Acknowledgements** This work was partially supported by Swedish National Space Board, Swedish Institute, Ministry of Sciences and Education of Russia, Russian Foundation for Basic Research, Russian Science Foundation.

## References

1. D. Golubev, L. Kuzmin, J. Appl. Phys. **89**, 6464 (2001)
2. R.C. Dynes, V. Narayanamurti, J.P. Garno, Phys. Rev. Lett. **41**(2), 1509 (1978)
3. J. Gildemeister, A. Lee, P. Richards, Appl. Phys. Lett. **74**(6), 868–870 (1999)
4. L. Kuzmin, D. Chouvaev, M. Tarasov, P. Sundquist, M. Willander, T. Claeson, IEEE Trans. Appl. Supercond. **9**(2), 3186 (1999)
5. M. Tarasov, V. Edelman, A. Ermakov, S. Mahashabde, L. Kuzmin, IEEE Trans. Terahertz Sci. Technol. **5**(1), 44 (2015)
6. M. Tarasov, L. Kuzmin, N. Kaurova, Instrum. Exp. Techn. **52**(6), 877 (2009)
7. P. Koppinen, I. Maasilta, Phys. Rev. Lett. **102**, 165502 (2009)
8. J. Muhonen, A. Niskanen, M. Meschke, Yu. Pashkin, J.S. Tsai, L. Sainiemi, S. Franssila, J. Pekola, Appl. Phys. Lett. **94**, 0731101 (2009)
9. G. Paraonau, A. Halvari, Appl. Phys. Lett. **86**, 093101 (2005)
10. T. Li, Yu. Pashkin, O. Astafiev, Y. Nakamura, J. Tsai, H. Im, Appl. Phys. Lett. **91**, 033107 (2007)
11. H. Nguyen, L. Pascal, Z. Peng, O. Buisson, B. Gilles, C. Winkelmann, Appl. Phys. Lett. **100**, 252602 (2012)
12. A. Timofeev, P. Helisto, L. Gronberg, A. Luukanen, H. Seppa, J. Hassel, Open Appl. Phys. J. **5**, 34–40 (2012)
13. M. Tarasov, V. Edelman, M. Fominsky, R. Yusupov, A. Yurgens, J. Radioelectron. **1**, 1 (2016)
14. A.V. Seliverstov, M.A. Tarasov, V.S. Edel'man, JETP Lett. **103**(7), 484 (2016)
15. L. Kuzmin, Physica B **284–288**, 2129 (2000)
16. L. Kuzmin, J. Phys: Conf. Ser. **97**, 012310 (2008)
17. I. Devyatov, M. Kupriyanov, JETPh Lett. **80**(10), 752–757 (2004)
18. I. Devyatov, P. Krutitsky, M. Kupriyanov, JETPh Lett. **84**(2), 61 (2006)
19. A. Semenov, I. Devyatov, M. Kupriyanov, JETPh Lett **88**(7), 514 (2008)
20. P. Virtanen, T.T. Hekkila, F.S. Bergeret, J.C. Cuevas, Phys. Rev. Lett. **104**, 247003 (2010)
21. M. Tarasov, V. Edelman, M. Fominsky, JETPh Lett. **92**(6), 460 (2010)
22. M. Tarasov, V. Edelman, L. Kuzmin, P. de Bernardis, S. Mahashabde, IEEE Trans. Appl. Supercond. **21**(6), 3635 (2011)
23. M.A. Tarasov, L.S. Kuz'min, N.S. Kaurova, Instrum. Exp. Technol. **52**(6), 877 (2009)
24. V. Edelman, G. Yakopov, Instrum. Exp. Technol. **56**(5), 613 (2013)
25. M.A. Tarasov, V.D. Gromov, G.D. Bogomolov, E.A. Otto, L.S. Kuzmin, Instrum. Exp. Technol. **52**(1), 74 (2009)
26. G. O'Neil, Improving NIS tunnel junction refrigerators: modelling, materials, and traps, Ph.D. Thesis, Univ. Colorado (2011)
27. M. Tarasov, V. Edelman, S. Mahashabde, L. Kuzmin, JETPh **119**(1), 107 (2014)
28. J.N. Ullom, P.A. Fisher, Phys. B **284**, 2036 (2000)
29. G.C. O'Neil, P.J. Lowell, J.M. Underwood, J.N. Ullom, Phys. Rev. B **85**, 134504 (2012)
30. M. Tarasov, L. Kuzmin, M. Fominsky, I. Agulo, A. Kalabukhov, JETP Lett. **78**(11), 714 (2003)
31. L. Kuzmin, I. Agulo, M. Fominsky, A. Savin, M. Tarasov, Supercond. Sci. Technol. **17**, S400–S405 (2004)
32. F.W.J. Hekking, Yu.V. Nazarov, Phys. Rev. B **49**, 6847 (1994)
33. S. Rajauria, P. Gandit, T. Fournier, F.W.J. Hekking, B. Pannetier, H. Courtois, Phys. Rev. Lett. **100**, 207002 (2008)

34. E. Otto, M. Tarasov, G. Petterson, D. Gustavsson, L. Kuzmin, Supercond. Sci. Technol. **20**, 1155 (2007)
35. J. Pekola, D. Anghel, T. Suppula, Appl. Phys. Lett. **76**(19), 2782 (2000)
36. J. Ullom, P. Fisher, M. Nahum, Nucl. Instr.and Methods in Phys. Res. **A 370**, 98 (1996)
37. H.Q. Nguyen, T. Aref, V.J. Kauppila, New J. Phys. **15**, 085013 (2013)
38. A.F. Andreev, Sov. Phys. JETP **19**(5), 1228 (1964)
39. I.A. Devyatov, M.Yu. Kupriyanov, JETP Lett. **80**(10), 646 (2004)

# Multichroic Polarization Sensitive Planar Antennas with Resonant Cold-Electron Bolometers for Cosmology Experiments


**L. S. Kuzmin and A. V. Chiginev**

**Abstract** Two types of planar multichroic antennas are reviewed. Frequency and beam characteristics of the antennas are calculated numerically. Both antennas are shown to have characteristics satisfying the ESA requirements.

## 1 Introduction. ESA Requirements

The origin of the Universe and the physics of its early moments is one of the major questions facing the modern science. Recently, a considerable progress in studying of Cosmic microwave background (CMB) has been made, and on its basis parameters of inflationary model of expansion of the Universe can be measured with an accuracy of several percent. Though, such fundamental questions as the nature of the dark matter and dark energy comprising 96% of Universe energy density, remain still open. The mechanisms which caused inflation also remain still misunderstood. Future observations of CMB could clarify all these issues, confirm, or disprove inflationary model of expansion of the Universe. Tools with an unprecedented accuracy and efficiency are necessary for the answer to these questions.

The American experiment, Background Imaging of Cosmic Extragalactic Polarization (BICEP2) has recently announced the detection of gravitational waves [1]. Formed in the early times of the Universe, gravitational waves had to leave their traces in the form of vortex B-mode polarization of the CMB according with the present

L. S. Kuzmin · A. V. Chiginev
Nizhny Novgorod State Technical University n.a. R.E. Alekseev, 603950 Nizhny Novgorod, Russian Federation

L. S. Kuzmin
Chalmers University of Technology, 41296 Gothenburg, Sweden
e-mail: leonid.kuzmin@chalmers.se

A. V. Chiginev (✉)
Institute for Physics of Microstructures, Russian Academy of Science (RAS), 603087 Nizhny Novgorod, Russian Federation
e-mail: chig@ipmras.ru



A. Sidorenko (ed.), *Functional Nanostructures and Metamaterials for Superconducting Spintronics*, NanoScience and Technology,
https://doi.org/10.1007/978-3-319-90481-8_6

theoretical models. The observation of B-mode was performed by a phased array of slot antennas. These results, however, contradict with Planck's dust measurements [2] and should be verified at other frequencies.

The measurement of the CMB polarization is a part of the ambitious COSMIC VISION 2015–2025 program of the European Space Agency (ESA). The COrE + and SPICA space missions are under consideration by ESA. The important goal for the ESA is to reduce size of the focal plane by arrangement of the multi-frequency detector array for simultaneous data acquisition [3]. This approach would reduce the aberration and improve uniformity of the beam pattern across the total focal plane.

In this review, we consider two kinds of antennas which can be used as multichroic ones. These are the seashell antenna and the cross-slot antenna. In addition to being able to operate as multichroic antennas, they also have polarization resolution needed for COrE mission. We perform numerical simulations of both antennas and obtain their beam parameters and frequency characteristics. At the end of the review, we compare the characteristics of these antennas.

## 2 Seashell Antenna

An example of the multichroic systems is a novel "Seashell" slot antenna [4, 5] (Fig. 1). This name of the antenna has been chosen due to the likeness of round loops of slots for different frequencies with a seashell. The seashell antenna has several main advantages compared to other concepts of multichroic antennas: sinuous antenna [6, 7] and cross-slot antenna [8–10] (see below). The main advantage of the seashell antenna in comparison with sinuous and cross-slot antennas is that it provides the opportunity for independent tuning of separate slots for each frequency. It is also quite compact and can be easily extended to a larger number of frequency channels by addition of proper slots. Moreover, this extension will not enlarge of the entire system because all new smaller slots will be placed inside larger slots.

The radiation patterns of the seashell antenna for 75 and 105 GHz channels are shown in Fig. 2. The beam has angular width of 26.5 and 16.8° at 75 and 105 GHz, respectively. The values of ellipticity of the beam at 75 and 105 GHz (defined as $(W_{\max} - W_{\min})/(W_{\max} + W_{\min})$) are approximately 3.5 and 4.7%. This fits the COrE requirements. The cross-polarization components are also good: −22 dB at 75 GHz and −35 dB at 105 GHz. The levels of side lobes are −15.5 dB at 75 GHz and −15.4 dB at 105 GHz. Thus, the beam characteristics of the seashell antenna with lens are good.

Frequency characteristics of the antenna have been calculated with parameters which are realistic for CEB: capacitance of the tunnel junction is 200 fF and absorber resistance is 20 Ω. It is seen that the frequency characteristics have resonant character (Fig. 3a). However, the non-resonant absorption appears due to Ohmic losses in metal, as it is seen on the S-parameter for 105 GHz slots. That is why the estimation of the FWHM of the resonances by usual way meets certain difficulties.

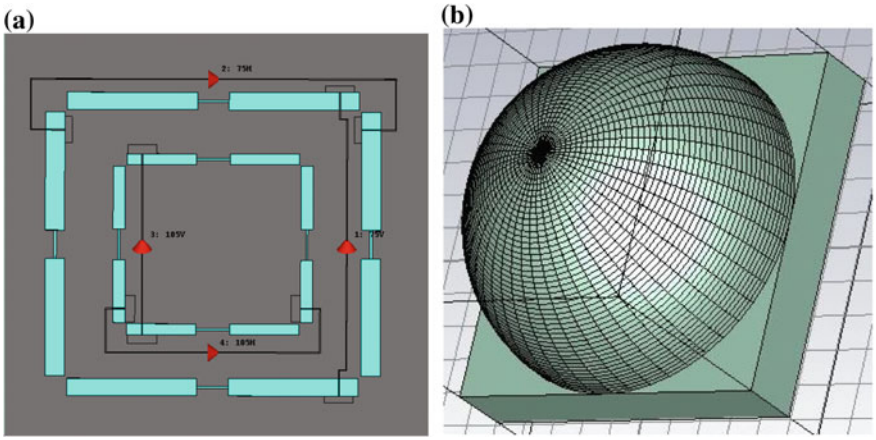


**Fig. 1** **a** A view of the seashell antenna. Slots are shown by blue. Ports for excitation are located in CEB places; **b** a view of the lens and Si substrate

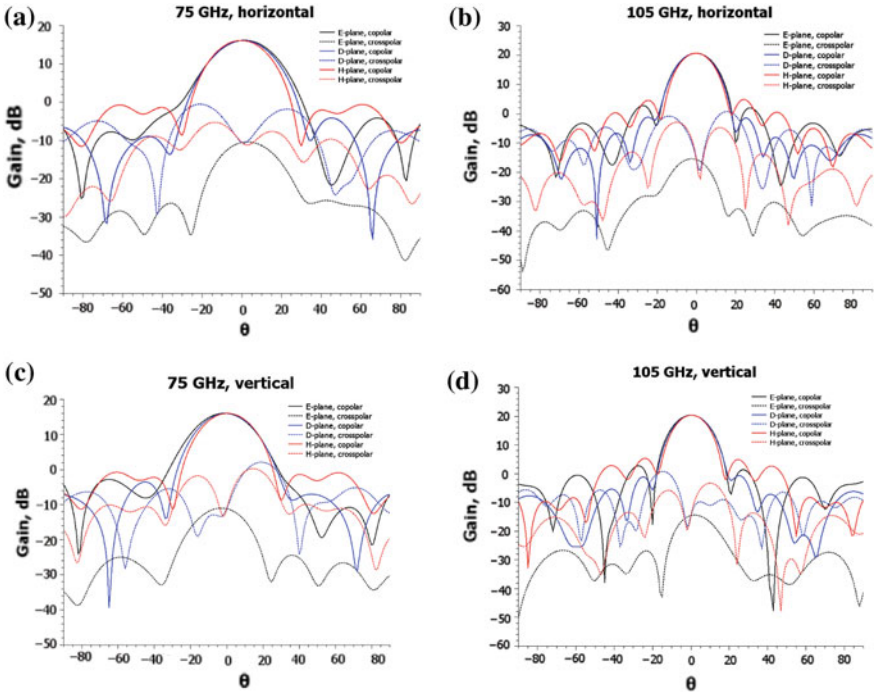


**Fig. 2** Radiation patterns for horizontal (**a**, **b**) and vertical (**c**, **d**) polarization, at 75 GHz (**a**, **c**) and 105 GHz (**b**, **d**)

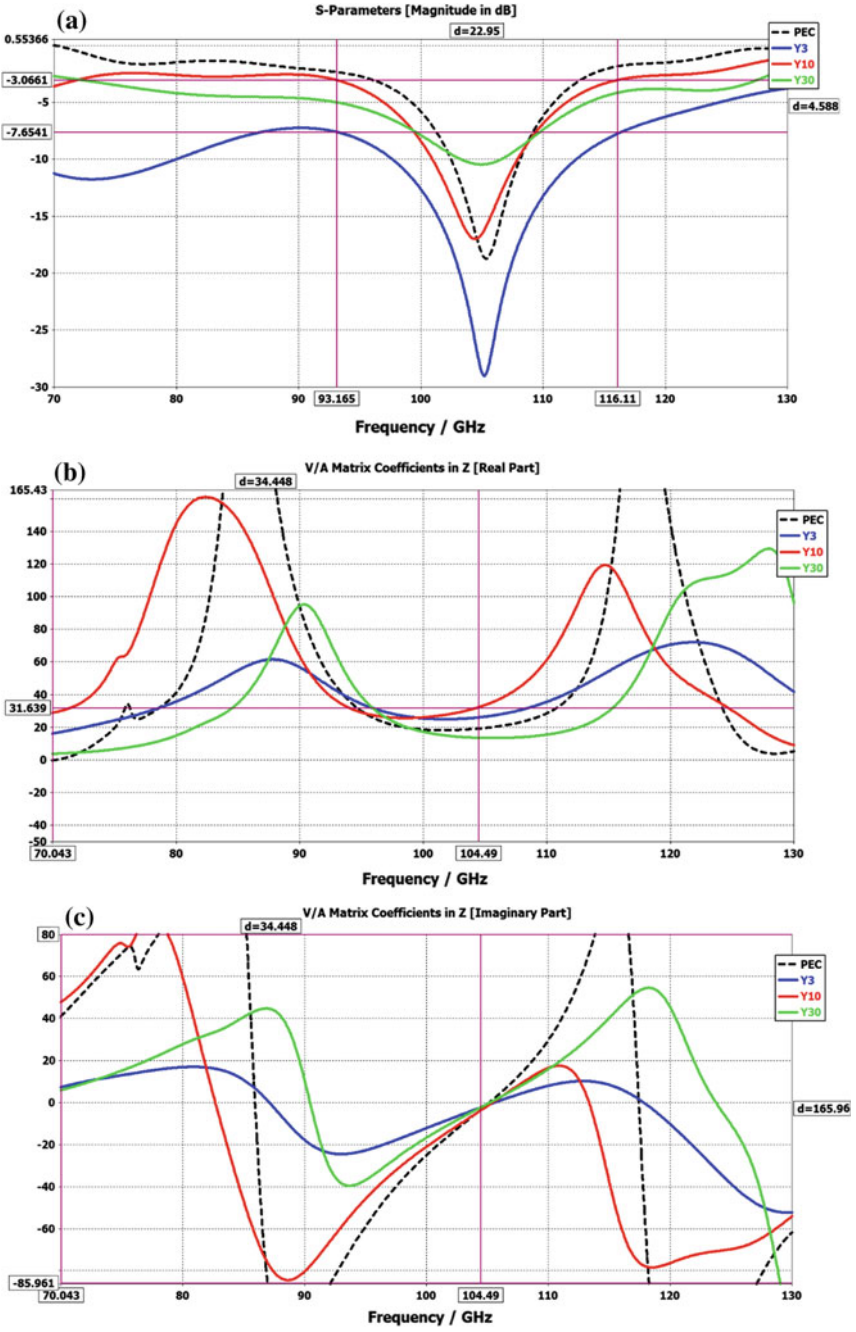


**Fig. 3** Influence of Ohmic losses on resonance structure. **a** S-parameters; **b** ReZ; **c** ImZ plotted at various σ. *Y*3: $\sigma = 1.5 \times 10^8\ \Omega^{-1}\ \mathrm{m}^{-1}$, *Y*10: $\sigma = 4.5 \times 10^8\ \Omega^{-1}\ \mathrm{m}^{-1}$, *Y*30: $\sigma = 1.5 \times 10^9\ \Omega^{-1}\ \mathrm{m}^{-1}$

The influence of losses in metal on resonance structure is illustrated in Fig. 3. It is seen that the resonances of ReZ and ImZ are less sharp at lower σ (Fig. 3b, c). At the same time, the frequency of the serial resonance is almost unchanged (Fig. 3c). On the other hand, ReZ increases near serial resonance with σ decrease and becomes closer to the port impedance 25 Ω (Fig. 3b). Thus, S-parameter has sharper resonance at lower σ, and another smooth resonance at a lower frequency appears.

Figure 4 illustrates the influence of CEB capacitance to S-parameters of the antenna. With capacitance decrease, the resonance shifts to a higher frequency and its width decreases. Also, the decrease in CEB capacitance results in appearance of another resonance at lower frequencies (Fig. 4a). The latter can be explained by addition of the impedance of the capacitor $Z_C = 1/i\omega C$ to the antenna impedance, which unavoidably lowers the ImZ curve at lower frequencies (Fig. 4c). It leads to appearance of another serial resonance to the left of the main parallel resonance. The frequency of this serial resonance depends on C and shifts to the right at lower C.

We noted here that in this consideration we do not include the modeling of the seashell antenna with RCEB, as we do with the cross-slot antenna (see below). This is mainly due to the fact that seashell antenna provides good frequency characteristics without any additional resonant circuit. However, it is also possible, if one wants to correct the frequency characteristics given by bare electrodynamics.

## 3 Cross-Slot Antenna

Another example of the multichroic antenna which can be used as part of the receiving system for COrE project is the cross-slot antenna (Fig. 5). Initially, the antenna of this kind was used as a single-frequency one [9, 10]. The main advantage of the cross-slot antenna in comparison with the seashell antenna is its more simple design. This antenna consists of four perpendicular slots, which cross each other at a distance of a quarter slot length from the end of the slot. Using microstrip lines, the signal from the opposite slots is applied to RCEBs, each tuned to its own resonant frequency. RCEBs are connected into gaps of microstrip lines. This connection provides an in-phase operation of the opposite slots, and hence the formation of the desired radiation pattern. The dielectric layer separating the ground plane from microstrip line is made from silicon. At the ends of the microstrip lines facing the antenna slots, shorting capacities are located. By the adjustment of these capacities, one can obtain desired frequency characteristics of the antenna. A lens with anti-reflective coating, located at the other side of the substrate, is responsible for beam formation (Fig. 5b).

We start with the description of the antenna with microstrip lines acting as waveguides. However, it is possible to use other kinds of waveguides, such as coplanar lines.

For numerical simulation, we use software package CST Microwave Studio. The calculations were performed in time domain. For excitations of slots, we use two ports located at RCEBs' places. The parameters of the antenna are selected so as to provide acceptable antenna characteristics in the two frequency bands required for

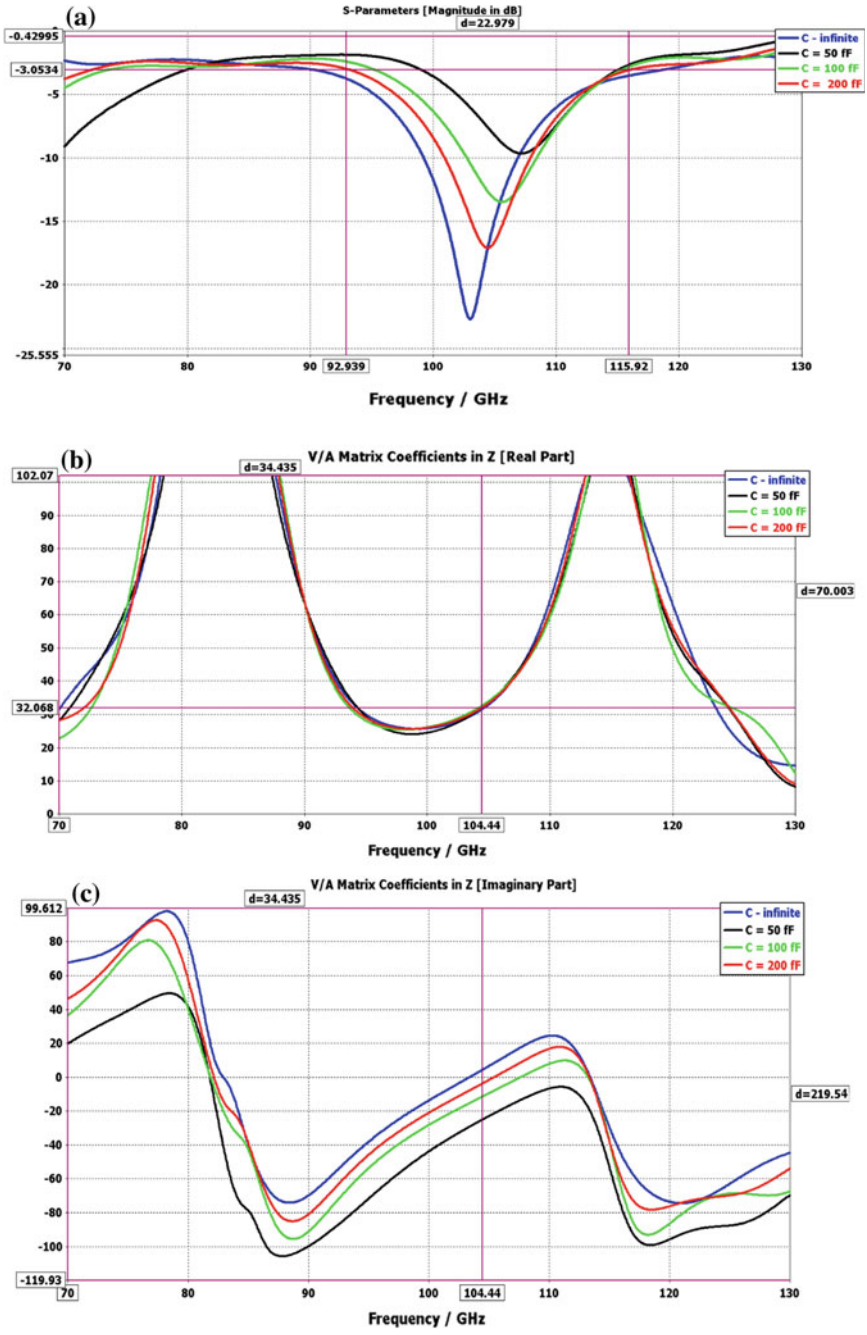


**Fig. 4** Effect of CEB capacitance on resonance characteristics. **a** S-parameter; **b** ReZ; **c** ImZ

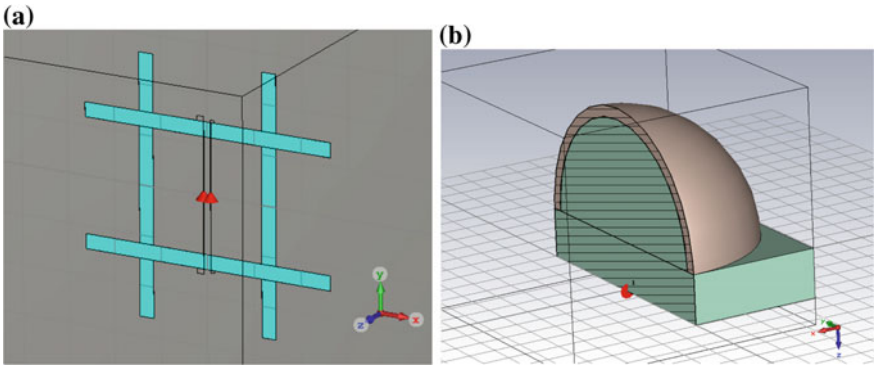


**Fig. 5** **a** A view of the cross-slot antenna. Slots are shown in blue; **b** a cross-cut of the lens and Si substrate

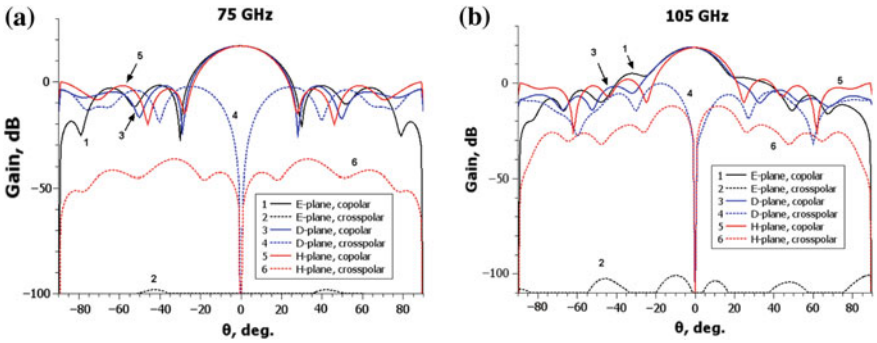


**Fig. 6** Radiation patterns of the cross-slot antenna at 75 GHz (**a**) and 105 GHz (**b**). Solid curves show the diagrams for main component of the field and dashed curves—the diagrams for cross-polar components. A Ludwig-3 basis [11] is used. Different cross-sections of the radiation diagrams are marked by different colors

COrE project—75 and 105 GHz. For simplicity, we restrict ourselves to consideration of one of the two polarizations of the antenna beam.

The radiation diagrams of the antenna are shown in Fig. 6.

Figure 6 shows that the cross-slot antenna has satisfactory characteristics of the radiation pattern. In particular, it should be noted that the presented antenna has a high resolution in polarization within the beam angular width, −3 dB power limited by a maximum (half-power). The characteristics of the antenna pattern are given in Table 1.

Figure 7 shows the frequency characteristics of the cross-slot antenna. They are calculated by connecting the ports with an impedance of 20 Ω into breaks of the strip lines connecting opposing slots (Fig. 7a). The characteristics have a resonant character, and the corresponding frequency resonances are close to the frequencies required for the project COrE-75 and 105 GHz (Fig. 7a). The real part of the antenna

**Table 1** Characteristics of the dual-frequency receiving systems

| | ESA requirements | Seashell antenna | | Cross-slot antenna | |
|---|---|---|---|---|---|
| | | 75 GHz channel | 105 GHz channel | 75 GHz channel | 105 GHz channel |
| Bandwidth at −3 dB, GHz | 20% of resonance frequency | 18.8 (H)<br>15.4 (V) | 19.3 (H)<br>22.3 (V) | 14.9 | 19.0 |
| Beam width, ° | 20 | 26.5 | 16.8 | 24.3 | 19.5 |
| Beam ellipticity, % | <5 | 3.5 (H)<br>2.7 (V) | 4.3 (H)<br>4.7 (V) | 4.2 | 0.3 |
| Polarization resolution, dB | 30 | −34.5 (H)<br>−28.6 (V) | −41.5 (H)<br>41.3 (V) | 23.4 | 29.6 |

impedance of 3.5 Ω for channel 75 GHz and 34 Ω to 105 GHz channel (Fig. 7b) However, as we will see below, this antenna provides good matching with the RCEB and gives the necessary resonance characteristics of the receiving system. From Fig. 7b, it is seen that the width of the resonance curves exceeds the values specified by the requirements of the ESA. Therefore, to obtain the desired width of the resonance curve we proposed to use the resonance properties of the RCEB.

For modeling of the RCEB, we used a series oscillatory circuit (Fig. 8a). Two of the oscillatory circuits tuned to frequencies close to, respectively, 75 and 105 GHz are connected to the ports. As a result of the calculation, we obtained the frequency characteristics of the antenna with RCEB (Fig. 8b). The calculations used the following parameters of discrete elements: inductances L75 = 130 pH, L105 = 120 pH, capacitances C75 = 41 fF, C105 = 18.5 fF. Active resistances of both circuits are equal to 15 Ω, which corresponds to the resistance of the RCEB absorber. Resonant frequencies of the oscillatory circuits are, respectively, 68.9 GHz and 106.8 GHz. The shifts of the resonance frequency of the circuits are due to the fact that in order to obtain the desired outcome of the resonant frequency of the complete system one has to compensate the imaginary part of the respective components of the impedance matrix at the resonant frequencies (Fig. 8b).

From Fig. 8b, it is seen that the frequency characteristics of the receiving system based on the cross-slot antenna are of the form of the resonant curves with frequencies corresponding to ones required by ESA-75 and 105 GHz. The linewidth of these resonances is 14.9 and 19.0 GHz in 75 and 105 GHz channels, respectively. These values are quite good for COrE. It also seen that the mutual influence of the two frequency channels is limited to the level of −10 dB.

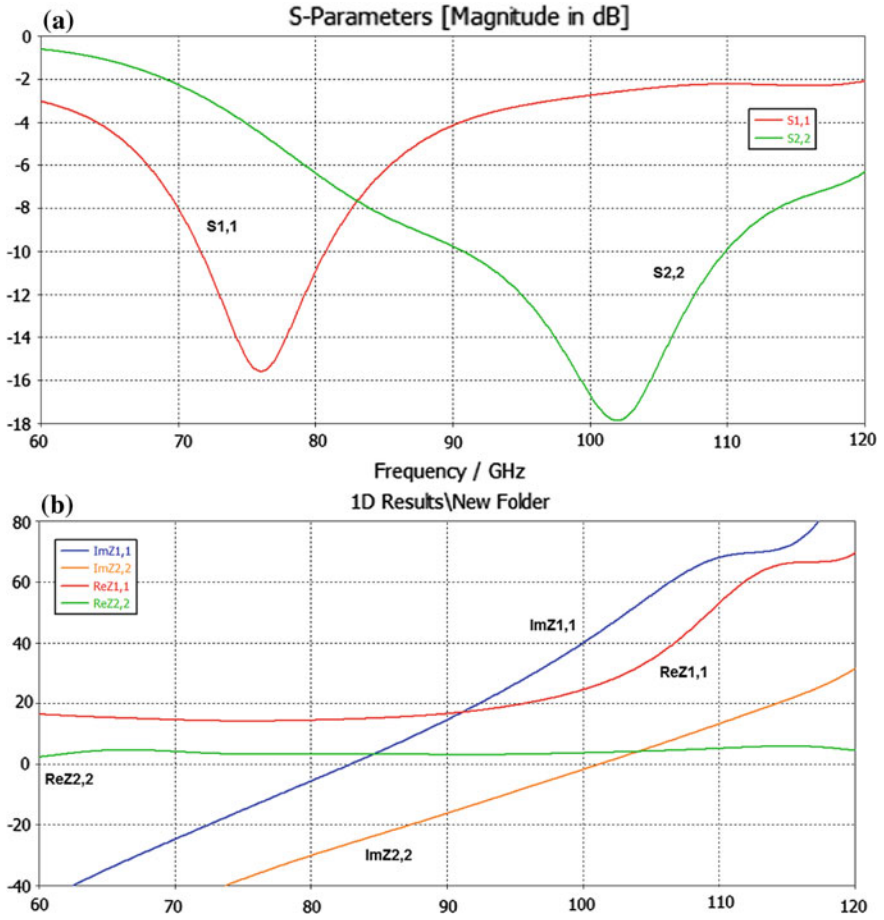


**Fig. 7** Frequency characteristics of the cross-slot antenna. **a** S-parameters, **b** Re and Im parts of the antenna impedances

## 4 Comparison and Discussion

The characteristics of the dual channel receiving system based on the seashell antenna and cross-slot antenna with RCEBs are given in Table 1. The indices H and V near some characteristics denote the relation to horizontal and vertical polarization, respectively.

Table 1 shows that the dual-frequency receiver system based on seashell and cross-slot antennas has good radiation pattern parameters and frequency characteristics, generally satisfying ESA requirements for the multi-frequency receiver systems intended for COrE project. Each system, both seashell and cross-slot antennas, has its own pros and contras. The seashell antenna has the following advantages—(a) each

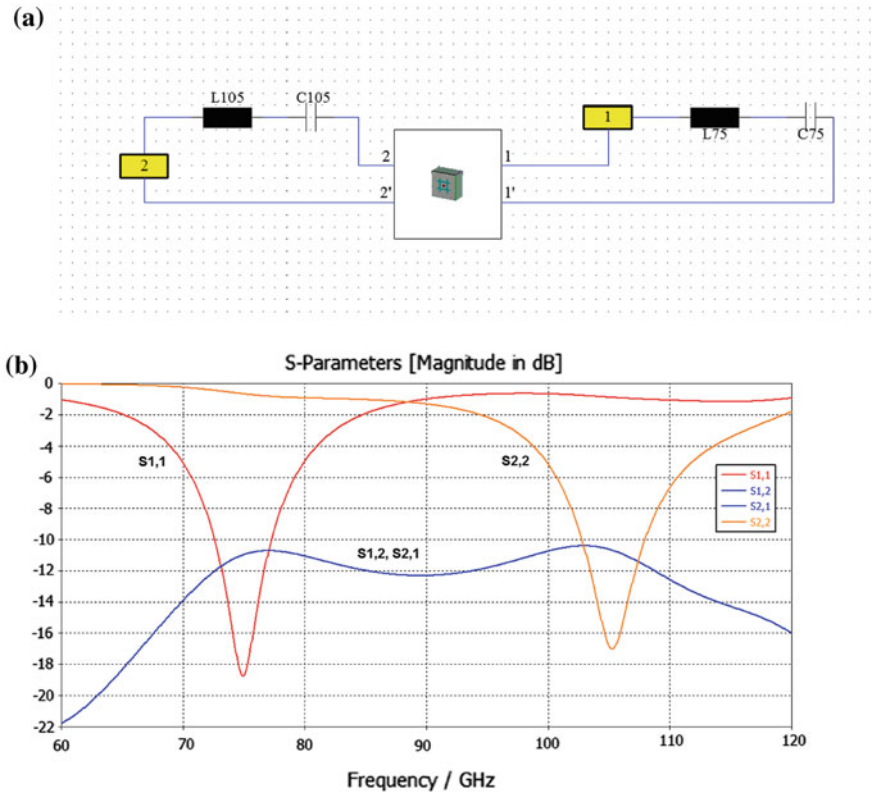


**Fig. 8** **a** Equivalent circuit of the cross-slot antenna with RCEBs; **b** S-parameters of the cross-slot antenna with serial oscillatory circuits which model RCEBs

channel can be tuned separately, (b) the number of channels can be easily increased. The cross-slot antenna has more simple design and is numerically proved to work properly as a dual-frequency antenna.

The work is supported by the Russian Science Foundation (Project 16-19-10468).

## References

1. BICEP2 collaboration, Phys. Rev. Lett. **112**, 2014101, arXiv:1403.3985 [astro-ph] (2014)
2. Planck and BICEP2/Keck collaboration, Phys. Rev. Lett. **114**, 10, 101301, arXiv:1502.00612 [astro-ph] (2015)
3. The ESA Tender ESTEC ITT AO/1-7256/ Next Generation Sub-millimetre Wave Focal Plane Array Coupling Concepts, February 2013
4. L.S. Kuzmin, A.V. Chiginev, E.A. Matrozova, A.S. Sobolev, Multifrequency Seashell slot antenna with cold-electron Bolometers for cosmology space missions. IEEE Trans. Appl. Supercond. **26**(3), 1–6 (2016)

5. L.S. Kuzmin, A.V. Chiginev, *Proceedings of SPIE - Millimeter, Submillimeter, and Far-Infrared Detectors and Instrumentation for Astronomy*, vol. VIII, ed. by W.S. Holland, J. Zmuidzinas, Proceedings of SPIE, vol. 9914, 99141U (2016). https://doi.org/10.1117/12.2232895
6. R.H. DuHamel. Dual polarized sinuous antennas. U.S. Patent 4658262, 1987
7. R. O'Brient et al., A dual-polarized broadband planar antenna and channelizing filter bank for millimeter wavelengths. Appl. Phys. Lett. **102**, 063506 (2013)
8. L.S. Kuzmin, A resonant Cold-Electron Bolometer with a kinetic inductance nanofilter. IEEE Trans. Terahertz Sci. Technol. **4**, 314–320 (2014)
9. G. Chattopadhyay, J. Zmuidzinas, A dual polarized slot antenna for millimeter waves. IEEE Trans. Antennas Propag. **46**(5), 736–737 (1998). https://doi.org/10.1109/8.668920
10. G. Chattopadhyay, D. Miller, H.G. LeDuc, J. Zmuidzinas, IEEE Trans. Microwave Theory Technol. **48**, 1680 (2000)
11. A.C. Ludwig, The definition of cross polarization. IEEE Trans. Antennas Propag. **21**(1), 116−119 (1973). https://doi.org/10.1109/TAP.1973.1140406

# Passive Millimeter-Wave Imaging Technology for Concealed Contraband Detection


**Jing-Hui Qiu, Jiaran Qi, Nan-nan Wang and Aleksandr Denisov**

**Abstract** In this chapter, we firstly introduce the fundamental radiation detection theory of the passive millimeter-wave imaging technique for human-body security inspections. A radiation temperature transfer model for the passive millimeter-wave near-field imaging is then proposed. The method to analyze the temperature contrast between the human body and the concealed objects under indoor and outdoor environments is presented accordingly. Furthermore, several key technologies involved in the passive millimeter-wave imaging systems are discussed in detail, including the millimeter-wave radiometer, the millimeter-wave feed antenna, the focusing antenna, and the quasi-optical theory. Finally, a prototype of a Ka-band passive millimeter-wave imaging system based on the focal plane array is manufactured. The system design process and the measurement results for some typical scenarios are elucidated.

## 1 Introduction

Objects in nature radiate electromagnetic waves of different spectra. Among them, the frequency band spanning from 30 to 300 GHz is usually referred to as extremely high frequency, with the corresponding wavelength varying from 1 cm to 1 mm, known as millimeter-wave. The millimeter-wave band lies between the infrared band and the microwave band, and hence has together their characteristics. Compared with the microwave frequency band, the millimeter-wave has shorter wavelength, indicating that a higher angular resolution can be obtained by the antenna of the same size. Meanwhile, the spectrum resources are very rich benefiting from the extremely wide frequency band. Compared with the infrared and visible light, millimeter-wave imaging system has a relatively low spatial resolution, but it can penetrate fog, cloud,

J.-H. Qiu · J. Qi (✉) · N. Wang · A. Denisov (✉)
Department of Microwave Engineering, School of Electronics and Information Engineering, Harbin Institute of Technology, Harbin 150001, China
e-mail: qi.jiaran@hit.edu.cn

A. Denisov
e-mail: denisov@qq.com



A. Sidorenko (ed.), *Functional Nanostructures and Metamaterials for Superconducting Spintronics*, NanoScience and Technology,
https://doi.org/10.1007/978-3-319-90481-8_7

and dust at atmospheric windows including 35, 94, 140, and 220 GHz. This property enables millimeter-wave imaging systems to operate in harsh weather conditions, which is of great significance in applications such as remote sensing, navigation, satellite communications, and military applications. Besides, millimeter-wave has the ability to penetrate the fabric, which makes it the most appealing technology in the airport security control, and other anti-terrorism applications [1, 2].

In recent years, terrorism has become increasingly rampant and security issues are receiving accordingly more and more attentions. The reliability and intelligence of the security system become very demanding. Currently, traditional security control devices applied in airports can only detect metallic objects in proximity to the human body and cannot locate the non-metallic objects. Although the X-ray backscatter human scanners can detect concealed objects of different material properties under the human clothing, its radiation is harmful to the human body, and it is thus not suitable for the general security check applications. Infrared imaging system based on the detection of surface temperature cannot achieve useful images when the targets are covered by the fabric. The millimeter-wave imaging system can, however, detect hazardous article concealed under the human clothing, including metal objects, plastic pistols, and explosives. The detected information by the millimeter-wave imaging system is more detailed and accurate and will greatly reduce the false alarm rate. Moreover, the passive millimeter-wave imaging technology is completely radiation-free, which promises it broad application prospects [3].

## 2 Theory of Passive Millimeter-Wave Imaging

All the media (such as gas, liquid, solid, and plasma) radiate electromagnetic energy, while the liquid and solid have continuous radiation spectra, which means that they radiate electromagnetic energy in the whole frequency band. The main principle of the passive millimeter-wave imaging technique is to receive the electromagnetic radiation of the target and background passively using the radiometer array, whose output voltage values are applied to measure the difference of the brightness temperatures and accordingly to produce the millimeter-wave image of the target and the background. The temperature sensitivity, in other words, the minimum temperature difference that can be detected, is one of the most important technical requirements of the passive millimeter-wave focal-plane-array imaging system. Many factors have a great influence on the temperature sensitivity of the imaging system, including emissivity, transmittance and reflectivity of the material, efficiency of the feed antenna, transmission characteristics of the focusing antenna, matching of the quasi-optical path, and the performance of the radiometer. Therefore, the analysis of the brightness temperature variation from the radiation source to the radiometer input, the millimeter-wave radiation characteristics of different substances, the optimization of the various parts of the imaging system, and the method to improve the temperature sensitivity play important roles in developing the passive millimeter-wave imaging system.

In this chapter, the radiation detection principle and approximate condition of the object in the millimeter-wave band are firstly analyzed based on Planck's radiation law, and the radiation temperature transfer model of the concealed items under human clothing is thus established. Then, brightness temperature variation from the target to the radiometer is discussed, and the brightness temperature of the object is thus mathematically expressed by the power-distribution function projected to the antenna aperture and the measured power received by the antenna. Finally, the factors affecting the temperature sensitivity of the passive millimeter-wave imaging system are elucidated.

## *2.1 Planck's Radiation Law–Blackbody Radiation Detection Theory*

In general, when electromagnetic waves are radiated onto the surface of the solids (or the liquids), part of the energy is absorbed while the rest is reflected or scattered. The blackbody can be defined as the ideal opaque material that absorbs all incoming radiation at all frequencies with no reflection. Thermodynamic equilibrium conditions indicate that the blackbody is not only a complete absorber, but also a complete emitter.

In 1901, the German physicist Planck proposed a quantitative description of the blackbody radiation characteristics of Planck's law based on quantum theory. It predicts that the blackbody radiates the energy at the same spectral brightness in all directions, that is, the spectral brightness of the blackbody is non-directional, and is only a function of temperature and frequency, which characterizes the unit solid angle, unit area, unit bandwidth radiation power. The expression of this law is as follows (2.1):

$$B_f = \frac{2hf^3}{c^2}\left(\frac{1}{e^{hf/kT}-1}\right) \tag{2.1}$$

where $B_f$ is the blackbody radiation spectrum brightness, unit $\mathrm{W}\cdot\mathrm{m}^{-2}\cdot\mathrm{Sr}^{-1}\cdot\mathrm{Hz}^{-1}$, $h$ is Planck's constant, $6.63\times10^{-34}$ J s, $f$ is the frequency, unit Hz, $k$ is Boltzmann's constant, $1.38\times10^{-23}$ J $\mathrm{K}^{-1}$, T denotes the absolute temperature, unit K, and c is the speed of light.

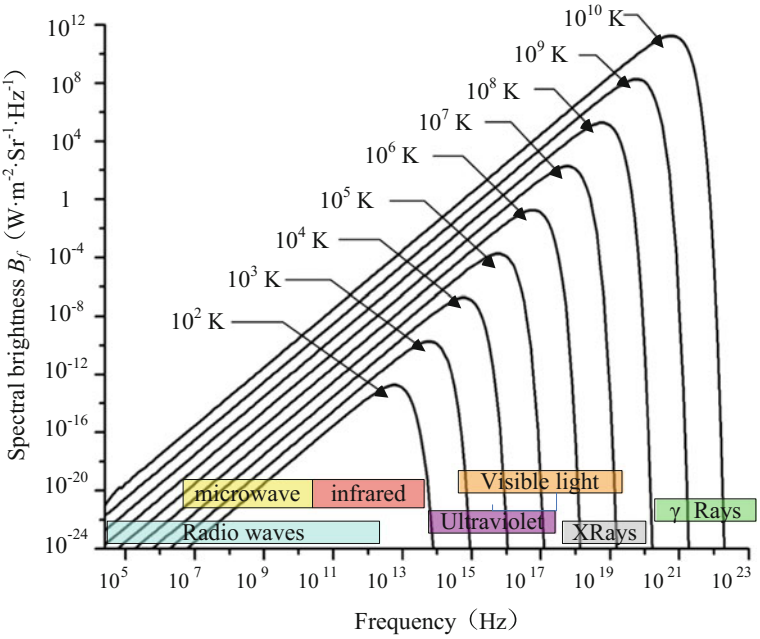


**Fig. 1** Planck's radiation law curve

In (2.1), there are only two variables $f$ and $T$. Figure 1 illustrates the variation of the Planck blackbody spectrum brightness with the frequency at different temperatures. It can be seen from the figure that the total level of the spectrum brightness increases with the increase of the temperature $T$; while the frequency at the maximum value of $B_f$ also increases with $T$. In the microwave band, as the frequency increases, the value of $B_f$ also grows.

When $hf/kT << 1$, that is, when the frequency is low enough, we have ($x << 1$)

$$e^x - 1 = (1 + x + \frac{x'}{2} + \cdots) - 1 \simeq x \tag{2.2}$$

Equation (2.1) can be reduced to

$$B_f = \frac{2f^2kT}{c^2} = \frac{2kT}{\lambda^2} \tag{2.3}$$

where λ is the wavelength.

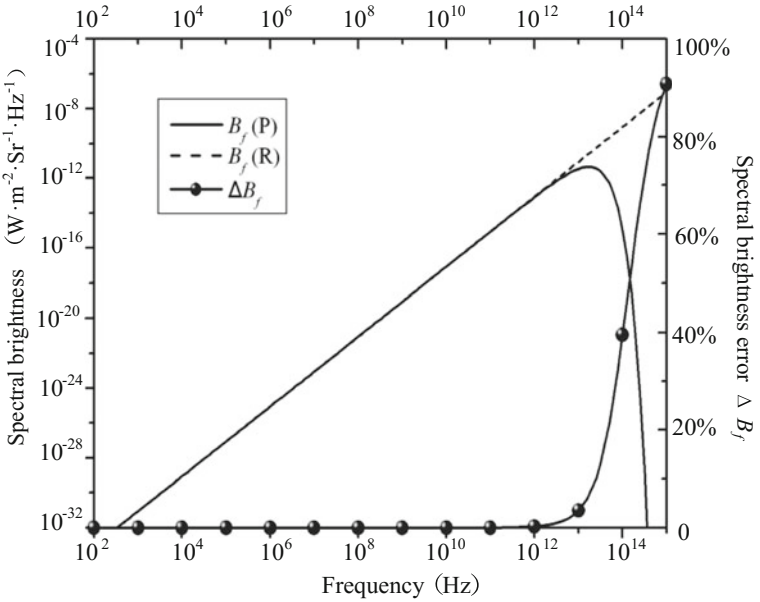


**Fig. 2** Approximate comparison of Planck's law and Rayleigh–Jeans law when T = 293 K

Equation (2.3) is called the Rayleigh–Jeans formula. In the microwave range, the Rayleigh–Jeans formula and the Planck blackbody radiation formula have little error and are simple in mathematics. If $B_f(P)$ is used to represent the spectral brightness calculated by the Planck blackbody formula, and the spectral brightness calculated by the Rayleigh–Jeans formula is expressed by $B_f(R)$, the error can thus be expressed as

$$\Delta B_f = \frac{B_f(P) - B_f(R)}{B_f(P)} \times 100\% = \left[1 - \frac{kT}{hf}\left(e^{hf/(kT)} - 1\right)\right] \times 100\% \qquad (2.4)$$

When $T$ equals the room temperature 293 K, the approximate analysis of Planck's law and Rayleigh–Jeans formula is shown in Fig. 2. It can be seen from the figure that when the frequency is less than 3 THz, the error of the two is less than 1%. In particular, when the frequency is around 35 GHz, the error is about 0.008%, and when the frequency is 94 GHz, the error is about 0.02%.

According to [1], the lossless microwave antenna is placed in an anechoic chamber maintained at a constant temperature $T$, and the total power received by the antenna is

$$P = A_r \int_f^{f+\Delta f} \iint_{4\pi} B_f(\theta, \varphi) F_n(\theta, \varphi) \mathrm{d}\Omega \, \mathrm{d}f \qquad (2.5)$$

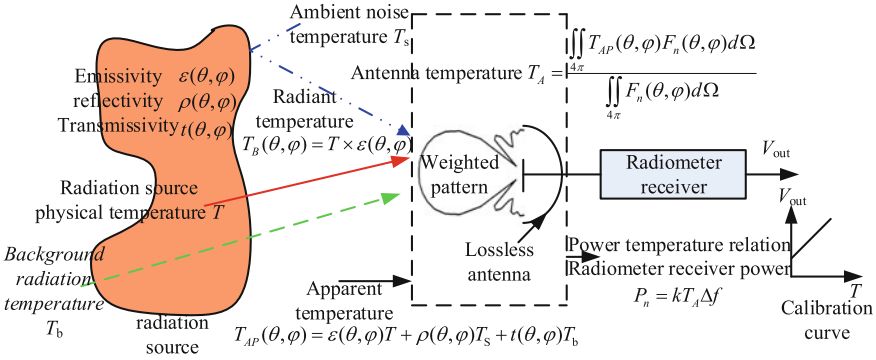


**Fig. 3** Radiation temperature transfer model

If the Rayleigh–Jeans formula is substituted into the above equation, the linear relationship between the temperature $T$ and the power $P$ can be observed in the frequency range $\Delta f$, as shown in (2.6). This result is of great importance, indicating that in some cases the temperature $T$ and the power $P$ can be equivalent [4–6].

$$P = kT\Delta f \tag{2.6}$$

## 2.2 *Radiation Temperature Transfer Model of the Passive Millimeter-Wave Near-Field Imaging*

Figure 3 shows the radiation temperature transfer model of the passive millimeter-wave near-field imaging. The relationship between the radiation source and the input power of the radiometer is mathematically determined by analyzing the relationship between physical temperature and brightness temperature of the radiation source, brightness temperature and the apparent temperature of the antenna, and the apparent temperature of the antenna and the measured radiation temperature of the antenna. Meanwhile, with the help of the radiometer calibration equation, the relationship between the radiation source and the output voltage of the radiometer is further established, which lays a theoretical foundation for the study of the contrast between concealed objects and human body.

As shown in Fig. 4, the apparent brightness temperature of human body and target mainly includes three parts: firstly, the clothing itself to the antenna radiation; secondly, the temperature of the environment after the reflection of the antenna radiation; thirdly, radiation from the bright temperature transmitted from clothing. In the third part, radiation from the bright temperature transmitted from clothing is complex, and it includes two parts, i.e., the radiation of the human body or the hidden object and the reflection from the human body on the equivalent ambient temperature. The equivalent ambient temperature includes the transmission of the

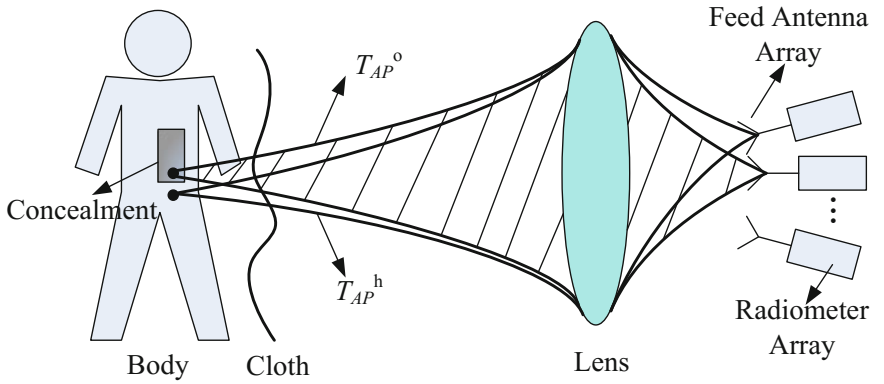


**Fig. 4** Schematic diagram of apparent brightness temperature difference between human body and concealed target

ambient temperature through the clothing, the radiation of the clothing itself, and the brightness temperature of the human body or the hidden object reflected by the clothing. According to this principle and radiation temperature transfer model of the passive millimeter-wave near-field imaging, we can calculate the brightness temperature differences between metals, non-metal concealed objects, and the human body under indoor and outdoor environments.

## 3 Millimeter-Wave Radiometer

Millimeter-wave radiometer is a kind of high-sensitivity receiver, and it measures the radiation from the objects under test in the millimeter-wave band. Nowadays, it has already been widely used in atmospheric, land, and marine remote sensing, providing an efficient method for us to sense our living environment.

### *3.1 Key Technical Parameters of Millimeter-Wave Radiometer*

The key technical parameters of millimeter-wave radiometer include temperature sensitivity, noise coefficient, bandwidth, integral time, veracity, and stability.

As aforementioned, temperature sensitivity is an important parameter to evaluate the performance of the radiometer. It matters whether the concealed objects under the human body could be detected by the imaging system.

According the literature [7, 8], the minimum detectable temperature difference is expressed as

$$\Delta T_{\min} = \sqrt{\Delta T_N^2 + \Delta T_G^2} \tag{3.1}$$

where $\Delta T_N$ is the indeterminacy caused by the system noisy temperature and $\Delta T_G$ is the indeterminacy caused by the system gain fluctuation.

In (3.1), the indeterminacy caused by the system noisy temperature is defined as

$$\Delta T_N = \frac{\alpha T_{\text{sys}}}{\sqrt{B\tau}} \tag{3.2}$$

where $T_{\text{sys}}$ is the equivalent temperature of the system, $\alpha$ represents the constant of the radiator, $B$ denotes the equivalent bandwidth of the radiator before demodulation, and $t$ is the integral time constant.

In the formula (3.1), the indeterminacy caused by the system gain fluctuation is defined as

$$\Delta T_G = T_{NE} \frac{\Delta G}{G} \tag{3.3}$$

where $\Delta G$ is the system gain fluctuation and $T_{NE}$ denotes the weighted value of the gain by the noisy temperature. The temperature sensitivity has a little difference because different kind of radiator has different radiator constants.

The direct detection radiometer belongs to full-power type of radiometer. Its temperature sensitivity mainly depends on the indeterminacy caused by the system noise temperature and the fluctuation of system gain. Equation (3.2) can be further expressed as

$$\Delta T_N = \frac{aT_{\text{sys}}}{\sqrt{B\tau}} = \frac{a(T_{AP} + T_{\text{REC}})}{\sqrt{B\tau}} \tag{3.4}$$

where $T_{\text{REC}}$ is the noisy temperature of the receiver itself, $T_{\text{REC}} = (N_f - 1)T_{sl}$, $T_{AP}$ denotes the received temperature, $N_f$ is the receiver's noisy temperature, and it equals to the specific value of input SNR and output SNR, and $T_{sl}$ denotes the environment temperature.

For the direct detection radiometer, $a = 1$. As $T_{AP}$ varies little, $N_f$ make an vital role in temperature sensitivity, and thus the important parameter are the noisy temperature $N_f$ of the receiver, the equivalent bandwidth $B$ of the radiator before demodulation, the integral time constant $t$, and the matching condition of each parts. A smaller $N_f$, a bigger the $B$, and a longer $t$ will lead to a higher temperature sensitivity.

Noisy figure $N_f$ and noisy coefficient $F$ are used to measure the system performance. The noisy coefficient $F$ is defined as the specific value of input SNR and output SNR,

$$F = \frac{SNR_i}{SNR_O} \tag{3.5}$$

The logarithmic of $F$ is defined as the noisy figure,

$$N_f(\mathrm{d}B) = 10\lg F \tag{3.6}$$

The cascaded system's noisy coefficient is (assuming the bandwidth is same)

$$F_{rn} = F_1 + \frac{F_2 - 1}{G_1} + \frac{F_3 - 1}{G_1 G_2} + \cdots \tag{3.7}$$

where $F_1$, $F_2$, and $F_3$ are the noisy coefficients of the first-, the second- and the third-order low-noise amplifiers, while $G_1$ and $G_2$ denote the gains of the first- and the second-order low-noise amplifiers.

It is obvious that the gain and the noisy figure of the first low-noisy amplifier have the most significant influence on the temperature sensitivity.

## *3.2 Millimeter-Wave Direct Detection Radiometer*

Direct detection radiometers have the advantages of small size, low power consumption, and wide operating bandwidth. We introduce in this section a Ka-band miniaturized direct detection radiometer. By optimizing the receiver structure, the radiometer is improved to have higher temperature sensitivity, better stability, and better consistency. The presented radiometer is suitable to form the receiver array of a passive millimeter-wave focal-plane-array imaging system.

The schematic diagram of the circuit of the direct detection radiometer is shown in Fig. 5. The radiometer applies the antipodal fin line at the input to achieve the waveguide-to-microstrip transition, and three cascaded low-noise amplifier (LNA MMIC) follows to achieve about 60 dB of radio frequency amplification on the input noise. After the square law detection, filtering, low-frequency amplification and integration, the radiometer finally outputs the voltage value corresponding to the brightness temperature of the target under test.

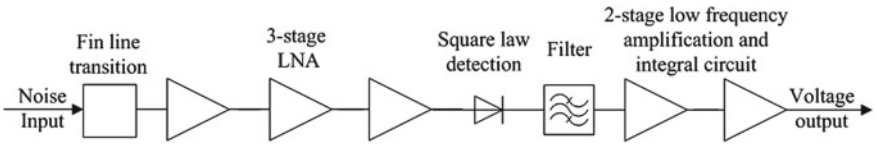


**Fig. 5** Schematic diagram of the circuit of the direct detection radiometer

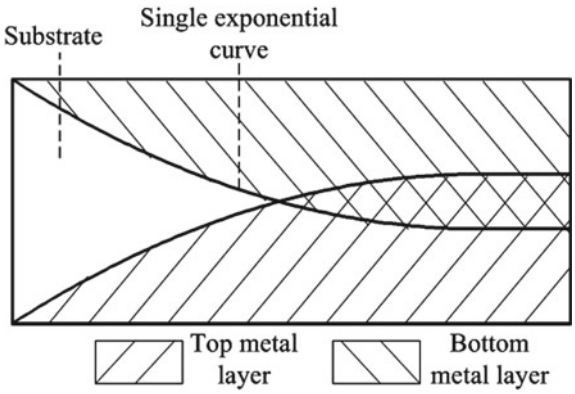


**Fig. 6** Schematic diagram of the waveguide-to-microstrip transition structure based on the antipodal fin line

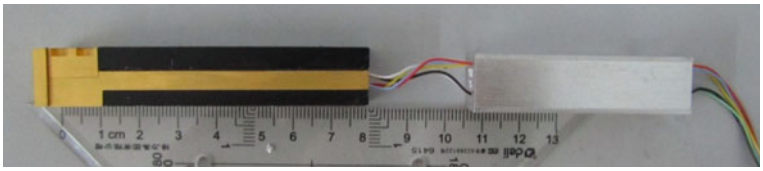

**Fig. 7** Photograph of direct detection receiver

The front end of Ka-band miniaturized direct detection radiometer applies the antipodal fin line structure to achieve the waveguide-to-microstrip transition. As shown in Fig. 6, both the top and the bottom metal coatings follow the exponential curve. The RT/Duroid5880 substrate with the relative permittivity of 2.22 and the thickness of 0.254 mm is chosen to support the structure. The total length of the waveguide-to-microstrip transition is 12 mm. The return loss and the insertion loss of the transition structure are simulated by CST Microwave Studio®. In the frequency range from 33 to 37 GHz, the return loss is less than 16 dB and the insertion loss is less than 0.12 dB. Figure 7 illustrates the appearance of the Ka-band miniaturized direct detection radiometer. The measured key specifications of the Ka-band radiometer are listed in Table 1.

**Table 1** The measured key specifications of the Ka-band radiometer

| Technical specifications | Measured values |
|---|---|
| Working frequency | 35 GHz ± 1.8 GHz |
| RF gain | 60 dB |
| Range of the detected brightness temperature | 263–333 K |
| Tangent sensitivity | −86 dBm |
| Integration time | 0.5 ms |
| Noise figure | ≤3.5 dB |
| Linearity | ≥0.999 |
| Stability (72 h) | <2 K |
| High frequency gain | 60 dB |
| Dimensions of RF front end | 14 mm × 14 mm × 80 mm |
| Operating mode | Direct detection |

## *3.3 Calibration Method for the Radiometer Array Adopted in the Passive Millimeter-Wave Imaging System*

The calibration of the millimeter-wave radiometer arrays is a key technology for the imaging applications. Its precision affects directly the image quality based on the detected millimeter-wave radiation.

The focal-plane-array imaging system usually adopts a sensor array, i.e., the radiometer array in our passive millimeter-wave imaging system, to realize the spatial sampling of the detected objects. In order to make every channel of the multi-channel radiometer array have good consistency, the calibration method has to be adopted properly. Radiometer calibration is basically to determine the corresponding linear relationship between the radiated noise power (equivalent to the antenna temperature $T_A$) and the output voltage $V_{\text{out}}$ of the radiometer. Theoretically, the following expression holds for a radiometer with acceptable linearity,

$$V_{\text{out}} = aT_A + b \tag{3.8}$$

where $a$ and $b$ are the coefficient to be determined by the calibration, $V_{\text{out}}$ denotes the radiometer output voltage, and $T_A$ is the antenna temperature. In order to determine the two calibration coefficients, we need to select two calibration sources as a priori including a room temperature source and a heated calibration source.

Assume that for the $i$th radiometer the measured voltage output is $V_{\text{COUT}}$ when it measures the room temperature source, and the measured voltage output reads $V_{\text{HOT}}$ when the heated temperature source is measured, we should have,

$$V_{\text{cout}}^{i} = a_i T_{\text{cold}} + b_i, \quad V_{\text{hout}}^{i} = a_i T_{\text{hot}} + b_i \tag{3.9}$$

We can then fix the coefficients of the $i$th radiometer by

$$a_i = \frac{T_{\text{hot}} - T_{\text{cold}}}{V^i_{\text{hout}} - V^i_{\text{cout}}}, \quad b_i = \frac{V^i_{\text{hout}} T_{\text{cold}} - V^i_{\text{cout}} T_{\text{hot}}}{V^i_{\text{hout}} - V^i_{\text{cout}}} \tag{3.10}$$

After determining the calibration coefficient, the linear relationship between the radiometer output voltage and noise temperature will be established, which reads

$$V^i_{\text{out}} = a_i T_A + b_i \tag{3.11}$$

For different radiometers, when the input antenna temperature $T_A$ is identical, their output voltages may be different since the calibration coefficients can be different. A proper calibration method has to be adopted to compensate the discrepancies of the multi-channel radiometers. One commonly applied algorithm is introduced as follows:

For an array of totally $N$ radiometers, the mean values $a_0$ and $b_0$ of the two calibration coefficients $a_i$ and $b_i$ ($i = 1, 2, \ldots, N$) are selected as a calibration standard. When the input antenna temperature is $T_A$, the calibrated output voltage should follow

$$V^0_{\text{out}} = a_0 T_A + b_0 \tag{3.12}$$

The output voltage value of the $i$th radiometer before calibration reads

$$V^i_{\text{out}} = a_i T_A + b_i \tag{3.13}$$

After calibration, its output voltage reads

$$\begin{aligned} V^i_{\text{out}}{}' &= (a_i + \Delta a_i) T_A + (b_i + \Delta b_i) \\ &= a_i T_A + \Delta a_i T_A + b_i + \Delta b_i \\ &= V^i_{\text{out}} + \Delta a_i T_A + \Delta b_i \end{aligned} \tag{3.14}$$

where $V^i_{\text{out}}$ is actual output voltage of the $i$th radiometer, $\Delta a_i = a_0 – a_i$ and $\Delta b_i = b_0 – b_i$. The calibration method makes every radiometer in the array have the same linearity. Hence, the output voltage values will be same when the input power is identical.

As to the selection of calibration source, it is better to choose the minimum and the maximum values of the possible input antenna temperatures of the imaging system. In human-body security inspection systems, we can adopt the absorbing materials to construct the calibration sources for their low reflectivity and high emissivity. Furthermore, copper plates/shells are chosen to support the absorbing materials, and provide calibration sources of different temperature with the help of heating devices. The room temperature (293 K) and 40 °C (313 K) are suitable for the room temperature source and the heated source for calibration. As shown in Fig. 8, the heated calibration source is realized by a copper shell uniformly coated with

the absorbing materials. The attached heater is controlled by a programmable PID regulator to keep the temperature of the heated source constantly at 40 °C. The room temperature calibration source can simply be realized by attaching uniformly the absorbing material inside the copper shell.

According to (3.3), the calibration process can reduce the influence of the system gain fluctuation on the temperature sensitivity and thus improve the output consistency of the radiometer array. We can hence ignore the influence of $\Delta T_G$ on the temperature sensitivity $\Delta T_{\min}$.

## 4 Passive Millimeter-Wave Near-Field Imaging Feed Antenna

In the passive millimeter-wave focal-plane-array imaging system, the feed antennas on the focal plane of the focusing antenna are required to distribute close to every other in order to provide sufficient spatial resolution, and thus it is necessary to adopt a feed antenna with a small cross section. On the other hand, the feed antenna must provide efficient illumination for the focusing antenna with the lowest possible overflow losses. The feed antenna has to provide high gain, which often requires the antenna to have a large cross section. This contradiction needs to be properly handled during the design of the focal plane antenna array. Many authors have proposed horn antennas, printed dipole, or tapered slot antennas. However, these feed antennas may fail to provide good illumination for the reflector or the focusing antenna, cannot be tightly arranged, or have poor cross-polarization isolation.

In this section, a novel dielectric rod antenna is proposed and optimized by the full-wave simulation. Experimental results confirm it a good candidate as a feed antenna for the passive millimeter-wave focal-plane-array imaging system. The antenna gain can be adjusted by changing the length of the dielectric rods rather than its cross section, which make it possible to realize a tightly arranged feed antenna array, with low overflow losses to achieve efficient illumination to the focusing antenna. These merits make the dielectric rod antenna as the feed suitable for the millimeter-wave focal-plane-array imaging.

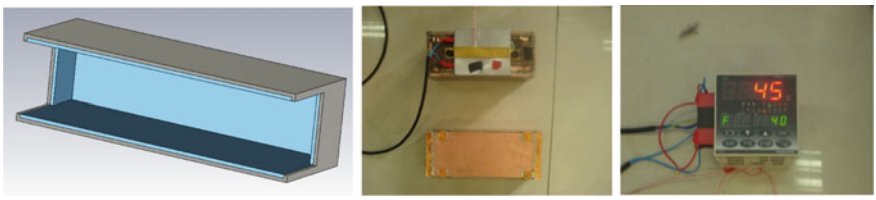


**Fig. 8** Calibration source model (left), the heated and the room temperature calibration sources (middle), the PID controller (right)

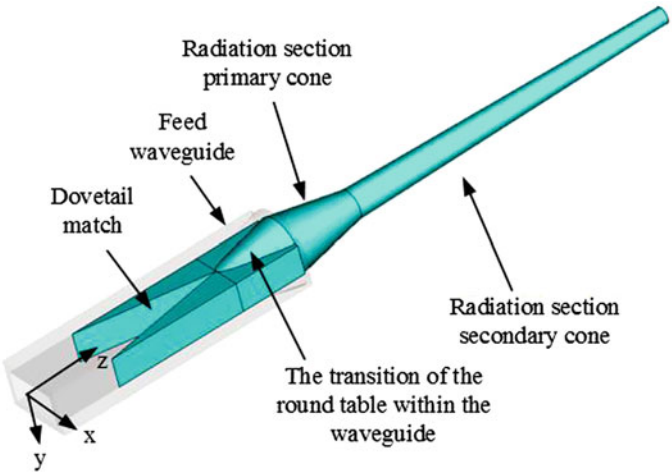


**Fig. 9** Geometrical details of the proposed dielectric rod antenna

The novel dielectric rod antenna is shown in Fig. 9. A rectangular waveguide is chosen to feed the antenna, while cylindrical dielectric rods form the main radiator. Firstly, a circular cone is truncated by the rectangular dielectrics forming a good transition from the rectangular cross section of the feed to the circular cross section of the radiator. Such a structure is convenient to install and feed, and can also optimize the radiation characteristics. Secondly, the dovetail matching and the circular cone transition are adopted to further smooth the transition from the feed to the radiator. These structures can reduce the input return loss, broaden the bandwidth, and increase the gain. These sections are inserted into the feed waveguide, whose inner wall is tightly attached to the dielectric rod antenna. Finally, two tapered cylindrical dielectric rods are optimized as the radiation segments of the antenna to reduce the antenna sidelobe level and thus to minimize the mutual coupling between the array elements.

The antenna prototype is shown in Fig. 10, which is mainly composed of Teflon, and the inner and outer surfaces of the feeding waveguide are coated with gold to reduce the metal losses. According to the analysis of the quasi-optical path, the radiation segment of the novel dielectric rod antenna has a length of 50 mm, while the dovetail matching of the antenna is fixed at $2\lambda_0$.

Figure 11 shows the simulation and measurement results of the proposed dielectric rod antenna. It can be seen that the VSWR of the antenna is less than 1.3 within the wide frequency range from 26.5 to 40 GHz, and in particularly, the VSWR is less than 1.2 in the frequency range from 28.5 to 37.3 GHz. The experimental results are in good agreement with the simulation ones.

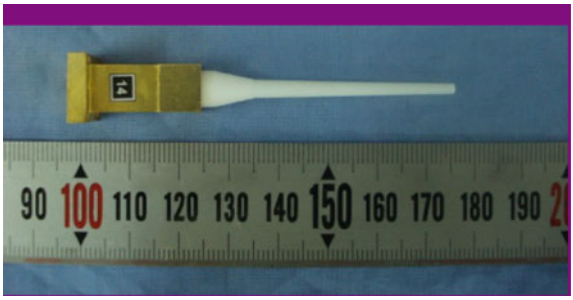


**Fig. 10** Physical structure of a new type of dielectric rod antenna

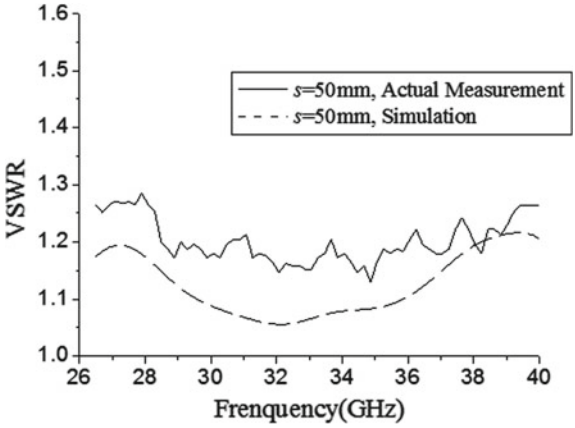


**Fig. 11** Simulated and measured VSWR of the antenna prototype as a function of frequency

Figure 12 shows simulated and measured radiation pattern of the proposed dielectric rod antenna. It is indicated that at 33, 35 and 37 GHz, the 10 dB beam width of the antenna is about 44°, and the measured gain is 16.3, 16.9 and 17.3 dB, respectively. The E-plane and the H-plane patterns have good symmetry. The first sidelobe level is about –20 dB, which is in good agreement with the simulation results.

Figure 13 shows the co-polarization and cross-polarization pattern of the dielectric rod antenna at 35 GHz frequency. It is shown that the measured cross-polarization level is less than –20 dB in the main radiation direction.

The coupling between antennas can make the radiation pattern worse, and the radiation characteristics of each element in the array will further be inconsistent. In the feed array of millimeter-wave imaging system, the space between the antenna elements is small, so the antenna coupling should be carefully considered. As shown

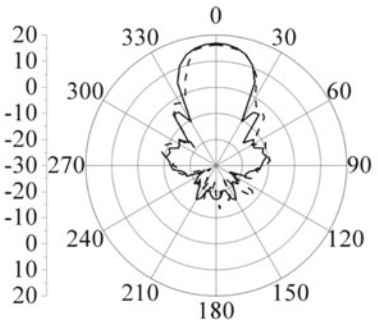


(a) E-plane =33GHz

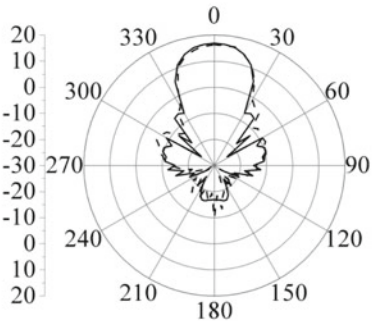


(b) E-plane =33GHz

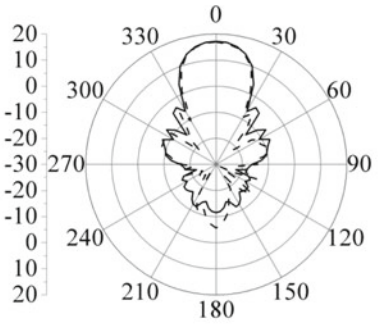


(c) E-plane =35GHz

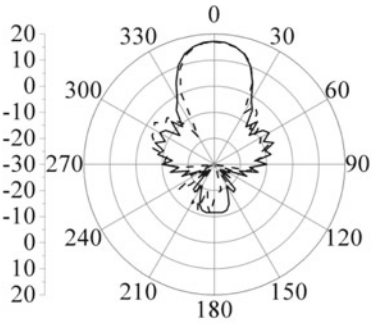


(d) H-plane =35GHz

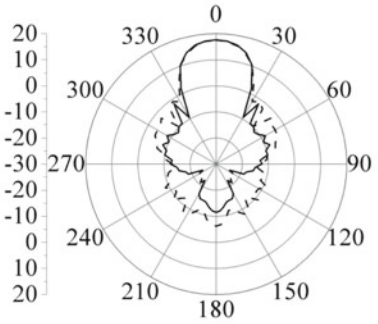


(e) E-plane =37GHz

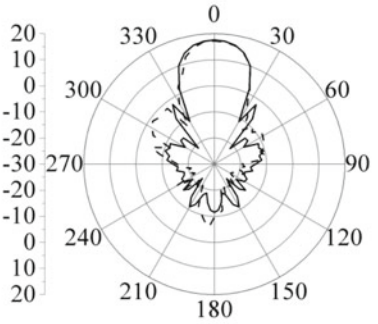


(f) H-plane =37GHz

**Fig. 12** Radiation pattern of the dielectric rod antenna (—Simulation Results, - - -Test Results)

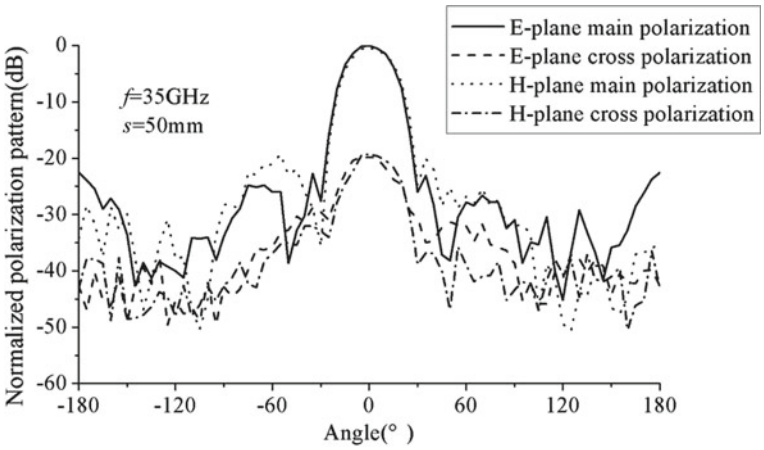


**Fig. 13** Measured co-polarization and cross-polarization levels of dielectric rod antenna

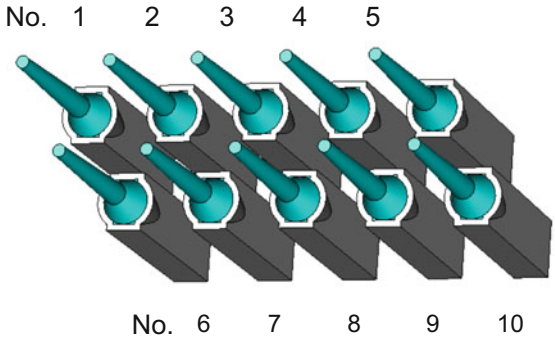


**Fig. 14** $2 \times 5$ elements dielectric rod antenna array

in Fig. 14, a dielectric rod antenna array consisting of 10 elements is constructed in the full-wave simulator, whose radiation length is set to 30 mm, and spacing is $1.5\lambda_0$. As shown in Fig. 15, the reflection loss of a single antenna element is less than –18 dB in the frequency band of 26.5–40 GHz, and the isolation of No. 3 from other antennas is more than 30 dB. According to the symmetry, the mutual coupling between the elements of the antenna array is less than –30 dB.

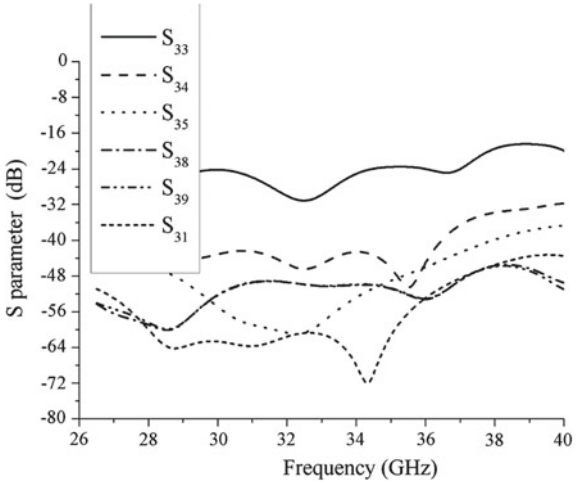


**Fig. 15** Simulation results of S-parameter of dielectric rod antenna array

## 5 Quasi-optical Theory and Focusing Antenna for Passive Millimeter-Wave Near-Field Imaging

In the passive millimeter-wave near-field imaging system, the objects under detection are often of small size. In order to get more details of the human body and the objects, we need to achieve high spatial resolution image. To fulfill this goal, we need to implement a focusing antenna between the feed antenna and the object plane. In order to improve the spatial resolution in the plane of the object under detection, we carefully design the quasi-optical path of the imaging system. Meanwhile, in order to improve the frame rate of the system to achieve real-time imaging, we implement further the mechanical scanning with the focal plane array. Such an imaging mechanism requires the shape distortion of the focal spot on the object planar as small as possible when the feed antenna deviates away from the focus of the focusing antenna.

The passive millimeter-wave imaging system usually requires a focusing antenna with double focal spots, which mainly includes the dielectric lens antenna and the ellipsoid reflector antenna. As an example, we will discuss the quasi-optical path design and the curvature selection for the dielectric lens antenna.

### *5.1 Quasi-optics Design Method*

Considering the calculation speed, the complexity, and the accuracy, fundamental mode Gaussian beam method is adopted to design the millimeter-wave imaging quasi-optical system. Gaussian beam method is a fitting to the characteristics of the

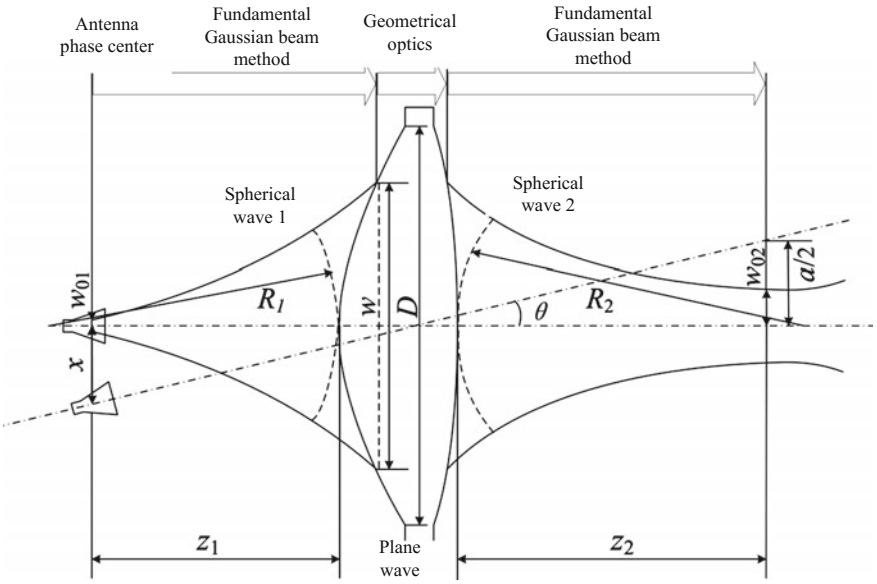


**Fig. 16** Quasi-optical path of a given dielectric lens antenna

electromagnetic wave propagation, whose fundamental mode has analytical expressions, and is of high accuracy in the millimeter-wave band [9, 10].

As shown in Fig. 16, the electromagnetic wave radiation from the object plane propagates as a Gaussian beam and is cut by the lens. Proper phase shifts are added by the lens so that the wave can be focused to the phase center of the receiving antenna, allowing highly efficient energy harvesting. If $r$ is the distance for a field point to the shaft, $w$ is the beam radius when the field strength decays to 1/e on the optical axis, $R$ is the radius of spherical wave front, $\lambda$ is the wavelength, then the normalized field intensity according to the Gaussian distribution on the plane $z$ ($z$ is a definition value) reads

$$E(r)/E(0) = \exp\left[-\left(r/w(z)\right)^2\right] \tag{5.1}$$

The beam waist plane is then defined as the plane where the minimum radius of the beam is observed. The minimum radius of the beam is called the waist radius $w_0$. $w_0$ and $w$ satisfy the following relations, which read

$$w = w_0 \cdot \left[1 + \left(\lambda z/\pi w_0^2\right)^2\right]^{0.5} \tag{5.2}$$

Radius of the spherical wave front satisfies the following formula, which reads

$$R = z + \left(\pi w_0^2/\lambda^2\right)/z \tag{5.3}$$

## 5.2 The Design of the Optical System Parameters

System parameters include the center wavelength λ, sight range $a \times b$, and the size of the focal spot $2\delta$. Besides, the receiving antenna array is linearly configured.

(1) In order to determine the object distance $z_2$ by the scanning angle and the field of view of the dielectric lens antenna, we have

$$z_2 = \frac{a}{2\tan\theta} \tag{5.4}$$

(2) In order to determine the size of the lens, we have

$$\delta = w_{02}\sqrt{\ln\sqrt{2}} = 0.59w_{02} \tag{5.5}$$

Considering the fact that the focal spot is getting larger when the feed is offset from the axes, we could get the following equation by letting $w_{02} = \delta$, which reads

$$w = \delta\left[1 + \left(\lambda z/\pi\delta^2\right)^2\right]^{1/2} \tag{5.6}$$

According to the normal distribution characteristics of the Gaussian beam, limited aperture of the lens must have the truncation effect on the Gaussian beam. Lens diameter can be estimated by the following formula, which reads

$$D = 0.6784w \cdot [T_E(\mathrm{d}B)]^{\frac{1}{2}} \tag{5.7}$$

where $D$ is the diameter of the lens and $T_\mathrm{E}$ is the truncated size.

(3) In order to determine the image distance $z_1$, one needs to comprehensively consider the arrangement of receiving antenna. Usually, the image distance is fixed by

$$z_1 = 1.2D \tag{5.8}$$

(4) Waist radius of the antenna $w_{01}$. In order to realize plane wave in the dielectric lens, the asymmetric structure is adopted. According to (2), we could get

$$w = w_0 \bullet \frac{\lambda z}{\pi w_0^2}\left[1 + \left(\frac{\pi w_0^2}{\lambda z}\right)^2\right]^{\frac{1}{2}} \approx \frac{\lambda z}{\pi w_0} \tag{5.9}$$

(5) The gain of receiving antenna reads

$$G \approx \frac{4\pi}{\theta_{\mathrm{HPBW}}^2} \tag{5.10}$$

The beam width at the distance z away from the antenna aperture follows

$$2w' = \theta_{\mathrm{HPBW}} \cdot z \tag{5.11}$$

Using the Gaussian beam method, we could express the antenna beam width by Taylor expansion, which reads

$$w = w_0 \bullet \frac{\lambda z}{\pi w_0^2}\left[1 + \left(\frac{\pi w_0^2}{\lambda z}\right)^2\right]^{\frac{1}{2}} \approx \frac{\lambda z}{\pi w_0} \tag{5.12}$$

Considering the half-power beam width and the 1/e field intensity distribution, we could get

$$\theta_{\mathrm{HPBW}} \approx \frac{1.18\lambda}{\pi w_{01}} \tag{5.13}$$

The gain of the receiving antenna can finally be calculated by

$$G \approx \frac{89.1 w_{01}^2}{\lambda^2} \tag{5.14}$$

## 5.3 *Design of Lens Curvature*

After determining the optical path parameters of the system, we should design an appropriate lens. As shown in Fig. 16, the spherical wave 1 emitted from a primary antenna is converted into a plane wave by the illumination surface of the lens. Based on the reversibility of optical path, the plane wave becomes a spherical wave 2 and converges to the image point after passing through the dark side of the lens. As shown in Fig. 17, aplanatic conditions of ray 1 and ray 2 emitted from point O are as follows:

$$\frac{R}{\lambda_0} = \frac{L}{\lambda_0} + \frac{R\cos\theta - L}{\lambda_d} \tag{5.15}$$

where $L$ is the distance from the feed antenna to the lens; $\lambda d$ is the wavelength of the electromagnetic wave in the lens. In the rectangular coordinate system with O as the source point and the x-axis as the optical axis, the following expression is available:

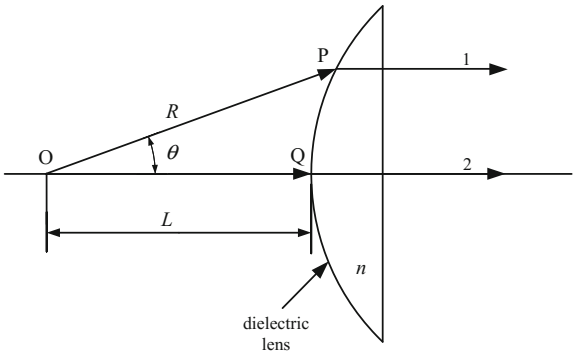


**Fig. 17** Schematic of length of dielectric lens

$$\frac{\left(x-\frac{nf}{n+1}\right)^2}{\left(\frac{f}{n+1}\right)^2}-\frac{y^2}{\frac{(n-1)f^2}{n+1}}=1 \tag{5.16}$$

It can be seen that the above equation is a hyperbolic one, that is, the focusing lens is designed as a hyperbolic lens. In one face, the spherical wave is modified to plane wave. The same idea can be used to design the other side of the lens shape. The plane wave is modified to another spherical wave and converges in a point in space. The dielectric lens should be selected with a material with small loss and moderate dielectric constant, such as Teflon, cross-linked polystyrene, and polystyrene.

The center frequency of the actual quasi-optical path system is 35 GHz, and the operating wavelength is about 8.57 mm, requiring a focal spot size of $2\delta = 100$ mm, and linear array antenna sight width of $a = 600$ mm. The designed system parameters are listed as follows: $z_2 = 2854$ mm, $w = 188$ mm, $D = 572$ mm, $z_1 = 686$ mm, $w_{01} = 9.97$ mm, $G = 20.8$ dB, $R_1 = 686$ mm, and $R_2 = 2854$ mm. The calculated parameters also meet the application conditions of the Gaussian beam method and hence can be used to design the corresponding double-sided lens. Let $f_1 = R_1, f_2 = R_2$ and choosing Teflon with refractive index $n = 1.45$ as the lens material, the contour lines of the lens can be obtained from (5.17) and (5.18). To realize the assembly of the lens, there is a 10 mm × 10 mm ring around the edge of the lens, and the corresponding lens contour equation is as follows:

$$\frac{(x+390.6)^2}{78400}-\frac{y^2}{86436}=1(x\le 0) \tag{5.17}$$

$$\frac{(x-1196.3)^2}{1356987}-\frac{y^2}{1496078}=1(x\ge 0) \tag{5.18}$$

where (5.17) is the contour equation of the lens illumination surface, and (5.18) is the lens dark side contour equation. The profile and the prototype of the lens are shown in Figs. 18 and 19.

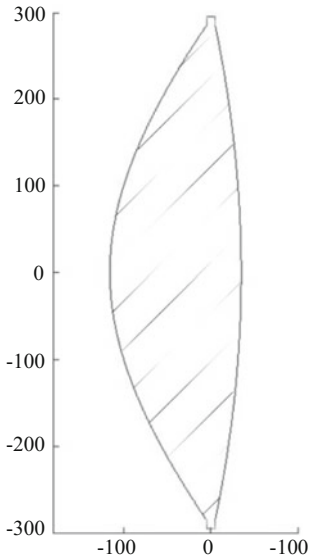


**Fig. 18** Profile of the dielectric lens

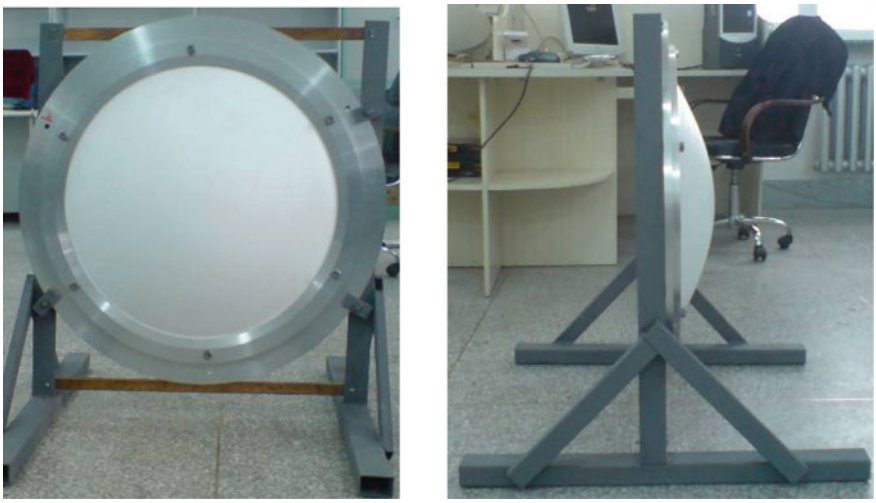

(a) Front view of the dielectric lens (b) Side view of a dielectric lens.

**Fig. 19** Photographs of the dielectric lens

**Fig. 20** Biased ellipsoidal reflector antenna

Similarly, the ellipsoidal reflector antenna can be designed using the fundamental mode Gaussian beam method. The biased ellipsoidal reflector antenna is shown in Fig. 20.

## 6 Passive Millimeter-Wave Near-Filed Imaging System

The key technologies about the multi-channel millimeter-wave focal-plane-array (FPA) imaging system are introduced in the previous sections of this chapter, i.e., analysis and design of quasi-optical path, focusing antenna, Ka-band miniaturized direct detection radiometer and dielectric-rod feed antenna with features of small cross section and low sidelobe level, respectively. Based on these research results, the overall multi-channel millimeter-wave focus plane array imaging system will be presented in this section including system structure and scanning method, sampling and focus plane array arrangement, and calibration method of system. The 20-channel and 70-channel PMMW imaging systems will be introduced as two examples.

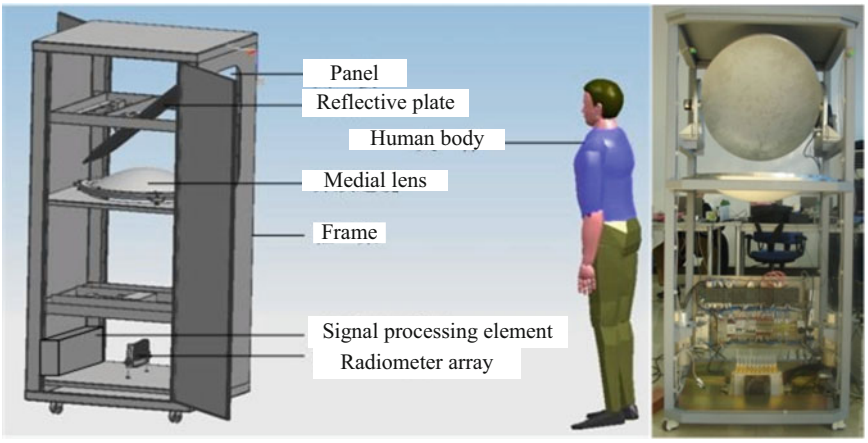


**Fig. 21** Illustration of PMMW focus plane array imaging system

## *6.1 20-Channel FPA System for Hidden Object Detection Under Human Clothing*

According to the previous analysis, a multi-channel millimeter-wave FPA imaging system is presented in Fig. 21. This system operates in the Ka-band. Its horizontal view sight is covered with 20-channel radiometers and feed arrays while the vertical view sight is covered with mechanical scanning of reflector in the range of $\pm 4.75°$. With the help of the ellipsoidal reflector antenna, the electromagnetic wave will be focus on the plane of $z_2 = 3$ m. On this plane, the area of sight view is 0.6 m(H) $\times$ 1 m(V). The diagram of system structure and the manufactured prototype are shown in Fig. 22 and Fig. 23, respectively.

As shown in Fig. 24, we took constant temperature water tank as background and set its temperature to 40 °C. In front of the tank was an iron ruler of 4 cm width. The millimeter-wave imaging picture is then presented in right one of Fig. 24. The ruler can be clearly seen so the spatial resolution is no bigger than 4 cm.

The optical picture and millimeter-wave image of a human with a metal wrench are shown in Fig. 25. The results indicate that this system can detect the metal and non-metal prohibited hidden objects under human clothing. Its temperature sensitivity is less than 1 K, and spatial resolution is no bigger than 4 cm. The system can be used for detecting the concealed objects under the clothing in the indoor environment.

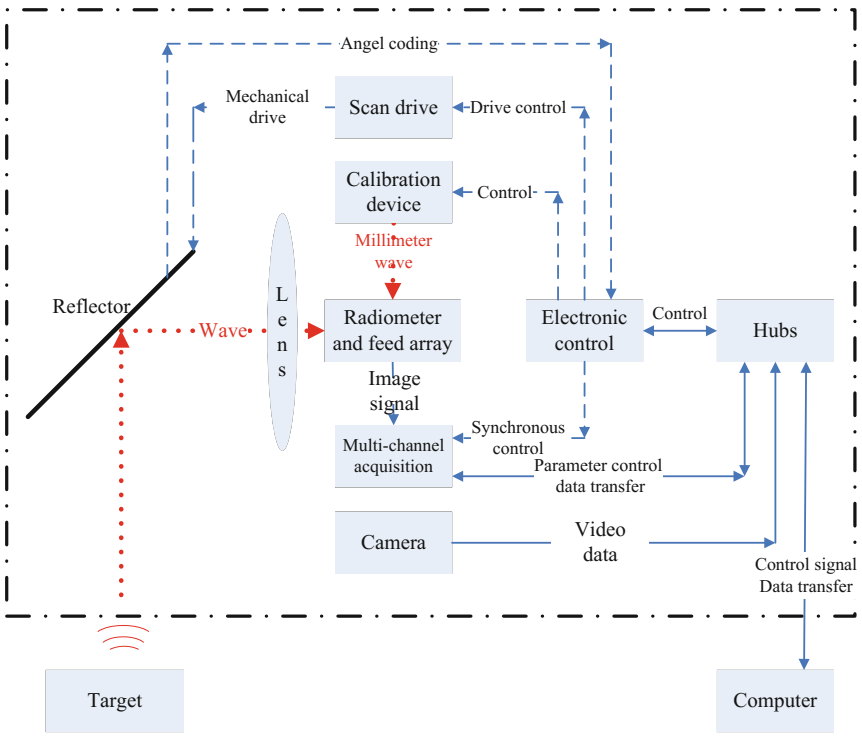


**Fig. 22** Diagram of PMMW focus plane array imaging system

## *6.2 High Spatial Resolution 70-Channel FPA System for Concealed Object Detection Under Human Clothing*

The diagram of 70-channel PMMW imaging system is shown in Fig. 26. The whole machine is composed of cabinet shell, scanning reflector rotating structure, elliptical surface focusing antenna, radiometer array, calibration system, and control device. The assembly process is from bottom to top.

The PMMW imaging system mainly consists of system framework subsystem, quasi-optical subsystem, radiometer array subsystem, data acquisition subsystem, data processing subsystem, and electronic control subsystem. The manufactured prototype of the 70-channel PMMW imaging system is presented in Fig. 27, and the test pictures from the imaging system can be seen in Fig. 28. Several key technical specifications can be found in Table 2.

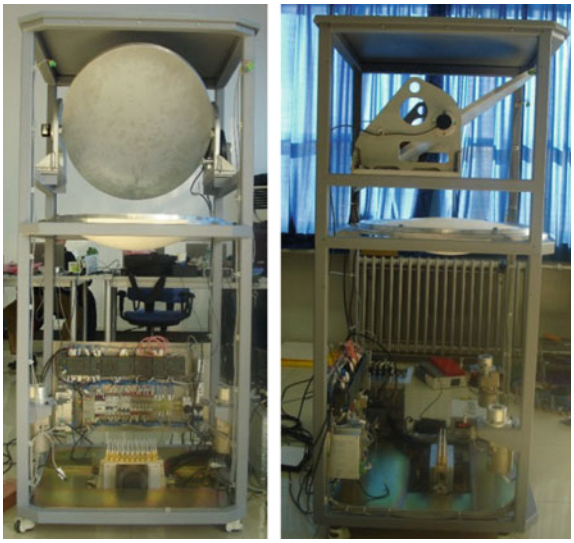

**Fig. 23** Practical machine of 20-channel PMMW focus plane array imaging system (the left is front view and the right is side view)

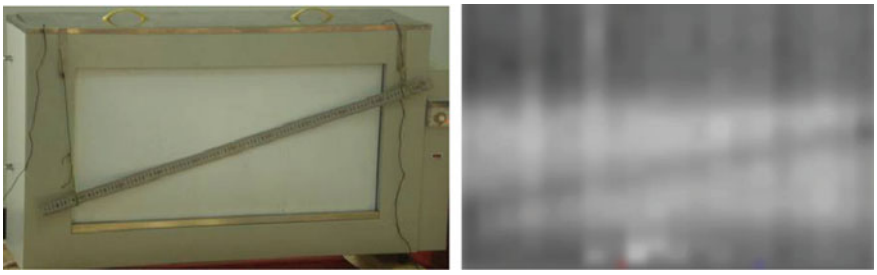

**Fig. 24** Constant temperature water tank, iron ruler, and millimeter-wave imaging picture

**Fig. 25** Detection test of hidden objects under human clothing (the target is a mental wrench, left one is optical picture while right one is millimeter-wave picture)

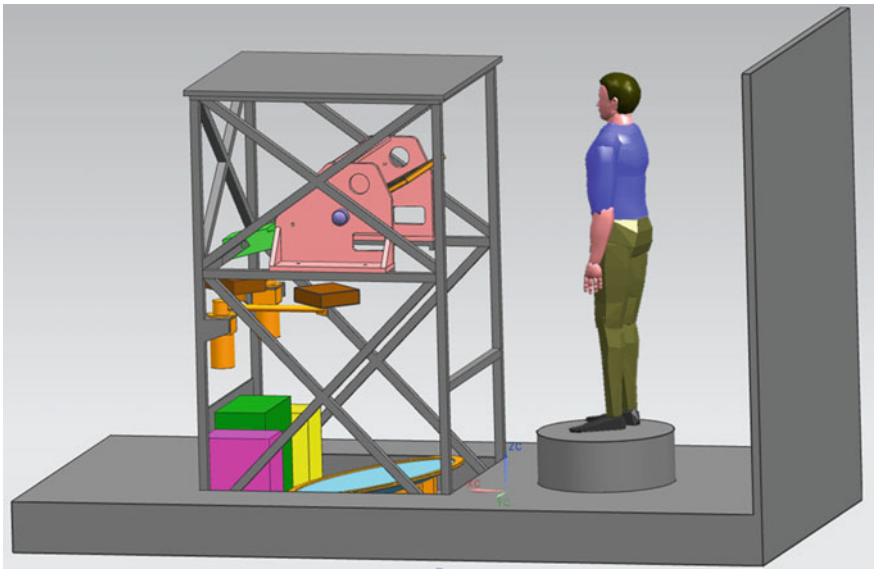

**Fig. 26** Diagram of system structure

**Fig. 27** 70-channel PMMW imaging system machine

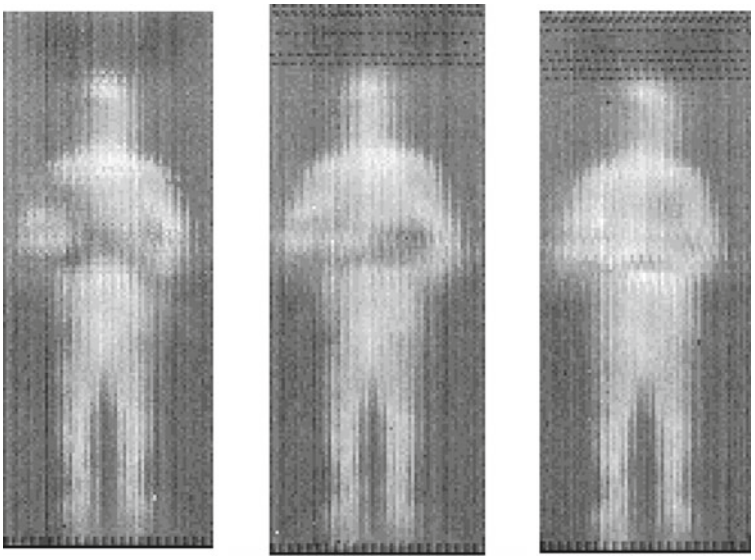


**Fig. 28** Picture from the 70-channel PMMW imaging system

**Table 2** Several key technical specifications of he 70-channel PMMW imaging system

| Technical specifications | Measurement results |
|---|---|
| Image primitive pixels | V174 × H70 |
| Sight view (FOV) | V2 m× H0.8 m |
| Center frequency | 35 GHz |
| 3 dB bandwidth | 4 GHz |
| Diameter of focus antenna | 1.3 m |
| System spatial resolution | 20–40 mm |
| System temperature sensitivity | <1 K |
| Imaging distance | 0.8 m (the distance between front panel and human body) |
| Imaging rate | 2 Hz |
| Imaging output pixels | V348 × H140 |
| Working temperature | 0–40 °C |
| Bright temperature input | 263–343 K |
| Human humidity | 10–95% (No condensation) |
| Data storage | Data of more than 10,000 human (decide by computer's memory) |
| System size | Width 1.4 m × thickness 1.6 m × height 2.3 m |

**Acknowledgements** The authors would like to express the sincere gratitude to Xinyu Yin, Mu Fang, Zifu Zhang, Hao Liu, Shanshan Xiao, Hanchi Ma, XuanZhai, BingxuZhao, QiangTong, HeZhang, Tianyao Du, Liqing Wang for their contributions in this work. Correspondence should be addressed to Prof. Jiaran Qi at qi.jiaran@hit.edu.cn.

## References

1. C. Chen, C.A. Schuetz, R.D. Martin, Analytical model and optical design of distributed aperture system for millimeter-wave imaging, in *Proceedings of SPIE*, vol. 7117. Millimetre Wave and Terahertz Sensors and Technology, 2008, pp. 711706-1–711706-11
2. P. Markus, D. Stephan, J. Matthias et al., The monitoring of critical infrastructures using microwave radiometers, in *Proceedings of SPIE*, vol. 6948, Orlando, FL, USA, 2008, pp. 1–12
3. G. Sinclair, R. Applebya, P. Cowarda, et al., Passive millimetre wave imaging in security scanning, in *Proceedings of SPIE*. Passive Millimeter- Wave Imaging Technology IV, vol. 4032, 2000, pp. 40–45
4. F.T. Ulaby, R.K. Moore, A.K. Fung, Microwave remote sensing—active and passive-volume I: Microwave remote sensing fundamentals and radiometry. Int. J. Remote Sens. **5**(2), 463–466 (1984)
5. Z.L. Xiao, J.Z. Xu, T.Y. Hu, Research on the transmissivity of some clothing materials at millimeter-wave band, in *International Conference on Microwave and Millimeter Wave Technology*, 2008, ICMMT 2008, Nanjing, 2008, pp. 1750–1753
6. R. Anderton, R. Appleby, P. Coward et al., Security scanning at 35 GHz, in *Proceedings of SPIE*, vol. 4373, Passive Millimeter-Wave Imaging Technology V, 2001, pp. 16–23

7. R. Pettai, *Noise in Receiving Systems* (Wiley, 1984), pp. 32–39
8. N. Skou, *Microwave Radiometer Design and Analysis* (Artech House, 1989), pp. 21–40
9. P.F. Goldsmith, E.L. Moore, Gaussian optics lens antennas. Microwave J. **27**, 153–157 (1984)
10. P.F. Goldsmith, Perforated plate lens for millimeter quasi-optical system. IEEE Trans. Antenna Propag. **39**(6), 834–838 (1991)

# Coupled Spin and Heat Transport in Superconductor Hybrid Structures


**Detlef Beckmann**

**Abstract** Superconductor–ferromagnet nanoscale hybrid structures have attracted considerable theoretical and experimental efforts, both due to the fundamental question of the competition of superconductivity and magnetism, and possible applications in superconducting spintronics and quantum information processing. Most of the attention has recently been focussed on magnetic Josephson junctions and the triplet proximity effect, and several chapters in this book are devoted to this topic. In addition to triplet Cooper pairs, superconductor–ferromagnet hybrid structures feature spin-polarized quasiparticle transport. Quasiparticles are exclusively responsible for heat transport in superconductors, since the Cooper pairs carry no entropy. In this chapter, we discuss recent developments in the investigation of coupled quasiparticle spin and heat transport in nanoscale superconductors with a spin splitting of the density of states. The coupling of spin and heat transport leads to very slow spin relaxation and giant thermoelectric effects, which could lead to interesting applications in thermometry or microrefrigeration.

## 1 Introduction

Hybrid structures of superconductors and ferromagnets have been studied intensely both experimentally and theoretically over the past few decades. These studies have been motivated by emergent phenomena due to the competition of superconductivity and magnetism [1–7]. The proximity effect between superconductors and ferromagnets gives rise to an induced Fulde–Ferrell–Larkin–Ovchinnikov state in the ferromagnet, which is characterized by an oscillatory dependence of the pair amplitude in the ferromagnet, and the presence of triplet Cooper pairs with zero projection along the magnetization axis. The oscillatory dependence leads to Josephson junctions with an intrinsic phase shift of $\pi$ at certain film thicknesses (or even arbitrary $\varphi$ in

D. Beckmann (✉)
Institute of Nanotechnology, Karlsruhe Institute of Technology, P.O. Box 3640, 76021 Karlsruhe, Germany
e-mail: detlef.beckmann@kit.edu



A. Sidorenko (ed.), *Functional Nanostructures and Metamaterials for Superconducting Spintronics*, NanoScience and Technology,
https://doi.org/10.1007/978-3-319-90481-8_8

suitable structures), with possible applications in superconducting digital and quantum circuits [8]. In addition, magnetic inhomogeneity can induce long-range spin-polarized supercurrents due to equal-spin triplet Cooper pairs [1]. Spin-polarized quasiparticle tunneling [9, 10] can be used, for example, as a tool to investigate spin-dependent material properties. Transport properties of superconductor–ferromagnet hybrid structures are now actively investigated as building blocks for superconducting spintronics.

Spintronics, in general, aims at implementing electronic functionality by utilizing the spin degree of freedom of the electron [11]. Spintronics is characterized by nonequilibrium spin accumulation and coupling of spin and charge currents. Spin caloritronics is a subfield of spintronics that emphasizes the coupling of spin and heat currents [12] and may eventually eliminate the charge degree of freedom entirely by using magnons [13]. A key consequence of the coupling of spin and heat currents is the generation of spin-dependent thermoelectric effects, with possible applications in thermometry and thermoelectric power conversion. In this chapter, we will discuss recent progress in the investigation of coupled spin and heat transport in superconductor hybrid structures.

## 2 Nonlocal Spin Transport

Nonequilibrium transport in spin-degenerate superconductors is characterized by quasiparticle distribution functions which reflect the twofold particle-hole degree of freedom, leading to two distinct modes of nonequilibrium. These are commonly called the longitudinal (or energy) mode and the transverse (or charge imbalance) mode. In quasi-equilibrium, where the distribution functions can be approximated by Fermi functions, the two modes are characterized by an effective temperature $T^*$ and a chemical potential shift $\Delta\mu$ of the quasiparticles (relative to the Cooper pairs) [14, 15]. Adding the twofold spin degree of freedom to the picture doubles the number of modes [16]. In addition to spin-dependent distribution functions, the quasiparticle spectrum can be spin-dependent in the presence of a Zeeman splitting [17, 18] or exchange interaction with a magnetic material [19, 20]. This leads to two possible realizations of spin accumulation in superconductors: spin-degenerate spectrum with spin-dependent distribution and spin-dependent spectrum with spin-degenerate distribution. We will be concerned here with the latter case.

It has been well known since the 1970s [17, 18] that thin superconducting films in an in-plane magnetic field can exhibit a sizeable Zeeman splitting of the quasiparticle density of states. The prime example is aluminum, where the weak spin-orbit scattering leads to well-resolved spin bands with negligible mixing between the two spin projections [21]. Figure 1 shows a scheme of spin injection and detection in high-field superconductors. In the following, we will deal only with tunnel junctions and denote ferromagnets, normal metals, insulators, and superconductors by F, N, I, and S, respectively. A ferromagnetic injector is biased at voltage $V$ relative to the superconductor. The density of states in the superconductor is spin split, either

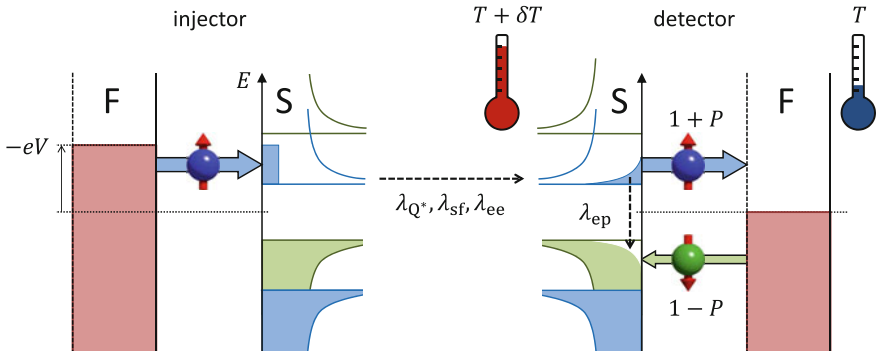


**Fig. 1** Scheme of spin injection and thermal spin transport in spin-split superconductors

by the Zeeman effect due to an applied magnetic field or by exchange interaction with a ferromagnetic insulator. Electrons tunneling from the injector into the superconductor create a nonequilibrium quasiparticle distribution, which contains charge imbalance, spin imbalance, and excess energy. In general, this will be a nonthermal distribution which cannot be described by an effective temperature and chemical potential. Charge imbalance relaxes over the length scale $\lambda_{Q*} \ll 1\,\mu$m at high magnetic fields [22]. The spin asymmetry of the distribution function decreases on the length scale $\lambda_{sf}$. $\lambda_{sf} \ll 1\,\mu$m in aluminum in the normal state [23–25] and tends to decrease in the superconducting state [26]. While charge and spin relaxation are mostly elastic under these conditions, the excess energy is subject to inelastic relaxation. Coulomb scattering leads to a thermalization of the quasiparticles among each others on the length scale $\lambda_{ee}$, leading to a hot quasiparticle distribution characterized by an effective temperature $T^* = T + \delta T$. While $\lambda_{ee}$ is not precisely known in the superconducting state, some features related to the thermalization process [27] may have been observed in experiments [28]. Due to the spin splitting of the density of states, the hot quasiparticle distribution is accompanied by a nonequilibrium spin accumulation, i.e., the quasiparticle heat current in the superconductor is accompanied by a spin current. The nonequilibrium spin accumulation is detected by observing the current flowing out of a FIS junction at zero bias. The generation of the detector current can be understood as a spin-dependent thermoelectric effect driven by the temperature difference between the hot quasiparticles and the cooler ferromagnetic detector, which will be described in more detail in Sect. 3. Finally, the quasiparticles cool to the bath temperature by electron–phonon scattering on the length scale $\lambda_{ep} \gg \lambda_{ee}$ [27, 29–31]. A detailed description of the different relaxation stages can be found in [27].

High-field spin transport in superconducting aluminum has recently been investigated experimentally [28, 32–37]. In Fig. 2a, the nonlocal conductance $g_{nl}$ of an iron–aluminum spin-valve structure is shown for different magnetic fields $B$ [32]. $g_{nl}$ is negligible at energies below the gap. At zero applied field, a small positive

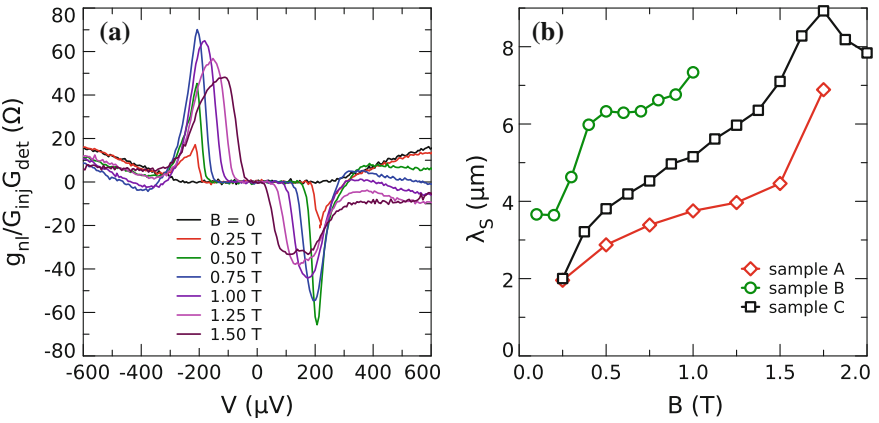


**Fig. 2** **a** Normalized nonlocal conductance $g_{\mathrm{nl}}/G_{\mathrm{inj}}G_{\mathrm{det}}$ as a function of injector bias $V$ for different magnetic fields $B$ in an iron–aluminum nonlocal spin valve at $T = 50$ mK. **b** Spin relaxation length $\lambda_{\mathrm{S}}$ for different samples as a function of magnetic field $B$. Data taken from [32, 33]

contribution due to charge imbalance is seen, which is symmetric with respect to bias polarity (i.e., the current is an odd function of bias). Upon increasing the field, a large signal develops in the bias range corresponding to the Zeeman splitting. This conductance signal is mainly odd in bias, i.e., the nonlocal current is an even function of bias. The symmetry of the signal reflects the thermal origin of high-field spin transport, since heating does not depend on bias polarity. Figure 2b shows the spin relaxation length $\lambda_{\mathrm{S}}$ as a function of magnetic field for different samples [32, 33], determined by tracking the decay of the nonlocal spin signal as a function of contact distance. It is of the order of 5 μm and increases with magnetic field. $\lambda_{\mathrm{S}}$ exceeds the normal-state spin relaxation length by about an order of magnitude. The slow spin relaxation in the superconducting state reflects the freeze-out of electron–phonon scattering at low temperatures.

## 3 Spin-Dependent Thermoelectric Effects

Thermoelectric effects are usually described by a matrix of transport coefficients connecting the driving forces (electric field $\boldsymbol{E}$ and thermal gradient $\nabla T$) to the resulting currents (charge current density $\boldsymbol{j}_c$ and heat current density $\boldsymbol{j}_Q$) [38]:

$$\begin{pmatrix} j_c \\ j_Q \end{pmatrix} = \begin{pmatrix} L_{11} & L_{12} \\ L_{21} & L_{22} \end{pmatrix} \begin{pmatrix} \boldsymbol{E} \\ -\nabla T \end{pmatrix}. \tag{1}$$

Each of the coefficients $L_{ij}$ is in general a tensor. The off-diagonal coefficients encode the thermoelectric effects, and in the linear-response regime they obey the Onsager

reciprocity relation [39] $L_{21} = TL_{12}$. Experimentally, one usually does not measure these coefficients directly (except for the electric conductivity $\sigma = L_{11}$). The heat conductivity is defined by $\boldsymbol{j}_Q = -\kappa \nabla T$ under the condition $\boldsymbol{E} = 0$ and is given by $\kappa = L_{22} - L_{21}L_{11}^{-1}L_{12}$. The Seebeck coefficient (also known as the thermopower) is defined by $\boldsymbol{E} = S\nabla T$ under the condition $\boldsymbol{j}_c = 0$ and is given by $L_{11}^{-1}L_{12}$. The Peltier coefficient is defined by $\boldsymbol{j}_Q = \Pi \boldsymbol{j}_c$ under the condition $\nabla T = 0$ and is given by $\Pi = TS$.

For ordinary metals, within the Sommerfeld expansion, the Seebeck coefficient is given by the Mott relation [40]

$$S = -eL_0 T \left. \frac{d \ln \sigma(\varepsilon)}{d\varepsilon} \right|_{\varepsilon=\varepsilon_F}, \tag{2}$$

where $L_0 = \pi^2 k_B^2/3e^2$ is the Lorenz number and $\sigma(\varepsilon)$ is the energy-dependent spectral conductivity. In the same approximation, the thermal conductivity is given by $\kappa \approx L_{22} \approx L_0 T\sigma$ (the Wiedemann–Franz law). From (2), it is apparent that thermoelectric effects only appear when particle-hole symmetry is broken. Also, one can infer that large thermoelectric effects require a spectral conductance that varies strongly on the energy scale $k_B T$. For ordinary metals, for example, $\sigma(\varepsilon)$ varies on the energy scale of the Fermi energy $\varepsilon_F$, and one finds $S \sim (k_B/e)k_B T/\varepsilon_F$, which is $\mathcal{O}(1\,\mu\,\mathrm{V/K})$ at room temperature, and vanishes for $T \to 0$. Large thermoelectric effects at low temperatures can be obtained, e.g., with Kondo alloys [41] or quantum dots [42]. Superconductors also have strongly energy-dependent spectra at low energies, but their intrinsic particle-hole symmetry and zero resistance seem to make them unsuitable for thermoelectricity, at least at first glance.

Nevertheless, the question of thermoelectric effects in superconductors is actually an old subject, dating back to Ginzburg's work in the 1940s [43]. The superconducting condensate itself carries no entropy, and therefore has neither thermal conductivity nor thermopower. A thermal gradient applied to a superconducting wire will, however, drive a quasiparticle current. The corresponding thermal and charge currents are reduced compared to the normal state by the opening of the energy gap. In addition, the thermoelectric current carried by the quasiparticles will be compensated by a counterflow of supercurrent, such that no thermoelectric voltage develops along the superconductor. Nevertheless, the thermoelectric current has an observable consequence: The supercurrent produces a phase difference between the ends of the superconducting wire. In bimetallic loops with different normal-state Seebeck coefficients, a net phase difference will remain, driving a circulating current around the loop. This current produces a measurable magnetic flux [44]. Numerous experiments have been performed, with sometimes contradictory results, and the subject continues to attract experimentalists [45].

A second type of thermoelectric effect can be observed in superconductor hybrid structures even if one neglects the normal-state Seebeck effect, i.e., when particle-hole symmetry is exact. In the presence of a supercurrent, the quasiparticle spectrum becomes anisotropic. In the clean limit, this can be described as a Doppler shift of the

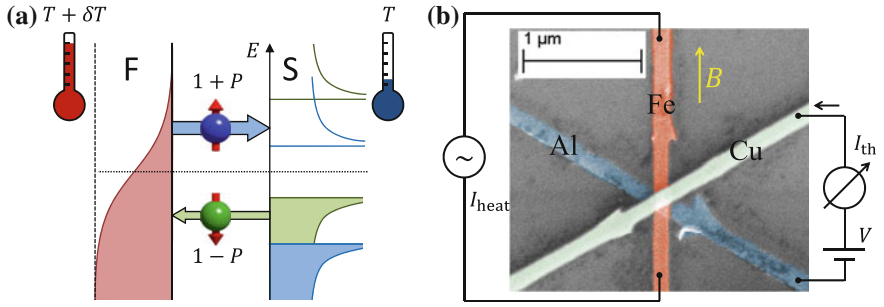


**Fig. 3** **b** Schematic view of the generation of spin-dependent thermoelectric effects in a FIS junction with a spin-split superconductor. **a** False-color scanning electron microscopy image of a sample with measurement configuration for thermoelectric measurements [55]

quasiparticle spectrum, with different excitation energies for quasiparticles moving parallel or antiparallel to the supercurrent. A thermal gradient then generates charge imbalance [46], which can be measured using normal metal junctions attached to the superconductor. Note that in this case, the problem of the superconducting short circuit is avoided by directly measuring the quasiparticle electrochemical potential using tunnel probes. In the diffusive limit, the resulting thermoelectric effect appears as a coupling term between longitudinal and transverse mode nonequilibrium [15, 47]. This mechanism of thermoelectric current generation can be observed in superconducting wires [48] and Andreev interferometers [49–51]. In the latter case, it leads to phase-dependent thermopower oscillations, which are accompanied by oscillations of the heat conductance [52]. Phase-dependent heat transport has recently also been observed in Josephson junctions [53, 54].

Recently, it has been predicted that a new type of spin-dependent thermoelectric effect can be observed in superconductor–ferromagnet hybrid structures [56–60]. The generation of thermoelectric currents in these structures is shown schematically in Fig. 3a. The density of states in the superconductor (S) is spin split, which can be either due to an applied magnetic field [58] or due to the proximity effect with a ferromagnet [56]. While the overall density of states still obeys particle-hole symmetry, the density of states for each spin breaks particle-hole symmetry. If a ferromagnet (F) is attached to the superconductor via a tunnel barrier, the junction conductance has a finite spin polarization $P$. Thermally excited electrons tunneling into and out of the superconductor are spin-selected by the Zeeman splitting of the density of states in the superconductor, and in conjunction with the finite polarization $P$, this leads to a net thermoelectric current. The charge current through the junction for arbitrary voltage bias $V$ and temperature difference $\delta T$ can be written as [58]

$$I_c(T, \delta T, V) = \frac{G_{\text{T}}}{e} \int \left[ N_0(\varepsilon) + \frac{P N_z(\varepsilon)}{2} \right] \times \left[ f_0(\varepsilon - eV, T + \delta T) - f_0(\varepsilon, T) \right] \mathrm{d}\varepsilon, \tag{3}$$

where $G_T$ is the junction conductance in the normal state, $N_0 = (N_+ + N_-)/2$, $N_z = (N_+ - N_-)$, $N_\pm$ are the densities of states for the two spin projections in the superconductor, and $f_0$ is the Fermi function. The term $PN_z$ is an odd function of energy and gives rise to the thermoelectric current. In the linear regime, in analogy to (1), the charge current $I_c$ and the heat current $I_Q$ through the junction can be written as [58]

$$\begin{pmatrix} I_c \\ I_Q \end{pmatrix} = \begin{pmatrix} g & \eta \\ \eta & g_{\mathrm{th}}T \end{pmatrix} \begin{pmatrix} V \\ \delta T/T \end{pmatrix}, \tag{4}$$

where $g$ is the electric conductance, $g_{\mathrm{th}}$ is the thermal conductance, and $\eta$ is the thermoelectric coefficient. The matrix has been written such that the Onsager symmetry between Seebeck and Peltier effect is explicit. For the spin current $I_s$ and the spin heat current $I_{Qs}$, one can write an additional matrix as

$$\begin{pmatrix} I_s \\ I_{Qs} \end{pmatrix} = \begin{pmatrix} Pg & \alpha \\ \alpha & gG_{\mathrm{th}}T \end{pmatrix} \begin{pmatrix} V \\ \delta T/T \end{pmatrix}, \tag{5}$$

where $\alpha$ describes a thermally driven spin current across the junction. It is related to the thermoelectric coefficient by $\eta = P\alpha$. Thus, the spin-dependent thermoelectric effect in these junctions is directly linked to the coupled spin and heat currents.

Figure 3b shows a scanning electron microscopy image of a hybrid structure used to measure spin-dependent thermoelectric effects. A thin aluminum oxide layer forms a tunnel barrier between a superconducting aluminum wire and a ferromagnetic iron wire. A superimposed copper wire serves as additional measurement lead. An ac heater current is passed along the iron wire to create a temperature difference $\delta T$ across the junctions, and the resulting thermoelectric current is measured using one of the copper leads using second harmonic detection.

Figure 4a shows the normalized thermoelectric coefficient $e\eta/G_T\Delta_0$ as a function of magnetic field for a FIS junction at different base temperatures $T_0$. Symbols are experimental data, lines are fits using (3). For these fits, the spectral properties of the superconductor were calculated self-consistently, using the model of [62]. To illustrate the physics, Fig. 4b shows $N_z$ as a function of energy and magnetic field for the fit at $T_0$ = 100 mK. At zero field, i.e., in the absence of spin splitting, $N_z$ = 0, and consequently there is no thermoelectric current. Upon increasing the field, $N_z$ becomes nonzero, and the spectral gap is gradually reduced. The thermoelectric current then becomes finite and increases up to the field where the spectral gap goes to zero, about 1 $T$ for this sample. At higher fields, the spin bands overlap, and the thermoelectric current decreases again, until it vanishes at the critical field of about 1.2 $T$. Increasing temperature increases the thermoelectric current, especially at small fields, due to thermal excitation above the gap. The Seebeck coefficient $S = \eta/gT$ calculated from the thermoelectric coefficient and the zero-bias conductance $g$ can be as large as $-100$ μV/K for these samples [55].

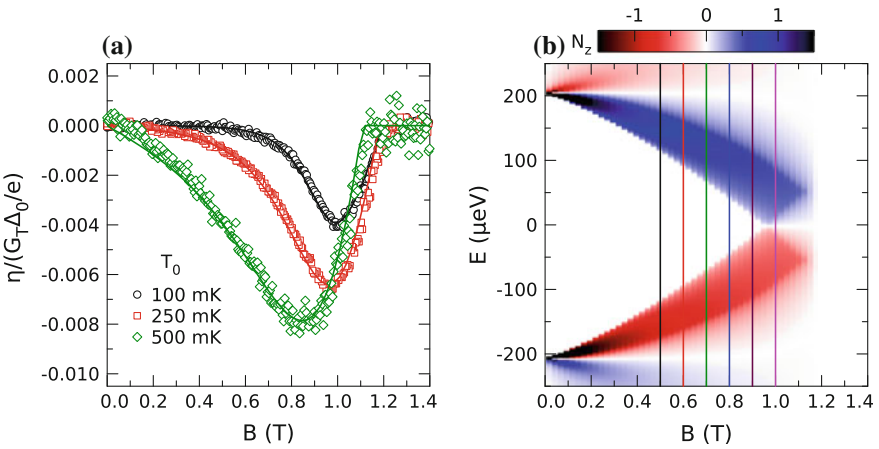


**Fig. 4** **a** Thermoelectric coefficient $\eta$ as a function of magnetic field $B$ of a FIS junction for different base temperatures $T_0$ [55]. **b** $N_z = N_+ - N_-$ as a function of magnetic field $B$ and energy $E$ calculated self-consistently for the same sample at $T = 100$ mK [61]. Vertical lines correspond to the traces in Fig. 5a

# 4 Possible Applications

## *4.1 Thermometry*

A typical application of thermoelectric effects is thermometry. Many different local electron thermometers have been developed for low-temperature mesoscopic systems, based, e.g., on NIS junctions, Coulomb blockade, or noise [63]. Apart from being useful for mesoscopic transport experiments, these thermometers can also be used for particle or radiation detectors. A thermometer should ideally have a linear response to temperature and a constant (and high) sensitivity. Figure 5a shows the dependence of the thermoelectric current on thermal excitation $\delta T$ for a FIS junction for different magnetic fields $B$. The signal is nonlinear at small fields, increases with increasing field, and is nearly linear for fields around 1 $T$. This behavior can be understood in terms of the density of states factor $N_z$ shown in Fig. 4b: At small fields, there is a finite spectral gap, and the nonlinearity of the thermoelectric current stems from excitation above the gap. Upon increasing the field, the gap decreases, and the thermoelectric current increases. At around 1 $T$, the superconductor becomes gapless, and the thermoelectric response is nearly linear. This regime is favorable for thermometry applications.

An interesting figure of merit for a thermometer is the intrinsic noise level $s_T = s_I/|\tau_I|$, where $s_I$ is the current noise and $\tau_I$ is the temperature-to-current transfer function. Both can be calculated within the tunnel limit [64]. $s_T$ scales with $\sqrt{R_T}$ and can be made small by using large-area, low-resistance junctions. For local thermometry, however, small junctions are needed, which are typically in the kΩ

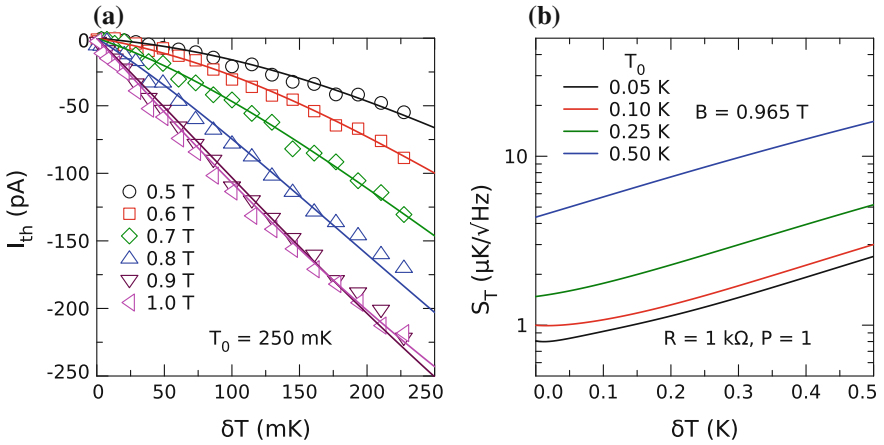


**Fig. 5** **a** Thermoelectric current as a function of thermal excitation $\delta T$ for different magnetic fields $B$ [61]. **b** Intrinsic noise level $s_T$ for a junction with $R = 1\,\mathrm{k}\Omega$ and $P = 1$ as a function of temperature difference $\delta T$ for different base temperatures $T_0$

range. Figure 5b shows the sensitivity of a hypothetical FIS thermometer, using the spectral properties of the actual sample shown in Fig. 5a, but a junction with $R_T = 1\,\mathrm{k}\Omega$ and optimized spin polarization $P = 1$. Spin polarization close to unity can be achieved by using a spin-filter tunnel barrier, such as EuS or EuO [65–67]. The magnetic field is chosen such that the superconductor is gapless, giving best sensitivity. The predicted sensitivity is nearly independent of temperature difference and better than $1\,\mu\mathrm{K}/\sqrt{\mathrm{Hz}}$ at low temperatures. This is quite competitive with other nanoscale local thermometers. Also, unlike NIS junction thermometers, the FIS thermometer is sensitive to the temperatures of both the normal metal and the superconductor. While the intrinsic sensitivity may be exceptional, it is crucial not to degrade sensitivity with the read-out scheme. Different read-out schemes based on solid-state amplifiers, SQUIDs, and temperature-to-frequency conversion by Josephson junctions have been analyzed in [64]. Achieving the favorable gapless state requires both spin splitting and a certain level of depairing, since pure spin splitting never leads to a gapless state. In the present experiments, the applied field provided both spin splitting via the Zeeman effect and Abrikosov–Gorkov-type depairing due to orbital effects [68, 69]. In principle, an external field can be omitted if the spin splitting is provided by exchange interaction [65–67] and the depairing is provided by magnetic impurities [68].

## 4.2 Cooling

A second application of thermoelectric effects is Peltier cooling. Local cooling of mesoscopic structures can be performed, e.g., by superconducting microrefrigerators based on NIS junctions [63, 70]. These operate under bias conditions just below the superconducting energy gap and provide cooling of the normal metal by "evaporating" electrons from the high-energy tail of the Fermi distribution into the superconductor. Indirectly, this electronic cooling can also be used to cool the lattice and nearby devices such as detectors.

According to Onsager reciprocity, the spin-dependent thermoelectric currents described above are accompanied by the Peltier effect. While thermoelectric coefficients (and Onsager relations) are usually defined in the linear transport regime, cooling requires finite bias and power to be useful. Therefore, an extension of the experiments to finite voltage bias is needed. Here, the thermoelectric transport coefficient is generalized to

$$\eta(V) = \frac{\partial I_c}{\partial \delta T}. \tag{6}$$

In the experiment, a dc voltage bias is combined with an ac heater current and second harmonic detection, as before. Figure 6a shows the thermoelectric coefficient of a NIS junction as a function of voltage bias for different magnetic fields. While $\eta(V = 0)$ is zero due to particle-hole symmetry, $\eta$ becomes nonzero at finite bias. In the NIS junction, $\eta$ is an odd function of bias and sharply peaked near the energy gap. At finite magnetic field, the spin splitting of the density of states is also visible. It should be noted that at high bias, the signals are at least an order of magnitude larger than the linear effect in the FIS junction shown in Fig. 4a. The nonlinear $\eta(V)$ in a FIS junction is shown in Fig. 6b. It is generally similar to the NIS sample, with the addition of the (small) linear effect at $V(0)$, which is hardly visible at this scale.

To elucidate the physics of the nonlinear thermoelectric coefficient, we compare it to the known cooling power of NIS microrefrigerators. After measuring $I_c(V)$ and $\eta(V)$, the cooling power for $\delta T \rightarrow 0$ can be determined using a generalization of Onsager relations to the nonlinear case [61],

$$I_Q(V) = \int (\eta(V) - I_c(V))\mathrm{d}V. \tag{7}$$

Figure 7a shows the cooling power for the FIS junction derived from the experimental data in Fig. 6b using (7). The data reproduce the known results from NIS microrefrigerators [63], with the addition of a small asymmetry due to the linear Peltier effect stemming from broken particle-hole symmetry. Again, this effect is fairly small for the samples investigated here, mainly due to the small spin polarization $P \approx 0.08$.

One can nevertheless use the experimental data to estimate the performance of an optimized device with $P = 1$. It is customary to define a coefficient of performance for coolers as the ratio of cooling power $I_Q$ to electric input power $I_c V$, i.e.,

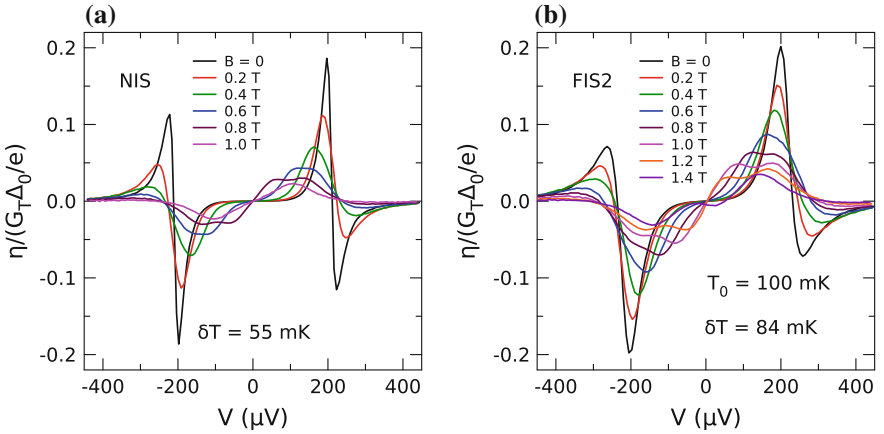


**Fig. 6** Nonlinear thermoelectric coefficient $\eta(V)$ as a function of bias voltage $V$ for different magnetic fields $B$ for a NIS sample (**a**) and for a FIS sample (**b**) [61]

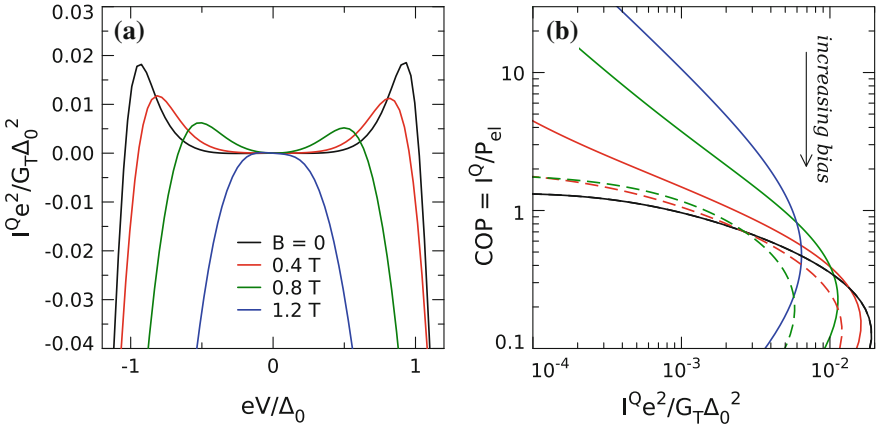


**Fig. 7** **a** Cooling power inferred from the experimental data in Fig. 6b. **b** Predicted coefficient of performance for a NIS cooler (dashed lines) and a FIS cooler with $P = 1$ (solid lines)

$COP = I_Q/I_c V$. Figure 7b compares the coefficient of performance of two hypothetical coolers, a NIS cooler (dashed lines) and a FIS cooler with $P = 1$ (solid lines), both with the spectral properties of the actual sample shown in Fig. 7a. For a wide range of magnetic fields and cooling powers, the FIS cooler is predicted to outperform the NIS cooler.

## 5 Conclusion and Outlook

We have discussed recent experimental and theoretical progress in the investigation of coupled spin and heat transport in nanoscale superconductors with a spin splitting of the density of states. In these systems, long-range thermal spin transport is observed, which is ultimately limited only by slow electron–phonon relaxation, at length scales exceeding the normal-state spin diffusion length by at least an order of magnitude. Coupled spin and heat transport leads to large spin-dependent thermoelectric effects, with Seebeck coefficients of the order of $-100$ μ V/K. These effects could have applications in superconducting spintronics, thermometry, particle and radiation detection, and microrefrigeration. While the samples used for the first proof-of-principle experiments were far from optimized, improved structures, e.g., using ferromagnetic insulators, could have exceptional performance [71]. Further efforts are needed to implement improved read-out schemes [64] and probe nonlocal effects and Onsager relations [56].

## References

1. F.S. Bergeret, A.F. Volkov, K.B. Efetov, Rev. Mod. Phys. **77**(4), 1321 (2005). https://doi.org/10.1103/revmodphys.77.1321
2. A.I. Buzdin, Rev. Mod. Phys. **77**(3), 935 (2005). https://doi.org/10.1103/revmodphys.77.935
3. M. Eschrig, Phys. Today **64**(1), 43 (2011). https://doi.org/10.1063/1.3541944
4. M.G. Blamire, J.W.A. Robinson, J. Phys.: Condens. Matter **26**(45), 453201 (2014). https://doi.org/10.1088/0953-8984/26/45/453201
5. J. Linder, J.W.A. Robinson, Nat. Phys. **11**(4), 307 (2015). https://doi.org/10.1038/nphys3242
6. M. Eschrig, Rep. Prog. Phys. **78**(10), 104501 (2015). https://doi.org/10.1088/0034-4885/78/10/104501
7. See also chapters 1, 2, 3 and 4 in this book
8. A.K. Feofanov, V.A. Oboznov, V.V. Bol'ginov, J. Lisenfeld, S. Poletto, V.V. Ryazanov, A.N. Rossolenko, M. Khabipov, D. Balashov, A.B. Zorin, P.N. Dmitriev, V.P. Koshelets, A.V. Ustinov, Nat. Phys **6**(8), 593 (2010). https://doi.org/10.1038/nphys1700
9. R. Meservey, P.M. Tedrow, Phys. Rep. **238**(4), 173 (1994). https://doi.org/10.1016/0370-1573(94)90105-8
10. D. Beckmann, J. Phys.: Condens. Mater **28**(16), 163001 (2016). https://doi.org/10.1088/0953-8984/28/16/163001
11. J.F. Žutić, S. Das Sarma, Rev. Mod. Phys. **76**(2), 323 (2004). https://doi.org/10.1103/revmodphys.76.323
12. G.E.W. Bauer, E. Saitoh, B.J. van Wees, Nat. Mater. **11**(5), 391 (2012). https://doi.org/10.1038/nmat3301
13. A.V. Chumak, V.I. Vasyuchka, A.A. Serga, B. Hillebrands, Nat. Phys. **11**(6), 453 (2015). https://doi.org/10.1038/nphys3347
14. M. Tinkham, J. Clarke, Phys. Rev. Lett. **28**(21), 1366 (1972). https://doi.org/10.1103/physrevlett.28.1366
15. G.S. Schmid, J. Low Temp. Phys. **20**(1-2), 207 (1975). https://doi.org/10.1007/bf00115264
16. J.P. Morten, A. Brataas, W. Belzig, Phys. Rev. B **70**(21), 212508 (2004). https://doi.org/10.1103/physrevb.70.212508
17. R. Meservey, P.M. Tedrow, P. Fulde, Phys. Rev. Lett. **25**(18), 1270 (1970). https://doi.org/10.1103/physrevlett.25.1270

18. P.M. Tedrow, R. Meservey, Phys. Rev. Lett. **26**(4), 192 (1971). https://doi.org/10.1103/physrevlett.26.192
19. D.R. Millis, J.A. Sauls, Phys. Rev. B **38**(7), 4504 (1988). https://doi.org/10.1103/physrevb.38.4504
20. T. Tokuyasu, J.A. Sauls, D. Rainer, Phys. Rev. B **38**(13), 8823 (1988). https://doi.org/10.1103/physrevb.38.8823
21. R. Meservey, P.M. Tedrow, R.C. Bruno, Phys. Rev. B **11**(11), 4224 (1975). https://doi.org/10.1103/physrevb.11.4224
22. F. Hübler, J. Camirand Lemyre, D. Beckmann, H. v. Löhneysen, Phys. Rev. B **81**(18), 184524 (2010). https://doi.org/10.1103/physrevb.81.184524
23. F.J. Jedema, A.T. Filip, B.J. van Wees, Nature **410**(6826), 345 (2001). https://doi.org/10.1038/35066533
24. F.J. Jedema, H.B. Heersche, A.T. Filip, J.J.A. Baselmans, B.J. van Wees, Nature **416**(6882), 713 (2002). https://doi.org/10.1038/416713a
25. F.J. Jedema, M.S. Nijboer, A.T. Filip, B.J. van Wees, Phys. Rev. B **67**(8), 085319 (2003). https://doi.org/10.1103/physrevb.67.085319
26. N. Poli, J.P. Morten, M. Urech, A. Brataas, D.B. Haviland, V. Korenivski, Phys. Rev. Lett. **100**(13), 136601 (2008). https://doi.org/10.1103/physrevlett.100.136601
27. I.V. Bobkova, A.M. Bobkov, Phys. Rev. B **93**(2), 024513 (2016). https://doi.org/10.1103/physrevb.93.024513
28. M.J. Wolf, C. Sürgers, G. Fischer, D. Beckmann, Phys. Rev. B **90**(14), 144509 (2014). https://doi.org/10.1103/physrevb.90.144509
29. M. Silaev, P. Virtanen, F.S. Bergeret, T.T. Heikkilä, Phys. Rev. Lett. **114**(16), 167002 (2015). https://doi.org/10.1103/physrevlett.114.167002
30. I.V. Bobkova, A.M. Bobkov, JETP Lett. **101**(2), 118 (2015). https://doi.org/10.1134/s0021364015020022
31. T. Krishtop, M. Houzet, J.S. Meyer, Phys. Rev. B **91**(12), 121407 (2015). https://doi.org/10.1103/physrevb.91.121407
32. F. Hübler, M.J. Wolf, D. Beckmann, H. v. Löhneysen, Phys. Rev. Lett. **109**(20), 207001 (2012). https://doi.org/10.1103/physrevlett.109.207001
33. M.J. Wolf, F. Hübler, S. Kolenda, H. v. Löhneysen, D. Beckmann, Phys. Rev. B **87**(2), 024517 (2013). https://doi.org/10.1103/physrevb.87.024517
34. M.J. Wolf, F. Hübler, S. Kolenda, D. Beckmann, Beilstein J. Nanotechnol. **5**, 180 (2014). https://doi.org/10.3762/bjnano.5.18
35. C.H.L. Quay, D. Chevallier, C. Bena, M. Aprili, Nat. Phys. **9**(2), 84 (2013). https://doi.org/10.1038/nphys2518
36. C.H.L. Quay, M. Weideneder, Y. Chiffaudel, C. Strunk, M. Aprili, Nat. Commun. **6**, 8660 (2015). https://doi.org/10.1038/ncomms9660
37. C.H.L. Quay, C. Dutreix, D. Chevallier, C. Bena, M. Aprili, Phys. Rev. B **93**(22), 220501 (2016). https://doi.org/10.1103/physrevb.93.220501
38. N.W. Ashcroft, N.D. Mermin, *Solid State Physics* (Holt, Rinehart and Winston, New York, 1976)
39. L. Onsager, Phys. Rev. **38**(12), 2265 (1931). https://doi.org/10.1103/physrev.38.2265
40. N.F. Mott, H. Jones, *The Theory of the Properties of Metals and Alloys* (Clarendon Press, Oxford, 1936)
41. J. Kondo, Prog. Theor. Phys. **34**(3), 372 (1965). https://doi.org/10.1143/ptp.34.372
42. C.W.J. Beenakker, A.A.M. Staring, Phys. Rev. B **46**(15), 9667 (1992). https://doi.org/10.1103/physrevb.46.9667
43. V.L. Ginzburg, Rev. Mod. Phys. **76**(3), 981 (2004). https://doi.org/10.1103/revmodphys.76.981
44. Y.M. Gal'perin, V.L. Gurevich, V.I. Kozub, Sov. Phys. JETP **39**(4), 680 (1974)
45. C.D. Shelly, E.A. Matrozova, V.T. Petrashov, Sci. Adv. **2**(2), e1501250 (2016). https://doi.org/10.1126/sciadv.1501250

46. C.J. Pethick, H. Smith, Phys. Rev. Lett. **43**(9), 640 (1979). https://doi.org/10.1103/physrevlett.43.640
47. P. Virtanen, T.T. Heikkilä, Phys. Rev. Lett. **92**(17), 177004 (2004). https://doi.org/10.1103/physrevlett.92.177004
48. J. Clarke, B.R. Fjordbøge, P.E. Lindelof, Phys. Rev. Lett. **43**(9), 642 (1979). https://doi.org/10.1103/physrevlett.43.642
49. J. Eom, C.J. Chien, V. Chandrasekhar, Phys. Rev. Lett. **81**(2), 437 (1998). https://doi.org/10.1103/physrevlett.81.437
50. Parsons, I.A. Sosnin, V.T. Petrashov, Phys. Rev. B **67**(14), 140502 (2003). https://doi.org/10.1103/physrevb.67.140502
51. V. Chandrasekhar, Supercond. Sci. Technol. **22**(8), 083001 (2009). https://doi.org/10.1088/0953-2048/22/8/083001
52. Z. Jiang, V. Chandrasekhar, Phys. Rev. B **72**(2), 020502 (2005). https://doi.org/10.1103/physrevb.72.020502
53. F. Giazotto, M.J. Martínez-Pérez, Nature **492**(7429), 401 (2012). https://doi.org/10.1038/nature11702
54. M. José Martínez-Pérez, F. Giazotto, Nat. Commun. **5**, 3579 (2014). https://doi.org/10.1038/ncomms4579
55. S. Kolenda, J. Wolf, M.D. Beckmann, Phys. Rev. Lett. **116**(9), 097001 (2016). https://doi.org/10.1103/physrevlett.116.097001
56. P. Machon, M. Eschrig, W. Belzig, Phys. Rev. Lett. **110**(4), 047002 (2013). https://doi.org/10.1103/physrevlett.110.047002
57. P. Machon, M. Eschrig, W. Belzig, New J. Phys. **16**(7), 073002 (2014). https://doi.org/10.1088/1367-2630/16/7/073002
58. Ozaeta, P. Virtanen, F.S. Bergeret, T.T. Heikkilä, Phys. Rev. Lett. **112**(5), 057001 (2014). https://doi.org/10.1103/physrevlett.112.057001
59. M.S. Kalenkov, A.D. Zaikin, Phys. Rev. B **90**(13), 134502 (2014). https://doi.org/10.1103/physrevb.90.134502
60. M.S. Kalenkov, A.D. Zaikin, Phys. Rev. B **91**(6), 064504 (2015). https://doi.org/10.1103/physrevb.91.064504
61. S. Kolenda, P. Machon, D. Beckmann, W. Belzig, Beilstein J. Nanotechnol. **7**, 1579 (2016)
62. J.A.X. Alexander, T.P. Orlando, D. Rainer, P.M. Tedrow, Phys. Rev. B **31**(9), 5811 (1985). https://doi.org/10.1103/physrevb.31.5811
63. F. Giazotto, T.T. Heikkilä, A. Luukanen, A.M. Savin, J.P. Pekola, Rev. Mod. Phys. **78**(1), 217 (2006). https://doi.org/10.1103/revmodphys.78.217
64. F. Giazotto, P. Solinas, A. Braggio, F.S. Bergeret, Phys. Rev. Appl. **4**(4), 044016 (2015). https://doi.org/10.1103/physrevapplied.4.044016
65. J.S. Moodera, X. Hao, G.A. Gibson, R. Meservey, Phys. Rev. Lett. **61**(5), 637 (1988). https://doi.org/10.1103/physrevlett.61.637
66. X. Hao, J.S. Moodera, R. Meservey, Phys. Rev. B **42**(13), 8235 (1990). https://doi.org/10.1103/physrevb.42.8235
67. P.M. Tedrow, J.E. Tkaczyk, A. Kumar, Phys. Rev. Lett. **56**(16), 1746 (1986). https://doi.org/10.1103/physrevlett.56.1746
68. A.A. Abrikosov, L.P. Gor'kov, Sov. Phys. JETP **12**, 1243 (1961)
69. K. Maki, Prog. Theor. Phys. **31**(5), 731 (1964). https://doi.org/10.1143/ptp.31.731
70. J.T. Muhonen, M. Meschke, J.P. Pekola, Rep. Prog. Phys. **75**(4), 046501 (2012). https://doi.org/10.1088/0034-4885/75/4/046501
71. J. Linder, M.E. Bathen, Phys. Rev. B **93**(22), 224509 (2016). https://doi.org/10.1103/physrevb.93.224509

# Lasing in Circuit Quantum Electrodynamics


**G. Oelsner and E. Il'ichev**

**Abstract** This chapter is devoted to special realizations of lasing on single artificial atoms. It is demonstrated that special properties of quantum systems, implemented as an electrical circuit, may be explored to repeat original quantum optic experiments and extend them to new regimes. As we will discuss, this can, for example, lead to the realizations of lasing that only requires two states of the artificial atom. There we make use of the relaxation and of special coupling properties that naturally are achieved in the field of the circuit quantum electrodynamics.

## 1 Introduction

Rapidly progressing miniaturization of solid-state scalable cryogenic devices reveals exciting novel physical phenomena and creates new challenges for their acceptable interpretation within modern quantum theory. Recent experiments have convincingly demonstrated that superconducting Josephson circuits, routinely used for superconducting electronics, under certain conditions, can be in a superposition of macroscopically distinct quantum states.

For such devices, fundamental concepts of quantum mechanics—quantum coherence and entanglement—plays a crucial role for describing of intriguing properties of superconducting structures discovered in last years. The better understanding of fundamental limitations on quantum coherence and entanglement in realistic Josephson circuits is extremely important from both fundamental and technological points

G. Oelsner · E. Il'ichev (✉)
Leibniz Institute of Photonic Technology, P.O. Box 100239, 07702 Jena, Germany
e-mail: evgeni.ilichev@leibniz-ipht.de
URL: https://www.leibniz-ipht.de

G. Oelsner
e-mail: gregor.oelsner@leibniz-ipht.de

E. Il'ichev
Novosibirsk State Technical University, 20 Karl Marx Avenue,
630092 Novosibirsk, Russia



A. Sidorenko (ed.), *Functional Nanostructures and Metamaterials for Superconducting Spintronics*, NanoScience and Technology,
https://doi.org/10.1007/978-3-319-90481-8_9

of view. In general, these specific quantum phenomena can be exploited to develop new scenarios for quantum information processing, sensing, and imaging.

The unit cell of such Josephson circuits is an effective two-level quantum system in a microwave domain, which is usually called a quantum bit or qubit. The implementation of Josephson quantum circuits for certain applications requires control and manipulation of qubits states. Because qubits are basically individual quantum systems; this task is similar to the well-known long-standing problem in quantum optics—realization of the control and manipulation of the dynamics of a microscopic quantum particle. This field has attracted the interest of experts since it can potentially lead to an emergence of novel physics.

One of the main systems providing certain achievement of these goals is cavity quantum electrodynamics (QED) in the regime of strong particle–photon coupling [1]. This strong interaction between the particle (for instance, a natural atom) and the cavity field (usually in the optical domain) is enabled by high resonator quality, allowing coherent interactions to dominate over dissipation. In particular, these systems can be used for investigations of quantum feedback and control, real-time observation of quantum dynamics [2], and more generally the study of quantum coherence features. Note that this activity has been awarded the Nobel Prize in Physics in 2012 (Serge Haroche and David J. Wineland "for ground-breaking experimental methods that enable measuring and manipulation of individual quantum systems").

In contrast to cavity QED, in the field of circuit QED microwave photons are stored in a resonator (for instance, on-chip, superconducting, and quasi-one-dimensional) and coupled to a solid-state qubit, which can be seen as superconducting macroscopic quantum system.

Properties of the systems based on the cavity QED or circuit QED are defined by the fundamental interaction between light and matter. For instance, to realize amplification of the optical signal, we can put many atoms to a cavity, excite them to get population inversion and, by making use of a simulated emission, obtain amplification. This effect is well known as lasing. For a single atom in a cavity QED system, it is more complicated to achieve because of the relatively weak atom–cavity coupling.

In contrast, for circuit QED, because of the relatively large size of the superconducting qubits, a reasonable coupling can be easily achieved. Recently even ultrastrong coupling [3] has been experimentally demonstrated. Therefore, single atom lasing can be realized.

In this chapter, we present results of the recent activity aiming to implement single atom lasing based on the circuit QED hardware.

## 2 Requirements for Lasing

A laser relies on the possibility of creating an inverse level population for a certain material and the coupling of the corresponding transition energy between the levels to a single mode of a low-loss cavity. Different schemes for achieving this population

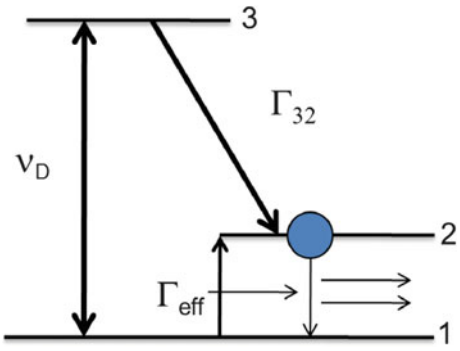


**Fig. 1** Simplified illustration for lasing in a three-level system, as explained in the main text

inversion have been discussed and realized. Especially, the first realization of lasing reported in the microwave domain [4] used a quite simple idea. There, the molecules that showed level inversion are sorted from the rest and brought into a cavity. Still the usual way of introducing a laser is done on explaining the relevant processes on a three-level system [5].

The system is strongly driven with a frequency $\nu_D$ between the lowest (first) and the highest (third) energy level (see Fig. 1). This driving approximately equalizes the population between these states since the rates for stimulated emission and absorption are equal. With a fast relaxation $\Gamma_{32}$ from the highest to the middle energy state together with a very small one $\Gamma_{21}$ between the lowest two levels, the population is concentrated on the second level. Thus, population inversion for these lowest states is achieved. In principle, the above-described processes can be summarized by an effective excitation rate $\Gamma_{\text{eff}}$ between the levels 1 and 2. Bringing this system into a cavity with high-quality factor leads to light amplification and thus lasing. This simple scheme is illustrated in Fig. 1.

For achieving this lasing effect, the ratio between the rates is of critical importance. The effective rate of excitation (due to pumping and relaxation) should be much faster than the coupling of the cavity field to the transition between the lowest levels. That is because the level inversion needs to be achieved before a photon can be absorbed by an atom. Still this coupling should be faster than the loss rate of the cavity for one photon inside to create another by stimulated emission before leaving the cavity. These requirements lead to the introduction of a lasing threshold given by the combined losses of the medium and the cavity that needs to be compensated by the pumping power. Note, more complicate level schemes can be used to improve the order of level inversion. For example, another level zero can be introduced below the lowest one on Fig. 1. The pumping is then carried out between this new lowest (zero) and the highest (third) level. An additional fast relaxation from the first to the zero state then lowers the population of level one and therewith increases the amount of population inversion between first and second level.

Usually in lasers, the coupling of an individual atom or molecule to the cavity field is rather weak. In this case, a large number of atoms is required to achieve the lasing effect. Furthermore, single atoms only have a negligible impact to the dynamics of the laser. A special case is realized if only a single atom is used. Such a single atom laser was only recently experimentally demonstrated in the optical domain [6]. There the regime of strong coupling between atom and cavity is required. The experimental realization here is based on the trapping of individual atoms [7–9] and their laser cooling [10, 11]. Those are methods that were developed in the field of cavity QED [12].

A single atom laser has certain difference to its counterparts involving a gain medium. First, as shown in the experiment, no pumping laser threshold is observed, meaning that at any pump power the light amplification is achieved. With choosing the right atom and a certain atomic transition together with achieving the required high quality of the cavity, all requirements as discussed in Fig. 1 are already fulfilled. In other words, as soon as the driving is started the internal rates of the system create the level inversion. As there is no additional medium, no other dissipative channels are present. Second, additional effects connected to the strong atom–photon interaction may occur. As example, the splitting of the states due to the driving (Autler–Townes effect) may be large for strong applied powers, such that atomic transition can be detuned from the cavity mode. Such "parasitic" effects, in principle, could interrupt the lasing process.

## 3 Circuit QED with Superconducting Quantum Systems

Superconducting macroscopic quantum systems rely on the quantization of the magnetic flux inside a closed loop [13, 14] or the quantization of the number of Cooper pairs on a superconducting island. Circuits of the first kind are usually called flux qubits [15] while members of the second type are named as charge qubits [16] or transmons [17].[1] Josephson junctions [18] serve as main building block for such quantum systems. The usual tunnel junction realization used in this field consists of a thin insulating layer usually formed by aluminum oxide between two superconducting electrodes. Then, Cooper pairs can tunnel between the superconducting islands and a flux quantum can cross a superconducting weak link providing a coupling of different charge or flux states, respectively. In Fig. 2, the flux and charge qubit are depicted schematically.

The type of qubit is defined by the parameters in the junction. Namely, the ratio between the Josephson coupling energy $E_J = I_C \Phi_0 / 2e$ and the charging energy $E_C = 2e^2/C$ defines the well-defined quantum variable phase or charge. Here, $I_C$ and $C$ are the junction's critical current and capacitance, respectively. The magnetic flux quantum $\Phi_0$ and the fundamental electric charge $e$ both also enter into the def-

[1] Note, this objects were first and are still considered as promising candidates to be main building blocks for quantum computing. That is the origin for the term qubit, as quantum bit.

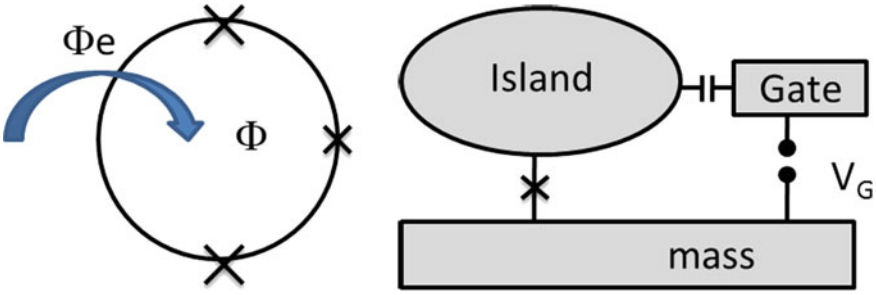


**Fig. 2** Schematics of a flux and a charge qubit are shown in the left and right image, respectively. Josephson junctions are indicated as crosses. The flux qubit consists of a superconducting ring interrupted by several Josephson junctions. Here, we present on possible realization with three junctions. The sizes and properties of the junctions define the qubit's parameters and the inductance of the ring is a measure of its coupling to external fields. Also, a flux bias $\Phi_e$ is required for proper qubit operation. The charge qubit is quite similar. The parameters here are defined by parameters of the Josephson junction as well and a voltage bias via a capacitance is required

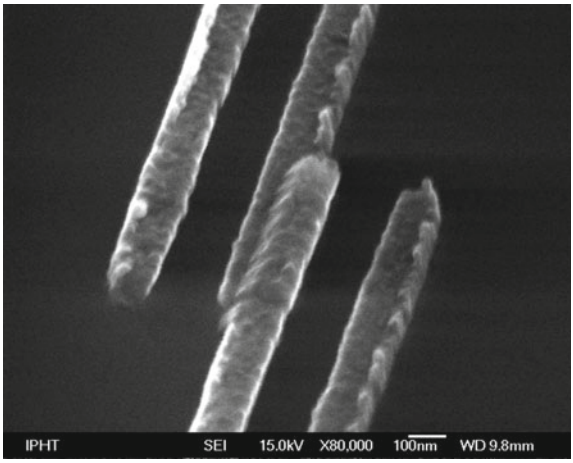


**Fig. 3** SEM-image of a single sub-micron Josephson junction fabricated by the shadow evaporation technique. The junction is formed in the overlap region of the two strips in the middle. A more detailed description of the fabrication process is presented in [19]

initions. In standard processes as, for example, the two-angle shadow evaporation technique for fabrication of aluminum-based Josephson junctions, the above energies can be influenced by the junction's size and by the thickness of the isolating barrier. As discussed in [19], sub-micron-sized junctions are required for achieving the appropriate energy scale. The picture of a typical junction is shown in Fig. 3.

Two main contributions to the qubit energy can be identified. They are first the self-energy of the corresponding qubit in an external magnetic or electric field for a certain number of quanta and secondly the coupling between different such number

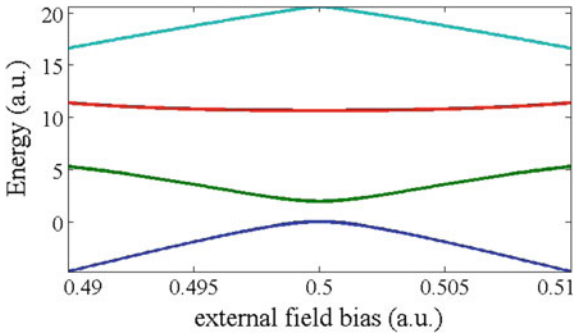


**Fig. 4** The four lowest energy levels of a flux qubit with its typical parameters are shown as a function of the external control field. As it is visible, the energy difference between the lowest to states is significantly smaller than to the other levels

states. The corresponding parameters for the lowest to levels can be introduced, respectively, as the energy bias $\varepsilon$ and the tunnel splitting at the energetic degeneracy $\Delta$. The interplay of self-energy and coupling forms a discrete energy spectrum and enables the coupling of external fields. They can be used for the modulation of energy splittings and transitions between energy levels. As example, numerical estimates of the lowest four levels of a typical flux qubit are given in Fig. 4.

Furthermore, the nonlinearity in the current-phase relation of the Josephson junction makes the energy levels non-equidistant. This property allows an individual addressing of state transitions, and a complete analogy to real atoms is achieved. Therefore, the term artificial atom is often used for corresponding superconducting circuits, although the transition frequencies lay in the GHz range and thus about six orders of magnitude below the optical ones of atoms. The dynamics of the lowest two states can be described by the use of the Pauli matrices $\sigma_x$, $\sigma_y$, and $\sigma_z$. The Hamiltonian of such undisturbed qubit is

$$H_q = \frac{h\upsilon_q}{2}\sigma_z. \tag{1}$$

Here, the transition frequency of the qubit is introduced as $\upsilon_q$. Its value depends on the energy bias and tunnel splitting as $\nu_q = \sqrt{\varepsilon^2 + \Delta^2}$.

An important difference between real and such superconducting artificial atoms is their size and therewith their coupling to external fields. For example, the diameter of a flux qubit is of the order of ten microns and the states of the qubit have a persistent current of about 100 nA. These values result in a magnetic moment that is about $10^6$ times the value of the Bohr magneton. This makes it rather easy to achieve the strong coupling regime as required for single atom lasing. SEM images from fabricated flux and charge qubits are shown in Fig. 5.

The role of the optical cavity is taken by superconducting resonators. Often, coplanar waveguide designs are used [20]. The central line is then interrupted twice,

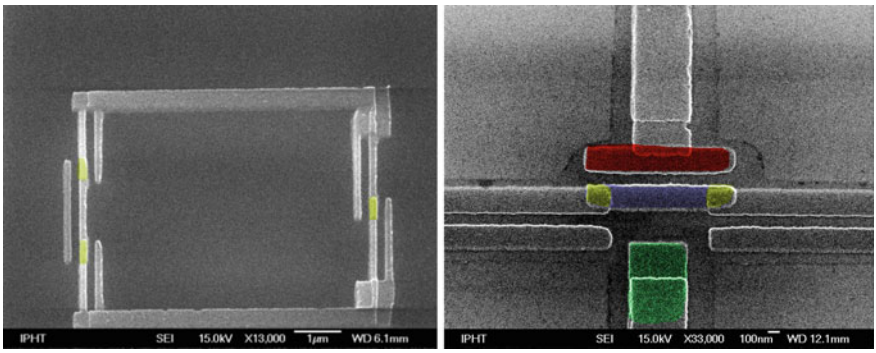


**Fig. 5** SEM images of a flux and a charge qubit are shown in the left and right picture, respectively. Josephson junctions are colored in yellow. The flux qubit consists of a superconducting loop interrupted by three junctions. The charge qubit is formed by the blue-colored island together with two gate electrodes. The green is heavily filtered and used for applying an energy bias. The red connects the charge qubit to a microwave line which can be used for a qubit spectroscopy

and the distance of the so formed capacitances defines the resonant frequency $\upsilon_r$. Due to the use of lossless materials, high-quality factors are achievable [21]. Standard quantum oscillator theory can be applied for the resonators [22], and for describing the dynamics, the photon creation $a^\dagger$ and annihilation operators $a$ can be used.

The coupling between an artificial atom and such a cavity can be engineered by special circuit design. The magnetic and electric oscillating fields produced by the standing electromagnetic wave inside of the resonator will couple over the mutual inductance or capacitance to the flux or charge qubit, respectively. In both this coupling process can be described by a coupling Hamiltonian

$$H_c = (g_x\sigma_x + g_z\sigma_z)\left(a + a^\dagger\right), \tag{2}$$

where $g_x$ and $g_x$ are the corresponding transverse and diagonal coupling terms. The occurrence of the diagonal coupling is a unique feature of tunable two-level systems at results from the superposition of flux and charge states for the respective qubit type. It can lead to effects that are not observable in first order at comparable real atoms. An example will be discussed below.

The large achievable coupling constant of the superconducting quantum bits is connected to similar strong couplings to external noise fields. Thus, strong dissipative processes are introduced which need to be considered for planning experiments and theoretical analysis. They are caught theoretically by introducing Lindblad terms to the corresponding equations. For a qubit, this includes relaxation with rate $\Gamma_r$ and pure dephasing $\Gamma_\varphi$ caused by low-frequency noise. The Lindblad term then reads [22, 23]

$$L = \frac{\Gamma_r}{2}(2\sigma_-\rho\sigma_+ - \sigma_+\sigma_-\rho - \rho\sigma_+\sigma_-) + \frac{\gamma_\varphi}{2}(\sigma_z\rho\sigma_z - \rho). \tag{3}$$

Here $\rho$ denotes the density matrix. Note, a thermal excitation can be neglected because the system is cooled far below a temperature that corresponds to the transition frequencies (cooled to about 10 mK while 120 mK–1 GHz). Both rates are typical in the order of MHz. With reducing the controllability of the artificial atoms also better coherence values are achievable [17, 24].

To conclude, with the superconducting artificial atoms and resonators, their coupling and relaxations, a complete analogy to the field of cavity QED in optics is achieved. This field is called circuit QED since all components can be engineered and are of macroscopic size. The strong coupling regime is therefore easily achieved, and prominent experiments as the vacuum Rabi splitting [25, 26], electromagnetically induced transparency [27], or the Autler–Townes effect [28] have been repeated at the microwave frequency range. In the following, several realized lasing schemes are presented.

## 4 Lasing by Single Superconducting Artificial Atoms

### *4.1 Standard Lasing Scheme*

The first realization of the lasing effect with a single artificial atom (in that case a Josephson-junction charge qubit) embedded in a superconducting resonator was demonstrated quite recently [29]. Such type of qubits is convincingly described by two different charge states. These states differ by one Cooper pair in the island.

In order to create a population inversion of the qubit levels, a special drain electrode was fabricated. This electrode is connected to the island via a tunnel junction (schematic see Fig. 6). A voltage applied to the drain electrode above the threshold value of $(2G + E_C)/e$ (where $G$ is the superconducting gap energy) causes two sequential single electron tunneling events by breaking a Cooper pair on the island. This process is described by the transition between energy levels which correspond to one $|1\rangle$ and zero $|0\rangle$ Cooper pairs on the island, respectively. After a tunneling of the "first" electron, the energy of the island increases the order of $G$ providing system "pumping", which is schematically shown in Fig. 1 by a transition between a first and a third level. The tunneling of the "second" electron provides the relaxation from the third level to the $|0\rangle$ energy level.

As it is well known from charge qubits dynamics, for relatively large positive gate voltage, the upper eigenstate of the qubit is nearly the $|0\rangle$ state. This means that the mechanism described above results a level population inversion. When the qubit level spacing is adjusted to the resonant frequency of a superconducting resonator of this integrated system, the energy accumulated in the qubit is transferred into the resonator as a photon. Here, the photons are generated by the same atom and one by one. This example clearly demonstrates that as soon as any weak pumping is applied, the lasing takes places. Therefore, for a single atom lasing, as we discussed above, there is no pumping threshold.

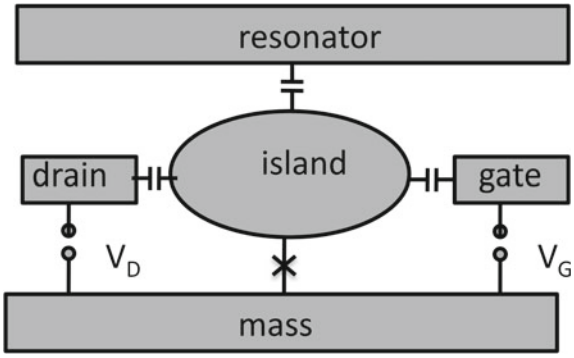


**Fig. 6** Schematic of the measurement setup for creating level inversion on a charge qubit. A drain electrode is added to break Cooper pairs and remove single electrons from the island. Also, a coupling to a resonator is provided by a capacitance

## *4.2 Dressed-State Lasing*

In contrast to the above presented and generally discussed lasing principle, for the dressed-state lasing only two instead of the minimal three levels are required to achieve the needed inverse population. In the following, the description is restricted to a flux qubit coupled to superconducting coplanar waveguide resonator. Still, the same applies to any tunable system with similar coupling to cavity fields.

In a first step, the inverse population needs to be created. For that purpose, a strong driving signal is applied close to one of the resonators harmonics. This ensures a good coupling of the microwave field to the artificial atom and large achievable photon numbers. The Hamiltonian for such a coupled and driven system is given by

$$H_d = h\upsilon_h\left(a_h^\dagger a_h + \frac{1}{2}\right) + \frac{h\upsilon_q}{2}\sigma_z + h(g_x\sigma_x + g_z\sigma_z)\left(a_h + a_h^\dagger\right) \tag{4}$$

Here, the subscript $h$ denotes the resonant frequency and ladder operators ($a_h$ $a_h^\dagger$) of the considered harmonic. Close to the resonant point $\upsilon_h = \upsilon_q$, the transverse coupling leads to an avoided level crossing due to the superposition of the states $|gN+1\rangle$ and $|eN\rangle$, where $N$ is the mean photon number inside the cavity and $g$ ($e$) denotes the qubit's ground (excited) state.

Therefore, a new basis of states given by

$$\begin{aligned} |1N\rangle &= \cos\theta|eN\rangle + \sin\theta|gN+1\rangle, \\ |2N\rangle &= \sin\theta|eN\rangle - \cos\theta|gN+1\rangle, \end{aligned} \tag{5}$$

can be used to discuss the system dynamics. Here, $\theta$ denotes the mixing angle between the states. The Hamiltonian is then modified to

$$H = h\upsilon_h \hat{n} + h\frac{\widehat{\Omega}_R}{2}. \tag{6}$$

The newly introduced diagonal operators $\hat{n} = \sum_N N(|1N\rangle\langle 1N| + |2N\rangle\langle 2N|)$ and $\widehat{\Omega}_R = \sum_N \Omega_R(N)(|1N\rangle\langle 1N| - |2N\rangle\langle 2N|)$ [22, 30] describe, respectively, the total number of excitations in the systems and the Rabi splitting. Note that the coupled qubit–harmonic field system is now written in the dressed-state basis. The obtained energy level structure is just a ladder of Rabi-split states. At each step of this ladder, the total number of photons, where the qubit's excited state is calculated as one and the ground state as zero, is conserved. The splitting of the two states at each step is given by the generalized Rabi frequency

$$\Omega_R = \sqrt{\delta_{qh}^2 + \Omega_0^2}, \tag{7}$$

which includes the detuning $\delta_{qh} = \upsilon_q - \upsilon_h$ between harmonic and qubit and the on-resonance splitting $\Omega_0$.

Furthermore, for high driving, the dependency of the Rabi frequency on the photon number can be neglected. Assuming a constant value $\Omega_R(N) = \Omega_R(\langle N\rangle)$, the photon degree of freedom can be traced out and an effective two-level system is found. Here, $\langle N\rangle$ is the mean value of photons of the coherent state in the driving resonator mode. The Hamiltonian of this effective two-level quantum system is the one of a two-level system and reads

$$\widehat{H} = \frac{h\Omega_R}{2}\sigma_z. \tag{8}$$

It is important to note that together with the rescaling of the energy levels also the populations of the levels are modified as well by the driving. It can be understood by making use of a simple example: A direct resonance of a strong driving with a two-level system equalizes the population on these two states. On the other hand, as seen in Fig. 7, for large positive detunings the lower Rabi level $|2N\rangle$ is formed by the qubit's ground state (horizontal levels in the figure), while for negative detunings the excited qubit state (hyperbolic line) defines the ground state. Assuming that a relaxation process brings the qubit always from the excited to the ground state, one can conclude that the level population in the dressed-state basis depends on the qubit–resonator detuning. This effect is illustrated in Fig. 8.

These illustrative considerations can be theoretically described by transforming the dissipative processes of the qubit that are described by (3), to the dressed-state basis [22, 30, 31]. For a change of the population, an effective excitation rate is introduced. The Lindblad term for the effective two-level system is modified and compared to the corresponding term for the qubit, to

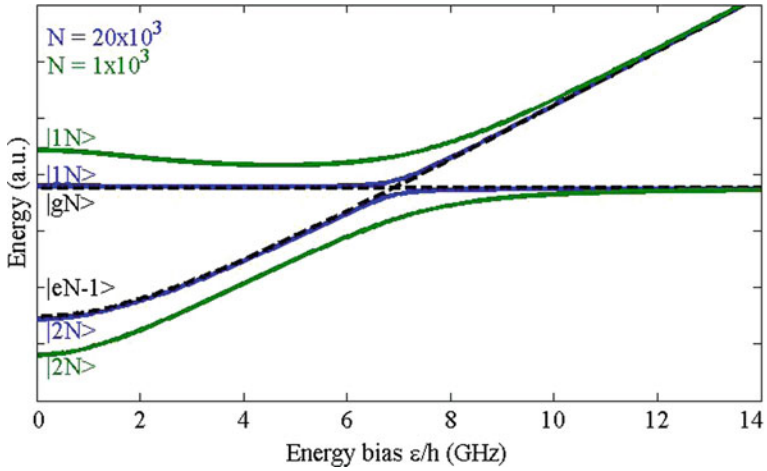


**Fig. 7** Illustration of the construction of the dressed-state basis in the vicinity of the resonance between the qubit's level splitting and the driving signal

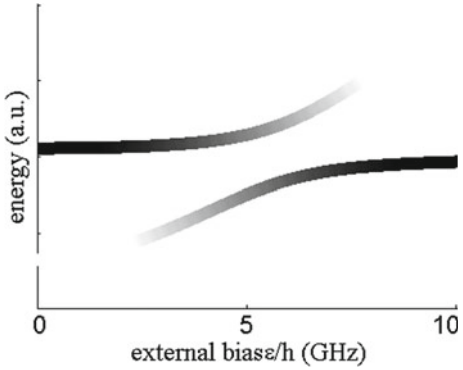


**Fig. 8** For a pair Rabi-split states at a high photon number in the resonator, the population of the levels is indicated by the strength of the line. At the resonance point close to a bias of 5 GHz, an equal distribution between the upper and lower Rabi level is achieved because of perfect superposition. In other words, the mixing angle $\theta$ between the states is $\pi/4$. If the qubit frequency is lower than the one of the driven resonator mode, level inversion of the Rabi-split states is achieved

$$\widehat{L} = \frac{\widehat{\Gamma}_r}{2}(2\sigma_-\rho\sigma_+ - \sigma_+\sigma_-\rho - \rho\sigma_+\sigma_-) + \frac{\widehat{\Gamma}_e}{2}(2\sigma_+\rho\sigma_- - \sigma_-\sigma_+\rho - \rho\sigma_-\sigma_+) + \frac{\hat{\gamma}_\varphi}{2}(\sigma_z\rho\sigma_z - \rho). \tag{9}$$

Here, the effective rates of relaxation $\widehat{\Gamma}_r$, excitation $\widehat{\Gamma}_e$, and pure dephasing $\hat{\gamma}_\varphi$ are used. Their dependency on the detuning and on-resonance Rabi splitting can be

found as it is demonstrated for example in [22]. Importantly, the difference between excitation and relaxation is given by

$$\widehat{\Gamma}_e - \widehat{\Gamma}_r = -\frac{\delta_{qh}}{\Omega_R}. \tag{10}$$

Above equation describes an equal effective relaxation and excitation in direct resonance at $\delta_{qh} = 0$. Away from the resonance point, the size of the detuning determines whether excitation ($\delta_{qh} < 0$) or relaxation is dominant ($\delta_{qh} > 0$). Therefore, in consistency with Fig. 8, it predicts a level inversion of the Rabi-split states.

Beside the realized level inversion, a coupling of this effective two-level system to the mode of a cavity is required for lasing. Here we note that the electric dipole moment of real atoms does not allow transitions between the pair of dressed states on one step of the dressed ladder. Also in optics, the achievable Rabi splittings is well below the eigenfrequencies of the system. On the other hand, strong couplings can be achieved for artificial atoms [3] providing level splittings of the size of the transition frequencies of the system already for moderate driving photon numbers. Additionally, it can be shown that the diagonal coupling term (proportional to $\sigma_z$ in (2)) results in the required coupling between the effective two-level system (given by (8) and (9)) and the cavity mode [22, 30]. The dressed qubit–resonator system then shows complete analogy to a standard qubit–resonator system. This statement can be summarized by the Hamiltonian

$$\widehat{H} = h\upsilon_h\left(a^\dagger a + \frac{1}{2}\right) + \frac{h\Omega_R}{2}\sigma_z + h\left(\frac{g_z\Omega_{R0}}{\Omega_R}\sigma_x + \frac{g_z\delta_{qh}}{\Omega_R}\sigma_z\right)\left(a^\dagger + a\right) \tag{11}$$

A possible experimental realization of lasing using a dressed system is as follows. A system of an artificial atom coupled to a cavity is strongly driven at one of the harmonics of the resonator. This driving rescales the energy levels and populations as discussed above. That system is probed with a weak input signal at the resonator's fundamental mode. If for a certain driving power and energy bias the effective two-level system that is created by dressing the qubit states is in resonance with the cavity mode, amplification and damping are observable. Whether higher or lower transmission is measured depends on the sign of the qubit's detuning $\delta_{qh}$.

In the following, the artificial atom is realized as a flux qubit coupled to a coplanar waveguide resonator. Its minimal level splitting $\Delta/h$ is 6 GHz, and the coupling constant between atom and cavity is 8 MHz. These parameters can be extracted from spectroscopic or ground-state measurements [32]. The resonator has a fundamental mode frequency $\upsilon_r$ of 2.5 GHz and a quality factor of about 70,000. A strong microwave signal is applied at the resonators fifth harmonic frequency and a weak probe signal close to its fundamental mode. The transmission amplitude for varying energy bias $\varepsilon$ of the qubit is shown in Fig. 9.

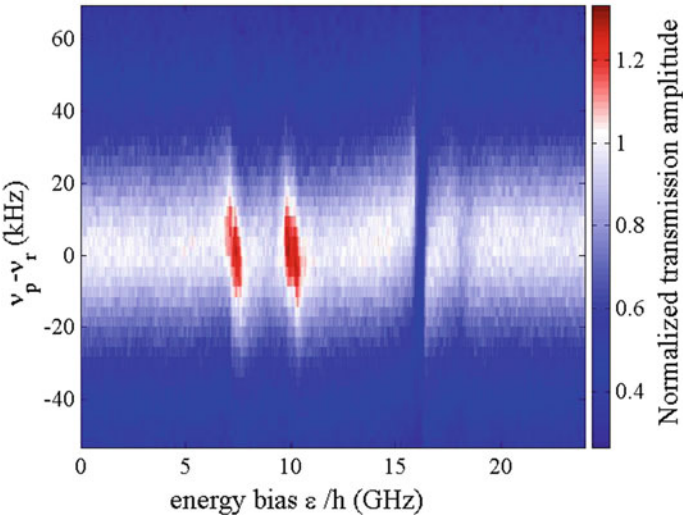


**Fig. 9** Transmission amplitude at different energy bias and for varying probing frequency $\upsilon_p$. At each bias point, the transmission as a function of the probe frequency reveals a Lorentzian-shaped curve. The system is strongly driven at the fifth harmonic. Its resonance with the qubit thus lays at an energy bias of about 11 GHz. At lower values, two regions of amplification are found. They correspond to the one- and two-photon resonance of the Rabi-split states with the qubits fundamental mode, $\Omega_R = k\nu_r$, with $k \in \{1, 2\}$. Also, the corresponding damping processes are visible at the resonance points with positive detuning

Experimentally, two bias values for amplification and damping are found. One is always corresponding to the one-photon interaction of the cavity mode with the Rabi-split states while the other is the similar two-photon process. The experimental results demonstrate a maximal increase of transmission in the order of 25% compared to undisturbed resonator. To estimate the influence of the external control parameters to this amplification effect, first, the probe power can be varied. Results of such experiment are presented in Fig. 10 for the two-photon amplification.

With decreasing probing powers the measured amplification is increased while it is always observed at the same energy bias. As discussed before for single atom lasing, the contributing rates, namely effective excitation, coupling to the cavity, and loss rate of the cavity, will define the power transferred to the cavity mode. Therefore, the amplification adds a constant signal to the probe beam. The increase in transmission then leads from its definition as output signal divided to input signal. Due to this division with decreasing probe signal and constant added signal by the resonance interaction with the level inversed Rabi levels, these measurement results are observed.

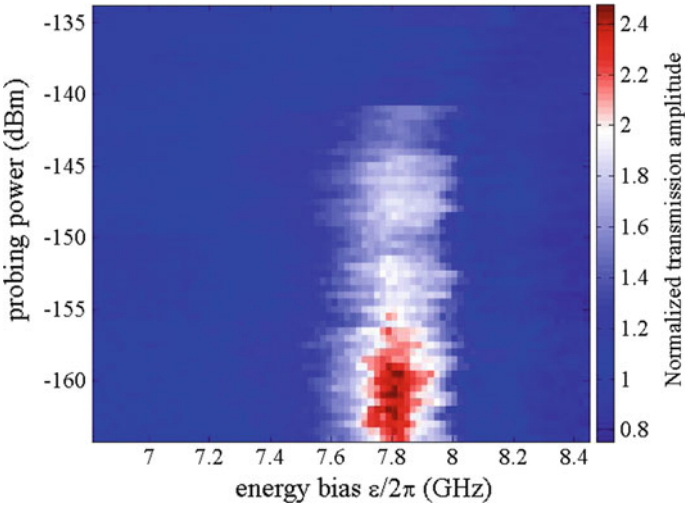


**Fig. 10** Probe power dependence of the two-photon amplification. Varying the probe power has no influence to the resonance condition that is $\Omega_R = 2\nu_r$. In other words, the bias point for amplification is stable. Still, the magnitude of amplification depends strongly on the probing power. With higher probing powers, the measured amplification is decreased

As seen from (7), two values contribute to the Rabi frequency. The first is the photon number in the driven harmonic of the resonator, represented by the on-resonance Rabi frequency $\Omega_{R0}$. The second is the qubit's energy bias that enters to the detuning. To keep the resonance condition $\Omega_R = k\nu_r$ at any energy bias, the driving strength should be adjusted. The result of an experimental test of this statement is shown in Fig. 11 for the two-photon amplification.

Note, the qubit's resonance with the driven harmonic is at a bias value of around 11 GHz. Thus for smaller values of the bias, the detuning is increased. To keep the resonance condition between the Rabi-split states and the fundamental cavity mode, the driving strength must be decreased. This explains the shift of the amplification point in the bias—driving power plane. Furthermore, the value of amplification also depends on the chosen parameters. An optimal point with maximal amplification is observed at a bias of about 7.6 GHz. The occurrence of optimal conditions results from the detuning-dependent effective excitation and coupling constant. The diagonal coupling in Hamiltonian (11) scales for small on-resonance splitting or large detuning with $1/\delta_{qh}$ while the difference between excitation and relaxation rate scales with $\delta_{qh}$.

Finally, because the amplification depends on the input probing power, it is worthwhile to determine the power emitted from the dressed qubit–resonator system. For this purpose, a special sample was designed, where a gold resistor is placed next to the flux qubit to enhance the relaxation [30]. This is because of the relaxation of the artificial atom changes to the effective excitation in the dressed basis at negative detunings. The qubit and resonator parameters, as well as optimal conditions for

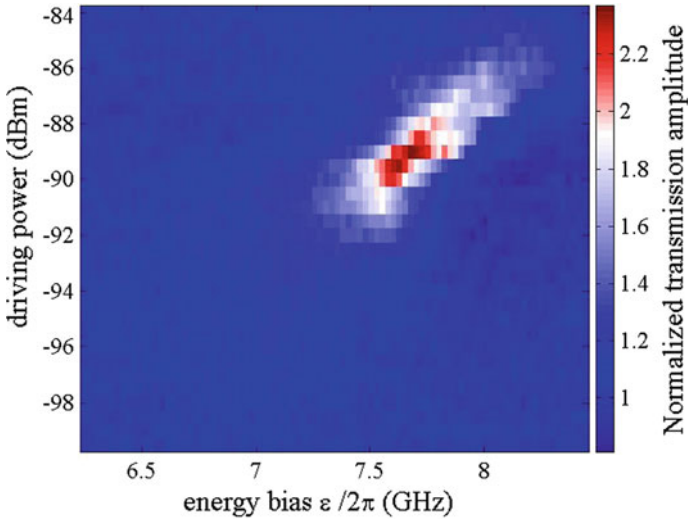


**Fig. 11** Driving power dependence. The transmission amplitude is plotted as a function of the energy bias and the driving power. To achieve amplification, the splitting of the Rabi-levels should correspond to the one of the cavities fundamental mode. This is demonstrated by the bias–power dependence of the amplification point. Also, an optimal working point with highest amplification is observed

amplification, are found similar to explained above. Still, in the experiment shown below, the strong drive was applied to the third instead of the fifth harmonic.

In order to measure the emission, the energy bias and driving strength at the third harmonic are both set to the optimal amplification point while no probe beam is applied. Then in consequence the driving signal is switched on and off, and in each case a spectrum around the resonators fundamental frequency is recorded. This procedure is repeated over 20,000 times. The averaged signals are plotted in Fig. 12. There a clear increase of the emitted power and a linewidth narrowing are visible if the driving signal is switched on. Both measured results indicate an energy transfer between dressed qubit system and the fundamental cavity mode so that "self-sustained oscillations" inside of the cavity are observed. This effect is thus single artificial atom lasing.

## *4.3 Landau–Zener–Stückelberg Lasing*

The above-discussed dressing of the states of an artificial atom is theoretically analyzed close to the resonance point between the qubit level spacing and frequency of the driving signal. Basically, this is caused by the fact that the diagonal coupling of the Rabi-split states to the fundamental cavity mode is reduced with increasing

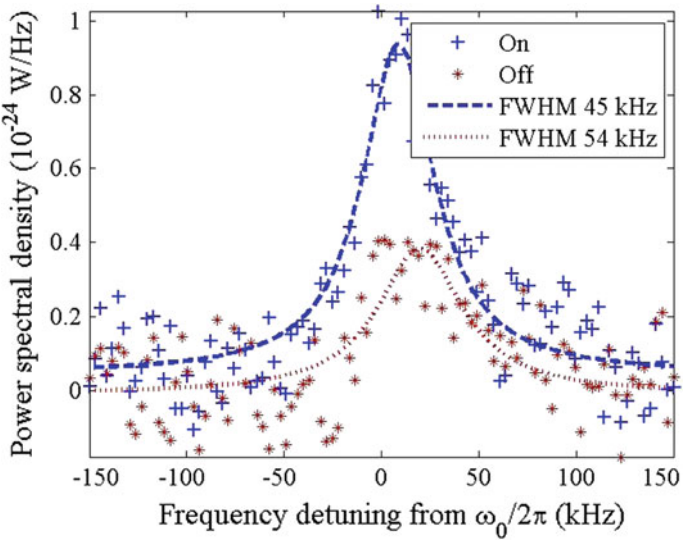


**Fig. 12** Emission from the dressed system. Compared to the thermal response at 20 mK (red stars), the emission with the dressing signal applied at the third harmonic of the resonator is more than doubled. Also, a linewidth narrowing of about 20% is observed. The linewidths are extracted from Lorentzian line fits as shown by the dotted and dashed lines. The noise background was subtracted

detuning. Nevertheless, as we demonstrate below, also for large values of detuning an inverse population and therefore lasing can be created.

This different lasing process requires similar experimental conditions. An artificial atom is placed inside and coupled to the field of a resonator. A strong microwave signal is applied to one of the harmonics, and a probe beam can be used at the fundamental mode to detect amplification. Here, the explanation is based on Landau–Zener–Stückelberg interferences during a drive period [33].

For understanding the process, let us note that the potential of an artificial atom is symmetric only at zero energy bias. For finite values, the asymmetry of the potential allows multiphoton interactions that are forbidden at real atoms because the dipole operator can only couple states with different parities [34, 35]. This occurrence of multiphoton processes can also be explained by the special situation of both, diagonal and off-diagonal coupling in the Hamiltonian (4) of such tune-able quantum system. As seen before, the diagonal coupling for examples couples the Rabi-split states that are already not allowed for real atoms. The system of eigenstates for such a qubit coupled to the fundamental mode of a cavity is sketched in Fig. 13.

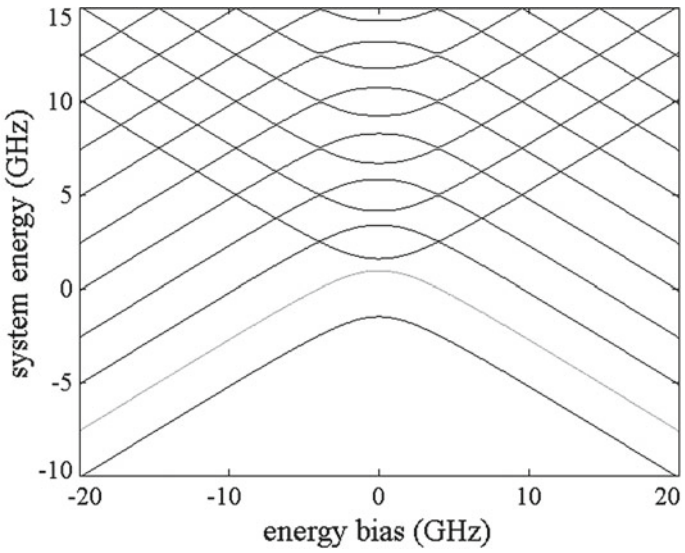


**Fig. 13** Energy level diagram of a tunable two-level system coupled to a cavity mode. The states with negative and positive curvature correspond, respectively, to the qubits ground and excited state for different number of photon in the cavity fundamental mode. At each crossing point of the levels, the degeneracies are lifted because of the interplay of diagonal and transverse coupling

It consists of a series of ground and excited states that are shifted due to different photon numbers in the cavity. For all states with negative curvature, the qubit is in its ground state. At each crossing point of two levels, their degeneracy is lifted because of the atom–field coupling. A strong driving signal applied to the qubit can now be seen as modulated energy bias. The phase acquired by the wave function during one period depends on the energetic state of the system. This statement immediately follows from the Schrödinger equation $i\hbar\dot{\Psi} = H\Psi$, with $\Psi$ being the wave function.

In addition, Landau–Zener transitions can occur close to the avoided level crossings adding certain phase values. Treating the problem numerical, the probability amplitudes for the levels can be determined from the Schrödinger equation. For the upper (and also lower) energetic state oscillations of the population are observed at certain energy biases and driving amplitudes. These are named Rabi-like oscillations. At points were their frequency consisting of one of the cavity amplification, and lasing can be observed. Note, the regions of amplification follow the typical Landau–Zener interference pattern as can be seen in Fig. 14. This effect was demonstrated on flux and newly created quantum phase slip qubits.

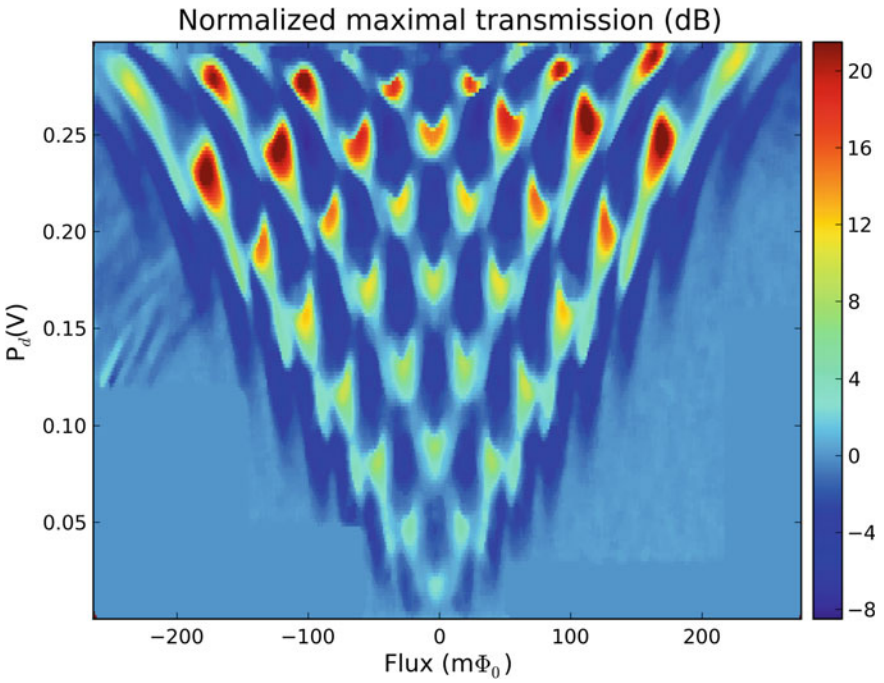


**Fig. 14** Landau–Zener–Stückelberg interference pattern measured in transmission on a superconducting flux qubit–resonator system. Amplification is observed when the frequency of the Rabi-like oscillations matches one of the cavity

## 5 Summary and Conclusion

The special properties of the circuit QED, especially the strong achievable (artificial) atom-field coupling, allow the repetition and extension of originally quantum optic experiments. Here, we focused on the field of a single atom lasing. The standard three-level lasing scheme was realized with a charge qubit. There the third level was formed by quasi-particle states.

The main focus in our discussion was put to dressed-state lasing because it extends the frame of lasing to unusual systems. As discussed, the special coupling conditions allowed the use of only two states of the artificial atom for creating population inversion. The used coupling to the Rabi-split states is forbidden in quantum optics at atoms since their dipole moments thus not have corresponding transition elements. Furthermore on experimental results, the properties of amplification and lasing were determined.

We concluded our discussion with the extension of the dressed-state lasing to regimes of large detuning. There the amplification and lasing effect is explained by the resonance between Rabi-like oscillations and the resonator.

**Acknowledgements** We would like to thank P. Neilinger, M. Grajcar, O. Astafiev, and S. Shevchenko for the nice collaboration as well as for providing and discussion of experimental results. E. I. acknowledges partial support from the Russian Ministry of Education and Science, within the framework of State Assignment 3.8051.2017.

## References

1. H.J. Kimble, Strong interactions of single atoms and photons in cavity QED. Phys. Scr. **T76**, 127 (1998)
2. C.J. Hood, T.W. Lynn, A.C. Doherty, A.S. Parkins, H.J. Kimble, The atom-cavity microscope: single atoms bound in orbit by single photons. Science **287**, 1447 (2000)
3. T. Niemczyk, F. Deppe, H. Huebl, E.P. Menzel, F. Hocke, M.J. Schwarz, J.J. Garcia-Ripoll, D. Zueco, T. Hümmer, E. Solano et al., Circuit quantum electrodynamics in the ultrastrong-coupling regime. Nat. Phys. **6**(10), 772–776 (2010)
4. J.P. Gordon, H.J. Zeiger, C.H. Townes, Molecular microwave oscillator and new hyperfine structure in the microwave spectrum of NH3. Phys. Rev. **95**(1), 282–284 (1954)
5. G. Grynberg, A. Aspect, C. Fabre, *Introduction to Quantum Optics: From the Semi-classical Approach to Quantized Light* (Cambridge University Press, 2010)
6. J. McKeever, A. Boca, A.D. Boozer, J.R. Buck, H.J. Kimble, Experimental realization of a one-atom laser in the regime of strong coupling. Nature **425**(6955), 268–271 (2003)
7. F.M. Penning, Die Glimmentladung bei niedrigem Druck zwischen koaxialen Zylindern in einem axialen Magnetfeld. Physica **3**(9), 873–894 (1936)
8. W. Paul, Electromagnetic traps for charged and neutral particles. Rev. Mod. Phys. **62**(3), 531–540 (1990)
9. W. Paul, H. Steinwedel, Notizen: Ein neues Massenspektrometer ohne Magnetfeld. Zeitschrift für Naturforschung A **8**(7), 448–450 (1953)
10. T.W. Hänsch, A.L. Schawlow, Cooling of gases by laser radiation. Opt. Commun. **13**(1), 68–69 (1975)
11. D.J. Wineland, R.E. Drullinger, F.L. Walls, Radiation-pressure cooling of bound resonant absorbers. Phys. Rev. Lett. **40**(25), 1639–1642 (1978)
12. H. Walther, B.T.H. Varcoe, B.-G. Englert, T. Becker, Cavity quantum electrodynamics. Rep. Prog. Phys. **69**(5), 1325–1382 (2006)
13. B. Deaver, W. Fairbank, Experimental evidence for quantized flux in superconducting cylinders. Phys. Rev. Lett. **7**(2), 43–46 (1961)
14. R. Doll, M. Näbauer, Experimental proof of magnetic flux quantization in a superconducting ring. Phys. Rev. Lett. **7**(2), 51–52 (1961)
15. J.E. Mooij, T.P. Orlando, L. Levitov, L. Tian, C.H. van der Wal, S. Lloyd, Josephson persistent-current qubit. Science **285**(5430), 1036–1039 (1999)
16. Y. Nakamura, Y.A. Pashkin, J.S. Tsai, Coherent control of macroscopic quantum states in a single-Cooper-pair box. Nature **398**(6730), 786–788 (1999)
17. J. Koch, T. Yu, J. Gambetta, A. Houck, D. Schuster, J. Majer, A. Blais, M. Devoret, S. Girvin, R. Schoelkopf, Charge-insensitive qubit design derived from the Cooper pair box. Phys. Rev. A **76**(4), 042319 (2007)
18. B.D. Josephson, Possible new effects in superconductive tunnelling. Phys. Lett. **1**(7), 251–253 (1962)
19. G. Oelsner, U. Hübner, S. Anders, E. Il'ichev, Application and fabrication aspects of sub-micrometer-sized Josephson junctions. Low Temp. Phys. (2017)
20. M. Göppl, A. Fragner, M. Baur, R. Bianchetti, S. Filipp, J.M. Fink, P.J. Leek, G. Puebla, L. Steffen, A. Wallraff, Coplanar waveguide resonators for circuit quantum electrodynamics. J. Appl. Phys. **104**(11), 113904 (2008)

21. P. Macha, S.H.W. van der Ploeg, G. Oelsner, E. Il'ichev, H.-G. Meyer, S. Wünsch, M. Siegel, Losses in coplanar waveguide resonators at millikelvin temperatures. Appl. Phys. Lett. **96**(6), 062503 (2010)
22. G. Oelsner, *Single Artificial-Atom Lasing of a Dressed Flux Qubit* (Cuvillier Verlag, Göttingen, 2017)
23. M.O. Scully, M.S. Zubairy, *Quantum Optics* (Cambridge University Press, Cambridge, 1997)
24. C. Rigetti, J.M. Gambetta, S. Poletto, B.L.T. Plourde, J.M. Chow, A.D. Córcoles, J.A. Smolin, S.T. Merkel, J.R. Rozen, G.A. Keefe, et al., Superconducting qubit in a waveguide cavity with a coherence time approaching 0.1 ms. Phys. Rev. B **86**(10), 100506(R) (2012)
25. A. Wallraff, D.I. Schuster, A. Blais, L. Frunzio, R.-S. Huang, J. Majer, S. Kumar, S.M. Girvin, R.J. Schoelkopf, Strong coupling of a single photon to a superconducting qubit using circuit quantum electrodynamics. Nature **431**(7005), 162–167 (2004)
26. A. Abdumalikov, O. Astafiev, Y. Nakamura, Y. Pashkin, J. Tsai, Vacuum Rabi splitting due to strong coupling of a flux qubit and a coplanar-waveguide resonator. Phys. Rev. B **78**(18), 180502(R) (2008)
27. A.A. Abdumalikov, O. Astafiev, A.M. Zagoskin, Y.A. Pashkin, Y. Nakamura, J.S. Tsai, Electromagnetically induced transparency on a single artificial atom. Phys. Rev. Lett. **104**(19), 193601 (2010)
28. M.A. Sillanpää, J. Li, K. Cicak, F. Altomare, J.I. Park, R.W. Simmonds, G.S. Paraoanu, P.J. Hakonen, Autler-townes effect in a superconducting three-level system. Phys. Rev. Lett. **103**(19), 193601 (2009)
29. O. Astafiev, K. Inomata, A.O. Niskanen, T. Yamamoto, Y.A. Pashkin, Y. Nakamura, J.S. Tsai, Single artificial-atom lasing. Nature **449**(7162), 588–590 (2007)
30. G. Oelsner, P. Macha, O.V. Astafiev, E. Il'ichev, M. Grajcar, U. Hübner, B.I. Ivanov, P. Neilinger, H.-G. Meyer, Dressed-state amplification by a single superconducting qubit. Phys. Rev. Lett. **110**(5), 053602 (2013)
31. S.N. Shevchenko, G. Oelsner, Y.S. Greenberg, P. Macha, D.S. Karpov, M. Grajcar, U. Hübner, A.N. Omelyanchouk, E. Il'ichev, Amplification and attenuation of a probe signal by doubly dressed states. Phys. Rev. B **89**(18), 184504 (2014)
32. A. Izmalkov, S.H.W. van der Ploeg, S.N. Shevchenko, M. Grajcar, E. Il'ichev, U. Hübner, A.N. Omelyanchouk, H.-G. Meyer, Consistency of ground state and spectroscopic measurements on flux qubits. Phys. Rev. Lett. **101**(1), 017003 (2008)
33. P. Neilinger, S.N. Shevchenko, J. Bogar, M. Rehak, G. Oelsner, D.S. Karpov, U. Hübner, O. Astafiev, M. Grajcar, E. Il'ichev, Landau-Zener-Stückelberg-Majorana lasing in circuit quantum electrodynamics. Phys. Rev. B **94**(9), 094519 (2016)
34. Y.-X. Liu, J.Q. You, L.F. Wei, C.P. Sun, F. Nori, Optical selection rules and phase-dependent adiabatic state control in a superconducting quantum circuit. Phys. Rev. Lett. **95**(8), 087001 (2005)
35. Y.-X. Liu, C.-X. Yang, H.-C. Sun, X.-B. Wang, Coexistence of single- and multi-photon processes due to longitudinal couplings between superconducting flux qubits and external fields. New J. Phys. **16**(1), 015031 (2014)

# Topology-Driven Effects in Advanced Micro- and Nanoarchitectures


**V. M. Fomin**

**Abstract** An overview is given about some of topological effects, owing to special geometries in real space, implemented by the high-tech self-organization techniques to fabricate micro- and nanoarchitectures. Self-assembled quantum volcanos, which are singly connected, surprisingly exhibit the Aharonov–Bohm behavior in experiment. This is explained by the fact that in a quantum volcano the electron wave functions are identical to the electron wave functions in a quantum ring from a topological point of view. Combination of a geometric potential and an inhomogeneous twist renders an observation of the topology-driven effects in the electron ground-state energy in Möbius rings at the microscale into the area of experimental verification. In inhomogeneous Möbius rings, a "Delocalization-to-localization" transition is found for the electron ground state. Advances in the high-tech roll-up fabrication methods have provided qualitatively novel curved superconductor micro- and nanoarchitectures, e.g., nanostructured microtubes, microhelices and their arrays. Vortex dynamics in open superconductor microtubes in the presence of a transport current are influenced by the interplay between the scalar potential and the inhomogeneous magnetic field component, which is normal to the surface. The rolled-up conical-shaped asymmetric microcavities provide a background to realize the spin–orbit interaction of light for the analysis of topological effects in the course of a non-Abelian evolution. Robustness of the topologically induced geometric phase of light opens novel ways of manipulating photons and thus implies promising perspectives of applications in on-chip quantum devices.

V. M. Fomin (✉)
Institute for Integrative Nanosciences (IIN), Leibniz Institute for Solid State and Materials Research (IFW) Dresden, Helmholtzstraße 20, 01069 Dresden, Germany
e-mail: v.fomin@ifw-dresden.de



A. Sidorenko (ed.), *Functional Nanostructures and Metamaterials for Superconducting Spintronics*, NanoScience and Technology,
https://doi.org/10.1007/978-3-319-90481-8_10

## 1 Introduction

Study of topological matter is one of the fascinating main roads of modern physics. Topology-driven concepts, like the geometric phase, the Aharonov–Bohm effect, topologic phases and phase transitions, topological origin of the quantum Hall effect, topological insulators, topological semimetals, topological superconductors, Majorana fermions, have revolutionized condensed matter physics.

The realm of topological matter can be conventionally subdivided into two categories. First, non-trivial topology occurs due to a special geometry of structures or fields in *real* space, e.g., quantum rings [1], Möbius rings [2], metamaterials of interlocked hollow semiconducting tori [3], optical waveguides [4], multi-terminal Josephson junctions [5], Skyrmions [6], and other topological spin and magnetic textures [7, 8]. Second, topologically protected surface/edge states governed by Dirac physics and/or topologically non-trivial electronic structure in the *momentum* space underlie quantum Hall effect [9, 10], quantum spin Hall effect [11], quantum anomalous Hall effect [12], topological insulators [13], topological superconductors [14], Weyl fermion semimetals [15], topological photonic crystals [16], topological acoustic metamaterials [17].

In this chapter, an overview is given about some of topology-driven effects, owing to special geometries in real space, implemented by the high-tech self-organization techniques to fabricate micro- and nanoarchitectures.

Advances of high-tech techniques for nanostructure fabrication have enabled generating topologically non-trivial manifolds at the micro- and nanoscale with man-made space metrics, which determine electronic, transport, optical and magnetic properties of such structures and novel potentialities of nanodevices due to their unique topology. Investigation of topologically non-trivial manifolds at the micro- and nanoscale is of immense importance for semiconductor, superconductor, and graphene physics as well as for electronics, magnetism, optics, optoelectronics, thermoelectrics, biophysics, and quantum computing. Doubly connected quantum ring-like structures provide a playground for the fundamental concepts pertinent to the quantum-mechanical paradigm, including the geometric phase and the related Aharonov–Bohm effect [1]. Self-assembled quantum volcanos, which are singly connected, surprisingly exhibit the Aharonov–Bohm behavior in experiment. This is explained by the fact that in a quantum volcano the electron wave functions are identical to the electron wave functions in a quantum ring from a topological point of view. Combination of a geometric potential and an inhomogeneous twist renders an observation of the topology-driven effects in the electron ground-state energy in Möbius rings at the microscale into the area of experimental verification. In inhomogeneous Möbius rings, a "Delocalization-to-localization" transition is found for the electron ground state [2].

Advances in the high-tech fabrication methods [18, 19] have provided qualitatively novel curved micro- and nanoarchitectures of superconductors, e.g., nanostructured microtubes, helical microcoils and their arrays. Their superconducting properties as well as possible applications remain largely *terra incognita*. Vortex dynamics in

rolled-up superconductor microtubes in the presence of a transport current [20] are determined by the interplay between the scalar potential and the inhomogeneous magnetic field component, which is normal to the surface. Rolling up a superconductor Nb nanomembrane into open tubes and helical microcoils allows for a new, highly correlated vortex dynamics regime that reveals a surprising (by a factor of 3) increase of a critical magnetic field for the beginning of vortex motion and a transition magnetic field between single- and many-vortex dynamic patterns in an open nanotube [20].

Production of curved superconductor structures opened up a possibility to influence the current density distribution by changing curvature. The combined effect of a curved geometry and pinning centers strongly depends on the location of those centers in an open superconductor microtube [21]. On both sides of the tube with respect to the magnetic field applied orthogonally to the tube axis, there occurs the branching of vortex nucleation periods [22]. Using an inhomogeneous transport current enables an efficient control over the branching and allows for a reduction of the average number of vortices that occur in the microtube per nanosecond [23].

The rolled-up conical-shaped asymmetric microcavities provide a background to realize the spin–orbit interaction of light for the analysis of topological effects in the course of a non-Abelian evolution [4]. In asymmetric microcavities, the geometric phase is straightforwardly detected through the polarization tilt angles, while the eccentricity of the elliptical polarization of light provides a measure of conversion between the clockwise- and counterclockwise-polarized components of a circular basis. Those topological effects open novel ways of manipulating photons and thus imply promising perspectives of applications in on-chip quantum devices.

## 2 Topologic Effects in Quantum Rings by Virtue of Doubly Connectedness

Among nano-objects with non-trivial shape and tailored energy spectra, which modern fabrication techniques are capable of producing, quantum rings [1, 24] are especially valuable. They are not singly connected quasi-zero-dimensional clusters of atoms or molecules on a 2D surface or in a 3D matrix, as long as they combine sizes at nanoscale with non-trivial topological properties, e.g., doubly connectedness for a ring or one-sidedness for a Möbius strip. Doubly connected (that is, ring-like) structures of size at the scale of nanometers are called quantum rings. They possess a unique density of states for charge carriers and various quantum fields and therefore reveal a broad variety of physical properties, which are fundamentally distinct from those of singly connected structures (e.g., quantum dots or quantum rods). This density of states gives rise to unique physical phenomena, in particular, persistent currents, and provides an unparalleled playground for the quantum-mechanical paradigm. Those physical properties can be governed by tuning the magnetic flux

threading the ring and changing the ring geometry, as well as by producing assemblies of quantum rings (see [1, 24] and references therein).

An unrivaled fundamental role of doubly connectedness (ring-topology) for manifestations of the quantum-mechanical paradigm was demonstrated in the framework of the theory of *geometric phase* [25–28]. Berry [28] suggested an intuitively appealing derivation of the geometric phase, which is recalled below. Let us consider a system with a Hamiltonian $H$, which depends on a set of time-dependent parameters $\mathbf{R} = \mathbf{R}(t)$ that form a closed path $C$ when time evolves between the initial instant $t=0$ and the final instant $t=T$: $\mathbf{R}(0) = \mathbf{R}(T)$. The corresponding evolution of the quantum-mechanical state of the system under analysis obeys the Schrödinger equation:

$$i\hbar|\dot{\psi}(t)\rangle = \widehat{H}(\mathbf{R}(t))|\psi(t)\rangle. \tag{2.1}$$

The eigenstates at any instant $t$ satisfy the stationary Schrödinger equation

$$\widehat{H}(\mathbf{R})|n(\mathbf{R})\rangle = E_n(\mathbf{R})|n(\mathbf{R})\rangle, \tag{2.2}$$

where the wave function $|n(\mathbf{R})\rangle$ is single-valued in the area, which includes $C$. Within the framework of the *adiabatic* approximation [29] (for a generalization to non-adiabatically evolving quantum systems, see [30]), the system, which has been prepared in one of the states $|n(\mathbf{R}(0))\rangle$ at the initial instant, will evolve with the Hamiltonian $\widehat{H}(\mathbf{R}(t))$, and it will occur in the state $|n(\mathbf{R}(t))\rangle$ at the instant $t$. The Schrödinger equation (2.1) acquires then the solution

$$|\psi(t)\rangle = \exp\left[-\frac{i}{\hbar}\int_0^t E_n(\mathbf{R}(\tau))d\tau\right]\exp[i\gamma_n(t)]|\psi(0)\rangle, \tag{2.3}$$

where the *geometric phase* $\gamma_n(t)$ satisfies the equation

$$\dot{\gamma}_n(t) = i\langle n(\mathbf{R}(t))|\nabla_{\mathbf{R}} n(\mathbf{R}(t))\rangle.$$

As a consequence, the phase change of the state represented by (2.3) accumulated on the path $C$

$$|\psi(T)\rangle = \exp\left[-\frac{i}{\hbar}\int_0^T E_n(\mathbf{R}(\tau))\mathrm{d}\tau\right]\exp\left[i\gamma_n(C)\right]|\psi(0)\rangle \tag{2.4}$$

contains the *geometric phase*

$$\gamma_n(C) = i\oint_C \langle n(\mathbf{R})|\nabla_{\mathbf{R}} n(\mathbf{R})\rangle \cdot \mathrm{d}\mathbf{R}$$

next to the dynamic phase

$$-\frac{i}{\hbar}\int_0^T E_n(\mathbf{R}(\tau))\mathrm{d}\tau).$$

Let us consider further a magnetic flux tube [31], which carries a magnetic flux $\Phi$. At those positions $\mathbf{R}$, which are outside of the flux tube, the magnetic field is absent, but there exist vector potentials $\mathbf{A}(\mathbf{R})$, which are gauge equivalent. For any closed path $C$, which is threaded by the magnetic flux tube, the equation

$$\oint_C \mathbf{A}(\mathbf{R})\cdot d\mathbf{R} = \Phi$$

holds true. For a particle carrying an electric charge $q$, the geometric phase accumulated along the path $C$

$$\gamma_n(C) = \frac{q}{\hbar}\oint_C \mathbf{A}(\mathbf{R})\cdot d\mathbf{R} = \frac{q}{\hbar}\Phi \tag{2.5}$$

does not depend on the state $|n(\mathbf{R})\rangle$. In other words, a charged particle *gains the geometric phase* when its coordinate encircles the magnetic flux tube over a closed path:

$$|\psi(\varphi = 2\pi)\rangle = \exp\left(i2\pi\frac{\Phi}{\Phi_0}\right)|\psi(\varphi = 0)\rangle. \tag{2.6}$$

Here, $\Phi_0 = h/e$ is the magnetic flux quantum, and $e$ is the elementary electric charge. The geometric phase occurring in (2.6) leads to numerous manifestations [1] of the quantum-interference effect, usually called Aharonov–Bohm effect [31, 32] (Fig. 1).

The cutting-edge fabrication and structural characterization techniques as well as the most advanced state-of-the-art theoretical approaches provided an insight into the structure of self-assembled InGaAs quantum rings [33, 34]. A high level of complexity of modeling was demonstrated to be needed for an adequate capture of the shape, size, and composition effects in quantum rings.

Based on the X-STM characterization data, a theoretical model describing the geometry and chemical composition of self-assembled quantum rings was developed [33, 35]. A model of the quantum ring shape (anisotropic "Quantum volcano") represented with an InGaAs layer of varying thickness, which is embedded in an infinite GaAs matrix, as well as the effective adiabatic electron potential, is shown in Fig. 2.

Though such a quantum crater is *singly connected*, it was shown that the Aharonov–Bohm-type behavior, which is attributed to doubly connected topologies, survived in such structures due to the exponentially rapid decay of electron wave functions toward the crater center. The resulting theory allowed for a quantitative explanation of the Aharonov–Bohm oscillations in the magnetization detected by using the torsion magnetometry on those quantum volcanos [36], as shown in Fig. 3. The anisotropic model of a quantum volcano [33, 35] has been widely exploited for

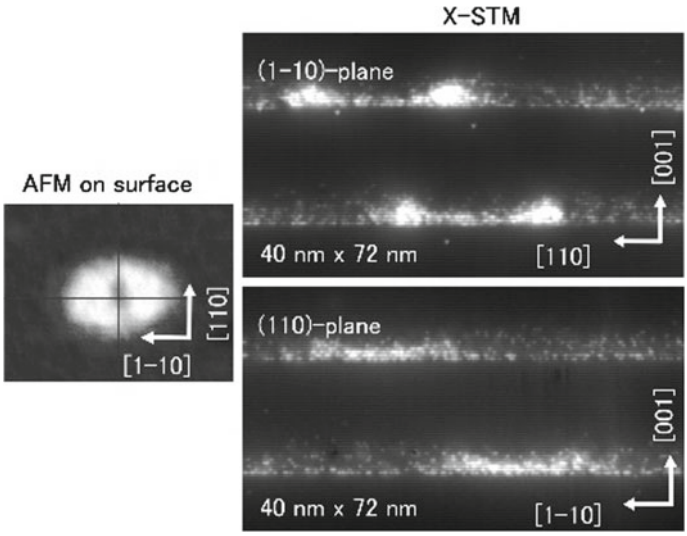


**Fig. 1** (l.h.s.) AFM image on surface of a quantum ring. (r.h.s.) X-STM image of filled states in a cleaved quantum ring in the (1–10) and (110) planes, $V_{\text{sample}} = -3$ V. The height changes from 0 (dark spots) to 0.25 nm (bright spots). (Adapted from [33] with the permission of AIP Publishing.)

interpretation of experiments on self-assembled InGaAs quantum rings, for instance magnetic response of excitons and biexcitons in a quantum ring [37] and polarization dependence of photoluminescence due to excitons and biexcitons in a quantum ring [38]. Deep analogies between the persistent currents in semiconductor quantum rings and superconducting currents in superconductor rings are of immense heuristic value for a unified description of topology-driven effects in semiconductors and superconductors [39].

For an extensive overview of the physics of quantum rings, from fundamental concepts through great challenges that were brilliantly overcome by both theory and experiment to unprecedented application perspectives, see [1].

## 3 Topologic Effects in Möbius Rings

The parametric representation $\boldsymbol{r}(u, v)$ of the infinitely thin 2D Möbius band centered at the origin of the $xy$-plane of central radius $R$ and width $L_y$ is [40]

$$x(u,v) = \left[R + \frac{L_y v}{2}\cos\left(\frac{u}{2}\right)\right]\cos(u),$$
$$y(u,v) = \left[R + \frac{L_y v}{2}\cos\left(\frac{u}{2}\right)\right]\sin(u),$$
$$z(u,v) = \frac{L_y v}{2}\sin\left(\frac{u}{2}\right), \tag{3.1}$$

where $0 \le u \le 2\pi$, $-1 \le v \le 1$. The centerline of the Möbius band is a circumference represented by (3.1) at $v = 0$. A key topological property of the Möbius band

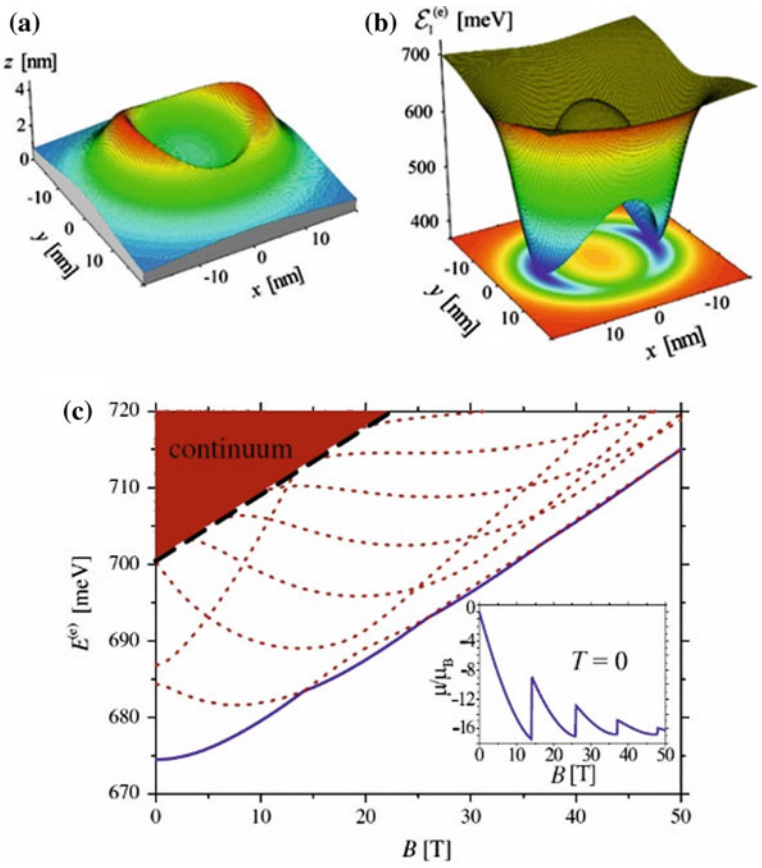


**Fig. 2** **a** Shape of an unstrained $In_{0.6}Ga_{0.4}As$ quantum volcano. **b** The adiabatic potential, which determines the electron motion in the quantum volcano. **c** Energies of the ground (solid line) and excited (dotted lines) states calculated for a quantum volcano. All energies are counted from the bottom of the conduction band in unstrained InAs. A dashed line, which indicates the region of continuum, is obtained from the numerical simulation; it is a guide to the eye. Inset: magnetic moment of the quantum volcano calculated at $T=0$. (Adapted from [35])

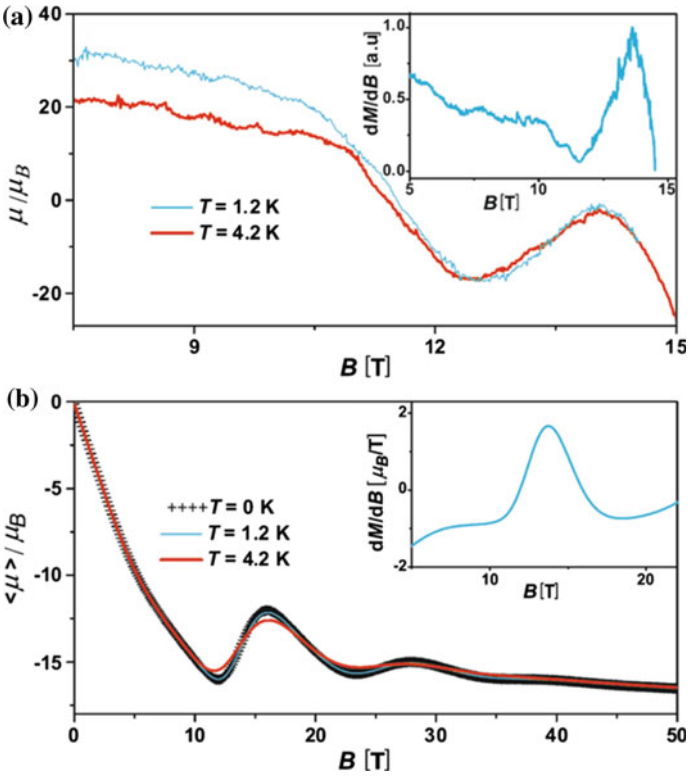


**Fig. 3** Magnetic moment per electron in self-assembled InAs/GaAs quantum volcanos, at 1.2 K and 4.2 K, as a function of the magnetic field. **a** Experiment: After subtracting the linear background from the measured signal, it was divided by the total number of electrons and averaged over a number of measurements. The first derivative of the measured magnetic moment with respect to the magnetic field at $T = 1.2$ K (inset). **b** Theory: Simulated magnetic moment and its first derivative (inset) for a single electron in a quantum volcano at different temperatures. (After [38])

is implemented in the transformation of the coordinate under one rotation along the centerline:

$$\boldsymbol{r}(u, v) = \boldsymbol{r}(u + 2\pi, -v). \tag{3.2}$$

The quantum-mechanical consequence of this property is that the boundary condition for the Dirichlet boundary problem for the scalar Schrödinger equation on the Möbius band is

$$\psi(u, 1) = \psi(u, -1) = 0, \quad \psi(u + 2\pi, v) = \psi(u, -v). \tag{3.3}$$

The single-valuedness of the wave function when the coordinate $u$ describes one rotation about the opening ($u \to u + 2\pi$) requires a simultaneous reflection of the

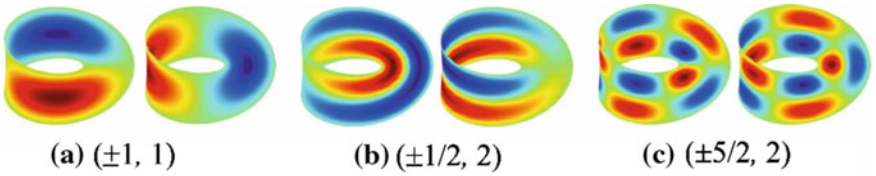


**Fig. 4** Wave functions with quantum numbers $(n_u, n_v)$ on a 2D Möbius band. The positive to negative values of the wave functions are represented by the colors red to blue, with green corresponding to zero. States with $n_v = 1$ and an integer number $|n_u|$ of wavelengths along the centerline (**a**) are similar to corresponding states in a quantum ring. States with $n_v = 2$ and a half-integer number $|n_u|$ of wavelengths along the centerline (**b**, **c**) are specific for a Möbius band. (Reprinted with permission from [40]. © 2012 by the American Physical Society)

coordinate $v$, which allows for a description in terms of an additional *topological phase shift* by $\pi$ due to the twist:

$$v \to \mathrm{e}^{i\pi} v. \tag{3.4}$$

Using the adiabatic ansatz for the wave function

$$\psi(u, v) = \psi_1(u)\psi_2(v) \tag{3.5}$$

and discarding the effects of curvature on the Laplace–Beltrami Hamiltonian [41], the wave functions can be approximately represented as a product of (i) a propagating wave $\psi_1(u) = \exp(ik_u u)$ with the wavenumber $k_u = n_u/R$ and the corresponding wavelength $\lambda = 2\pi/|k_u|$ in the centerline direction and (ii) a standing wave

$$\psi_2(v) = \begin{cases} \cos(\pi n_v v), & n_v = 1, 3, 5, \ldots \\ \sin(\pi n_v v), & n_v = 2, 4, \ldots \end{cases} \tag{3.6}$$

with the wavenumber $k_v = \pi n_v / L_y$, where $n_v = 1, 2, \ldots$, in the direction orthogonal to the centerline. As follows from the relation $2\pi R = |n_u|\lambda$, the number of waves along the centerline of the Möbius band is $|n_u|$. If $n_v$ is odd, then $\psi_2(-v) = \psi_2(v)$, and $\psi_1(u + 2\pi) = \psi_1(u)$, so that the number of wavelengths on the centerline is an integer $|n_u| = 0, 1, 2, \ldots$, similar to a quantum ring (Fig. 4a). If $n_v$ is even, then $\psi_2(-v) = -\psi_2(v)$, and $\psi_1(u + 2\pi) = (-1)^{i\pi}\psi_1(u)$, so that the number of wavelengths on the centerline is half-integer $|n_u| = 1/2, 3/2, \ldots$ (Fig. 4b, c). In the latter case, a half-integer number of waves along the centerline is complemented with an effective additional half-wave due to the twist-induced topological phase shift by $\pi$, what allows for a constructive interference of the propagating waves. In analogy with this behavior, a Möbius-type soliton in a nonlinear ring describing spin-wave propagation in a magnetic film with low loss subject to a longitudinally applied field requires two rounds about the ring, in order to return to the initial phase condition [42].

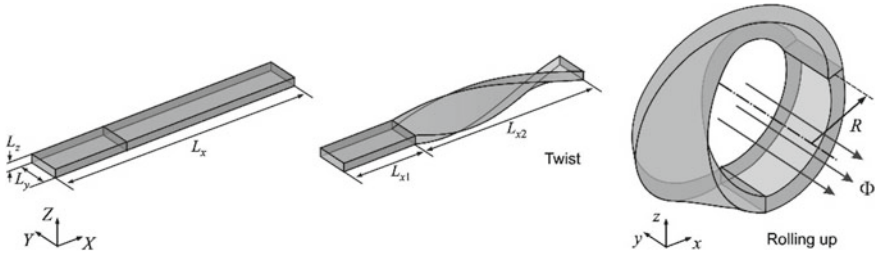


**Fig. 5** Construction of a Möbius ring with inhomogeneous twist out of the parallelepiped-shaped strip with length $L_x$, width $L_y$, and thickness $L_z$. Twist over the length interval $L_{x2}$ is followed by rolling up to produce the Möbius ring with characteristic radius $R = L_x/2\pi$. The relative extent of the untwisted part of the Möbius ring is denoted as $\eta = L_{x1}/L_x$ (the ratio of the length of the untwisted part of the ring $L_{x1}$ to the whole circumference $L_x$). A magnetic flux Φ threads the Möbius ring through its opening. (After [2])

The Möbius band is a 2D parametrized surface with only one side and only one boundary. Twisting a planar parallelepiped-like strip by 180° around the axis along its long side, rolling it up, and joining the butt ends orthogonal to that axis according to the procedure proposed by Möbius [43] for fabrication of a Möbius band out of a 2D rectangular strip result in a 3D object, which is called Möbius ring (see Fig. 5). It is bounded by two surfaces, one of width $L_y$ and another one of width $L_z$. Those surfaces are double-sided. But moving on one of these surfaces of the Möbius ring from any point, after one revolution ($2\pi$ rotation) around the $y$-axis, one arrives at the opposite size of the Möbius ring; it is necessary to perform two revolutions ($4\pi$ rotation) around the $y$-axis, in order to return to the original point.

A "Delocalization-to-localization" transition has been predicted [2] for the electron ground state in a nanoscale Möbius ring with inhomogeneous twist. Such structures attract increasing interest because of the advances in fabrication techniques. When increasing the relative extent of the untwisted part of the Möbius ring $\eta = L_{x1}/L_x$, the ground-state wave function occurs expelled from the twisted region (Fig. 6a), while the first excited state wave function penetrates the twisted region (Fig. 6b). This occurs due to the twist-dependent contribution to the kinetic energy operator of the electron, which is equivalent to a decrease of the electronic effective mass in the twisted region. Owing to the geometric potential [44], the ground-state energy of an electron in a cylindrical ring shifts downward (Fig. 7a). As compared to the case of a cylindrical ring of the same width, thickness, and circumference, the ground-state energy of an electron in a Möbius ring shifts upward (Fig. 7a). As seen from Fig. 7a, the contribution of twist to the kinetic energy operator is much larger than that of the geometric potential. A tailoring of the energy spectrum can be performed in a non-ideal quantum ring with inhomogeneous radius due to the occurrence of an inhomogeneous geometric potential, but it is less prominent as compared to the effect of twist in an inhomogeneous Möbius ring.

The upward shift of the ground-state energy of an electron in a Möbius ring (as shown in Fig. 7a) has the same topological origin as the increase of the vacuum

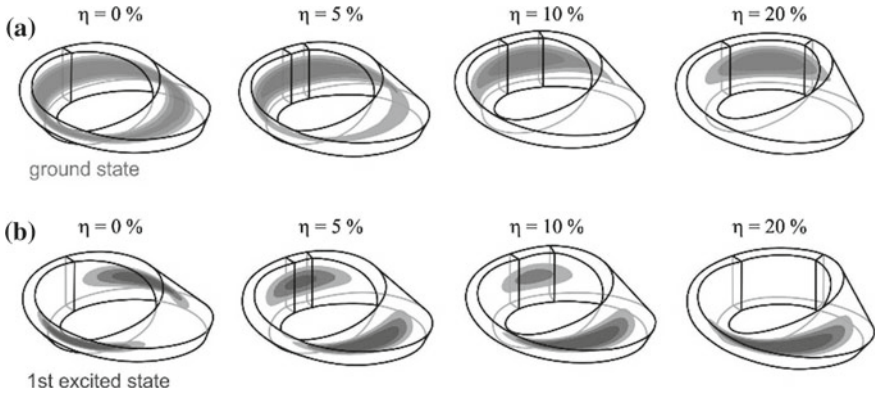


**Fig. 6** Squared modulus of the wave function for the ground **a** and first excited states **b** for an electron in a Möbius ring, which possesses inhomogeneous twist, as a function of the relative extent of the untwisted part of the ring. A reducing color intensity represents three isosurfaces of the squared modulus of the wave functions at the levels of 0.7, 0.5, and 0.3 of their respective maximal values. The structural parameters taken for the finite-difference calculation are: radius $R = L_x/2\pi = 10$ nm, width $L_y = 8$ nm, and thickness $L_z = 2$ nm. (After [2])

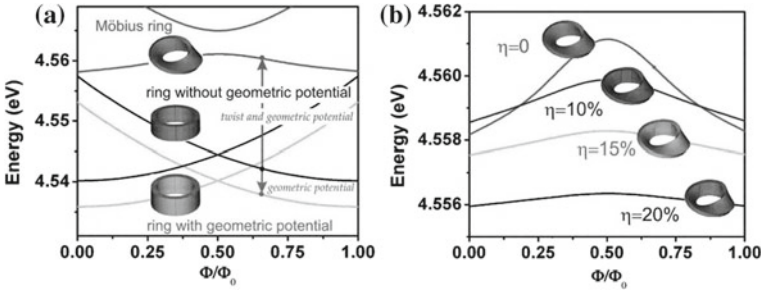


**Fig. 7** Ground-state energies for an electron confined to a Möbius ring as a function of the relative magnetic flux. **a** Comparison of the ground-state energies for electrons in an ideal quantum ring (black line), a quantum ring with geometric potential (light gray line) and a Möbius ring (gray line). **b** When the relative extent of the untwisted part increases, expulsion of the electron wave function from the twisted region gives rise to flattening of the ground-state energy as a function of the magnetic flux owing to an enhanced localization. Parameters are the same as in Fig. 6. (After [2])

energy of quantum fields in cosmological theories of twisted fields and/or twisted space in a closed Universe [45–48]. For instance, a twist at the ultra-large scale (introduced by the size of the Universe $a \sim 3 \times 10^{27}$ m) raises the average vacuum energy density of a scalar massless quantum field only by a tiny quantity $6 \times 10^{-118}$ eVm$^{-3}$, which is far beyond the limits of experimental accessibility. Remarkably, in a Möbius ring of volume $V = 1 \times 10^3$ nm$^3$ represented in Fig. 5, the twist-induced shift of the ground-state energy without a magnetic field constitutes $\Delta E = 22$ meV, what corresponds to the energy density as high as $2.2 \times 10^{22}$ eVm$^{-3}$. Therefore, the

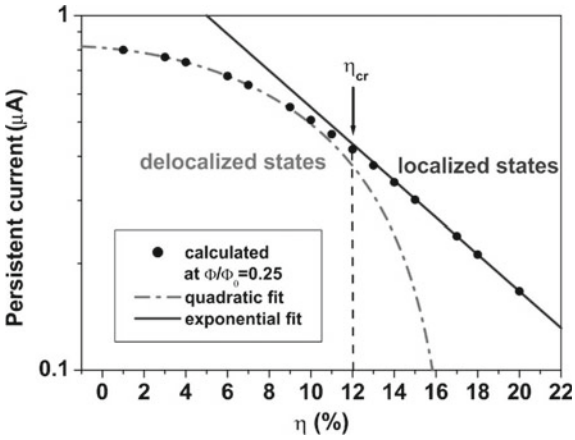


**Fig. 8** A "Delocalization-to-localization" transition in a Möbius ring with inhomogeneous twist manifested in terms of a persistent current as a function of the relative extent of the untwisted part. The values of the persistent current are calculated at $\Phi/\Phi_0 = 0.25$. Parameters are the same as in Fig. 6. (After [2])

effects of twisted fields on the energy density in a closed Universe can be modeled in the laboratory on the Earth due to advancements in fabricating self-assembled micro- and nanostructures possessing non-trivial topology.

The enhanced trend to localization leads to flattening of the ground-state energy of an electron as a function of the magnetic flux as shown in Fig. 7b. The persistent current in the $n$th eigenstate with the eigenenergy $E_n(\Phi)$ is determined by the equation $I_n(\Phi) = -dE_n(\Phi)/d\Phi$. As seen from Fig. 8, above a certain critical value of the relative extent of inhomogeneity $\eta_{cr} \sim 12\%$, the electronic state becomes appreciably localized near the untwisted region. The delocalized (at $\eta < \eta_{cr}$) states manifest a slow, quadratic decay of the persistent current with increasing the relative extent of the untwisted part $\eta$. At the same time, the localized (at $\eta > \eta_{cr}$) states are characterized by a fast, exponential decay. In summary, a "Delocalization-to-localization" transition occurs at $\eta_{cr}$. Importantly, the position of this transition can be effectively controlled by the geometric characteristics of both twist ($L_{x1}$, $L_{x2}$) and rolling up ($R$).

## 4 Superconducting Vortices: Topological Defects in Micro- and Nanoarchitectures

The *ring* is topologically equivalent to both the *open cylinder* and the *punctured plane.* If the superconductor order parameter

$$\psi(r, \varphi) = f(r)\exp(in\varphi) \tag{4.1}$$

winds around an opening in the plane at $r = 0$, then we are dealing with a *topological defect* [48], which cannot be eliminated (that is, the winding number $n$ cannot be changed) in a continuous way. In this terms, an Abrikosov vortex (antivortex) [49] is a topological defect with winding number $n = 1$ ($n = -1$) and $f(0) = 0$. The pattern of superconducting vortices in a micro- or nanoarchitecture represents therefore an

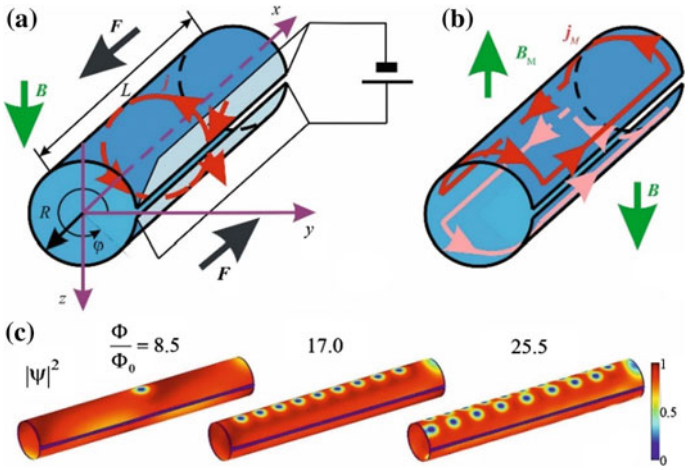


**Fig. 9** **a** Schematic image of an open superconductor tube. An applied transport current is shown with heavy red arrows. Electrodes connected to both banks of a slit are represented semitransparent. **b** Schematic representation of Meissner currents in the open superconductor tube. The magnetic field $\mathbf{B}_M$, which is induced by Meissner (screening) currents, partly compensates the applied magnetic field **B**. **c** Distribution of the superconducting order parameter at three values of the magnetic flux for the dimensionless transport current density $j = 1.65$ (the unit of current density is $8.57 \times 10^9$ $Am^{-2}$) in an open Nb tube with radius $R = 500$ nm, length $L = 3.5$ μm, and a slit width 105 nm (Reprinted with permission after [20]. © 2012 American Chemical Society.)

important study case for arranging topological defects in confined geometries. If an open tube is subjected to a magnetic field applied orthogonally to its axis (Fig. 9a), two *disconnected* Meissner currents $\boldsymbol{j}_M$ arise in the upper and lower half-cylinders represented in Fig. 9b with red and pink, correspondingly. As distinct from that, only a single Meissner current flows in a planar film along its edges.

The vortex matter in the open microtube was described using the time-dependent Ginzburg–Landau equation for a 2D model (which dealt with vortex "slices" rather than with long vortex lines implemented in 3D) with appropriate boundary conditions of no normal superconducting current at surfaces except electrodes. A transport current with density $\mathbf{j} = j\mathbf{e}_\varphi$ was imposed through the electrodes attached to both banks of the slit as schematically represented in Fig. 9a [20]. In the subsequent work, the effect of pinning centers, the renormalization of the magnetic field in tubes of finite thickness, the evolution of the scalar potentials described by the Poisson equation, and inhomogeneity of the transport current were included in the analysis.

The normal component of the magnetic field is maximal ($B_n = B$) in the domains on the microtube, where the normal vector is close to or coincides with the direction of the external magnetic field, and minimal in the domains, where the normal vector is close to or coincides with the direction opposite to the external magnetic field. The above-mentioned domains are favorable for the presence of vortices. For

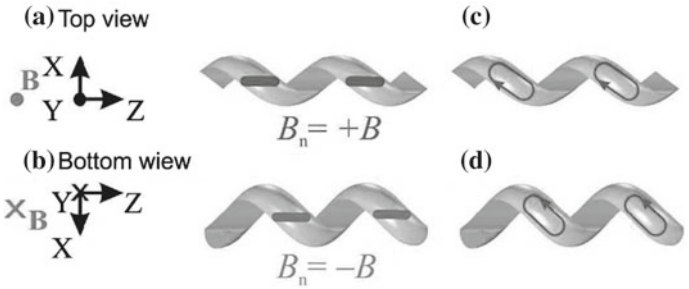


**Fig. 10** Schematic image of a helical microcoil. The z-axis is selected along the helix axis. The y-axis is selected along the magnetic field **B**, which is orthogonal to the helix axis. **a** [**b**] Schematic representation of the domains with the maximal [minimal] normal components of the applied magnetic field $B_n = B$ [$B_n = -B$]. **c** [**d**] Schematic image of the screening (Meissner) currents in the top [bottom] helix half-turns (After [50]. © IOP Publishing. Reproduced with permission. All rights reserved.)

a superconductor helical microcoil with $N$ windings [50], there are $2N$ disconnected areas favorable for the occurrence of vortices in each half-turn as shown in Fig. 10.

Each vortex moves being governed by the Lorentz force of density $\mathbf{F} = \mathbf{j}_{tot} \times \mathbf{B}$ owing to the total current density $\mathbf{j}_{tot} = \mathbf{j} + \mathbf{j}_M + \mathbf{j}_{vortices}$, which includes the transport current density $\mathbf{j} = j\mathbf{e}_\varphi$, a Meissner (screening) current density $\mathbf{j}_M$, and a current density $\mathbf{j}_{vortices}$ of other vortices. The presence of two systems of Meissner (screening) currents as shown in Fig. 9b is crucial for the novel dynamical properties of superconducting vortices in the open microtube as a function of its dimensions, the applied magnetic field, and the transport current [20]. When the magnetic field exceeds a certain value $B_{cr}$, the vortices systematically nucleate at each edge, move along the tube and denucleate at an opposite edge (see Fig. 9c).

Vortices move in opposite directions in the upper and lower half-cylinders, as soon as they meet there opposite directions of the transport current. The resulting Lorentz force possessing opposite directions at $\varphi = \pi/2$ and $\varphi = 3\pi/2$ is illustrated in Fig. 8a with heavy black arrows. Such a behavior is typical of open tubes. When the magnetic field further increases beyond a certain value, no vortices occur owing to strong Meissner (screening) currents.

In order to quantify the vortex dynamics in the system, two characteristic times are introduced as shown in Fig. 11a, b: the period of vortex nucleation at an edge ($\Delta t_2$) and the duration of movement of a vortex along the tube ($\Delta t_1$). The dependence of $\Delta t_1$ ($\Delta t_2$) on the magnetic field applied to a system is shown in Fig. 11c for different radii of the nanotube. The key conclusion of that research is that the critical magnetic field for beginning of vortex dynamics increases by a factor of more than 3 for the nanotube in comparison with a planar membrane (see a heavy arrow in the upper inset to Fig. 11c). These results demonstrate perspectives of tailoring non-equilibrium properties of vortices in curved superconductor nanomembranes leading to their application as tunable superconducting flux generators for fluxon-based information technologies.

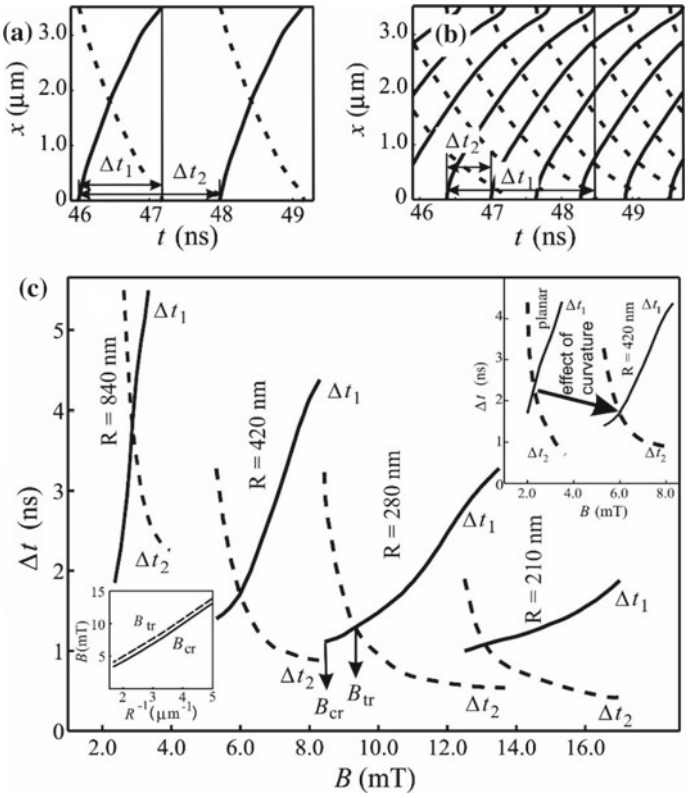


**Fig. 11** Vortex dynamics at **a** $\Phi/\Phi_0 = 8.5$ and **b** $\Phi/\Phi_0 = 11$ in open Nb tubes possessing $L = 3.5$ μm and $R = 280$ nm. Solid (dashed) lines represent vortex trajectories on the lower (upper) half-cylinders. **c** Two characteristic times of vortex dynamics: the time-of-flight $\Delta t_1$ (solid lines) and the period nucleation at an edge $\Delta t_2$ (dashed lines) as a function of the magnetic field. Upper inset: characteristic times of vortex dynamics for a planar film possessing $L_x = 3.5$ μm and $L_y = 2\pi \times 420\,\text{nm} \approx 2.6$ μm. Lower inset: Critical magnetic field for the start of vortex motion $B_{cr}$ and transition magnetic field $B_{tr}$ in tubes possessing $L = 3.5$ μm (Reprinted with permission after [20]. © 2012 American Chemical Society)

The dynamics of superconducting vortices in upper and lower half-cylinders are strongly correlated in symmetric pure open tubes [20]. The presence of pinning centers [21] or inhomogeneous currents [23], which lift the symmetry of half-cylinders with respect to reflection in the plane that includes the tube axis and the centerline of the slit, reduces those correlations. If an inhomogeneous transport current is introduced into an open Nb nanotube through multiple electrodes, a tunable branching of the vortex nucleation period occurs [23] (Fig. 12). The average number of vortices that occur in the microtube per nanosecond can be significantly decreased by using the inhomogeneous transport current. This effect is of immanent importance for energy dissipation reduction in diverse superconductor applications, for instance,

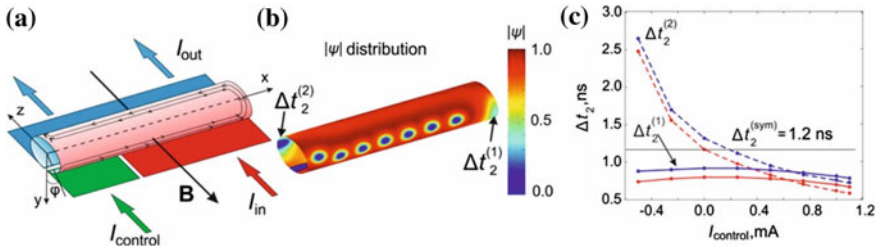


**Fig. 12** **a** Schematic image of an open Nb nanotube with inhomogeneous electrodes. **b** Vortex dynamics at the magnetic field $B = 10$ mT, $T = 0.95T_c$. Typical distribution of the order parameter and denotations of the nucleation periods in the proximate $\Delta t_2^{(1)}$ and distant $\Delta t_2^{(2)}$ parts of the tube. **c** Branching of the nucleation period due to inhomogeneous transport current in the tubes with $R = 400$ nm (red) and 600 nm (blue), $L = 3.36$ at $I_{in} = 1.7$ mA μm as a function of the control current (After [23]. © IOP Publishing. Reproduced with permission. All rights reserved.)

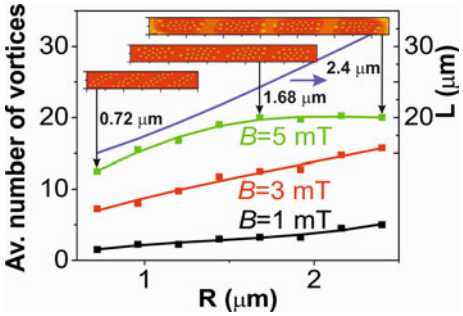


**Fig. 13** Average numbers of vortices per half-turn calculated as a function of the radius of a helical microcoil made from the strip of width $W = 3$ μm with the pitch distance $P = 6$ μm at the applied magnetic fields $B = 1$ mT, 3 mT, and 5 mT. The length of the helical coil along the centerline $L$ is shown with a dotted line. Insets: distributions of the order parameter for three values of the radius $R = 0.72$ μm, 1.68 μm, and 2.4 μm (gray: $|\psi| = 1$, white: $|\psi| = 0$). (After [50]. © IOP Publishing. Reproduced with permission. All rights reserved.)

for extension of the spectrum of superconductor-based sensors to the low-frequency range.

For superconductor helical microcoils, the distribution and number of vortices in a quasi-stationary pattern are governed by their confinement to the ultrathin helical microcoil. Consequently, they can be controlled by the helical radius (see Fig. 13), the helical pitch distance, and the helical stripe width [13]. In the helical microcoil, quasi-degeneracy of vortex patterns is revealed to occur under the condition that the total number of vortices is incommensurable with the number of half-turns. Interestingly, superconductor helical microcoils with decreasing radius provide a realization of a transition from the vortex pattern peculiar to a planar stripe to that of an open microtube.

## 5 Topologic States of Light in Microcavities

Modern advances in nanofabrication have provided novel high-tech materials for nanophotonics with tailored optical properties. A Möbius-ring resonator [51] and a rolled-up asymmetric microcavity [4] are representative examples, which give rise to fascinating topological effects by virtue of Möbiosity, spin–orbit coupling, and non-Abelianism.

### *5.1 Resonant Modes of Light in a Möbius-Ring Resonator*

In-plane polarized light reveals a non-trivial topological evolution in the course of a resonant propagation in a Möbius-ring resonator made of a twisted dielectric strip with the refraction index $n$ [51]. The strip thickness $L_z$ is assumed to be much smaller than the light wavelength: $d < \lambda/n$, so that the electric field is assumed to be stringently confined within the strip in the course of propagation. The strip width is taken larger than the wavelength, and the strip length is selected in the micrometer range to support optical modes in the visible spectral range. Figure 14 shows amplitude profiles for resonance modes of light in a cylindrical ring resonator and a Möbius-ring resonator with $n_u = 8$ and $n_u = 7.5$, respectively, as well as the numbers of antinodes along the centerline.

The integer linearly polarized resonance modes in a cylindrical ring are invariant under rotations at $2\pi$ around the $z$-axis, which is analogous to the rotational symmetry of a boson field:

$$\mathbf{E}(u + 2\pi) = \mathbf{E}(u). \tag{5.1}$$

In a cylindrical ring, a translation of the electric field around the $z$-axis by $2\pi$ returns it to the original position (Fig. 15a). The half-integer linearly polarized resonance modes in a Möbius ring are invariant under rotations at a minimum of $4\pi$ rather than $2\pi$ around the $z$-axis, in analogy to the rotational symmetry of fermions [52]:

$$\mathbf{E}(u + 2\pi) = -\mathbf{E}(u), \;\; \mathbf{E}(u + 4\pi) = \mathbf{E}(u). \tag{5.2}$$

Due to the twist, a translation of the electric field around the $z$-axis by $2\pi$ results in a vector reversal (Fig. 15b). Thus, Möbiosity introduces a key property of *fermions* to the *bosonic* electromagnetic field.

The structure of the amplitude profiles for resonance light modes reveals a remarkable similarity to the structure of the electronic wave function in a Möbius ring with a half-integer number $n_v$ shown in Fig. 4 (lower panel). However, when a linearly polarized light enters the Möbius-ring resonator with an appreciable contrast of refractive indices, the optical electric field is forced to remain parallel to the plane of the twisted strip, and consequently, the polarization orientation continuously varies

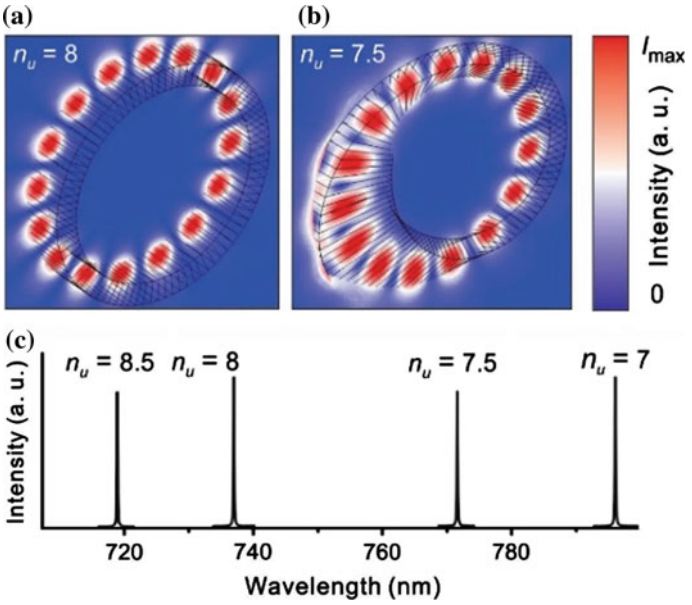


**Fig. 14** Amplitude profiles for the resonance modes of light with integer and non-integer number of wavelengths along the centerline for a cylindrical ring resonator **a** at $n_u = 8$ and a Möbius-ring resonator **b** at $n_u = 7.5$. Both structures are formed, as shown in Fig. 5 for a Möbius-ring resonator, of equivalent strips with $L_x = 2510$ nm, $L_y = 320$ nm, $L_z = 80$ nm with a refractive index $n = 3.5$ and immersed in air. Numbers of antinodes along the centerline are $N = 16$ and $N = 15$, correspondingly. **c** Calculated resonant spectra of intensity for two resonant modes of the cylindrical ring resonator ($n_u = 7, 8$) and two resonant modes of the Möbius-ring resonator ($n_u = 7.5, 8.5$). (After [51])

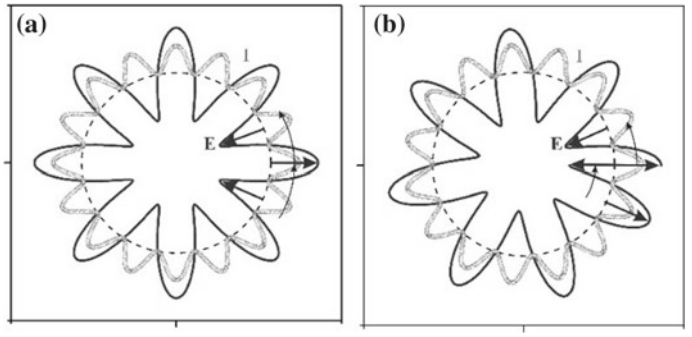


**Fig. 15** Distributions of the electric field **E** (solid line) and intensity $I$ (open circles) for linearly polarized resonance modes around the centerline (dashed line) in the tangential plane for (**a**) a cylindrical ring resonator ($n_u = 8$) and (**b**) a Möbius-ring resonator ($n_u = 7.5$)

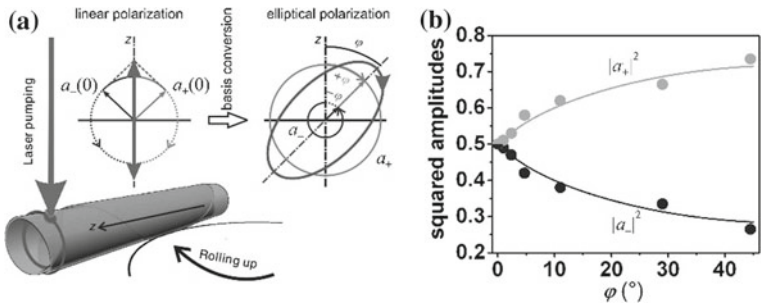


**Fig. 16** **a** Rolled-up cone-shaped microtube cavity and the elliptical polarization state of light occurring due to the basis conversion. **b** Conversion between the clockwise (light gray) and anti-clockwise (black) basis states. Lines represent the squared amplitudes of the circularly polarized waves as a function of the geometric phase calculated according to (5.11). The experimental data are shown with circles. (After [4]. This work is licensed under a Creative Commons Attribution 4.0 International License, http://creativecommons.org/licenses/by/4.0/.)

along the twisted strip during propagation. This behavior represents an adiabatic parallel transport of linearly polarized light in a smoothly curved Möbius ring [53] and allows for an interpretation [51] in terms of a geometric phase introduced by the twist as given by (3.4).

Similar numerical simulations revealed occurrence of half-integer plasmonic modes in metallic Möbius rings at the nanoscale [54].

## 5.2 *Optical Spin–Orbit Coupling and Non-Abelian Evolution of Light in Asymmetric Microcavities*

In conical-shaped asymmetric microcavities, the optical spin–orbit coupling is enabled, and as a consequence, a non-cyclic optical geometric phase acquired in the course of a non-Abelian evolution is observed [4]. Namely, in a rolled-up asymmetric microcavity being pumped by a laser beam (532 nm), the incoming linearly polarized light is found to evolve as the elliptically polarized one, the major axis being tilted out of the tube axis by an angle $\varphi$ (Fig. 16a).

Propagation of light in an inhomogeneous anisotropic dissipationless medium with dielectric permittivity tensor $\hat{\varepsilon}(\mathbf{r})$ is described by the wave equation [55, 56]

$$[\mathcal{L}^2\Delta - \mathcal{L}^2\nabla\nabla + \hat{\varepsilon}(\mathbf{r})]\mathbf{E} = 0, \tag{5.3}$$

where $\mathcal{L} = \frac{c}{\omega}$ is the vacuum wavelength divided by $2\pi$. In a weakly anisotropic medium,

$$\hat{\varepsilon}(\mathbf{r}) = \varepsilon_0(\mathbf{r})\hat{I} + \widehat{\Delta}(\mathbf{r}, \mathbf{p}),$$

where hats denote matrices; $\hat{I}$ is a unit matrix. The wave equation (5.3) is solved in the first weak-anisotropy $\left(\mu_A = \frac{\Delta}{\varepsilon_0} \ll 1\right)$ and geometric-optic $\left(\mu_{GO} = \frac{\lambda}{\mathcal{L}} \ll 1\right)$ approximations [56]. The evolution of the polarization along a ray from the initial polarization $\mathbf{a}(0)$ is approximately described by the path integral over the phase coordinates $(\mathbf{p}, \mathbf{r})$ of the zero-approximation light ray:

$$\mathbf{a}(L) = \int \exp\left[i\widehat{\Phi}\right]\mathcal{D}\mathbf{p}\mathcal{D}\mathbf{r}\,\mathbf{a}(0) \tag{5.4}$$

with the phase

$$\widehat{\Phi} = \frac{1}{\mathcal{L}}\int_L \boldsymbol{p}\cdot \mathrm{d}\boldsymbol{r}\hat{I} + \int_0^L \boldsymbol{a}(\boldsymbol{p})\cdot\dot{\boldsymbol{p}}\hat{\sigma}_z \mathrm{d}\ell + \frac{1}{2\mathcal{L}}\int_0^L \hat{\delta}(\mathbf{p}, \mathbf{r})\mathrm{d}\ell. \tag{5.5}$$

The first term in (5.5) describes classical dynamics of the center of a wave packet in the circular basis; it is the same for both polarizations and does not change the polarization characteristics. In what follows, it will be disregarded without loss of generality. The second term in (5.5) is the spin–orbit interaction, which gives rise to the geometric phase, like in (2.3). The third term stands for the effect of the weak anisotropy of the medium; $\hat{\delta}(\boldsymbol{p}, \boldsymbol{r})$ is a transform of the tensor $\widehat{\Delta}(\mathbf{r}, \mathbf{p})$. Unlike the spin–orbit interaction, the third term in (5.5) contains all three Pauli matrices. The component proportional to $\hat{\sigma}_z$ renormalizes the spin–orbit interaction. The components proportional to $\hat{\sigma}_x$ and $\hat{\sigma}_y$ are anticommutative with each other and with the spin–orbit interaction [57]. This implies the *non-Abelian* evolution of light represented by (5.4).

## 5.3 Non-Abelian Evolution of Light Polarization

An approximate description of the evolution of polarization in a non-Abelian system is introduced by (5.4) and (5.5). A parametrization of that evolution is performed in terms of two parameters along the ray, $\varphi = \varphi(L)$ and $C_A = C_A(L)$, describing the geometric phase and the magnitude of the anisotropy effect:

$$\mathbf{a} = \mathbf{a}(L) = \widehat{\mathrm{M}}\mathbf{a}(0). \tag{5.6}$$

The mapping matrix

$$\widehat{\mathrm{M}} = \exp[i(\varphi\hat{\sigma}_z + C_A\hat{\sigma}_x)] \tag{5.7}$$

is analytically calculated by expanding the exponential in a power series of its argument:

$$\widehat{\mathrm{M}} = \hat{\mathrm{I}} + i(\varphi\hat{\sigma}_z + C_A\hat{\sigma}_x) - \frac{1}{2!}(\varphi\hat{\sigma}_z + C_A\hat{\sigma}_x)^2 - \frac{i}{2!}(\varphi\hat{\sigma}_z + C_A\hat{\sigma}_x)^3 + \cdots$$

Taking into account the basic properties of the Pauli matrices [57]:

$$\hat{\sigma}_x^2 = \hat{\sigma}_z^2 = \hat{\mathrm{I}},\ \hat{\sigma}_z\hat{\sigma}_x + \hat{\sigma}_x\hat{\sigma}_z = 0,$$

we arrive at

$$\widehat{\mathrm{M}} = \hat{\mathrm{I}} + i(\varphi\hat{\sigma}_z + C_A\hat{\sigma}_x) - \frac{1}{2!}(\varphi^2 + C_A^2)\hat{\mathrm{I}} - \frac{i}{3!}(\varphi\hat{\sigma}_z + C_A\hat{\sigma}_x)(\varphi^2 + C_A^2) + \cdots$$

Arranging coefficients for each of the independent matrices, we find an analytic representation

$$\widehat{\mathrm{M}} = \hat{\mathrm{I}}\cos\left(\sqrt{\varphi^2 + C_A^2}\right) + i(\varphi\hat{\sigma}_z + C_A\hat{\sigma}_x)\frac{\sin\left(\sqrt{\varphi^2 + C_A^2}\right)}{\sqrt{\varphi^2 + C_A^2}}. \tag{5.8}$$

or in the explicit form ($\chi = \sqrt{\varphi^2 + C_A^2}$)

$$\widehat{\mathrm{M}} = \begin{vmatrix} \cos\chi + i\varphi\frac{\sin\chi}{\chi} & iC_A\frac{\sin\chi}{\chi} \\ iC_A\frac{\sin\chi}{\chi} & \cos\chi - i\varphi\frac{\sin\chi}{\chi} \end{vmatrix}. \tag{5.9}$$

It is noteworthy that both parameters responsible for the geometric phase $\varphi$ and the magnitude of the anisotropy effect $C_A$ are entangled in each matrix element due to the non-Abelian nature of the system.

According to (5.9), the action of the mapping matrix on a linearly polarized initial basis $\mathbf{a}(0) = \frac{1}{\sqrt{2}}\begin{pmatrix}1\\1\end{pmatrix}$ results in

$$\begin{pmatrix} a_+ \\ a_- \end{pmatrix} = \widehat{\mathrm{M}}\frac{1}{\sqrt{2}}\begin{pmatrix}1\\1\end{pmatrix} = \frac{1}{\sqrt{2}}\begin{pmatrix} \cos\chi + i(C_A + \varphi)\frac{\sin\chi}{\chi} \\ \cos\chi + i(C_A - \varphi)\frac{\sin\chi}{\chi} \end{pmatrix}. \tag{5.10}$$

Due to the anisotropy effect, the squared amplitudes of the circularly polarized components

$$|a_+|^2 = \frac{1}{2}\left(1 + 2C_A\varphi\frac{\sin^2\chi}{\chi^2}\right),\ |a_-|^2 = \frac{1}{2}\left(1 - 2C_A\varphi\frac{\sin^2\chi}{\chi^2}\right) \tag{5.11}$$

become different, which implies an elliptical polarization of the electromagnetic wave. This is a manifestation of the *conversion of basis* occurring due to the non-Abelian dynamics of the system. According to (5.11), the norm of the polarization vector is conserved: $|a_+|^2 + |a_-|^2 = 1$. The plots of the squared amplitudes of (5.11) in Fig. 16b represent conversion of the circular basis.

A correspondence principle to the emergence of geometric phase in isotropic systems is demonstrated in the limit $C_A \to 0$, when the basis

$$\begin{pmatrix} a_+ \\ a_- \end{pmatrix} = \frac{1}{\sqrt{2}} \begin{pmatrix} \exp(i\varphi) \\ \exp(-i\varphi) \end{pmatrix} \tag{5.12}$$

describes the geometric phase $\varphi$ for the clockwise and $-\varphi$ for the anticlockwise circular polarizations.

Introducing the inverse function to $\varphi = \varphi(L) \Rightarrow L = L(\varphi)$, the dependence of the anisotropy parameter on the ray length gives rise to the link between the parameters, which determine the mapping matrix: $C_A = C_A(L(\varphi)) \to C_A(\varphi)$.

The resonant light experiences the non-Abelian evolution in the rolled-up asymmetric microcavity. The polarization state, as described by the eccentricity and the tilt angle, continuously changes during the resonant light propagation in the microcavity, as shown in Fig. 16a. It is experimentally detected, when the light escapes from the microcavity. At that point, the final state of the evolution of light has been reached. The ray length from the light pumping until the light escape is determined by the quality factor of the asymmetric microtube cavity. In the course of this process, the major axes of the evolving polarization state trace a helical spiral around the axis of the microtube. Matching (5.11) to the experimentally detected squared amplitudes of the circularly polarized components for $\varphi$ ranging from 0 to 44.5° (Fig. 16b) allows for the following numerical fitting:

$$C_A = 0.318 \times \varphi^{-0.433}. \tag{5.13}$$

Using the mapping matrix (5.10) and the numerical fitting (5.13), a plot of the non-Abelian evolution on the Poincaré sphere is obtained that is represented in Fig. 17. For the interval 0 to 44.5°, the calculated curve nicely matches the experimental data shown with circles [4]. In Fig. 17, the plot is continued until $\varphi = 720°$, beyond the experimentally achieved range. The curve encircles the $z$-axis, and at every next round, it steadily approaches the equator of the Poincaré sphere, which corresponds to the linear polarization of light. In summary, in rolled-up asymmetric microtube resonators, the non-cyclic geometric phase as well as the photon basis conversion occurs during a non-Abelian evolution.

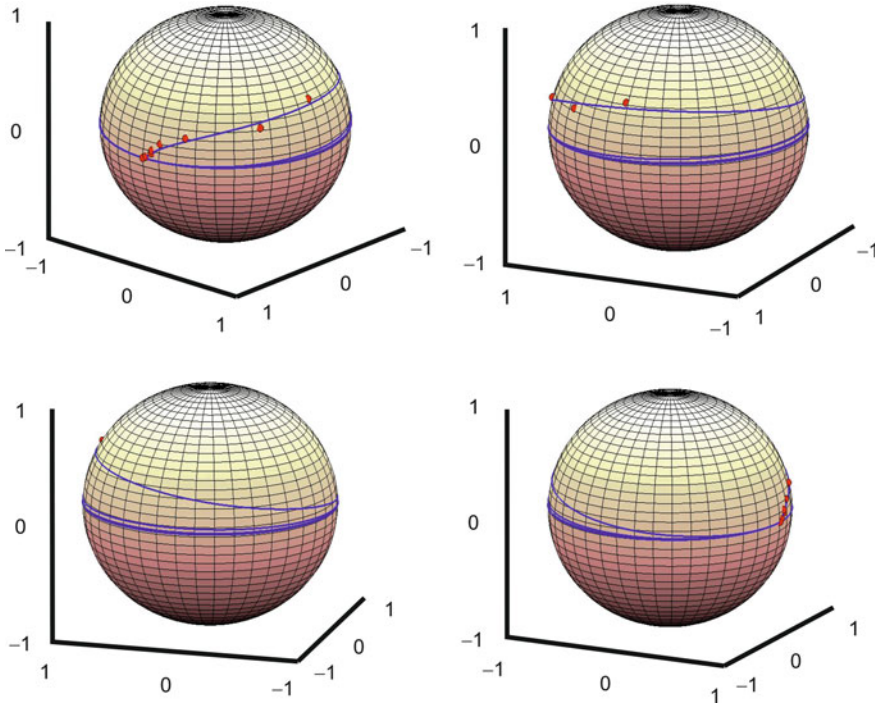

**Fig. 17** Illustration of the non-Abelian evolution calculated using (5.10) and (5.13) as a curve on the Poincaré sphere. In order to facilitate perception, the Poincaré sphere is represented from different points of view. The experimental data of [4] are shown with circles

## 6 Conclusions

Ring-like (doubly connected) and twisted micro- and nanoarchitectures possess unique densities of states for electrons, holes, spins, plasmons, photons, and phonons and hence exhibit a broad variety of non-trivial quantum-interference effects, which can be efficiently controlled by the geometric parameters of a ring-like system and tuned by the magnetic flux piercing it. Those effects open new pathways for advances in such fields as photon-, fluxon-, and spin-based quantum computing, magnetic memory, photonic detectors and emitters, as well as engineering of novel electronic, magnetic, spintronic, plasmonic, photonic, and phononic metamaterials.

Both quantum relativity and cosmic topology reveal remarkable analogies to condensed matter physics, although these disciplines consider systems of length scales many orders apart. The observation of non-uniform quantum states of the electron or other quantum fields in inhomogeneous Möbius rings would enable the table-top demonstration of the forces that contributed to shaping the spatial structure of the Universe.

In an open superconductor micro- or nanotube, characteristic times of superconducting vortex dynamics are cardinally distinct from those in a planar film of the same size at the same applied magnetic field. This difference occurs not only due to inhomogeneity of the component of the magnetic field, which is normal to the cylindrical surface, but also due to correlation between the patterns of the superconducting order parameter in the opposite half-cylinders. Tailoring properties of vortex matter in rolled-up superconductor nanoarchitectures implies their promising applications, e.g., as tunable flux generators for fluxonic information processing technologies, in particular, quantum computing.

Optical spin–orbit coupling occurring in rolled-up asymmetric microcavities gives rise to a non-cyclic optical geometric phase acquired in the course of the non-Abelian evolution. This novel study case of non-Abelianism implies great application perspectives for asymmetric microcavities in on-chip quantum devices through topology-driven manipulation of photons.

In summary, topology-driven physical effects occurring owing to a special geometry of novel micro- and nanostructures in real space open up a cornucopia of efficiently controllable properties and hence reveal new avenues to boost the development of strategic areas of nanotechnology.

**Acknowledgements** The author is grateful to A. V. Chaplik, J. T. Devreese, J. M. García, V. N. Gladilin, S. Kiravittaya, P. M. Koenraad, S. L. Li, L. B. Ma, R. O. Rezaev, O. G. Schmidt, and L. Wendler for fruitful collaborations in the field of the topology-driven effects in advanced nanoarchitectures.

## References

1. V.M. Fomin (ed.), *Physics of Quantum Rings* (Springer, Berlin-Heidelberg, 2014) 487 p.; *Physics of Quantum Rings*, 2nd edn. (Springer, Berlin-Heidelberg, 2018) (in press)
2. V.M. Fomin, S. Kiravittaya, O.G. Schmidt, Phys. Rev. B **86**, 195421 (2012)
3. C. Kern, M. Kadic, M. Wegener, Phys. Rev. Lett. **118**, 016601 (2017)
4. L.B. Ma, S.L. Li, V.M. Fomin, M. Hentschel, J.B. Götte, Y. Yin, M.R. Jorgensen, O.G. Schmidt, Nat. Commun. **7**, 10983 (2016)
5. R.-P. Riwar, M. Houzet, J.S. Meyer, Y.V. Nazarov, Nat. Commun. **7**, 11167 (2016)
6. N. Romming, C. Hanneken, M. Menzel, J.E. Bickel, B. Wolter, K. von Bergmann, A. Kubetzka, R. Wiesendanger, Science **343**, 636 (2013)
7. O.V. Pylypovskyi, V.P. Kravchuk, D.D. Sheka, D. Makarov, O.G. Schmidt, Y. Gaididei, Phys. Rev. Lett. **114**, 197204 (2015)
8. D.R. Streubel, P. Fischer, F. Kronast, V.P. Kravchuk, D.D. Sheka, Y. Gaididei, O.G. Schmidt, D. Makarov, J. Phys. D: Appl. Phys. **49**, 363001 (2016)
9. K. v. Klitzing, G. Dorda und M. Pepper, Phys. Rev. Lett. **45**, 494 (1980)
10. D.J. Thouless, M. Kohmoto, M.P. Nightingale, M. den Nijs, Phys. Rev. Lett. **49**, 405 (1982)
11. M. König, S. Wiedmann, C. Brüne, A. Roth, H. Buhmann, L.W. Molenkamp, X.-L. Qi, S.-C. Zhang, Science **318**, 766 (2007)
12. C.-Z. Chang, J. Zhang, X. Feng, J. Shen, Z. Zhang, M. Guo, K. Li, Y. Ou, P. Wei, L.-L. Wang, Z.-Q. Ji, Y. Feng, S. Ji, X. Chen, J. Jia, X. Dai, Z. Fang, S.-C. Zhang, K. He, Y. Wang, L. Lu, X.-C. Ma, Q.-K. Xue, Science **340**, 167 (2013)
13. Y. Xu, I. Miotkowski, C. Liu, J. Tian, H. Nam, N. Alidoust, J. Hu, C.-K. Shih, M.Z. Hasan, Y.P. Chen, Nat. Phys. **10**, 956 (2014)

14. C. Beenakker, L. Kouwenhoven, Nat. Phys. **12**, 618 (2016)
15. S.-Y. Xu, I. Belopolski, N. Alidoust, M. Neupane, G. Bian, C. Zhang, R. Sankar, G. Chang, Z. Yuan, C.-C. Lee, S.-M. Huang, H. Zheng, J. Ma, D.S. Sanchez, B.K. Wang, A. Bansil, F. Chou, P.P. Shibayev, H. Lin, S. Jia, M.Z. Hasan, Science **349**, 613 (2015)
16. L. Lu, J.D. Joannopoulos, M. Soljačić, Nat. Phys. **12**, 627 (2016)
17. R. Süsstrunk, S.D. Huber, Science **349**, 47 (2015)
18. V.Y. Prinz, V.A. Seleznev, A.K. Gutakovsky, A.V. Chehovskiy, V.V. Preobrazenskii, M.A. Putyato, T.A. Gavrilova, Physica E **6**, 828 (2000)
19. O.G. Schmidt, K. Eberl, Nature **410**, 168 (2001)
20. V.M. Fomin, R.O. Rezaev, O.G. Schmidt, Nano Lett. **12**, 1282 (2012)
21. R.O. Rezaev, V.M. Fomin, O.G. Schmidt, Physica C **497**, 1 (2014)
22. R.O. Rezaev, E.A. Levchenko, O.G. Schmidt, V.M. Fomin, Russ. J. Phys. **5**, 35 (2015)
23. R.O. Rezaev, E.A. Levchenko, V.M. Fomin, Sup. Sci. Technol. **29**, 045014 (2016)
24. V.M. Fomin (ed.), *A special issue on modern advancements in experimental and theoretical physics of quantum rings*. J. Nanoelectron. Optoelectron. **6**, 1–86 (2011)
25. S.M. Rytov, Dokl. Akad. Nauk SSSR **18**, 263 (1938). [English translation in: B. Markovsky, S.I. Vinitsky (eds.), *Topological Phases in Quantum Theory* (World Scientific, Singapore, 1989), pp. 6–10.]
26. V.V. Vladimirskii, Dokl. Akad. Nauk SSSR **21**, 222 (1941). [English translation in: B. Markovsky, S.I. Vinitsky (eds.), *Topological Phases in Quantum Theory* (World Scientific, Singapore, 1989), pp. 11–16.]
27. S. Pancharatnam, Proc. Ind. Acad. Sci. A **44**, 247 (1956)
28. M.V. Berry, Proc. R. Soc. London A **392**, 45 (1984)
29. M. Born, V. Fock, Z. Phys. **51**, 165 (1928)
30. Y. Aharonov, J. Anandan, Phys. Rev. Lett. **58**, 1593 (1987)
31. Y. Aharonov, D. Bohm, Phys. Rev. **115**, 485 (1959)
32. W. Ehrenburg, R.E. Siday, Proc. R. Soc. Lond. B **62**, 8 (1949)
33. P. Offermans, P.M. Koenraad, J.H. Wolter, D. Granados, J.M. García, V.M. Fomin, V.N. Gladilin, J.T. Devreese, Appl. Phys. Lett. **87**, 131902 (2005)
34. V.M. Fomin, V.N. Gladilin, J.T. Devreese, P. Offermans, P.M. Koenraad, J.H. Wolter, J.M. García, D. Granados, AIP Conf. Proc. **772**, 803 (2005)
35. V.M. Fomin, V.N. Gladilin, S.N. Klimin, J.T. Devreese, N.A.J.M. Kleemans, P.M. Koenraad, Phys. Rev. B **76**, 235320 (2007)
36. N.A.J.M. Kleemans, I.M.A. Bominaar-Silkens, V.M. Fomin, V.N. Gladilin, D. Granados, A.G. Taboada, J.M. García, P. Offermans, U. Zeitler, P.C.M. Christianen, J.C. Maan, J.T. Devreese, P.M. Koenraad, Phys. Rev. Lett. **99**, 146808 (2007)
37. T.-C. Lin, C.-H. Lin, H.-S. Ling, Y.-J. Fu, W.-H. Chang, S.-D. Lin, C.-P. Lee, Phys. Rev. B **80**, 081304(R) (2009)
38. H.D. Kim, K. Kyhm, R.A. Taylor, G. Nogues, K.C. Je, E.H. Lee, J.D. Song, Appl. Phys. Lett. **102**, 033112 (2013)
39. J.T. Devreese, V.M. Fomin, V.N. Gladilin, J. Tempere, Physica C **470**, 848 (2010)
40. Z. Li, L.R. Ram-Mohan, Phys. Rev. B **85**, 195438 (2012)
41. J. Gravesen, M. Willatzen, Phys. Rev. A **72**, 032108 (2005)
42. S.O. Demokritov, A.A. Serga, V.E. Demidov, B. Hillebrands, M.P. Kostylev, B.A. Kalinikos, Nature **426**, 159 (2003)
43. A.F. Möbius, Berichte über die Verhandlungen der Königlich Sächsischen Gesellschaft der Wissenschaften. Mathematisch-physikalische Klasse **17**, 31 (1865)
44. R.C.T. Da Costa, Phys. Rev. A **23**, 1982 (1981)
45. C.J. Isham, Proc. R. Soc. London A **362**, 383 (1978)
46. J.S. Dowker, R. Banach, J. Phys. A **11**, 2255 (1978)
47. B.S. DeWitt, C.F. Hart, C.J. Isham, Physica **96A**, 197 (1979)
48. J.P. Sethna, *Statistical Mechanics: Entropy, Order Parameters, and Complexity* (Oxford University Press, Oxford, 2006)
49. M. Tinkham, *Introduction to Superconductivity* (McGraw-Hill Inc, Singapore, 1996)

50. V.M. Fomin, R.O. Rezaev, E.A. Levchenko, D. Grimm, O.G. Schmidt, J. Phys.: Condens. Mater. **29**, 395301, 1 (2017)
51. S.L. Li, L.B. Ma, V.M. Fomin, S. Böttner, M. R. Jorgensen, O.G. Schmidt, arXiv:1311.7158 [physics.optics], 1–9 (2013)
52. D.J. Ballon, H.U. Voss, Phys. Rev. Lett. **101**, 247701 (2008)
53. M.V. Berry, Nature **326**, 277 (1987)
54. Y. Yin, S. Li, V. Engemaier, E.S.G. Naz, S. Giudicatti, L. Ma, O.G. Schmidt, Laser & Photonics Rev. **11**, 1600219 (2017)
55. K.Y. Bliokh, D.Y. Frolov, Y.A. Kravtsov, Phys. Rev. A **75**, 053821 (2007)
56. K.Y. Bliokh, A. Niv, V. Kleiner, E. Hasman, Nat. Photonics **2**, 748 (2008)
57. M. Le Bellac, *Quantum Physics* (Cambridge University Press, Cambridge, 2006), p. 85

# Functional Magnetic Metamaterials for Spintronics


**Yu. P. Sharaevsky, A. V. Sadovnikov, E. N. Beginin, A. Yu. Sharaevskaya, S. E. Sheshukova and S. A. Nikitov**

**Abstract** An overview of functional magnonic metamaterials is presented. We consider three types of the magnetic structures. First, we demonstrate the frequency-selective spin-wave transmission in irregular tapered magnonic strip with a periodical width modulation. By using space- and time-resolved Brillouin light scattering spectroscopy technique, we measured the features of the intermodal interaction and scattering at the boundaries of the periodical structures. In the vicinity of the band-gap frequency region, the spin-wave spatial patterns depend on the mode interaction in the width-modulated confined magnonic structure. We believe that these results

Yu. P. Sharaevsky · A. V. Sadovnikov · E. N. Beginin · A. Yu. Sharaevskaya · S. E. Sheshukova
S. A. Nikitov (✉)
Laboratory "Metamaterials", Saratov State University, 83 Astrakanskaya Str., Saratov 410012, Russia
e-mail: nikitov@cplire.ru
URL: http://www.cplire.ru/html/index.html

Yu. P. Sharaevsky
e-mail: sharaevskyyp@info.sgu.ru
URL: https://www.sgu.ru/person/sharaevskiy-yuriy-pavlovich

A. V. Sadovnikov
e-mail: sadovnikovav@gmail.com
URL: https://www.sgu.ru/person/sadovnikov-aleksandr-vladimirovich

E. N. Beginin
e-mail: egbegin@gmai.com
URL: https://www.sgu.ru/person/beginin-evgeniy-nikolaevich

A. Yu. Sharaevskaya
e-mail: annasharik2@gmail.com
URL: https://www.sgu.ru/

S. E. Sheshukova
e-mail: sheshukovase@yandex.ru
URL: https://www.sgu.ru/

Yu. P. Sharaevsky · A. V. Sadovnikov · E. N. Beginin · A. Yu. Sharaevskaya · S. E. Sheshukova
S. A. Nikitov
Kotel'nikov Institute of Radioengineering and Electronics, Russian Academy of Sciences, Moscow 125009, Russia



A. Sidorenko (ed.), *Functional Nanostructures and Metamaterials for Superconducting Spintronics*, NanoScience and Technology,
https://doi.org/10.1007/978-3-319-90481-8_11

are important for control of the spin-wave propagation in width-modulated magnetic structures for future spintronic and magnonic devices. Second, we consider the irregular magnetic strip with the tapered region. We show that the broken translational symmetry leads to the switching of the mode interferential pattern. We also demonstrate that the non-uniform magnetic field profile forms the conditions for the local three-magnon decay in the irregular magnetic strip. These findings are important for the planar magnonic network concept as the "Beyond CMOS" computing techniques. Next, we propose the side-coupled magnonic crystal with the defect area inside. The coupling of the defects leads to the complicated spin-wave transmission spectra due to the coexistence of the multiple defect modes inside the frequency range of the magnonic band gap. Finally, we present the results of the study of the transformation of dynamic magnetization patterns in a bilayer multiferroic structure. This phenomenon is described with a simple electrodynamic model based on the numerical finite-element method. The studied confined multiferroic strip can be utilized for the fabrication of integrated dual tunable functional devices for magnonic applications.

## 1 Introduction

The concept of the metamaterials as the composite media with artificially created periodic or irregular structural elements is widely recognized (see, e.g., [1] and references therein). The demonstrative example is the photonic crystals which can be referred to as the metamaterials based on dielectric mediums with periodic variation of the refractive indices [2]. It is possible to effectively control the wave characteristics in metamaterials by choosing parameters of structural elements (sizes, geometry, and period). This opens the possibility of fabrication of metamaterial-based signal processing devices in the optical frequency range. It should be noted that the basic concepts of metamaterials can be used effectively for magnetic and multiferroic materials, which can be tuned by external electric and magnetic fields (saturation magnetization, magnetic permeability, etc.).

The study of the physical processes in the magnetic metamaterials led to the formation of a new scientific direction—magnonics [3–6]. In the framework of magnonics, the magnetization dynamics is studied in magnetic media with different spatial dimensions of one- and two-dimensional structural elements. In particular, magnonic crystals (MCs) have been fabricated on the basis of magnetic metamaterials, as an analogy of photonic crystals [7]. The wave processes in MCs are determined by the spin-wave propagation in magnetically ordered media. Spatial variations of material parameters of the medium, magnetic fields, or boundary conditions can form the magnetic metamaterial (periodic or irregular).

The number of unique properties of magnetic metamaterials should be emphasized, e.g.,

- The characteristic frequencies of the wave processes depend on magnitude and direction of the external magnetic field and can be tuned by in a wide frequency range from MHz to THz [8].
- The dispersion characteristics of waves depend on the direction of their propagation relative to the direction of the static magnetic fields. Moreover, the dispersion can be either positive or negative [9].
- Dispersion characteristics of spin waves in structures based on magnetic metamaterials strongly depend on the boundary conditions.
- The spin-wave wavelength varies from 0.1 to 1000 μm for a fixed value and orientation of magnetic field.

These features of wave processes in magnetic metamaterials provide a possibility to create the MCs with functional properties by the decrease in structural elements' size to the nanometer scale. Magnon spintronics is formed in the last decades as a new promising scientific direction [6]. In contrast to electronic devices, where the transfer of electric charge is essential, in spintronics devices the spin transfer (spin current, spin waves, spin-polarized current) in ferromagnetic structures is considered. Integration of spintronics and magnonics elements in the semiconductor-based electronics makes possible the fabrication of the functional devices for signal processing, storage, and transmitting the information flows with the high speed and low power consumption.

Nowadays, the next problems in spintronics and magnonics based on magnetic metamaterials should be addressed:

- Fabrication of micro- and nano-sized magnetic structures with optimal conditions for the spin transport and spin-wave propagation;
- Improvement of the efficiency of interaction between magnetic and electronic subsystems (spin waves and spin current);
- Tunability of the magnetic metamaterials, in particular, fabrication of electrically controlled metamaterials by the variation of the dielectric and magnetic permeabilities.

In this chapter, we present the theoretical and experimental results of spin-wave properties in magnetic metamaterials. We demonstrate the spin-wave control in the confined magnetic waveguiding structures. Both the frequency filtering and spatial filtering are considered. We focus on the magnonic crystals and irregular magnonic and multiferroic waveguides, which are the building blocks of any complex integral magnonic network, acting as the transmission line between signal processing devices. We also address the coupling of spin waves in the side-coupled topology of the magnonic architecture.

## 2 Spin Waves in Width-Modulated Magnonic Crystal

Periodic magnetic structures have been extensively studied in the past decades. The periodicity can be created by, e.g., the modulation of the magnetic properties of materials [10], periodically varying geometrical parameters: the thickness or width of planar spin-wave (SW) waveguides [7], fabricating periodic arrays of magnetic nano-dots [4], spatial modulation of the applied magnetic field [11]. Such artificially fabricated MCs [7] demonstrate the formation of magnonic band gaps (frequencies, in which the SWs are exponentially decayed due to the Bragg reflections). Fabrication of MCs based on yttrium iron garnet (YIG) films leads to the extension of the application area of magnetic thin films in the perspective direction of functional magnonics and spintronics [12–17]. In [18], the spin-wave filters based on the width-modulated MCs were studied theoretically. MCs based on thin film of YIG can be used as the element base for the fabrication of various devices for the signal processing in the microwave frequency range (couplers, power dividers, delay lines, and tunable filters) and offer the possibilities to flexibly control the SW characteristics due to small magnetic losses in YIG. In [19], the MC-based tunable microwave phase shifter has been proposed. The characteristics of SW in MCs can be varied over a wide range with variation of an external magnetic field and the existence of variety of the dispersion types of propagating waves (surface and volume, forward and backward) [9]. The downscaling of YIG waveguiding strips to micro- and nano-sizes leads to the practical applications as "Beyond CMOS" systems and integration in the semiconductor signal processing, generation, and storage systems [20]. It is worth to note that the miniaturization of the planar YIG waveguides and fabrication of magnetic micro- and nano-strips leads to the necessity for the control of the mode excitation and propagation along the waveguides [21, 22].

Experimental measurement of the spatial distribution of the spin-wave amplitudes can be performed by various methods, for example, microwave probes. It is known that the spatial resolution of the probe methods becomes insufficient for the micro- and nano-sized waveguides. We use the Brillouin light scattering (BLS) technique of magnetic materials [23] as an instrument for spatial and spatiotemporal properties of SW propagation in irregular YIG strip with periodically modulated width.

The laser patterning technique is the most quick and convenient methods for MCs' fabrication [24, 25]. The monocrystalline $d$ = 10-μm-thick Bi-doped YIG film with saturation magnetization of $4\pi M_0$ = 1350 G was used for laser patterning in the fabrication of width-modulated MC. YIG film was grown on gadolinium gallium garnet (GGG) substrate with the thickness of 500 μm. The fabricated irregular magnonic waveguide consists of two sections: the regular waveguides with the width of $w_{01}$ = 2000 μm and $w_0$ = 353 μm. Both sections were connected by taper region with linear variation of width (see Fig. 1a).

Magnonic crystal with periodic sequence of rectangular notches on the edges was fabricated in narrow section by laser scribing technique [24]. The geometrical dimensions of this structure are shown in Fig. 1a. The edge width was $b$ = 60 μm and height $a$ = 60 μm. The total length of irregular waveguide was 7.04 mm, and the length

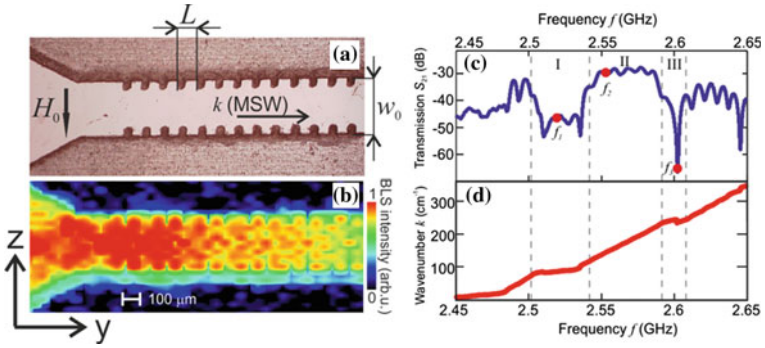


**Fig. 1** **a** Photograph of the width-modulated section of periodic waveguide with the following dimensions: $L$ = 122 μm, $w_0$ = 353 μm. **b** The spatial distribution of MSSW intensity $I(y, z)$ (frequency $f$ = 2.541 GHz). **c** The transmission characteristic of MSSW. The red circles indicate the frequencies, where the BLS measurements were performed: $f_1$ = 2.519 GHz, $f_2$ = 2.55 GHz, $f_3$ = 2.608 GHz. Regions I, II, and III denote the areas with different spin-wave dynamics. **d** Dispersion of MSSW in width-modulated magnonic strip

of narrow waveguide with MC was 5 mm. The 30-μm-width microstrip antennas of length of 3 mm are used for magnetostatic wave (MSW) excitation. The input antenna is attached to the wide part of the irregular waveguide at 1.5 mm from the beginning of the periodic structure in the narrow waveguide. The output antenna is located in the narrow part at distance of $h$ = 5 mm from the input. The applied magnetic field $H_0$ = 444 Oe is oriented in the plane of the waveguide along the microstrip antenna (along $z$-axis). In this case, surface magnetostatic waves (MSSWs) are excited.

The transmission characteristic of MC was measured by vector network analyzer (VNA). Spatiotemporal distribution of intensity of MSSW in MC was measured using BLS technique. Figure 1b demonstrates the spatial distribution of MSSW intensity $I(y, z)$, at the frequency of 2.541 GHz. The transmission characteristic (amplitude of $S_{21}$ coefficient) measured at input power of $P_{in}$ = –30 dBm was shown in Fig. 1c. The dispersion characteristic of MSSW $k(f)$ (Fig. 1d) ($k$ is a wave number) was obtained by means of the phase-frequency shift of wave between microstrip antennas. Three typical frequency regions with different levels of attenuation of MSSW in the transmission characteristic can be distinguished in Fig. 1c. Region I is located near the lower cutoff frequency of MSSW with the wave numbers about $k \sim 100$ cm$^{-1}$. In the region III, the wave propagates with wave number of $k \sim 240$ cm$^{-1}$. MSSW propagates with relatively low attenuation of –30 dB in the region II.

The spatial distribution of the MSSW intensity in MC at different frequencies was investigated by BLS technique. The microwave pulses with duration of $\tau$ = 200 ns, input power $P_{in}$ = –10 dBm, and repetition period $T_i$ = 1.5 μs were used for waveguide excitation. Spatial scanning was performed with resolution $\Delta y = \Delta z =$ 0.03 mm. The intensity of scattered light on MSW is given by [23] and reads as $I(y, z, t) \propto |m(y, z, t)|^2$, where $m(y, z, t)$ is the amplitude of MSW. The intensity of MSW is defined as integration over repetition period $T_i$ and waveguide width $w_0$:

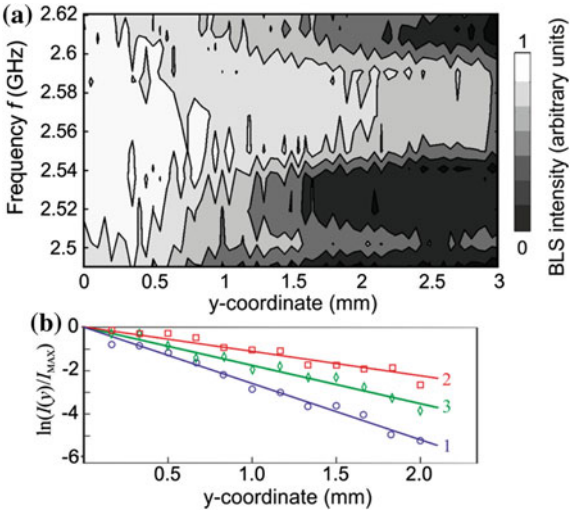


**Fig. 2** **a** Spatio-frequency distribution of MSSW intensity $I(f, y)$ in MC. The forbidden bands are clearly distinguished in the regions I and III depicted in Fig. 2.; **b** spin-wave normalized integrated intensity as a function of propagation distance y. Open circles denote the first forbidden gap of MC (the frequency of input signal $f_1 = 2.519$ GHz), squares—transmission band ($f_2 = 2.55$ GHz), diamonds—second forbidden gap ($f_3 = 2.608$ GHz)

$J(f, y) = \int_0^{T_i} \int_0^{w_0} I(f, y, z, t)\mathrm{d}z\mathrm{d}t$, where $f$ is the frequency of MSW. The spatial frequency distribution of the integrated intensity $J(f, y)$ is shown in Fig. 2a. The beginning of MC in the narrow part of waveguide corresponds to coordinate $y_{MC} = 0.25$ mm. The widths of first and second forbidden bands are 50 and 10 MHz, respectively.

The position of these regions on the frequency axis corresponds to regions I and III in Fig. 1c. Spin-wave intensity as a function of propagation distance is shown in Fig. 2b. Here, we plot the value of $J(f, y)/J(f, 0)$ as a function of $y$-coordinate at the different frequencies of input signal. Measurement of the decay length $L_{dis}$ (distance at which the intensity of SW falls to $(1/e)$ of its initial value) of SW was obtained from BLS experiment at different frequencies of the applied microwave signal: at $f_1$, $L_{dis} = 0.39$ mm; at $f_2$, $L_{dis} = 0.57$ mm; at $f_3$, $L_{dis} = 0.89$ mm.

The first and second forbidden bands were formed due to the scattering of MSSW on the periodic waveguide edges, formed by width modulation. The estimation of the distance along which MSSW propagates with significant decay reveals the sufficient distance from the beginning of the MC to formation of rejection band. Figure 3b demonstrates that this distance is equal to 10 period of structure. Spatial distribution of waves in MC is characterized by the integrated intensity $J(y, z) = \int_0^{T_i} I(y, z, t)\mathrm{d}t$. The modes of MSSW are distributed in the regular part of the narrow waveguide before the beginning of MC (in the region $y < y_{MC}$) with transverse amplitude distribution, given by $\sin(n\pi z/w_0)$, where $n = 1, 3, 5$. Thus, the multimode regime of spin-wave excitation and propagation in MC was observed [26].

The spatial distributions of the MSSW modes corresponds to the interference pattern of the width modes with $n = 1$ and $n = 3$. Figure 3 shows the spatial distributions of the integrated intensity $I(y, z)$ at frequencies $f_1, f_2$, and $f_3$. The spatial spin-wave

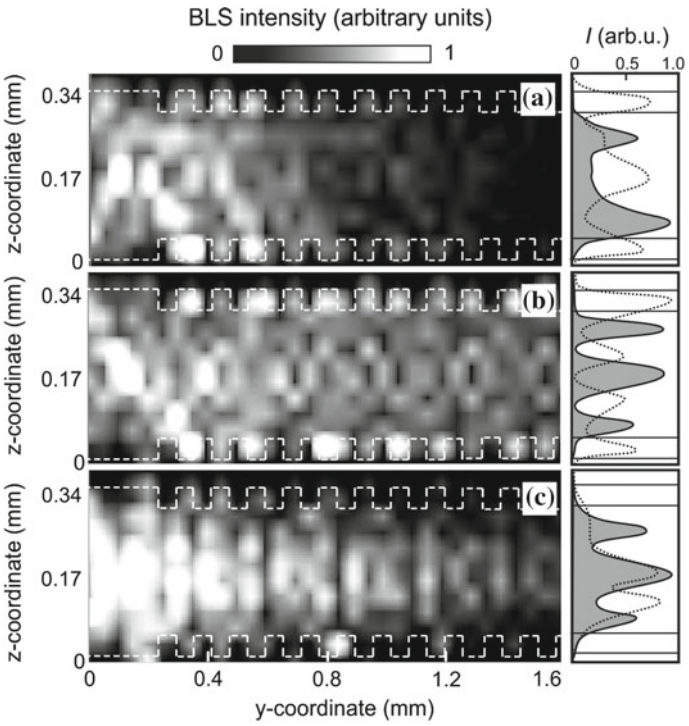


**Fig. 3** Spatial distribution of MSSW intensity $I(y, z)$ in MC at different frequencies of the input microwave signal: **a** $f_1 = 2.519$ GHz, **b** $f_2 = 2.55$ GHz, **c** $f_3 = 2.608$ GHz. The right panels show the transverse distribution of spin-wave intensity in the cross section $y_1 = 0.7$ mm and $y_2 = 0.76$ mm (for the wide (dashed curves) and narrow (solid curves) parts of the MC)

patterns are formed due to the superposition of the incident and scattered modes with different mode index $n$.

Next, we consider the regions I and III. The coefficient of wave reflection from one period of MC can be written in the form [11] $\Gamma_n = (k_{0n} - k_{1n})/(k_{0n} + k_{1n})$, where $k_{0n}$, $k_{1n}$ are the wave numbers at frequency $f$ in waveguides of width $w_0$ and $w_1 = w_0 - 2a$, respectively. The value of $\Gamma_n$ was estimated using the dispersion characteristics of MSSW in confined magnetic strip [21]. It was shown that in the region I (Fig. 4a) the main role in the formation of the spatial pattern of intensity plays the spin-wave intermode interaction and their scattering at the boundaries of the magnonic structure. These mechanisms lead to a rapid spatial damping of MSSW and formation of a broad forbidden gap. As it is shown in Fig. 3b, in the region II the coefficient $\Gamma_n$ decreases and the redistribution of the MSSW intensity from the edge of MC to its longitudinal axis is observed. Dissipation efficiency of MSSW on periodic waveguide edges decreases, and during wave propagation, the profile of the transverse intensity distribution $I(y,z)$ is approached to the distribution in the form $\sin^2(\pi z/w_0)$ for the fundamental mode. This leads to the formation of the Bragg

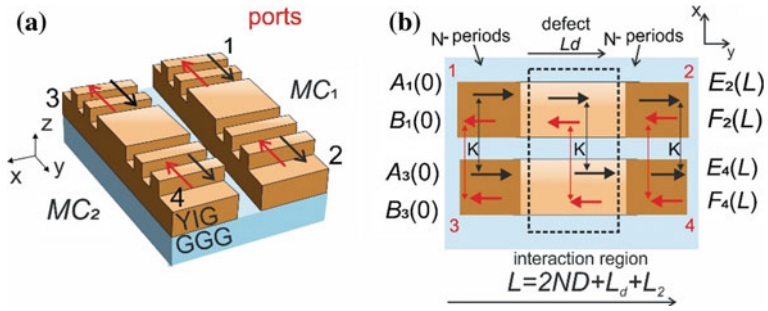


**Fig. 4** **a** Schematic side-coupling magnonic crystals with broken translational symmetry and **b** view in $(x, y)$ plane

forbidden gap. Figure 3c demonstrates that in the frequency range III the regime of spin-wave propagation with low damping and multimode nature of the transverse distribution are observed. The transverse distributions of intensity in the wide and narrow parts of MC at $y_1 = 0.7$ mm and $y_2 = 0.76$ mm are shown in right panels of Fig. 3. Note that the spin-wave intensity distribution $I(z)$ is transformed with the increase in the signal frequency (from frequency $f_1$ to the frequency $f_3$).

Thus, the multimode propagation of MSSW in irregular width-modulated YIG waveguide was studied experimentally. The use of tapered region of YIG waveguide leads to the tuning of band-gap frequencies of MC due to the wavenumber control of magnonic crystal's width modes. The spatial frequency characteristics at the frequency of the forbidden band gaps of MC were experimentally studied. Two forbidden bands of widths 40 and 10 MHz were observed. The features of the intermodal interaction of width modes and their scattering at the boundaries of the waveguide have been investigated experimentally using space- and time-resolved Brillouin light scattering spectroscopy. We show that near the band-gap frequency region the formation of the spatial pattern of spin wave depends on the mode interaction in the periodically width-modulated YIG strip. These effects should be taken into account when constructing mathematical models of spin-wave propagation in MC and fabrication of functional magnonic frequency-selective devices. Recent development of YIG thin-film fabrication enables lithography pattering of periodic strips with even smaller scale [27].

## 3 Defect Spin-Wave Modes Coupling in Magnonic Crystals

Some attractive features of spin-wave propagation in MCs are interesting for microwave signal processing on the basic magnonic band gaps with strong response to various imperfections of a periodic surface of MC [28]. Creating structural defects in magnonic crystals leads to their translational symmetry breakdown, whereas local modification of the thickness of one of the layers in an one-dimensional (1D) MC

leads to appearance of the discrete levels within the band gap at the frequencies according to the half wavelength of standing wave resonance peaks along defect layer length [7]. Depending upon the defect size and composition, existence of a single defect with variation of geometry and magnetic parameters may lead to appearance of one or several defect modes. Also defect modes can be interesting for improvement in quality for selective filters, microwave generators, and signal processing [29–31].

Defects on periodic lattice can be created by using another material. For instance, a structural or compositional defect could be a strip element, of a different width or material, in an otherwise perfect periodic multicomponent array of strips. Attention to defect properties refers to photonic crystals and has attracted owing to their physical properties and wide potential for applications [32].

In addition to the presence of structural defects, coupled periodic magnonic structures have relevant interest for controlling forbidden bands. In this chapter [33], main features of formation band gaps in the proposed two coupled 1D MCs separated by a dielectric layer were identified and studied. Following, we consider the model of the layered structure, which consists of two adjacent 1D magnonic crystals with broken translation symmetry in each MC. Such model combines coupled periodic structures and the presence of defects. The presented results of theoretical measurements of the defect modes and its behavior in the spin-wave spectra in coupled 1D MC were obtained. Interest to such structures with defects is based on the possibility to applying of selective switching components.

We investigated two laterally coupled magnonic crystals ($MC_1$ and $MC_2$) composed of ferrimagnetic yttrium iron garnet ($Y_3Fe_5O_{12}$) film situated on gadolinium gallium garnet (GGG) with defect in lattice (see Fig. 4a) and top view (see Fig. 4b) in ($x$, $y$) plane of such four-port structure with coupling along structure length.

It is suggested that MCs consist of regular waveguide segments (elementary layers) of thickness $d_1$ and $d_2$ and the spatial period $D = L_1 + L_2$ ($L_1$ and $L_2$ are the lengths of regular waveguides with thicknesses $d_1$ and $d_2$) [34, 35]. Regions with defects propose as segments of waveguides with length and thickness—$L_d$ and $d_1$. We assume that in each segment of elementary layer the total field is the superposition of magnetostatic waves propagating in the $+y$ and $-y$ directions. Also, two MCs with defects are waveguides in which waves propagating related to coupling coefficient $K$. Ports of coupled MCs are shown as (see Fig. 4b) vectors-columns of amplitudes of magnetostatic waves in the cross section $y = 0$ and $y = L$:

$$\vec{\psi}(0) = \begin{pmatrix} A_1(0) \\ B_1(0) \\ A_3(0) \\ B_3(0) \end{pmatrix}, \vec{\psi}(L) = \begin{pmatrix} E_2(L) \\ F_2(L) \\ E_4(L) \\ F_4(L) \end{pmatrix},$$

where—$A_1(0)$, $A_3(0)$, $B_1(0)$, $B_3(0)$—amplitudes of the incident and reflected waves in ports 1 and 3; $E_2(L)$, $E_4(L)$, $F_2(L)$, $F_4(L)$—amplitudes of the transmitted and incident waves in ports 2 and 4.

Using the transmission matrix method, it can be shown that the wave amplitudes in the ($y = 0, L$) profiles are related by the following expression:

$$\vec{\psi}(0) = \overleftrightarrow{M}\vec{\psi}(L), \tag{1}$$

where $\overleftrightarrow{M}$ is the transfer matrix for coupled structure.

Further, expression for the transfer matrix was calculated. Expression for segments $L_1$, $L_2$, and $L_d$ was obtained according to the theory of coupled waves. Such expression provides connection between wave amplitudes at ports with transmission matrices in the form:

$$\overleftrightarrow{M}_j = \begin{pmatrix} \alpha_j & 0 & -\beta_j & 0 \\ 0 & \alpha_j^* & 0 & \beta_j^* \\ \beta_j & 0 & \alpha_j & 0 \\ 0 & -\beta_j^* & 0 & \alpha_j^* \end{pmatrix} \tag{2}$$

where $\alpha_j = e^{-ik_j L_j}\cos(KL_j)$, $\beta_j = e^{-ik_j L_j}\sin(KL_j)$, $\alpha_j^*, \beta_j^*$ are complex conjugate quantities, the index $j$ corresponds to segments of regular waveguides and defect takes the values—*1, 2*. The wave numbers $k_j$ and frequency $f$ in case of distribution MSSW are related by [36]:

$$k_j = \frac{1}{2d_j}\ln\left(\frac{(\mu-1)^2 - \mu_a}{(\mu+1)^2 - \mu_a}\right) \tag{3}$$

where $\mu = \frac{f_H(f_H+f_M)-f^2}{f_H^2-f^2}$, $\mu_a = \frac{f_M f}{f_H^2-f^2}$ $f_M = \gamma 4\pi\ M_0$, $M_0$—saturation magnetization, $f_H = \gamma H_0$, $\gamma$—gyromagnetic ratio, $H_0$—external static magnetic field. Further, we consider the interaction region for waveguides of different thickness $d_j$. Compared to fields of magnetostatic waves at the boundaries, transfer matrices and the amplitudes of the incident, reflected, and transmitted MSSWs in the compound region were obtained:

$$\overleftrightarrow{G}_s = \begin{pmatrix} \rho & \eta & 0 & 0 \\ \eta & \rho & 0 & 0 \\ 0 & 0 & \rho & \eta \\ 0 & 0 & \eta & \rho \end{pmatrix} \tag{4}$$

where $\rho = (1 - sB)^{-1}$, $\eta = sB(1 - sB)^{-1}$ $B = (d_1 - d_2)/(d_1 + d_2)$, $s$=*+1, −1* for incident waves on the connection from the side of thick ($d_1$) and thin ($d_2$) elementary layer. Based on the transmission matrices (1, 2, 4), we calculate a transfer matrix for one period $D$ of coupled MCs in the form:

$$\overleftrightarrow{M}_D = \overleftrightarrow{M}_1 \overleftrightarrow{G}_+ \overleftrightarrow{M}_2 \overleftrightarrow{G}_-. \tag{5}$$

Thereafter, we calculated the resulting transmission matrix for considered coupled MCs with a symmetric position of defects; such matrix will be in the form:

$$\overleftrightarrow{M} = \overleftrightarrow{M}_D^N M_d \overleftrightarrow{G}_+ M_2 \overleftrightarrow{G}_- \overleftrightarrow{M}_D^N, \tag{6}$$

where $N$ is the number of periods before and after matrix of defect.

Expressions for the coupling matrix of regular waveguide segments (2) include the coupling coefficient $K$. Without loss of generality, the coupling coefficient is assumed in the form:

$$K = \frac{\pi}{2L} Z, \tag{7}$$

where $Z$—number of wave pumps between magnonic structures, $L = 2^{ND} + L_d + L_2$—length of coupled structure.

Further, we calculated the transmission $T_2 = E_2(L)/A_1(0)$, $T_4 = E_4(L)/\mathrm{A}_1(0)$ and reflection coefficients $R_1 = B_1(0)/\mathrm{A}_1(0)$, $R_3 = B_3(0)/\mathrm{A}_1(0)$ from the ports of coupled MCs. Such dependencies for MSSW are solved by (1) with respect to unknown coefficients and taking into account the dispersion relation from (3). The calculation results of characteristics of the structure MC-MC with defects for $T_2$, $T_4$, $R_1$, $R_3$ are presented in Fig. 5a–e. Thickness of thick layers is $d_1 = 15$ μm, and thickness of thin layers is $d_2 = 13$ μm. Period of structures is D = 200 μm, number of periods is $2N = 30$, length of thick and thin layers is $L_1 = L_2 = 100$ μm, length of defect layer is $L_d = L_1$. Saturation magnetization is $M_0 = 1750/(4\pi)$ G, and applied magnetic field is $H_0 = 1000$ Oe. Assume the case that the power was inserted through the first port ($A_1(0) \neq 0$, $A_3(0) = F_2(L) = F_4(L) = 0$).

First, we consider defect-free side-coupled MCs with weak coupling coefficient $Z = 2$. Characteristics for second and fourth ports $T_2$ and $T_4$ for such structure are shown in Fig. 5a. Note that signals in both structures are decreased in area of Bragg frequency. Also we observed that pumping from one structure to another in frequency intervals ($4.91 \leq f_1 \leq 4.93$ GHz, $4.98 \leq f_2 \leq 4.99$ GHz) is proceeded. It is important to note that in coupled MCs with defects with weak coupling properties will be same as the defect-free MCs.

By increasing coupling between MCs ($Z$—the number of pumping), transition characteristics are significantly changed (see Fig. 5b, c). In the regions ($4.92 \leq f_1 \leq 4.94$ GHz, $4.98 \leq f_2 \leq 5$ GHz) on transmission characteristic $T_2$, two defect modes appear (green dashed lines in Fig. 5c) at non-Bragg frequencies ($f_1 \approx 4.955$ GHz, $f_2 \approx 4.99$ GHz) for crystals with defects with $Z = 5$, according to another MC ($T_4$), there is a decrease in signal at these frequencies. It is possible to observe the difference between the characteristics for MCs with defects and defect-free MCs (see Fig. 5b, c). It can also be noted that in the region of the Bragg frequency the signal propagates in only one of the structures (decrease in transmission coefficient $T_4$). Such effect can be obtained by the presence of coupling between structures. Occurrence of defect

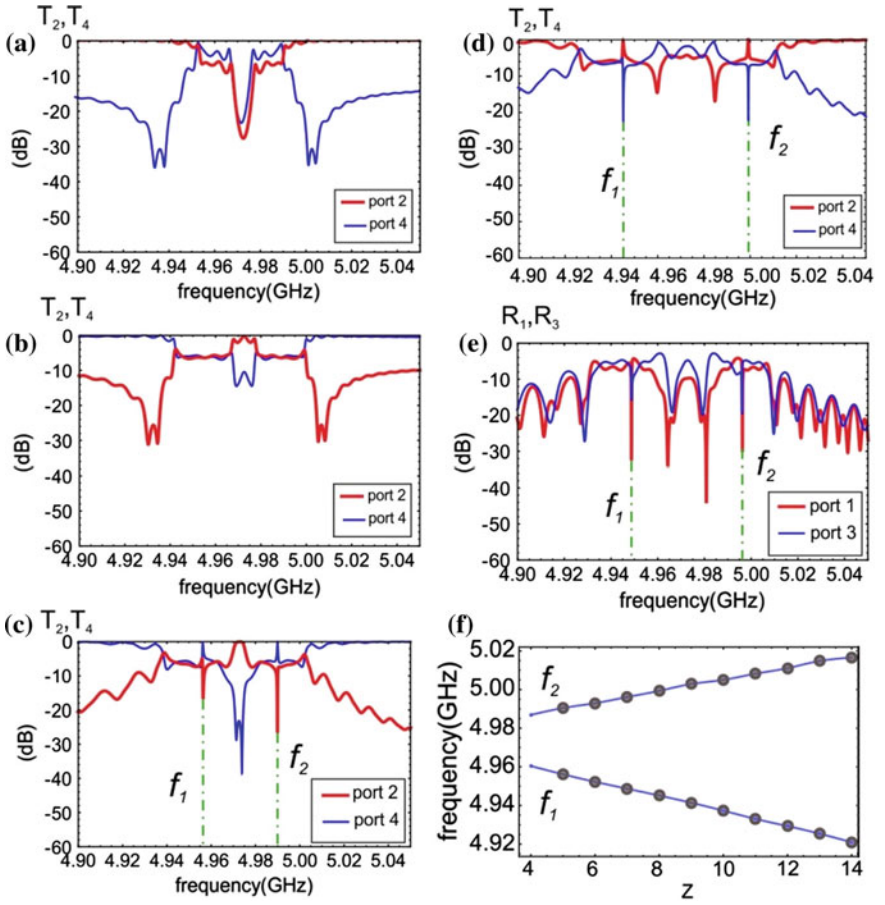


**Fig. 5** Transmission coefficients $T_2$ (red curve) and $T_4$ (blue curve): **a** Z = 2, **b** Z = 5 for defect—free MCs; **c** Z = 2, **d** Z = 5, **e** Z = 7, **e** reflection coefficients $R_1$ (red curve), $R_3$ (blue curve) Z = 7 for MCs with defects; **f** frequency position of defect modes of parameter Z. Defect modes' peaks showed by green dash-dotted line

modes on the transmission ($T_2$, $T_4$) and reflection ($R_1$, $R_3$) coefficients with further increasing coupling (Z = 7, see Fig. 5d, e) is shown. Location of these defect modes within the gaps was mainly dependent on the dimension of the defects and relation between the defect size and the period of the magnonic crystal lattices. Such effect according to experimental results in 1D MCs with defect was observed in [31], where defect modes for MSSW within the magnonic Bragg band gaps were founded. In the proposed coupled MCs, the two magnonic forbidden bands are located in the regions with defect modes at the values of –6 dB (see Fig. 5c–e) by analogy with two forbidden bands at frequency spectra in coupled MCs without defects [33].

According to coupling increase, defect mode with the low frequency is shifted down, and defect mode with the high frequency is shifted up in frequency spectra (see Fig. 5f). Consequently, the possibility of controlling the position in the spectrum of defect modes is shown. Besides, such method allows to calculate characteristics in planar complicated magnonic structure, which have more than two output ports. Also, the structure with any number of MC with defects can be designed.

We constructed transfer matrix for propagating MSSW in side—coupled MCs with coupling along structure length. Considered model describes the features of existence defect modes in such structure. Hence, appearance of two defect modes in transmission and reflection dependencies by analogy with two band-gap formation in vertical-coupled MCs was demonstrated [33]. Also, we have shown the possibility of controlling such peaks' position in frequency spectra by changing the coupling coefficient. One final comment is that the results can be used for creating planar controlled elements for magnonic and spintronic logic devices.

## 4 Multimode Surface Magnetostatic Wave Propagation in Irregular Planar Magnonic Structure

Magnonic strips based on thin YIG film can be used as basic elements for the fabrication of functional spintronic and magnetoelectronic devices, such as couplers, waveguides, filters, and delay lines (see, e.g., [37]). The characteristics of such devices can be varied in a broad range due to the coexistence of multiple physical phenomena, e.g., the possibility of frequency tuning by an external magnetic field, the existence of variety of the dispersion types of propagating spin waves (on surface and in volume, forwards and backwards), the coexistence of various nonlinear effects, such as self-modulation, soliton generation, and propagation. The spectrum and propagation characteristics of magnetostatic surface spin waves (MSSWs) in regular finite-width ferrite waveguide were investigated both experimentally and theoretically in [21, 22], but the multimode MSSW propagation in irregular planar ferrite waveguides requires more detailed investigation. Experimental measurement of the spin-wave intensity distribution can be performed by number of experimental methods, for example, microwave probes. However, the spatial resolution of the probe methods is insufficient for the geometrical dimensions less than hundreds of microns, mainly due to electromagnetic cross talk. Nowadays, the spatial characteristics of spin waves in planar micron and submicron waveguides are experimentally studied by the space- and time-resolved Brillouin spectroscopy (BLS) (see, e.g., [23]). Here, we present the results of experimental study of multimode spin-wave propagation in irregular planar YIG structures in different frequency ranges. Planar waveguides were fabricated by the precise laser cutting technique from YIG films on gadolinium gallium garnet (GGG) substrate. The regular planar YIG waveguides has trapezoidal form with the geometrical dimensions $1 \times 5$ mm$^2$. Thickness of the ferrite was $d = 7.7$ μm, and the saturation magnetization was $4\pi M_0 = 1750$ G. Irregular structure

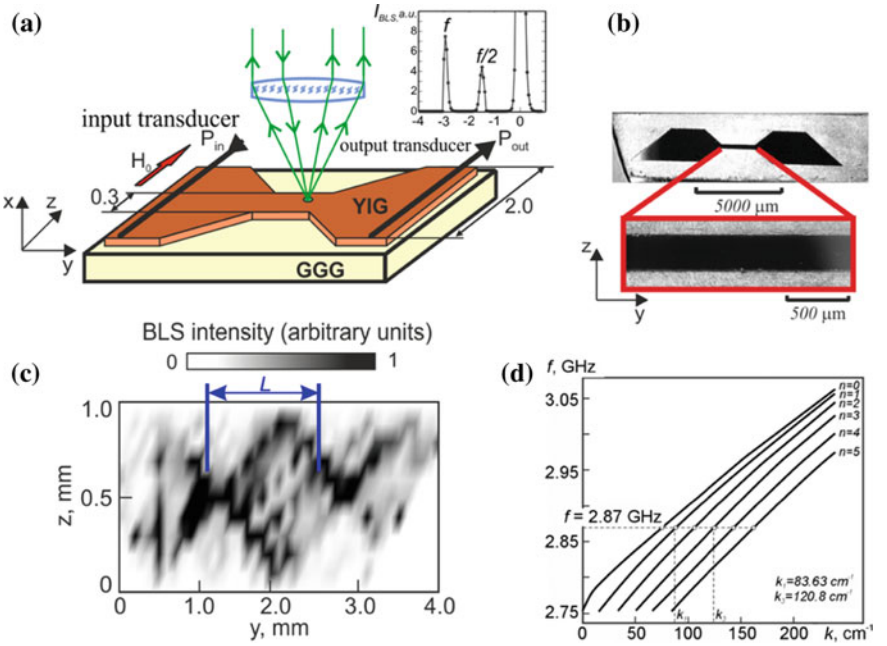


**Fig. 6** **a** Experimental setup with tapered YIG waveguide and the example of obtained BLS spectra (inset). **b** Photograph of the fabricated structure. **c** Spatial distribution of the MSSW in a regular waveguide. **d** Dispersion for the MSSW modes

consisted of two regular waveguides of different width and the taper region between them (Fig. 6a, b). MSSW was excited by 30-μm-width microstrip antenna. Bias magnetic field was applied along the microstrip antennas. Spatiotemporal distribution of high-frequency spin-wave magnetization $\vec{m}(t, y, z)$ in the waveguide was obtained by spatial scanning with laser beam focused on the surface of the structure.

The BLS measurement of the spectrum and intensity of inelastically scattered light $I(t, y, z) \sim |\vec{m}(t, y, z)|^2$ was performed in the configuration of the backscattering BLS scheme (Fig. 6a). Figure 6c shows the experimentally obtained stationary spatial distribution of $I(y, z)$ for the MSSW propagating in a regular 1-mm-width YIG waveguide. The dark areas correspond to larger values of spin-wave intensity. The linear propagation regime was considered. Input signal frequency was $f = 2.87$ GHz, and input power was $P_{in} = -20$ dBm. External magnetic field was $H_0 = 440$ Oe. In the general case, the magnetization in the waveguide can be represented as a superposition of the waveguide modes $\vec{m}(x, y, z) = \sum_n \alpha_n(z)\vec{m}_n(x)e^{-ik_n y}$, where $\alpha_n(z) \sim \sin(n\pi z/w)$ is the amplitude coefficient, $n = 1, 2, 3 \ldots$ is mode number, $w$ is the waveguide width, $k_n$ is wave number of $n$th mode, and $\vec{m}_n(x)$ is high-frequency magnetization component. Spatial distribution of magnetization in Fig. 7a corresponds to a superposition of first and third odd transverse spin-wave modes which are symmetrical with respect to the longitudinal axis of regular waveguide.

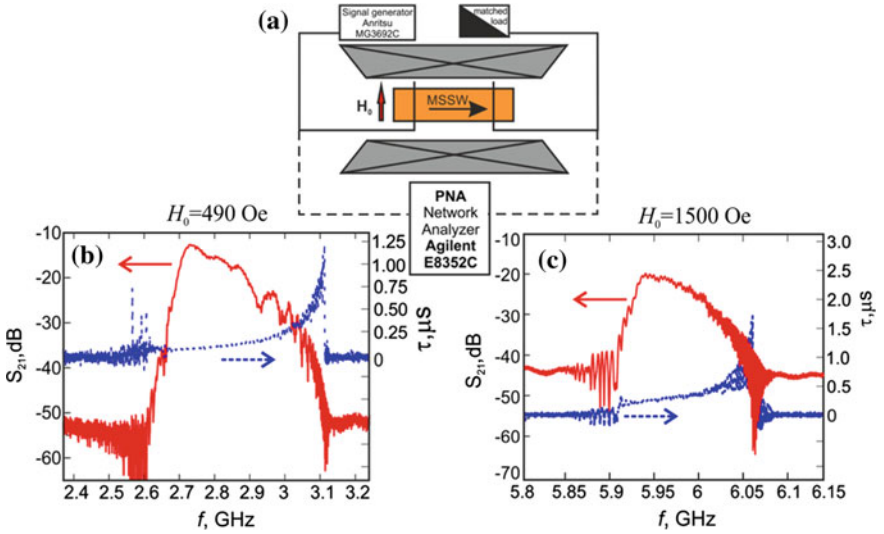


**Fig. 7** Microwave experiment scheme (**a**), transmission coefficient and group delay for different values of bias magnetic field $H_0$ = 490 Oe (**b**), and $H_0$ = 1500 Oe (**c**)

Experimental value of the beat length was $L = 1.4$ mm. Dispersion characteristics of the width spin-wave modes are depicted in Fig. 7b. The theoretical calculation of the beat length gives the value of $L = 2\pi/k_1 - k_3 = 1.6$ mm, which is in good agreement with the experimental results. Microwave characteristics (Fig. 7) of irregular waveguide for different values of the external magnetic field ($H_0 = 490$ Oe (Fig. 7b), $H_0 = 1500$ Oe (Fig. 7c)) were measured by a vector network analyzer in linear regime of MSSW propagation ($P_{in} = -30$ dBm) (Fig. 7a). The solid line denotes the frequency dependence of the $S_{21}$ transmission coefficient, and dashed line shows the group delay $\tau$ (time of MSSW propagation from input to output antenna). The excitation band of MSSW depending on the value of external magnetic field was $\Delta f = 100 \div 500$ MHz, the minimum insertion loss was $12 \div 20$ dB, and group delay was of $200 \div 800$ ns.

The results of the measurement of the stationary spin-wave spatial distribution of magnetization for irregular waveguide are shown in Fig. 8a, b. The input signal frequency was $f = 2.872$ GHz, and external bias field was $H_0 = 490$ Oe. The mode decomposition reveals that the superposition of MSSW modes with $n = 1$ and $n = 3$ in the region of regular waveguide is observed.

The tapered region of magnonic strip is formed in the region where the width of the waveguide is linearly decreased from 2 to 0.3 mm. It should be noted that in this region of magnonic structure, the distribution of magnetization is symmetrical with respect to the longitudinal $y$-axis of the structure. An increase in the amplitude of the magnetization at the edges of the taper waveguide is observed in BLS results. As it is shown in Fig. 9b, where the dependence of $I(y)$ is depicted, regarding the

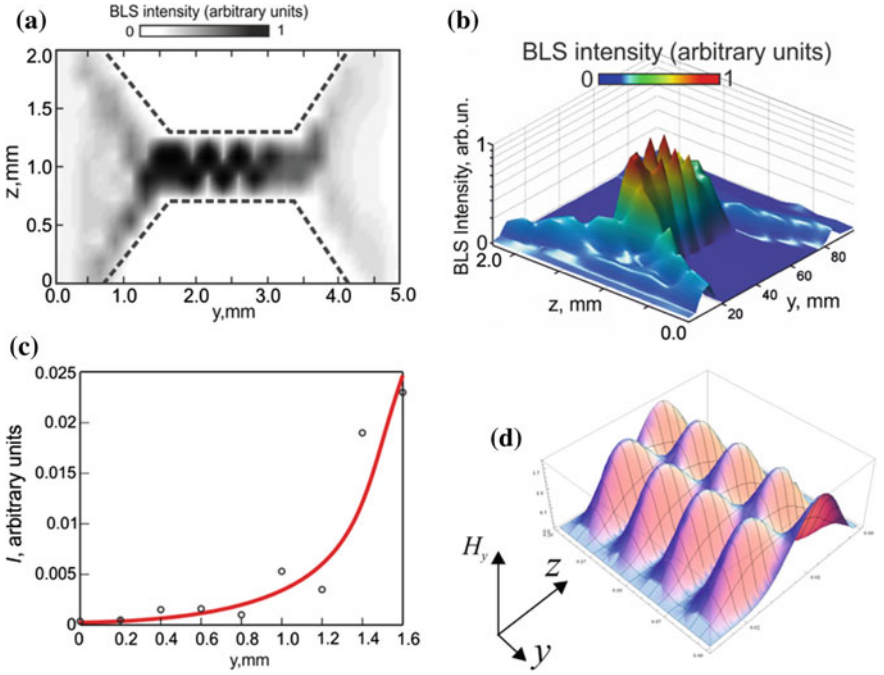


**Fig. 8** Spatial distribution of the MSSW in irregular waveguide (**a**, **b**) and intensity distribution along *y*-axis inside tapered region of the structure (**b**) (circles denoted measured values, solid line—approximation). **d** The results of numerical simulation

reference value ($y = 0$ mm), an increase in intensity by 50 times ($y = 1.6$ mm) was observed.

Inside the narrow waveguide region ($0.6 \leq z \leq 1.4$ mm and $1.6 \leq y \leq 3.6$ mm in Fig. 8a) the magnetization pattern corresponds to a superposition of spin-wave first and second ($n = 1$ and $n = 2$) spin-wave modes (Fig. 8a) and the beating length was estimated to be of $L = 0.5$ mm. The results of the calculation of the wave numbers of these modes give the beating length of $L = 0.63$ mm. Thus, the good accordance between the calculation and experimental data was found. In this case, there is a symmetry breaking in the spatial distribution of magnetization intensity with respect to the longitudinal *y*-axis. The results of numerical simulation of width mode interference are shown in Fig. 8d and are in good agreement with the experimental data (in the region of the regular section of the considered structure).

Figure 9 shows the BLS map of distribution of magnetization in the narrow waveguide region with three input signal frequencies at the value of bias magnetic field $H_0 = 1500$ Oe.

The magnetization in a narrow waveguide in the region of small wave numbers of MSSW at frequency of $f = 5.94$ GHz has a complex spatial pattern. One can assume that in the input section of the narrow waveguide a large number of modes

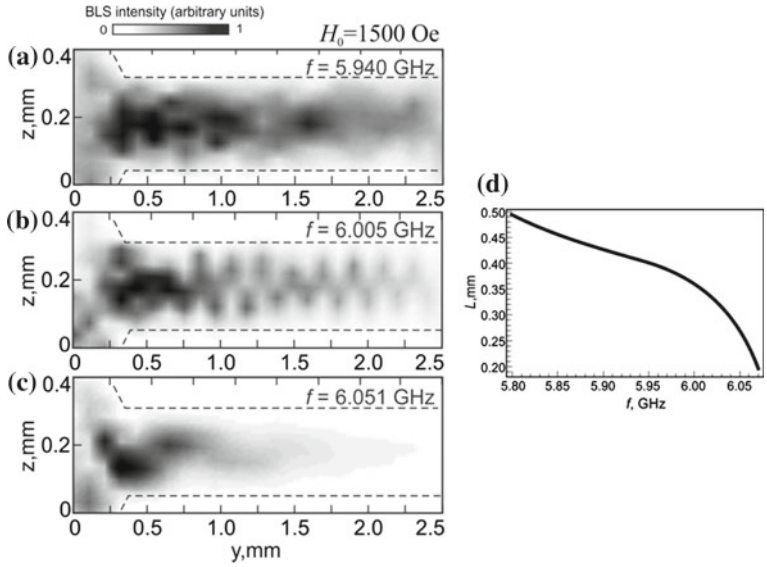


**Fig. 9** Spatial distribution of BLS intensity for the MSSW in narrow area of irregular waveguide for different values of input signal frequency (**a**)–(**c**) and beat length dependency on the frequency for superposition of first and second MSSW modes (**d**)

can be excited; however, the narrow section of the magnonic waveguide does not have enough length to form a regular spatial pattern of the spin-wave intensity. In the middle of the MSSW spectrum at the frequency of $f = 6.005$ GHz, the spatial distribution of the first and second ($n = 1$ and $n = 2$) waveguide modes was formed. The beating length in this case was $L = 0.2$ mm. At the frequency of $f = 6.051$ GHz near the upper frequency limit of the MSSW excitation, the spin-wave decays rapidly along the waveguide (see transmission characteristics in Fig. 7c) without the formation of the distinguished spatial pattern of the spin-wave intensity. The results of numerical calculation of the beating length $L$ as a function of the frequency (for a field $H_0 = 1500$ Oe) are shown in Fig. 9d. The beat length is decreased as the frequency is increased.

It is worth to note that the internal magnetic field is non-uniform inside the 500-μm-width section of the irregular waveguide due to magnetic shape anisotropy. Thus inside the regular section, the internal magnetic field is decreased in the region near the waveguide's edge. This leads to the interesting effect in the frequency region where three-magnon (3 M) decay processes is possible. It is known that the products of the 3 M decay in the case of MSSW propagation at the frequency of $f_0$ are the SWs at the frequency of $f_0/2$ [9, 38]. It is also known that there is a power threshold for 3 M processes, which is decreased with the MSSW's wave number decrease. This fact opens the possibility of SW generation due to 3 M processes in the region of the decreased internal magnetic field. Thus, the power threshold is reduced in the area in the vicinity of waveguide's edge.

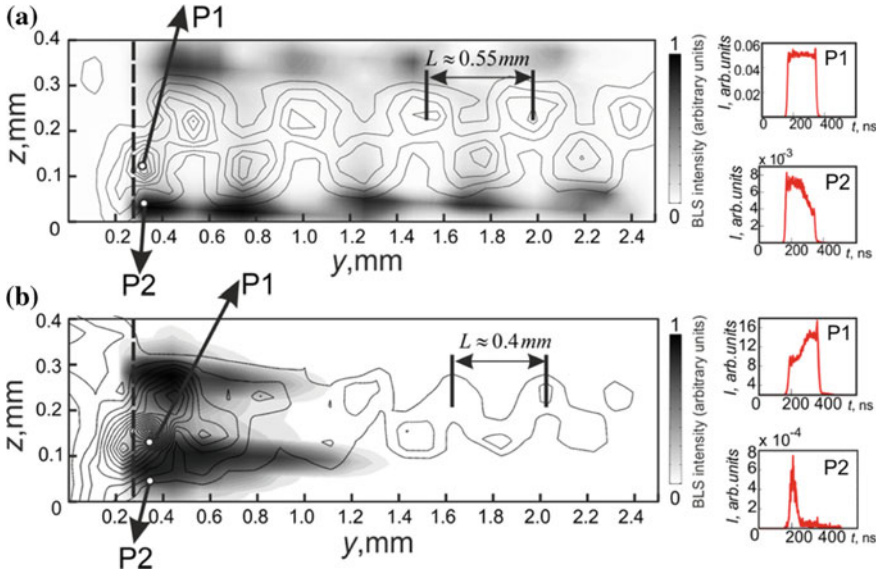


**Fig. 10** **a** Spatial distribution of MSSW in irregular waveguide, measured at the frequency of $f$ = 2.872 GHz (isolevel lines) and at $f$ = 2.872/2 = 1.436 GHz (grayscale). Input signal frequency is $f$ = 2.872 GHz. **b** Spatial distribution of MSSW in irregular waveguide, measured at the frequency of $f$ = 2.981 GHz (isolevel lines) and at $f$ = 2.981/2 = 1.4905 GHz (grayscale). Input signal frequency is $f$ = 2.981. Right panels correspond to the MSSW time profile at the positions, which are denoted with the open circles and referred to as "P1" and "P2." Beating length of first and second width modes is denoted as $L$. All shown data are presented for $H_0$ = 490 Oe

The local generation of SW is shown in Fig. 10a for $H_0$ = 490 Oe. Here, the spatial distribution of MSSW measured at the frequency of $f$ = 2.872 GHz (isolevel lines) and at $f$ = 2.872/2 = 1.436 GHz (grayscale) is depicted. In both cases, the input signal frequency was $f$ = 2.872 GHz. The similar results were obtained for MSSW at the frequency of $f$ = 2.981 GHz (Fig. 10b). Right panels in Fig. 10 correspond to the MSSW time profile at the positions of 40 μm from the waveguide's edge (referred to as "P2") and at the positions of 100 μm from the waveguide's edge (referred to as "P1"). One can observe the well-defined pulse time profile at the point "P2," which is the result of 3 M decay process. This also confirms that the 3 M processes are arisen from the non-uniformity of the internal magnetic field and occur in the area of reduced $H_{\text{int}}$.

Thus, the experimental study of magnetic strip reveals the localization of the parametrical processes in irregular YIG waveguides. It was shown that in the case of a regular waveguide, the beating of width modes with numbers $n = 1$ and $n = 3$ forms the spatial spin-wave pattern. The width mode transformation in tapered area of YIG waveguide is observed in the case of irregular magnonic waveguide. Thus, the first and third width modes in the wide area of magnetic structure are transformed into MSSW modes of order $n = 1$ and $n = 2$ in the narrow part of waveguide. This

fact can be explained by an axial symmetry breaking with respect to longitudinal axis ($y$-axis in Fig. 10) of the irregular magnonic waveguide.

## 5 Transverse Mode Coupling in Confined Multiferroics

Dual tunability is the key advantage of multiferroic-based devices operating in microwave and terahertz frequency range. Magnetic tuning can be typically performed by means of the variation in an angle or/and value of bias magnetic field, while electric tuning is realized by the variation in an applied electric field [39–41], which causes change of dielectric permittivity of the ferroelectric layer. Multiferroic waveguide with dual tunability, fabricated from ferrite-ferroelectric bilayer, can be used as a phase shifter [42–44] or tunable filter [45]. The novel concept of planar magnonic devices requires the reduction of transversal size of multiferroic strip. This leads to the necessity of the control of characteristics of waves propagating in confined bilayers. The interference of spin-wave modes quantized in the direction along the short axis of magnetic waveguide was studied in detail, performing BLS probing techniques, providing direct visualization of spin-wave propagation with the spatial and temporal resolution. It was shown in the previous subsection that the beating of the spin-wave width modes [46] in magnetic waveguide is responsible for the formation of a spatial pattern, which leads to a periodic focusing and defocusing of the spin-wave energy along the wave propagation direction. In this section, we demonstrate that the confined multiferroic bilayer consists of yttrium iron garnet (YIG) and barium strontium titanate (BST) layers which can act as the spin-wave power concentrator. By using space-resolved BLS technique, we show that the transverse size of spin-wave beam decreases due to the coupling between magnetic and ferroelectric films. This phenomenon can be used both for nonlinear application, due to confinement of magnetization in the center of multiferroic waveguide, and for the fabrication of integrated magnonic functional devices with dual tunability of transmission and processing of microwave-frequency signals.

The schematic of the experimental setup is shown in Fig. 11a. Magnetic layer was fabricated from single-crystalline YIG ($Y_3Fe_5O_{12}$ (111)) film with saturation magnetization of $M_0$ = 139 G. YIG film of thickness of 10 μm was epitaxially grown on a 500-μm-thick gadolinium gallium garnet ($Gd_3Ga_5O_{12}$ (111), GGG) substrate. Magnetic waveguides of 2 mm width were formed on GGG substrate by the laser scribing technique [25, 47]. The ferroelectric layer with in-plane dimension of $2 \times 5.5$ mm consists of a ceramic barium strontium titanate slab ($Ba_{0:6}Sr_{0:4}TiO_3$) with the static relative dielectric permittivity of 2750 and thickness of 500 μm. We use the typical microstrip delay line for microwave measurements. The microwave transducers with width of 30 μm and length of 2 mm are used for spin-wave (SW) excitation. Input and output transducers are attached to the YIG film (see Fig. 11a) at a distance of 9 mm from each other.

The uniform static magnetic field $H_0$ = 1310 Oe was applied in the plane of the waveguides along the $y$-direction for effective excitation of magnetostatic surface

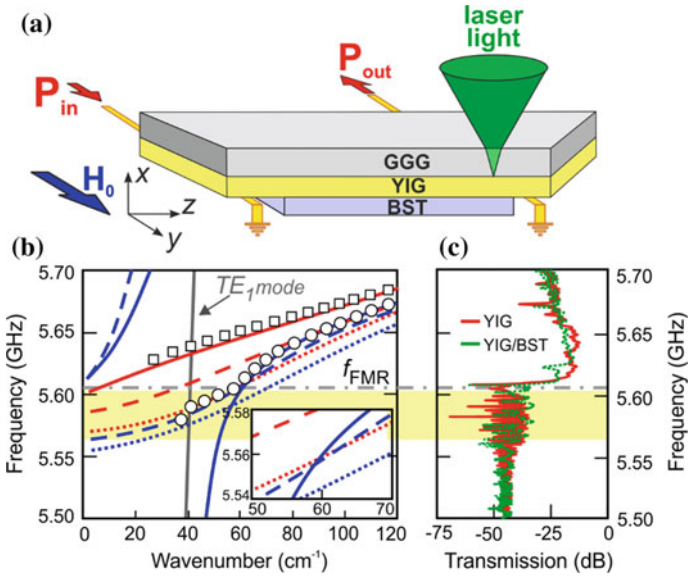


**Fig. 11** **a** Schematic of the experiment. BLS experiment was performed in backscattering configuration. Bias magnetic field is directed along the *y*-axis; value of static applied magnetic field is $H_0$ = 1310 Oe. **b** FEM calculation results of dispersion characteristics for first (solid lines) and third (dashed lines) transversal modes of MSSW (red lines) and HSEW (blue lines). The results of microwave measurements are plotted with open squares (for MSSW) and open circles (for HSEW). Dashed–dotted line marks the frequency of the uniform ferromagnetic resonance $f_{\mathrm{FMR}}$. **c** Transmission characteristics, measured with signal network analyzer for YIG film (red solid curve) and YIG/BST bilayer (green dashed curve)

waves (MSSWs) [9, 36]. As spin wave propagates along *z*-direction, it starts to transform to hybrid spin-electromagnetic wave (HSEW) in the region where YIG film is in contact with the BST slab. HSEW propagates along the bilayer and then reaches the YIG film where it transforms back to the MSSW and is received by the output microstrip antenna [40, 41]. Transmission and dispersion of bilayer structure were experimentally measured using E8362C PNA microwave network analyzer. The input power of the microwave signal was 0.1 μW in order to avoid nonlinear effects [9]. In order to obtain the reference characteristics, we experimentally measure the dispersion of MSSW in magnetic YIG strip without BST layer. This result is shown in Fig. 11b with the open squares. Next, we experimentally measure the dispersion of HSEW for bilayer structure. These results are also depicted in Fig. 11b with open circles. The transmission response is shown in Fig. 11c both for the YIG strip and for the bilayer. Slight difference in the insertion loss is clearly seen near the lower cutoff frequency of MSSW equal to the frequency of ferromagnetic resonance of in-plane magnetized film [9] $f_{\mathrm{FMR}} = \sqrt{H_0(H_0 + 4\pi M_0)} = 5.606\,\mathrm{GHz}$, where $\gamma$ = 2.8 MHz/Oe is the electronic gyromagnetic ratio. It is seen that in the bilayer structure the transmission is lower than in solitary YIG film. This can be explained

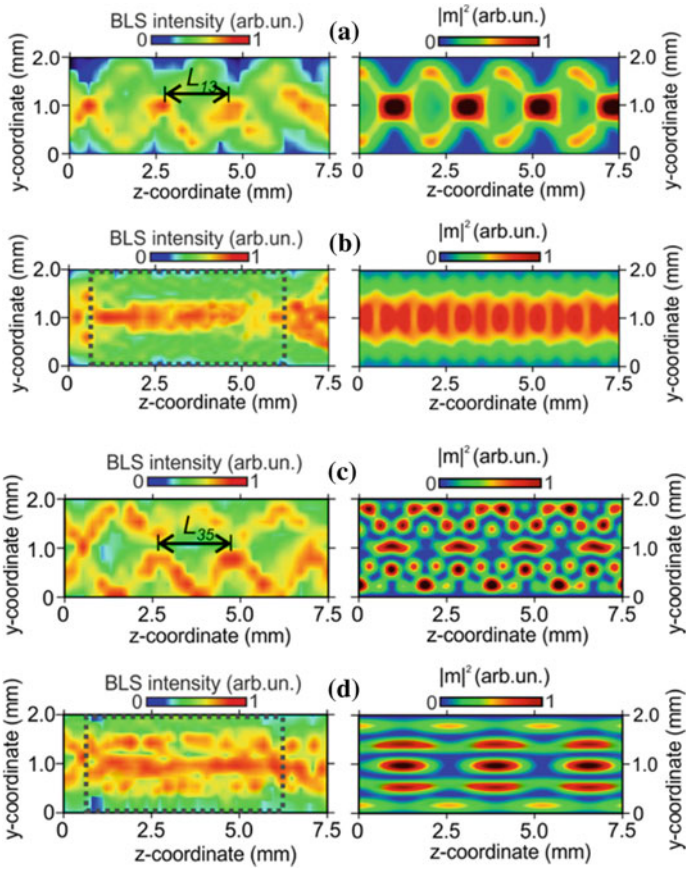


**Fig. 12** Normalized color-coded BLS intensity map (left panels) and FEM simulation of magnetization squared spatial map recorded at the excitation frequency of 5.615 GHz (**a**, **b**) and 5.590 GHz (**c**, **d**) for YIG film (**a**, **c**) and YIG/BST (**b**, **d**). Edges of BST slab is guided with dashed lines. All the shown data were obtained at $H_0$ = 1310 Oe

by the excitation and coupling of waves propagating in composite YIG/BST structure [40–44].

The finite size of bilayer structure leads to the multimode propagation of waves [19] and to the formation of complicated patterns of magnetization distribution in the YIG layer [26, 46]. The transparent for wavelength of the green laser (532 nm) substrate opens the possibility to visualize the magnetization distribution in the magnetic layer. The results of BLS measurement of the magnetization squared ($|m|^2$) at the frequency of input microwave signal of 5.615 GHz are depicted in the left panels of Fig. 12a, b for the solitary YIG and YIG/BST bilayer, respectively. The cross-like pattern is formed predominantly by the first and third transversal modes' beating.

The value of $L$ parameter (mode beating length), shown in Fig. 12a, can be used to estimate the differences between the wave numbers of first ($k_1$) and third ($k_3$) transversal modes: $L = 2\pi/\Delta k_{13}$, where $\Delta k_{13} = |k_1 - k_3|$ is the difference between the wave numbers of third and first modes. The confinement of wave is clearly observed in Fig. 12b (left panel) in the region, where the BST layer is placed over the YIG film.

For numerical simulation of spatial magnetization distribution in bilayer structure, the numerical scheme from [48–50] was used. By means of finite-element method (FEM), the straightforward solution of system of Maxwell equations was performed. Electrodynamic characteristics of both the MSSW and HEMSW modes were calculated. Dispersion of first and third transverse modes is shown in Fig. 11b with the solid and dashed lines, respectively. Red lines denote the dispersion of MSSW in the 2-mm-width YIG strip, and blue lines denote the dispersion of HSEW in bilayer. It is important to note that for HSEW the dispersion curve of first mode intersects the dispersion curve of third mode in the frequency region of $f_{\mathrm{FMR}}$. This leads to the significant decrease in the value of $\Delta k_{13}$ and, as a consequence, to the increase in $L$. The results of FEM simulation of spatial propagation of the first and third transversal modes are shown in the right panel of Fig. 12. Here, we assume that no reflections from the beginning and the end of BST layer are taken into account. It is worth to note that for YIG strip with the geometrical aspect ratio (width/thickness) similar to our structure not only first and third modes should be taken into account but also fifth transversal mode contributes to the spatial distribution of propagating wave. Thus, we simulated the beating of first, third, and fifth modes, which is noticeable in Fig. 12b as a slight modulation in the beam width of wave propagating along $z$-axis.

The transformation of spatial magnetization distribution is caused by two main factors: changing of $\Delta k_{13}$ value and transformation of transversal modes' profiles in bilayer structure in comparison with magnetic strip. MSSW in YIG and slow electromagnetic wave with transverse electric polarization in BST slab are effectively coupled near the lower cutoff frequency of MSSW transverse modes [21]. This leads to the increase in wave numbers of first and third transversal modes in YIG/BST structure in comparison with YIG strip. As a result, $\Delta k_{13}$ is decreased and can reach zero value (see Fig. 13a) at the frequency, where dispersion curves of first and third HSEW modes are intercrossed. This leads to the increase in $L$. If $L > l_{\mathrm{w}}$, where $l_{\mathrm{w}} = 5.5$ mm is the length of confined multiferroic strip; mainly, the first mode will contribute to the spatial map of dynamic magnetization (Fig. 12b). The transverse mode profiles in the bilayer structure are transformed due to coupling of magnetostatic wave in YIG and slow electromagnetic wave in BST. In particular, in Fig. 13b, c the transformation of first and third modes is demonstrated. In considered frequency range, determined by the value of $H_0$, only the first eigenmode of the slow TE1 electromagnetic wave in BST layer can be excited. This mode is effectively coupled with the transverse modes of magnetostatic wave. The first mode of magnetic strip has a distribution similar to one of BST layer. The overlapping of the profiles of third YIG mode (Fig. 13c) and fundamental BST mode occurs mainly in the central part of confined bilayer. This leads to significant change in profile of third HSEW mode, while first mode profile almost unchanged due to the coupling. This spatial

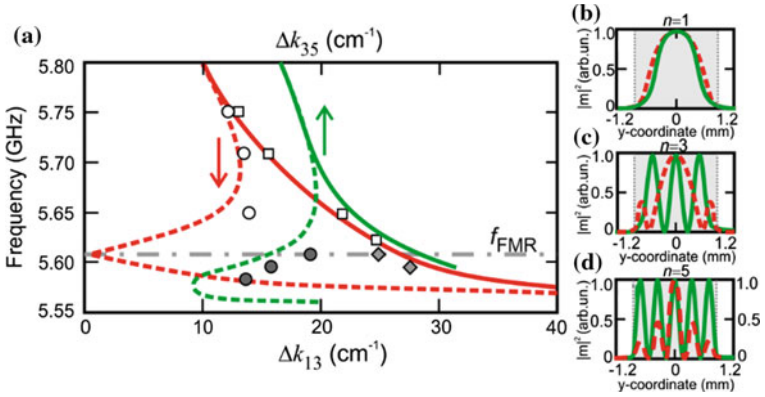


**Fig. 13** **a** Frequency dependence of $\Delta k_{13}$ and $\Delta k_{35}$ for YIG strip (solid red and green curves) and YIG/BST composite bilayer (dashed red and green curves). Experimental data from BLS map are depicted with open circles for YIG/BST and with open squares for YIG strip. Profiles for first (**b**) and third (**c**) transverse modes obtained from FEM calculation at the frequency of 5.615 GHz. Solid green curves denote the profile for the modes of YIG strip and dashed red curves correspond to YIG/BST structure. Gray area shows the lateral confinement of bilayer

profile transformation mainly of third transversal modes leads to the confinement of magnetization in the center of composite YIG/BST strip. This effect can be used in the nonlinear applications of multiferroics [51, 52] due to the possibility of ferroelectric layer to local amplification of HSEW amplitude in the center of bilayer structure. Thus, using the space resolved BLS technique we demonstrate the transformation of transverse mode profiles of the hybrid waves propagating in the YIG/BST bilayer. This transformation leads to the redistribution of the magnetization precession area inside the YIG film. In particular, the numerical simulations show that the spin-wave energy is confined in the center of the magnetic film due to changing of first and third modes' beating length and transformation of the transverse mode profiles. These results lead to the fabrication of the complex multichannel multiferroic arrays and gratings [53].

## 6 Conclusion

Magnetic metamaterials are the key element of "The beyond CMOS" technology due to the tunability in wide frequency range, radiation resistance, low power consumption, and the possible scaling in nano-sizes.

We describe in this chapter only a small part of magnonic structures, which can be referred as the functional magnetic metamaterials. We emphasize that the progress in this magnon spintronics concept in the last decades is possible due to the development of the experimental methods of spin-wave detection and fabrication techniques.

Magnonic crystals and irregular magnetic and multiferroic strips are the building blocks of any complex integral magnonic network for high-speed signal processing devices.

**Acknowledgements** This work was supported in a part by the Grant from Russian Science Foundation (Project No. 16-19-10283, 14-19-00760) and the Grant of the President of Russian Federation (No. MK-3650.2018.9).

## References

1. N. Engheta, R.W. Ziolkowski, *Metamaterials: Physics and Engineering Explorations* (Wiley, IEEE Press, 2006)
2. J.D. Joannopoulos, S.G. Johnson, J.N. Winn, R.D. Meade, *Photonic Crystals: Molding the Flow of Light*, 2nd edn. (Princeton University Press, Princeton, 2008)
3. S.A. Nikitov, D.V. Kalyabin, I.V. Lisenkov, A.N. Slavin, Y.N. Barabanenkov, S.A. Osokin, A.V. Sadovnikov, E.N. Beginin, M.A. Morozova, Y.P. Sharaevsky, Y.A. Filimonov, Y.V. Khivintsev, S.L. Vysotsky, V.K. Sakharov, E.S. Pavlov, Phys. Usp. **58**, 1099 (2015)
4. V.V. Kruglyak, S.O. Demokritov, D. Grundler, J. Phys. D Appl. Phys. **43**, 264001 (2010)
5. V.E. Demidov, S. Urazhdin, A. Zholud, A.V. Sadovnikov, A.N. Slavin, S.O. Demokritov, Sci. Rep. **5**, 8578 (2015)
6. A.V. Chumak, V.I. Vasyuchka, A.A. Serga, B. Hillebrands, Nat. Phys. **11**, 453–461 (2015)
7. S.A. Nikitov, Ph. Tailhades, C.S. Tsai, J. Magn. Magn. Mater., **236**, 320–330 (2001)
8. Y. Haiming, O. Kelly, V. Cros, R. Bernard, P. Bortolotti, A. Anane, F. Brandl, F. Heimbach, D. Grundler, Nat. Commun. 11255 (2016)
9. A.G. Gurevich, G.A. Melkov, *Magnetization Oscillations and Waves* (CRC-Press, London, New York, 1996)
10. B. Obry, P. Pirro, Th. Bracher, A. Chumak, J. Osten, F. Ciubotaru, Appl. Phys. Lett. **102**, 202403 (2013)
11. A.V. Chumak, P. Pirro, A.A. Serga, M.P. Kostylev, R.L. Stamps, H. Schultheiss et al., Appl. Phys. Lett. **95**, 262508 (2009)
12. A.V. Chumak, V.S. Tiberkevich, A.D. Karenowska, A.A. Serga, J.F. Gregg, A.N. Slavin et al., Nat. Commun. **1**, 141 (2010)
13. S.A. Odintsov, A.V. Sadovnikov, A.A. Grachev, E.N. Beginin, Yu.P. Sharaevskii, S.A. Nikitov, JETP Lett. **104**, 8 (2016)
14. A.V. Sadovnikov, E.N. Beginin, S.A. Odincov, S.E. Sheshukova, Yu.P. Sharaevskii, A.I. Stognij, S.A. Nikitov, Appl. Phys. Lett. **108**, 172411 (2016)
15. A.V. Sadovnikov, E.N. Beginin, M.A. Morozova, Yu.P. Sharaevskii, S.V. Grishin, S.E. Sheshukova, S.A. Nikitov, Appl. Phys. Lett. **109**, 042407 (2016)
16. V.E. Demidov, S. Urazhdin, A. Zholud, A.V. Sadovnikov, S.O. Demokritov, Appl. Phys. Lett. **106**, 022403 (2015)
17. C.S. Davies, A. Francis, A.V. Sadovnikov, S.V. Chertopalov, M.T. Bryan, S.V. Grishin, D.A. Allwood, Y.P. Sharaevskii, S.A. Nikitov, V.V. Kruglyak, Phys. Rev. B **92**, 020408(R) (2015)
18. S.-K. Kim, K.-S. Lee, D.-S. Han, Appl. Phys. Lett. **95**, 082507 (2009)
19. K.H. Chi, Y. Zhu, C.S. Tsai, J. Appl. Phys. **115**, 17D125 (2014)
20. H. Yu, G. Duerr, R. Huber, M. Bahr, T. Schwarze, F. Brandl, D. Grundler, Nat. Commun. **4**, 2702 (2013)
21. T.W. O'Keeffe, R.W. Patterson, J. Appl. Phys. **67**, 4868–4895 (1978)
22. S.N. Bajpai, J. Appl. Phys. **58**, 910 (1985)
23. S.O. Demokritov, B. Hillebrands, A.N. Slavin, Phys. Rep. **348**, 441–489 (2001)
24. E.N. Beginin, A.V. Sadovnikov, Yu.P. Sharaevskii, S.A. Nikitov, Bull. Russ. Acad. Sci. Phys. **77**, 12 (2013)

25. E.N. Beginin, A.V. Sadovnikov, Yu.P. Sharaevsky, S.A. Nikitov, Solid State Phenom. **215**, 389–393 (2014)
26. V.E. Demidov, S.O. Demokritov, K. Rott, P. Krzysteczko, G. Reiss, Phys. Rev. B **77**, 064406 (2008)
27. Y. Sun, Y.-Y. Song, H. Chang, M. Kabatek, M. Jantz, W. Schneider et al., Appl. Phys. Lett. **101**, 152405 (2012)
28. M. Krawczyk, H. Puszkarski, Phys. Rev. B **77**, 054437 (2008)
29. V.V. Kruglyak, M.L. Sokolovskii, V.S. Tkachenko, A.N. Kuchko, J. Appl. Phys. **99**, 08C906 (2006)
30. M. Krawczyk, H. Puszkarski, Phys. Rev. B **77**, 054437 (2008)
31. Yu. Filimonov, E. Pavlov, S. Vystostkii, S. Nikitov, Appl. Phys. Lett. **101**, 242408 (2012)
32. K. Di, V.L. Zhang, M.H. Kuok, H.S. Lim, S.C. Ng, Phys. Rev. B, **90**, 060405R (2014)
33. M.A. Morozova, A.Yu. Sharaevskaya, A.V. Sadovnikov, S.V. Grishin, D.V. Romanenko, E.N. Beginin, Yu.P. Sharaevskii, S.A. Nikitov, J. Appl. Phys. **120**, 223901 (2016)
34. E.N. Beginin, Yu.A. Filimonov, E.S. Pavlov, S.L. Vysotskii, S.A. Nikitov, Appl. Phys. Lett. **100**, 252412 (2012)
35. J.M. Bendickson, J.P. Dowling, M. Scalora, Phys. Rev. E **53**, 4107 (1996)
36. R.W. Damon, J.R. Eshbach, J. Phys. Chem. Solids **19**, 308 (1961)
37. B. Lenk, H. Ulrichs, F. Garbs, M. Münzenberg, Phys. Rep. **507**, 107–136 (2011)
38. C. Mathieu et al., Phys. Rev. B. **67**, 104402 (2003)
39. V.E. Demidov, S. Urazhdin, A. Zholud, A.V. Sadovnikov, A.N. Slavin, S.O. Demokritov, Sci. Rep. **5**, 8578 (2015)
40. V.B. Anfinogenov, T.N. Verbitskaya, Y.V. Gulyev, P.E. Zilberman, S.V. Meriakri, Y.F. Ogrin, V.V. Tikhonov, Sov. Tech. Phys. Lett. **12**, 389 (1986)
41. V.B. Anfinogenov, T.N. Verbitskaya, P.E. Zilberman, G.T. Kazakov, S.V. Meriakri, V.V. Tikhonov, Sov. Phys. Tech. Phys. **35**, 1068 (1990)
42. V.E. Demidov, B.A. Kalinikos, P. Edenhofer, J. Appl. Phys. **91**, 10007 (2002)
43. V.E. Demidov, B.A. Kalinikos, S. Karmanenko, A. Semenov, P. Edenhofer, I.E.E.E. Trans, Microwave Theory Tech. **51**, 2090–2096 (2003)
44. Y.K. Fetisov, G. Srinivasan, Appl. Phys. Lett. **87**, 103502 (2005)
45. A.B. Ustinov, G. Srinivasan, B.A. Kalinikos, Appl. Phys. Lett. **90**, 031913 (2007)
46. V.E. Demidov, S.O. Demokritov, IEEE Trans. Magn. **51**, 0800215 (2015)
47. S. Sheshukova, E. Beginin, A. Sadovnikov, Y. Sharaevsky, S. Nikitov, I.E.E.E. Magn. Lett. **5**, 1–4 (2014)
48. A.V. Sadovnikov, K.V. Bublikov, E.N. Beginin, S.A. Nikitov, J. Commun. Technol. Electron. **59**, 914–919 (2014)
49. A.V. Sadovnikov, E.N. Beginin, K.V. Bublikov, S.V. Grishin, S.E. Sheshukova, Y.P. Sharaevskii, S.A. Nikitov, J. Appl. Phys. **118**, 203906 (2015)
50. A.V. Sadovnikov, A.G. Rozhnev, Appl. Nonlinear Dyn. [Izvestiya VUZ: (in Russian)] **20**(1) (2012)
51. V.E. Demidov, B.A. Kalinikos, P. Edenhofer, Tech. Phys. **47**, 343 (2002)
52. A.B. Ustinov, A.V. Kondrashov, A.A. Nikitin, M.A. Cherkasskii, B.A. Kalinikos, JETP Lett. **100**, 835 (2015)
53. A.V. Sadovnikov, A.A. Grachev, E.N. Beginin, S.E. Sheshukova, Yu.P. Sharaevskii, S.A. Nikitov, Voltage-controlled spin-wave coupling in adjacent ferromagnetic-ferroelectric heterostructures. Phys. Rev. Appl. **7**, 014013 (2017)

# Quantum Transport, Superconductivity, and Weak Ferromagnetism at Bicrystal Interfaces of Bi and 3D Topological Insulator BiSb


**Fiodor M. Muntyanu, Andrzej Gilewski, Andrzej J. Zaleski, Vitalie Chistol, Viorel Munteanu, Krzysztof Rogacki and Anatolie Sidorenko**

**Abstract** This chapter reviews the results of study of electronic quantum transport, superconductivity, and magnetic phenomena of bicrystals of Bi and BiSb alloy system at temperatures 1.8–100 K and magnetic fields up to 400 kOe. A similar Fermi surface (FS) consisting of crystallite interfaces (CIs) and bulk crystallites has been found. In the quantum transport oscillations spectrum, a number of new oscillation harmonics have been detected, characterizing the much larger cross-sectional areas of FS in CIs than in Bi single crystals. A number of quantum Hall plateaus were observed in inclination-type bicrystals. They vanish after the magnetic field reversal and thereby indicate that the flow of Dirac fermions is dependent on the field orientation. It has been found that the semiconductor–semimetal transition is induced in the central and adjacent layers of the CIs at different values of the magnetic field.

F. M. Muntyanu (✉) · V. Munteanu · A. Sidorenko
Institute of Electronic Engineering and Nanotechnologies, Academy of Sciences of Moldova, 2028 Chisinau, Moldova
e-mail: muntean_teodor@yahoo.com

V. Munteanu
e-mail: viorash_md@mail.ru

A. Sidorenko
e-mail: anatoli.sidorenko@kit.edu
URL: http://nano.asm.md

A. Gilewski
Magnet, 50421 Wroclaw, Poland
e-mail: giland@wp.pl

A. J. Zaleski · K. Rogacki
Institute of Low Temperatures and Structural Research, Polish Academy of Sciences, 50-950 Wroclaw, Poland
e-mail: andrzej.j.zaleski@wp.pl

K. Rogacki
e-mail: k.rogacki@int.pan.wroc.pl

V. Chistol
Technical University of Moldova, 2004 Chisinau, Moldova
e-mail: chistol_vitalie@yahoo.com



A. Sidorenko (ed.), *Functional Nanostructures and Metamaterials for Superconducting Spintronics*, NanoScience and Technology,
https://doi.org/10.1007/978-3-319-90481-8_12

Two/one superconducting phases with the onset of transition $\leq 36$ K are observed at CIs of bicrystals, while the rhombohedral Bi and 3D topological insulator (TI) BiSb are diamagnetic and do not exhibit superconductivity. In large crystallite disorientation angle BiSb interfaces, both superconductivity and weak ferromagnetism were revealed simultaneously.

## 1 Introduction

Semimetallic Bi and Sb are among the most intensively studied materials in solid-state physics. Excellent concordance between the energy spectrum calculations of these materials and almost all available experimental methods has been achieved. It has been found that FS of Bi consists of one hole ellipsoid of revolution located at the T point and three equivalent electron pockets at the L points of the Brillouin zone. The hole pocket of Bi is extended along the trigonal axis $C_3$, while the isoenergetic surfaces of electrons are highly elongated in a direction close to bisector axes $C_1$ of a crystal. The FS of bulk single crystalline Sb consists of three electronic pockets at the L points and six hole isoenergetic surfaces at the H points of the Brillouin zone. These features of FS greatly enhance the interest in electron transport research at low temperatures. Topological situation for Bi, Sb, and their alloys has been elucidated in detail in [1–4].

$Bi_{1-x}Sb_x$ ($0.07 \leq x \leq 0.2$) alloys are typical representatives of the 3D topological insulators (TIs) [1, 2, 4], which constitute a recently discovered class of fascinating new materials with well-marked properties due to the unusual topological quantum states and the bulk Dirac particles [2, 3]. 3D TIs are insulators in the bulk; however, they have topologically protected metallic surface states with an unconventional spin texture and electron dynamics [3, 5]. It should be noted that the first 3D TI, which was theoretically predicted and experimentally detected by spin-ARPES [1, 4], was the bismuth-antimony alloys system.

The energy spectrum of $Bi_{1-x}Sb_x$ ($0 \leq x \leq 0.2$) alloys is derived from that of bismuth. An increase in Sb content $x$ in the alloys leads to drastic changes in the spin–orbit interaction and in the electronic band structure, especially at $L$ points of the bulk Brillouin zone (see Fig. 1c).

Therefore, for $x = 0.04$, the gap between $L_a$ and $L_s$ pockets in energy spectrum of Bi closes and a 3D Dirac point takes place. If $x$ increases again, the gap at L points reopens, the overlapping of Bi specific bands ($L$-$T_{45}$) disappears, and the bismuth-antimony alloys become an inverted-band semiconductors up to $x = 0.2$. Subsequently at $x > 0.2$, the alloys recovered semimetallic properties and exhibited characteristics of a strong $Z_2$ ($\upsilon_0 = 1$) TI, similar to those of Sb. Numerous studies show that the topological phase in $Bi_{1-x}Sb_x$ is due to an odd number of band inversions, asymmetric Dirac surface state, and the absence of backscattering [5].

The surface electronic structure of $Bi_{1-x}Sb_x$ alloys, consisting of one electron pocket centered around the $\Gamma$ point and six hole pockets on the line between $\Gamma$

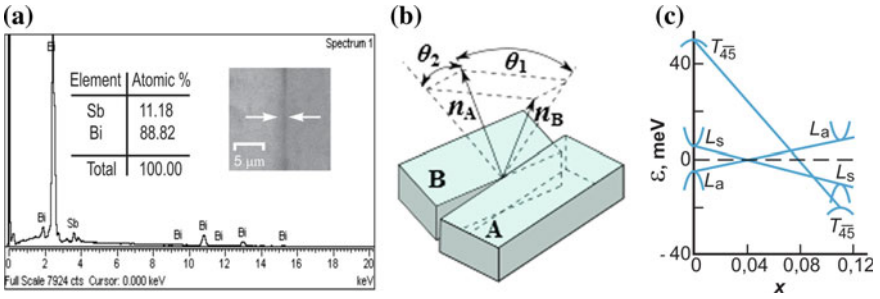


**Fig. 1** **a** EDS spectrum of $Bi_{0.882}$ $Sb_{0.118}$ bicrystal; inset: Photograph of $Bi_{0.925}$ $Sb_{0.075}$ bicrystal. The arrows indicate the CI location. **b** Schematic representation of bicrystal: $\theta_1$, relative CI disorientation angle; $\theta_2$, rotation angle in an interface plane. **c** Energy diagram of the spectrum reconstruction in BiSb alloys at low Sb concentrations

and M points of the 111 surface Brillouin zone [3, 4], is very similar with that of semimetals Bi and Sb.

Unusual opportunities occur when using bulk and low-dimensional structures of these materials because of large possibilities of studying various phenomena due to manifestations of Dirac electrons, Majorana excitations, and specific effects with respect to spin and charge transport. In this context, a very special role in revealing the diversity of these phenomena can be played the bicrystals of 3D TIs consisting of bulk crystallites and the nano-width (~ 100 nm) crystallite interfaces (CIs). Bicrystal interfaces play a significant role in the manifestation of numerous anomalies of physical properties associated with the band structure reconstruction and phonon spectrum modification. CIs, which have a high perfection and properties similar to those of grain boundaries of nano-objects, are more affordable in experimental research. On the other hand, the CIs can be superconducting under certain influential circumstances, such as: high concentration of charge carriers, changes in crystal stoichiometry, presence of numerous structural defects, manifestations of stress states and high density of deformations, existence of large areas of poor fit disorder, forms of amorphous or liquid layers. Numerous new phenomena [6, 7] were predicted in low-dimensional specimens (interfaces, surfaces, etc.) and hybrid structures with a proximity-induced superconductivity and ferromagnetism. A wonderful feature of Bi and $Bi_{1-x}Sb_x$ [8–10] interfaces is that they manifest superconductivity with $T_c \leq 21$ K, while single crystalline Bi and $Bi_{1-x}Sb_x$ alloys are diamagnetic and non-superconducting.

Studies of Bi and $Bi_{1-x}Sb_x$ bicrystals by using the quantum oscillations in high magnetic fields revealed [11, 12] the same FS consisting of CI component layers and the bulk crystallites as well as considerable distorted carrier pockets at bicrystal interfaces.

There is a vast ability to manipulate the superconducting and magnetic states at crystallite interfaces by using the proximity effect and varying the spin splitting, arising from the effect of external magnetic field or the exchange field of a ferro-

magnetic insulator. In this regard, the CIs as superconductor/ferromagnetic hybrid structures can exhibit large thermoelectric effects, generation and propagation of highly spin-polarized current, etc., thereby opening new perspectives in the development of various devices based on interplay between superconductivity and weak magnetism in interfaces of 3D TI $Bi_{1-x}Sb_x$ ($0 < x < 0.2$), such as spin injection devices, superconductor/ferromagnetic hybrid structures, thermoelectric devices.

Here, we report on the quantum transport and FS rearrangement in Bi and BiSb crystallite interfaces, the high-field peculiarities of the galvanomagnetic effects in bicrystal with superconducting nano-width CIs, the coexistence of *s*uperconductivity and weak ferromagnetism at the bicrystal interfaces.

## 2 Samples and Experimental Procedure

High quality of Bi and $Bi_{1-x}Sb_x$ ($0 \leq x \leq 0.2$) bicrystals was prepared by the horizontal zone recrystallization method using the double seed technique. The samples were prepared in the form of rectangular bars ($1 \times 2 \times 4$ mm$^3$), where the fraction of the interface volume in the overall volume of the bicrystal was ~$10^{-4}$.

Two types (see Fig. 1b) of bicrystals were prepared: inclination type (crystallographic axes of the crystallites are revolved in a single plane) and twisting type (crystallographic axes of crystallites are revolved in two planes).

Depending on disorientation angle of crystallites and the type of conductivity of CIs, the bicrystals were divided into two groups: small crystallite disorientation angle (SDA) bicrystals with $\theta_1 < 9°$ and large crystallite disorientation angle (LDA) bicrystals with $\theta_1 > 26°$. In our case, SDA and LDA bicrystals exhibited *n*-type and p-type conductivity, respectively.

The composition of the samples was controlled by SEM instrument equipped with Oxford and PV 9800 energy-dispersive X-ray (EDX) analyzers (example is given in Fig. 1a). The width of CIs was estimated by means of SEM and from the quantum oscillations [11]. It was found that the bicrystal interfaces consist of a solitary central part (the thickness ~60 nm) and two similar adjacent layers (~20 nm thick each).

The magnetic and galvanomagnetic phenomena of the bicrystals were studied in temperature range 1.6–100 K using Quantum Design SQUID magnetometer and a physical property measuring system (PPMS) with a 140 kOe magnet. Resistivity was measured in a standard four-probe circuit. The longitudinal Hall effect (longitudinal configuration: magnetic field $\boldsymbol{H}$ parallel to the Hall voltage $\boldsymbol{E}$ and both perpendicular to the current $\boldsymbol{I}$, $\boldsymbol{H} \| \boldsymbol{E}_{\perp}$ **I**) was chosen as the most convenient research method for investigating the quantum oscillation of bicrystals. Contact electrodes for studies of resistivity and Hall effect ($\rho_{ij}$ ($H_i$)) were soldered directly on the bicrystal CIs by electrospark welding. The quantum oscillations of $\rho_{ij}$ ($H_i$) were registered in stationary (up to 180 kOe) and pulse magnetic fields (up to 400 kOe).

# 3 Results and Discussion

## *3.1 Fermi Surface Rearrangement in Bi and $Bi_{1-x}Sb_x$ ($x < 0.18$) Bicrystals*

Determination of the FS shape features is one of the most important steps in predicting the basic electronic properties in condensed matter physics and better understanding of all the properties of metals, semimetals, and doped semiconductors.

Since the FS of single crystalline Bi and $Bi_{1-x}Sb_x$ ($x < 0.18$) alloys is highly anisotropic and has complex structure [13], the spectrum of transport quantum oscillations exhibits some harmonics, beating of oscillations, suppression of harmonics by spin splitting, displacement of oscillations peaks in the magnetic field, etc. On the other hand, the anisotropy of isoenergetic surfaces results in magnetic field dispersed oscillations and their spectrum can rather easily be separated on harmonics for some field orientations. By the fact that most of the experimental techniques of FS study, practically, are discovered at Bi, its FS is known in all finest details. This considerably facilitates band structure investigations of Bi and BiSb bicrystals.

### 3.1.1 Small Crystallite Disorientation Angle Interfaces of Bi Twisting Bicrystals

Ordinarily, in Bi SDA bicrystals, quantum oscillations of resistivity $\rho_{ij}$ ($H$) describe Fermi surface of crystallites and layer components of crystallite interface. Examples of these quantum oscillations are given in Fig. 2. We reliably registered oscillations of $\rho_{ij}(H)$ for crystallites. The periods of these oscillations are the same in magnitude as those of single crystalline Bi (see Fig. 4, curves 1, 2, 3) and unambiguously suggest that the density of electrons and holes in crystallites of bicrystals as well as in single crystalline Bi is almost equal ($n, p \sim 3 \times 10^{23}$ m$^{-3}$).

In addition to the above-mentioned periods of quantum oscillations in SDA bicrystals, a number of new harmonics are manifested at different directions of the magnetic field [11]. For example, two new frequencies of quantum oscillations of $\rho_{ij}$ ($H$) in bicrystals of Bi are revealed at $H \parallel$ CI (close to $C_3$ axis), while in [14] was observed, that at the magnetic field orientation $H \parallel C_3$, the magnetoresistance of bismuth monocrystalline monotonically increases up to 450 kOe and, in the magnetic fields $H > 100$ kOe the Shubnikov-de Haas oscillations disappear. At the same time, in SDA bicrystals, the longitudinal Hall quantum oscillations also occur and at higher fields (see Fig. 2), but their frequencies exceed frequencies typical for extreme cross-sectional areas of the FS of Bi by approximately 5 and 10 times. The $\rho_{ij}$ ($H$) oscillations of first and second frequency appear at $H >$ (25–35) kOe and $H > 90$ kOe, respectively. The evaluated cyclotron orbit diameter corresponding to fields of the first component appearance (depending on crystallites disorientation angles of bicrystals) is about (100–140) nm; this value correlates with the CI width determined by SEM. The diameter of cyclotron orbits of charge carriers corresponding to

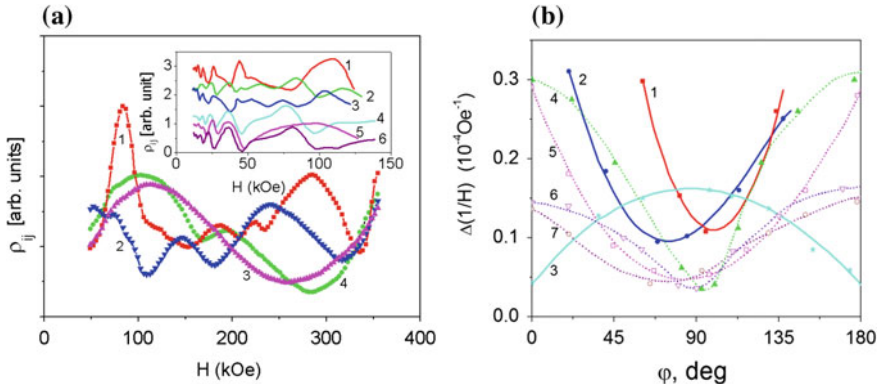


**Fig. 2** **a** Quantum oscillations of the longitudinal Hall resistance $\rho_{ij}(H_i)$ in Bi SDA bicrystals with $\theta_1 = 5°$ and $\theta_2 = 5.5°$. 1, $H \parallel C_3$; 2, $H \parallel C_1$; 3, $[H, C_3] \sim 10°$; 4, $H \parallel C_2$; 1, $T = 1.5$ K; 2, 3, 4, $T = 4.2$ K. The monotonic part of resistivity has been subtracted. Here $C_1$-bisectrix, $C_2$-binary, and $C_3$-trigonal axes. Inset: Example of the angular dependences of the quantum oscillations of $\rho_{ij}(H_i)$ in bicrystal with $\theta_1 = 8.6°$ and $\theta_2 = 4°$. 1, $H \parallel C_3$; 2, $[H, C_3] \sim 31°$; 3, $[H, C_3] \sim 20°$; 4, $[H, C_3] \sim 17°$; 5, $[H, C_3] \sim 8°$; 6, $[H, C_3] \sim 11°$ (the monotonic part of $\rho_{ij}(H_i)$ has been subtracted). **b** The angular dependences of oscillation periods of $\rho_{ij}(H_i)$ in the crystallite binary plane of SDA Bi bicrystals. 1, 2, 3, crystallites; 4, 6, CI with $\theta_1 = 5°$and $\theta_2 = 5.5°$; 5, 7, CI with $\theta_1 = 8.6°$ and $\theta_2 = 4°$

field of the second harmonic appearance is about (60–80) nm; this value apparently characterizes the thickness of central layers of CIs. In this regard, the width of the CI central part with high density of states is about (60–80) nm and the width of two adjacent layers from which the area of a spatial charge is distributed in the crystal volume takes value ~(20–30) nm each. Figure 2b shows the angular dependences of the periods of quantum oscillations of $\rho_{ij}(H_i)$ for the adjacent layers of the CI of SDA bismuth bicrystals.

The structure of the electron Fermi surface of adjacent layers is same as in crystallites (three electron pockets in L points of the Brillouin zone). On the other hand, the isoenergetic surfaces are less anisotropic and have a higher volume than electronic pockets of crystallites. The ratio of semiaxes considerably differs from the similar ratio in single crystalline Bi (for example, the ratio of semiaxes of electronic quasiellipsoid of the adjacent layers of bicrystal with $\theta_1 = \mathbf{5}°$ and $\theta_2 = \mathbf{5.5}°$ makes **1:1.34:12.6** while in single crystalline bismuth it makes **1:1.40:14.8** [13]). So, in SDA Bi bicrystals, not only an increase in the electron concentrations, but also change in the shape of the FS is observed. The estimated density of electrons in adjacent layers of SDA bicrystals is **~0.67** $\times 10^{20}$ $m^{-2}$, which is three orders higher than in Bi thin films of similar sizes.

Quantum oscillations of $\rho_{ij}(H)$ from the CI central layers of the Bi bicrystals were clearly recorded in the magnetic field oriented along the CI plane; upon a deviation from it by more than 10° they disappeared. However, the obtained data suggest that in CI central layers the electron density is the highest (**~1.5** $\times 10^{20}$ $m^{-2}$).

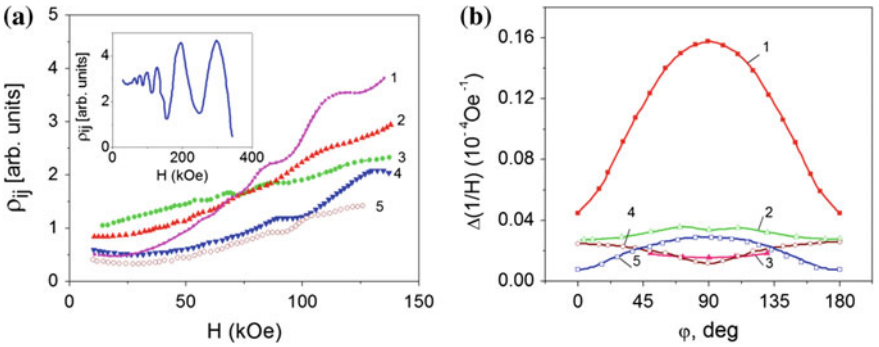


**Fig. 3** **a** Quantum oscillations of the magnetoresistance $\rho_{ij}(H)$ in LDA Bi bicrystals with $\theta_1$ = 62° and $\theta_2$ = 2° at 4.2 K. The magnetic field rotation in the binary plane: 1, $[H, C_3] \sim 60°$; 2, $[H, C_3] \sim 120°$; 3, $[H, C_3] \sim 140°$; 4, $[H, C_3] \sim 40°$; 5, $[H, C_3] \sim 20°$. Inset: The quantum oscillations of the longitudinal Hall resistance $\rho_{ij}(H_i)$ for $H$ in the CI plane. The monotonic part of Hall resistivity has been subtracted. **b** Example of the angular dependences of the oscillation periods within the crystallite binary plane in single crystalline Bi and LDA bicrystals. 1, Single crystalline Bi; 2, 3, CI with $\theta_1$ = 62° and $\theta_2$ = 2°; 4, CI with $\theta_1$ = 27° and $\theta_2$ = 10°; 5, CI with $\theta_1$ = 33° and $\theta_2$ = 9°; 2, adjacent layers; 3, central part of bicrystals

### 3.1.2 Large Crystallite Disorientation Angle Interfaces of Twisting Bi Bicrystals

Typically, in twisting LDA bicrystals of Bi observed only quantum oscillation of $\rho_{ij}(H)$, connected with hole FS of the crystallite interface (see Fig. 3a, inset). These oscillations contain two new harmonics (start at $H > (20 \div 25)$ kOe and $H > 100$ kOe), specifying that the width of the CI in SDA and LDA bicrystals is close in values and also that the hole concentration (bicrystals had $p$-type of conductivity) is ~$2.5 \times 10^{20}$ $m^{-2}$ in the CI central layer and ~$1.2 \times 10^{20}$ $m^{-2}$ in the adjacent layers. Note that these values are higher, than that in SDA bicrystals.

The oscillations of $\rho_{ij}(H)$ in the CI adjacent layers (see Fig. 3a) were clearly recorded in large angular intervals of magnetic field rotation, while quantum oscillations from the CI central layer were detected in the angular intervals $\pm 40°$ near $H \parallel C_3$. Angular dependences of the oscillation periods of $\rho_{ij}(H)$ are given in Fig. 3b. It is evident that the FS of the central and adjacent layers of the LDA Bi bicrystals consists of one weakly anisotropic hole pocket. Its shape essentially differs from that of hole ellipsoid of single crystalline Bi (the ellipsoid of revolution extended along the $C_3$ axis with the ratio of cross-sectional area $S_1/S_3$ **= 3.327** [13]). So, the hole ellipsoid of revolution in pure Bi turns to a deformed hole pocket in bicrystal CI with all three main cross-sectional areas different on size. The hole FS of the central part of LDA bicrystals in the studied angular intervals of the magnetic field rotation is almost similar to FS of the adjacent layers, and both considerably surpass in volume those of single crystalline Bi. Thus, the shape, elongation, and volume of

isoenergetic surfaces at CI undergo essential changes that finally stimulate electron pair correlation.

The same FS restructuring features have been detected [12] at the interfaces of twisting bicrystals of 3D TI $Bi_{1-x}$ $Sb_x$ ($0.06 \leq x \leq 0.2$) alloys.

### *3.2 High-Field Quantum Transport in Bi and BiSb Bicrystals*

The studying of bicrystals of Bi and $Bi_{1-x}$ $Sb_x$ ($0 \leq x \leq 0.2$) alloys in high magnetic fields is aimed at revealing the specific features of the interaction of charge carriers in systems of different dimensions, including the boundary of a quasi-two-dimensional superconductor and a 3D TI.

Figure 4 shows the magnetoresistance and the longitudinal Hall quantum oscillations of SDA Bi and BiSb bicrystals of inclination and twisting types. The oscillations spectrum contains frequencies from the FS of crystallites and interfaces. At 20 kOe in bicrystals of inclination type, the oscillation peaks take an unusual configuration (see Fig. 4a) and their position is essentially shifted [15] from the quantum oscillation maxima in Bi single crystalline samples [13]. In addition, between the peaks, along with minima in magnetoresistance, a number of Hall quasi-plateaus (~30, ~60, ~150 kOe) were found; this finding indicates the occurrence of bulk electron fractionalization.

It should be noted that the Hall plateaus and changes in the shapes of oscillation peaks are clearly pronounced only in SDA bicrystals of the inclination type, having a lower level of disorder strength and dislocation density. Thus, the presence of non-interacting carriers that contributes to fractionalization seems to be problematic in all other studied bicrystals.

Another interesting feature of the development of Hall plateaus is that they vanish after the magnetic field reversal and thereby indicate that, at least in SDA bicrystals, the flow of Dirac fermions along the CI plane is sensitive to the field orientation and the localization process runs only in a specific direction of the magnetic field.

The two new harmonics of quantum oscillations are observed (see Fig. 4b) almost in all the studied Bi [11] and $Bi_{1-x}Sb_x$ bicrystals (see Fig. 4d).

The oscillation spectra of the $Bi_{1-x}Sb_x$ bicrystals were analyzed graphically according to $H_n^{-1}$ position of the oscillation peaks versus the Landau level index $n$. The relation between $H_n^{-1}$ and $n$ is described by the formula: $1/H_n = ne/(hN_s)$, where $e$ is the elementary charge, $h$ is Planck's constant, and $N_s$ is the surface density of states. The $H_n$-$n$ dependencies for three $Bi_{1-x}Sb_x$ bicrystals are shown in Fig. 4d, inset. The results point out that the interface electronic states are of the Schrödinger type, since $n$ takes integer values (for Dirac electrons $n_D = n+½$). From the temperature dependencies of the oscillation amplitudes and the extreme cross-sectional areas of the isoenergetic surface of the CI layers, the carrier's cyclotron masses were evaluated. They exceed several times the respective crystallite parameters [13].

For example, in magnetic field directed along the CI of the $Bi_{0,93}Sb_{0,07}Te$ bicrystal, the cyclotron mass of carriers $m_c/m_e$ (where $m_e$ is the free electron mass) in crystallites

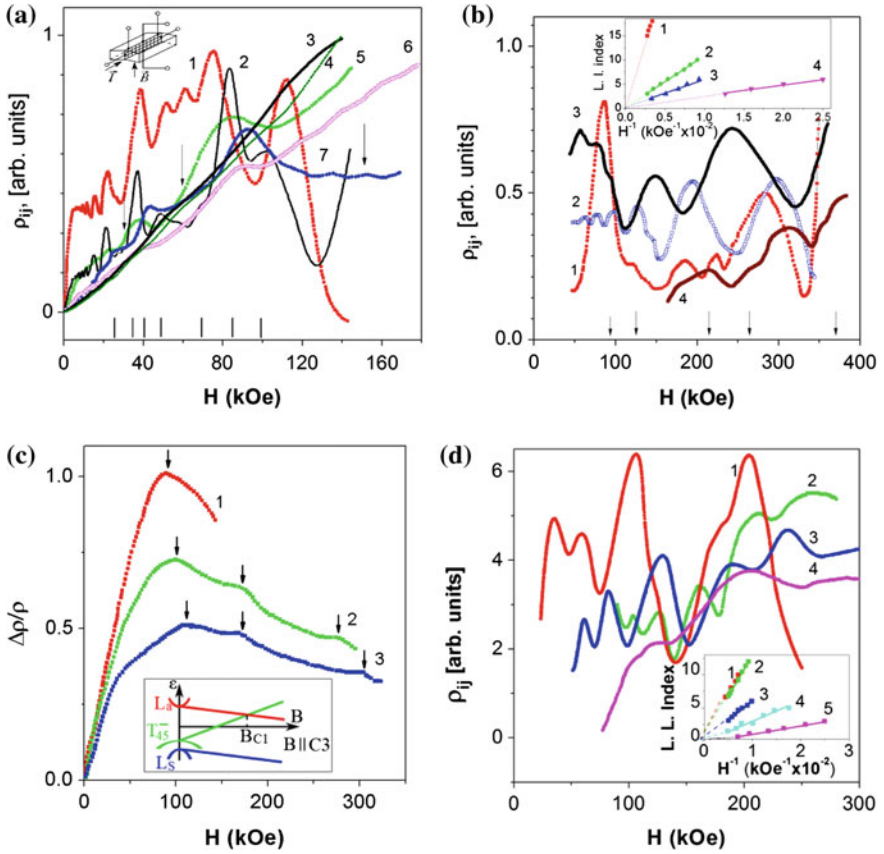


**Fig. 4** Example of the quantum oscillations of magnetoresistivity $\rho_{ii}(H_i)$ and longitudinal Hall resistivity $\rho_{ij}(H_i)$ in bicrystals of inclination (**a**) and twisting (**b**, **c**, **d**) types in Bi (**a**, **b**) and $Bi_{1-x}Sb_x$ (**c**, **d**) alloys. (**a**) 1, $\rho_{ij}(H_i{}^+)$; 2, 5, 6, $\rho_{ij}(H_i)$; 3, $\rho_{ij}(H_i{}^-)$; 4, $\rho_{ii}(H)$; 1, 3, 5, 6 T = 4.2 K; 2, 4, T = 2.1 K; 1, 3, $\theta_1 = 4°$; 2, 4, $\theta_1 = 5°$; 5, $\theta_1 = 7°$; 6, $\theta_1 = 8°$. The marks indicate the oscillation peaks in Bi single crystalline. (**b**) 1, 2, 3, $\rho_{ij}(H_i)$; 3, $\rho_{ij}(H_i)$; 1, T = 1.5 K; 2, 4, T = 4.2 K; 3, T = 1.6 K; 1, $\theta_1 = 5°$, $\theta_2 = 5.5°$; 2, $\theta_1 = 62°$, $\theta_2 = 2°$; 3, $\theta_1 = 3°$, $\theta_2 = 5°$; 4, $\theta_1 = 29°$, $\theta_2 = 11°$. The monotonic part of resistivity has been subtracted. Inset: the $H^{-1}$ position of the $\rho_{ij}(H_i)$ oscillation peaks versus their Landau level index (L.L. Index $n$); 1, 2, for the oscillation curve 4; 3, 4, for the oscillation curve 2. **c** (1) single crystal, $x = 0.08$; (2) and (3) bicrystals: (2) $x = 0.08$, $\Theta_1 = 4°$, $\Theta_2 = 2°$; (3) $x = 0.09$, $\Theta_1 = 12°$, $\Theta_2 = 2°$. Arrows indicate the magnetic fields at which the semiconductor–semimetal transition takes place. Inset: schematic view of the band movement in magnetic fields directed along the $C_3$ axis in bulk crystalline $Bi_{1-x}Sb_x$ ($0.07 < x < 0.15$). $B_{C1}$ is the value of the magnetic field in which the semiconductor–semimetal transition takes place. **d** Example of the quantum oscillations of magnetoresistivity and longitudinal Hall resistivity in LDA bicrystals of pure $Bi_{1-x}Sb_x$ ($x = 0.08$, 0.12, 0.15) and doped $Bi_{0.93}Sb_{0.07}Te$ at 4.2 K: 1, $\rho_{ii}(H)$, $x = 0.08$, $\Theta_1 = 15°$, $\Theta_2 = 3°$; 2, $\rho_{ij}(H_i)$, $x = 0.12$, $\Theta_1 = 12°$, $\Theta_2 = 2°$; 3, $\rho_{ii}(H)$, $Bi_{0.93}Sb_{0.07}Te$, $\Theta_1 = 19°$, $\Theta_2 = 2°$; 4, $\rho_{ii}(H)$, $x = 0.15$, $\Theta_1 = 15°$, $\Theta_2 = 3°$. The magnetic field is oriented along the $C_3$ axis of crystallites. Inset: L. L. index, $n$, versus $H_n^{-1}$

and CI adjacent and central layers is 0.05, 0.25, and 0.5, respectively. The density of states, $N_s$, of the CI layers of these bicrystals was also estimated from the quantum oscillations [11]. The following values for $N_s$ are obtained: $(0.2–0.3)\cdot10^{19}$ $m^{-2}$ for adjacent, and $(1.5–2.5)\cdot10^{19}$ $m^{-2}$ for central layers. These values are several orders of magnitude higher than for similarly thick films of $Bi_{1-x}Sb_x$ alloys [16].

The single crystalline $Bi_{1-x}Sb_x$ ($0.07 < x < 0.15$) alloys allow to reach the ultra-quantum limit (UQL) in lower magnetic fields compared with Bi. In the UQL, the electrons (or holes) occupy the lowest ($j = 0$) Landau level. Beyond the UQL, the band edge displacement $\Delta\varepsilon$ takes place (see inset of Fig. 4c); it depends on the ratio of spin $\Delta\varepsilon_s$ and orbital $\Delta\varepsilon_o$ level splitting: $\Delta\varepsilon = ½h\omega(1 - \Delta\varepsilon_s/\Delta\varepsilon_o)$. Consequently, the various electronic phase transitions occur in high magnetic fields, such as the semiconductor–semimetal transition, semimetal–semiconductor transition.

Figure 4c shows the field dependency of magnetoresistance $\Delta\rho/\rho$ in a single crystal and twisting SDA bicrystals of $Bi_{1-x}Sb_x$ ($0.07 < x < 0.15$) alloys. For magnetic field oriented along the CI plane, Shubnikov–de Haas oscillations are observed up to 20 kOe. In higher fields at H ~ 85 kOe, the semiconductor–semimetal transition takes place (see the maxima in Fig. 4a) [16] both in the single crystal (curve No 1) and in the SDA bicrystals (curves No 2, 3). The first maximum of $\Delta\rho/\rho$ of bicrystals is detected at the same field as for the single crystal, which means that the transition is induced in crystallites. For fields higher than 110 kOe, an additional maximum is observed in the bicrystals only. We believe that the second maximum reflects the semiconductor–semimetal transition in the adjacent layers of CI. For fields higher than 250 kOe, third maximum appears; it can be attributed to the semiconductor–semimetal transition in the central layer of the CI of the SDA bicrystals. Both of these maxima (second and third) occur at different fields for the bicrystals with different disorientation angles $\Theta_1$ and $\Theta_2$.

It is remarkable that the transitions appear at different fields; therefore, the cyclotron mass of the carriers and the ratio of spin and orbital level splitting $\Delta\varepsilon_s/\Delta\varepsilon_o$ in crystallites and in the CI should differ considerably. This implies a growth of the spin–orbit interaction at the CI and the existence of gapless electronic states at the bicrystal boundary.

### *3.3 Superconductivity and Weak Ferromagnetism at the Interface of Bicrystals of Bi and 3D Topological Insulator BiSb*

We recall that, in the normal state, bulk single crystalline Bi and 3D TI $Bi_{1-x}Sb_x$ ($0 \le x \le 0.2$) are diamagnetic and do not exhibit superconductivity above 30mK. On the other hand, pressurized samples, disordered thin films, amorphous specimens, nanowires, and other nanometer objects show superconductivity at temperatures up to (4–7) K.

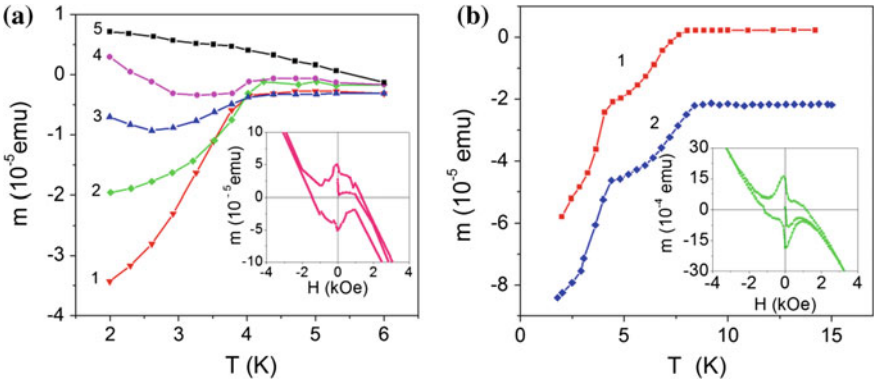


**Fig. 5** **a** Temperature dependences of a magnetic moment and magnetic hysteresis loop in Bi SDA bicrystals with $\theta_1 = 5°$ and $\theta_2 = 5.5°$; 1–50 Oe, 2–100 Oe, 3–200 Oe, 4–400 Oe, 5–800 Oe. Inset: magnetic hysteresis loop at $T = 3$ K. **b** Temperature dependences of magnetic moment and magnetic hysteresis loop in Bi LDA bicrystals. 1–$\theta_1 = 29°$, $\theta_2 = 11°$; 2–$\theta_1 = 62°$, $\theta_2 = 2°$; 1–10 Oe; 2–20 Oe. Inset: **b** magnetic hysteresis loop of Bi bicrystal with $\theta_1 = 29°$ and $\theta_2 = 11°$ at 2 K. The magnetic field is orientated along the CI plane

Using contact and non-contact signal recording methods (transport effects, magnetic moment, magnetic susceptibility, specific heat, etc.) we detect [17] two new superconducting transitions with $T_{c1} \sim (3.7–4.6)$ K and $T_{c2} \sim (8.3–21)$ K at the bicrystal interfaces of Bi and BiSb bicrystals [8], while $T_{\text{onset}}$ takes values of up to 36 K.

Figure 5 shows temperature dependences of the magnetic moment of twisting Bi bicrystals. Two superconducting phases were observed at the CI of LDA bicrystals. On the other hand in SDA bicrystals, only one superconducting phase ($T_c \sim 4.3$ K) is revealed; the superconducting parameters differ from values of LDA bicrystals. For example, in a bicrystal with $\theta_1 = 5°$ and $\theta_2 = 5.5°$, the $H_{c2}(T)$ dependence has a slope of $dH_{c2}/dT \sim 2.97$ kOe/ K, an upper critical field $H_{c2}(0) \sim 8.8$ kOe, and coherence length $\xi\,(0) \sim 19$ nm. For LDA bicrystals, these parameters are presented in [8, 9, 11] and have the following values: $dH_{c2}/dT \sim 3$ kOe/K, $H_{c2}(0) \sim 25$ kOe, $\xi\,(0) \sim 12$ nm (for the superconducting phase with $T_c \sim 8.4$ K) and $dH_{c2}/dT \sim 5.5$ kOe/ K, $H_{c2}(0) \sim 16.6$ kOe, $\xi\,(0) \sim 14$ nm (for the phase with $T_c \sim 4.3$ K). The evaluation of $H_{c2}(0)$ was carried out by using well-known WHH formula [18]:

$$H_{c2}^{\text{orb}}(0) = -0.69\, T_c (dH_{c2}/dT)_{T=T_c}. \tag{1}$$

Coherence length $\xi(0)$ in LDA and SDA superconducting phases is much smaller than the width of the CI central layer ($d_1 \sim 60$ nm); therefore, the adjacent layers do not improve conditions for correlation of the Cooper pairs in the CI central layer.

The magnetic hysteresis loop of LDA and SDA interfaces (see Fig. 5) shows the behavior for strong type-II superconductor and becomes reversible above 2.5 kOe. The magnetization curve at $T \sim 2$ K exhibits a large hysteresis, they are almost symmetrical, the remnant moment is significant at zero applied field, and the screening

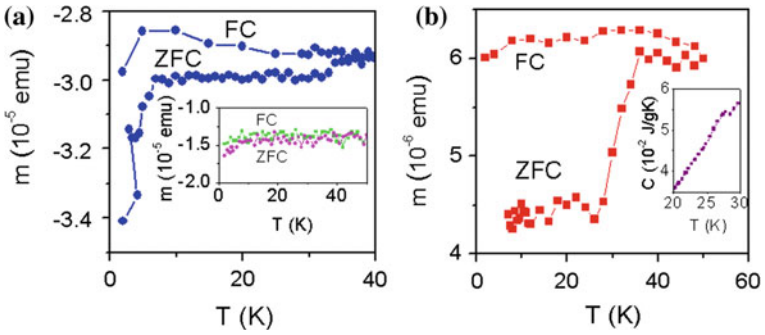


**Fig. 6** Temperature dependences of ZFC and FC curves in $Bi_{1-x}$–$Sb_x$ ($x \leq 0.2$) bicrystals: **a** $Bi_{0.94}$ $Sb_{0.06}$ Te, $\Theta_1 = 9°$, 50 Oe, ($H \perp$ CI). Inset: (H|| CI); **b** $Bi_{0.85}$ $Sb_{0.15}$, $\Theta_1 = 15°$, $\Theta_2 = 3°$, 50 Oe, ($H \perp$ CI). Inset: Temperature dependence of specific heat of $Bi_{0.85}$ $Sb_{0.15}$, $\Theta_1 = 15°$, $\Theta_2 = 3°$

effects in the interfacial plane are weak, since the interfacial thickness is less than 2λ (λ is the penetration depth).

As noted above, the interface of twisting bicrystals have a modified shape of the isoenergetic surfaces and higher carrier densities, which are beneficial for superconductivity as favor [11] electron pairing and substantially enhances $T_c$ (to more than 10.4 K).

Taking into account the CI $T_c \sim 10.4$ K and a bulk Debye energy of 10 meV for Bi, using the approximate McMillan formula [19], a coupling constant of 0.71 was extracted, which shows that the electron–phonon interaction at the CI of bicrystals is strong enough. The magnetic hysteresis loops and the current–voltage characteristics [8] of Bi interfaces clearly indicate the behavior of strong type-II superconductors with a energy gap value $2\Delta(0) \approx 3.3$ meV.

In spite of the fact, that the carriers concentration in CI of inclination type is almost an order of magnitude lower than that at the twisting CI, the highest $T_c$ is observed in the first case. For example, $T_c$ of the first superconducting phase in one of the pure Bi bicrystals of the inclination type with $\Theta = 5°$ achieves ~ 21 K (see Fig. 7, curve 2), while $T_c$ of the second superconducting phase is nearly same as in twisting bicrystals [8].

At $T < 30$ K in studied bicrystals, two kinds of $m(T)$ dependences are observed—-diamagnetic and paramagnetic. Estimations of carrier density $N_{\text{para (dia)}}$ from the Hall effect and Shubnikov–de Haas oscillations show that $N_{\text{para}}$ at the paramagnetic CIs exceeds almost 1.5–2 times $N_{\text{dia}}$ at the diamagnetic CIs; therefore, the main reason of paramagnetism is higher carrier concentration.

Figure 6a shows zero-field-cooled (ZFC) and field-cooled (FC) temperature dependences of magnetic moment of bicrystals of $Bi_{1-x} - Sb_x$ ($x \leq 0.2$) alloys, which in a magnetic field perpendicular to the CI plane ($H \perp$ CI) branch at temperature $T_b \sim 36$ K.

It should be noted that, in diamagnetic samples below $T_b$, both in the ZFC and FC dependences, an enhancement of the diamagnetic signal and the magnetic flux expul-

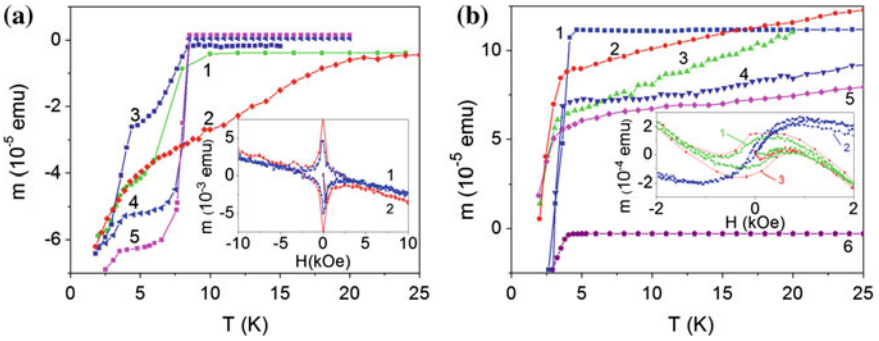


**Fig. 7** Temperature dependences of magnetic moment and magnetic hysteresis loops in bicrystals with (**a**) two or (**a**) one superconducting transitions. **a** (1) $Bi_{0.93}Sb_{0.07}Sn$, $\theta_1 = 4.6°$, $\theta_2 = 1°$, (2) Bi, $\theta = 5°$, scale for $m(T)$ 1:4, (3) $Bi_{0.85}Sb_{0.15}$, $\theta_1 = 4°$, $\theta_2 = 1°$, (4) $Bi_{0.93}Sb_{0.07}Sn$, $\theta_1 = 4°$, $\theta_2 = 1°$, scale for$m(T)$ 1:2, (5) $Bi_{0.94}Sb_{0.06}Te$, $\theta_1 = 9°$, $\theta_2 = 2°$, scale for $m(T)$ 1:2; Inset: $Bi_{0.93}Sb_{0.07}Sn$, $\theta_1 = 4.6°$, (1) 2 K, (2) 5 K; **b** (1) $Bi_{0.93}Sb_{0.07}Sn$, $\theta_1 = 75°$, $\theta_2 = 4°$, scale for $m(T)$ 1:4 (2) $Bi_{0.93}Sb_{0.07}Sn$, $\theta_1 = 68°$, $\theta_2 = 2°$, scale for $m(T)$ 1: 10, (3) $Bi_{0.85}Sb_{0.15}Te$, $\theta_1 = 19°$, $\theta_2 = 3°$, scale for $m(T)$ 20:1, (4) $Bi_{0.94}Sb_{0.06}Te$, $\theta_1 = 69°$, $\theta_2 = 2°$, (5) $Bi_{0.82}Sb_{0.18}Sn$, $\theta_1 = 18°$, $\theta_2 = 5°$, scale for $m(T)$ 300:1, (6) $Bi_{0.85}Sb_{0.15}$, $\theta_1 = 12°$, $\theta_2 = 5°$; Inset: $Bi_{0.85}Sb_{0.15}$, $\theta_1 = 12°$, $\theta_2 = 5°$, (1) 10 K, (2) 300 K, (3) 1.8 K; (**c**)

sion is observed. Detection of the well-pronounced Meissner effect shows that, at the CI of bicrystals, there is the superconducting material in an amount sufficient for affecting the magnetic moment value. In this connection, unusually high $T_c$ superconductivity of twisting interfaces surrounded by a similar non-superconducting material is an unwonted manifestation.

No sign of branching of ZFC and FC curves in the field ($H = 50$ Oe) H|| CI at $T > 9$ K could be detected.

It is known that the branching point of ZFC and FC curves in superconductors reflects the transition temperature $T_c$. Therefore, we conclude that the temperature of the superconducting transition onset in these CIs can achieve a value of 36 K, which is an extraordinary case for the group-VB semimetals and their alloys.

Typical examples of FC and ZFC curves of $Bi_{1-x}-Sb_x$ ($x \leq 0.2$) paramagnetic bicrystals in fields $H \perp$ CI are shown in Fig. 6b. An abrupt downturn of ZFC magnetic moment is observed. Moreover, the behavior of ZFC and FC curves sharply changes in a temperature range (35–28 K) and the specific heat exhibits a well-expressed jump (see Fig. 6b, inset), which indicates the second-order phase transition evidently caused by superconductivity.

Figure 7 shows the hysteresis loops and temperature dependences of magnetic moment of the bicrystals of Bi and $Bi_{1-x}Sb_x$ ($0 < x < 0.2$) alloys. At $T \leq 36$ K, the CIs exhibit one (for various samples $T_c \sim 3.7$–$4.6$ K) or two ($T_{c1} \sim 8.3$–$21$ K, $T_{c2} \sim 3.7$–$4.6$ K) superconducting transitions. In the one transition CI (Fig. 7b), the hysteresis loops are typical for weak ferromagnetic and develop against a paramagnetic background.

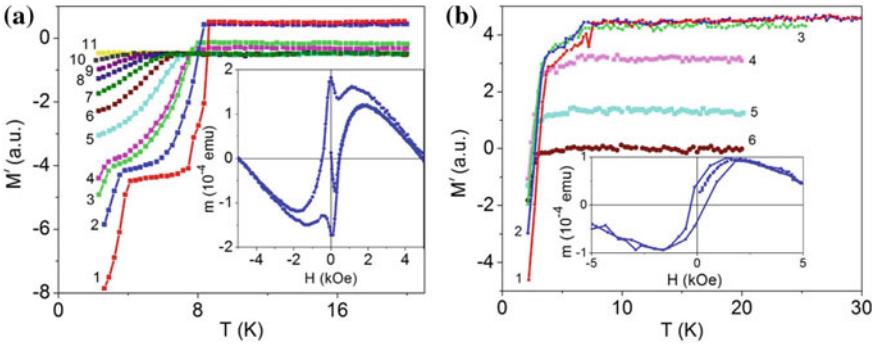


**Fig. 8** Temperature and magnetic field dependences of the real (M′) part of ac-magnetic moment and magnetic hysteresis loops in bicrystals of inclination type. **a** $Bi_{0.85}Sb_{0.15}Sn$, $\theta = 19°$; 1–0; 2–0.4 kOe; 3–1.5 kOe; 4–2 kOe; 5–4 kOe; 6–6 kOe; 7–8 kOe; 8–10 kOe; 9–12 kOe; 10–15 kOe; 11–20 kOe. Inset: magnetic hysteresis loops at 1.8 K. **b** $Bi_{0.85}Sb_{0.15}Te$, $\theta = 16°$; 1–0; 2–0.1 kOe; 3–0.2 kOe; 4–0.5 kOe; 5–1 kOe; 6–1.5 kOe. Inset: magnetic hysteresis loops at 1.9 K

In most samples with two superconducting transitions (Fig. 7a), the loops are symmetric and typical for strong type-II superconductors; however, there are also those (especially in specimens of inclination type with higher Sb content), which exhibit ferromagnetic loops (see Fig. 8a, b). Note that weak ferromagnetic loops are not registered in the CI of Bi bicrystals. Consequently, their manifestation is specific only for interfaces of $Bi_{1-x}Sb_x$ ($0 < x < 0.2$) alloys, which are 3D TI.

The temperature dependencies of resistivity $\rho(T,H)$ of SDA bicrystals of $Bi_{1-x}Sb_x$ ($x < 0.2$) alloys with two superconducting transitions are shown in Fig. 9a–d.

It was found that, for various samples, $H_{c2}^{orb}(0)$ lies (see also [10]) within the range of 24–27 kOe (the first superconducting phase with higher $T_c$) and 11–16 kOe (the second phase with lower $T_c$).

Critical paramagnetic field $H_{c2}^{p}(0)$ estimated from the relation $\mu_B H_{c2}^{p}(0) = 1.84 kT_c$ ($\mu_B$ is Bohr's magneton) takes a value of 232 kOe (first superconducting phase) and 120 kOe (second superconducting phase), which is much higher than the upper orbital critical field.

The Maki parameter $\alpha = \sqrt{2}\, H_{c2}^{orb}(0)/H_{c2}^{p}(0)$ at our CIs is very small ($\alpha \approx 0.1$–$0.14$), the spin-paramagnetic effect is negligible, and the conventional orbital upper critical field at zero temperature fully determines the magnitude of $H_{c2}(0)$.

The upper critical field anisotropy $\gamma = H_{c2}^{\parallel}(0)/H_{c2}^{\perp}(0)$ at the CIs of bicrystals of $Bi_{1-x}Sb_x$ ($x < 0.2$) alloys is weak, decreases from $\gamma \approx 1.3$–$1.5$ (near $T_c$) up to $\gamma \approx 1.0$–$1.1$ (at $T \approx 0$ K), and slightly deviates from the similar dependences of a one-band superconductor.

The Ginzburg–Landau coherence lengths $\xi$ can be estimated using the formula $\xi^2 = \phi_0/2\pi\, H_{c2}^{\perp}(0)$, where $\phi_0$ is the flux quantum. It is found that in the first superconducting phase of CIs of our bicrystals $\xi_1 \approx 11$–$12$ nm, whereas in the second phase $\xi_2 \approx 14$–$17$ nm.

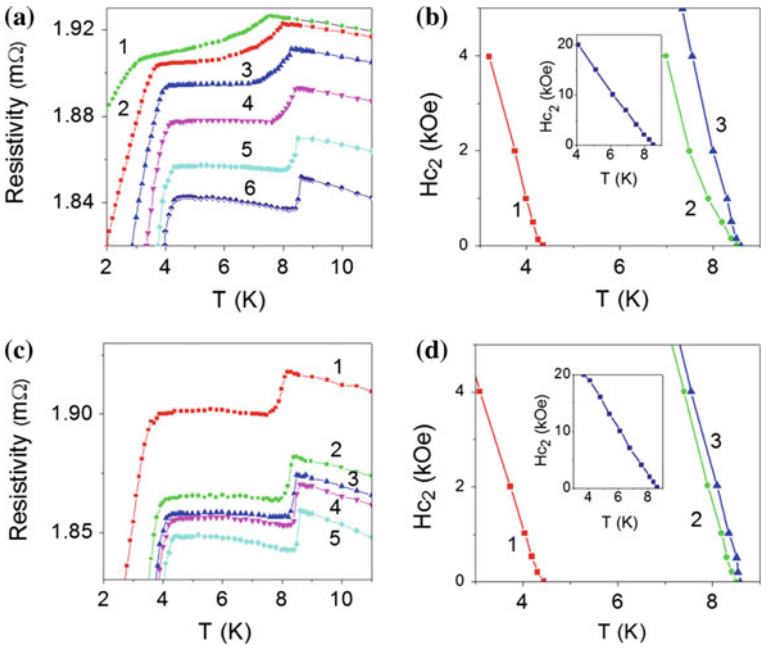


**Fig. 9** Temperature dependences of the resistivity and upper critical magnetic field $H_{c2}$ $(T)$ in bicrystal of $Bi_{0,93}Sb_{0,07}$ alloy with ~0,01 *at.*%Sn and $\theta_1 = 4.6°$, $\theta_2 = 1°$. **a**, **b** The magnetic field is perpendicular to CI plane; **c**, **d** the magnetic field is parallel to CI plane; **a** 1, 5kOe; 2, 4kOe; 3, 3kOe; 4, 2kOe; 5, 1kOe; 6, 0.5kOe; **b** 1, 3, onset, 2, midpoint; inset: transition *1*, midpoint; **c** 1, 7kOe; 2, 4 kOe; 3, 2kOe; 4, 1 kOe; 5, 0.5kOe; 1, 3, onset, 2, midpoint; inset: transition 1, midpoint

Note that the hysteresis loops of SDA bicrystals lead to lower critical field values of $H_{c1}$ ~ (100–130) Oe. The loops are roughly symmetric and exhibit nearly reversible behavior for $H$>2 kOe.

The temperature dependences of magnetic moment and upper critical fields of LDA CIs of $Bi_{1-x}Sb_x$ ($0<x<0.2$) bicrystals are given in Fig. 7 and [9, 10]. The values of $H_{c2}$ (T) and $dH_{c2}/dT$ are lower [17] than the values at interfaces with two superconducting transitions. For instance, $dH_{c2}/dT$ take a value of (0.9– 1.5) kOe/K, while $H_{c2}$ (0) ≈ 2.6–3.7 kOe. This value determines a zero-temperature coherence length $\xi \approx 30$–35 nm and a superconducting layer thickness of about 100–120 nm that is in good agreement with SEM data (see Fig. 1a).

The hysteresis loops in LDA interfaces clearly stand out against the paramagnetic background of $m(T)$ with a temperature-dependent saturation moment $m_s \approx (0.7–1.2) \times 10^{-5}$ emu/g at $H \leq \pm 2$ kOe; they exhibit ferromagnetic properties, despite diamagnetic response at $T_c < 5$ K; their width decreases with increasing temperature, and their form is also slightly modified.

Thus, some LDA and SDA interfaces of 3D TI $Bi_{1-x}$-$Sb_x$ ($x \leq 0.2$) alloys exhibit simultaneously ferromagnetism and superconductivity [10, 17]. Coexistence of magnetic and superconducting states in dimensionally limited systems has been reported

recently [20, 21]. According to [22], magnetism is due to rather confined electrons around vacancies, and the superconductivity is caused by electrons in paired state. Therefore, we assume [10] that the manifestation of magnetism at 3D TI interfaces is due to the effect of a strongly pronounced structural disorder [10]. An increase in the structural disorder leads to the breaking of electron pairs in different areas of the CIs and to the formation of a ferromagnetic underlying electronic structure, interacting with Cooper-paired electrons.

## 4 Conclusions

It has been found that the FS consisting of layer components of Bi and BiSb bicrystal CIs is similar to those of single crystalline specimens, while the shape and volume of isoenergetic surfaces vary significantly, which finally stimulate electron pair correlation.

In Bi and 3D TI $Bi_{1-x}Sb_x$ ($0 \leq x \leq 0.2$) bicrystals, two new frequencies of quantum oscillation of longitudinal Hall effect belonging to the FS of components of the CIs were found. A quantum Hall quasi-plateau in bicrystals of the inclination type was detected; it disappeared at magnetic field reversal; this finding suggests that the flow of Dirac fermions along the CI plane is sensitive to the field orientation.

At the interfaces of Bi and 3D TI $Bi_{1-x}Sb_x$ ($0 \leq x \leq 0.2$) bicrystals, two new superconducting transitions were observed, while bulk single crystals of these materials are not superconductors.

The interfaces of 3D TI $Bi_{1-x}Sb_x$ ($0 \leq x \leq 0.2$) exhibit simultaneously weak ferromagnetism and superconductivity. The CI of Bi bicrystals show only superconductivity and do not wholly satisfy the conditions of topological insulator manifestations.

## References

1. L. Fu, C.L. Kane, Topological insulators with inversion symmetry. Phys. Rev. B **76**, 045302 (2007)
2. L. Fu, C.L. Kane, E.J. Mele, Topological insulators in three dimensions. Phys. Rev. Lett. **98**, 106803 (2007)
3. J.C.Y. Teo, L. Fu, C.L. Kane, Surface states and topological invariants in three-dimensional topological insulators: application to Bi1 − xSbx. Phys. Rev. B **78**, 045426 (2008)
4. D. Hsieh, D. Qian, L. Wray, Y. Xia, Y. Hor, R.J. Cava, M.Z. Hasan, A topological insulator in a quantum Hall phase. Nature (London) **452**, 970 (2008)
5. P. Roushan, J. Seo, C.V. Parker, Y.S. Hor, D. Hsieh, D. Qian, A. Richardella, M.Z. Hasan, R.J. Cava, A. Yazdani, Topological surface states protected from backscattering by chiral spin texture. Nature **460**, 1106 (2009)
6. Q.D. Gibson, D. Gibson, L.M. Schoop, L. Muechler, L.S. Xie, M. Hirschberger, N.P. Ong, R. Car, R.J. Cava, Three-dimensional Dirac semimetals: design principles and predictions of new materials. Phys. Rev. B **91**, 205128 (2015)

7. Linder Jacob, Tanaka Yukio, Yokoyama Takehito, Sudbo Asle, Nagaosa Naoto, Interplay between superconductivity and ferromagnetism on a topological insulator. Phys. Rev. B **81**, 184525 (2010)
8. F.M. Muntyanu, A. Gilewski, K. Nenkov, J. Warchulska, A. Zaleski, Experimental magnetization evidence for two superconducting phases in Bi bicrystals with large crystallite disorientation angles. Phys. Rev. B **73**, 132507 (2006)
9. F.M. Muntyanu, A. Gilewski, K. Nenkov, A. Zaleski, V. Chistol, Superconducting crystallite interfaces with Tc up to 21 K in Bi and Bi-Sb bicrystals of inclination type. Solid State Commun. **147**, 183 (2008)
10. F.M. Muntyanu, A. Gilewski, A.J. Zaleski, V. Chistol, K. Rogacki, Coexistence of superconductivity and weak ferromagnetism at the interface of twisting bicrystals of 3D topological insulator $Bi_{1-x}Sb_x$ ($0.07 < x < 0.2$). Phys. Lett. A **381**, 2040 (2017)
11. F.M. Muntyanu, A. Gilewski, K. Nenkov, A. Zaleski, V. Chistol, Fermi-surface rearrangements in Bi bicrystals with twisting superconducting crystallite interfaces. Physical Review B **76**, 014532 (2007)
12. F.M. Muntyanu, Yu.A Dubkovetskii, S.F. Kim, G.A. Kiosse, Rotation of the fermi surface in the transition layer of bicrystals of an anisotropic metal. Phys. Solide State **39**, 1525 (1997)
13. V.S. Edel'man, Electron in bismuth. Adv. Phys. **25**, 555 (1976)
14. K. Hiruma, N. Miura, Magnetoresistance study of bi and Bi–Sb alloys in high magnetic fields. Ii. Landau levels and semimetal-semiconductor transition. J. Phys. Soc. Jpn. **52**, 2118 (1983)
15. F.M. Muntyanu, A. Gilewski, V. Nenkov, A.J. Zaleski, T. Palewski, V. Chistol, High-field peculiarities of galvanomagnetic quantum oscillations in Bi bicrystals with nano-width superconducting crystallite interfaces. Solid State Commun. **158**, 9 (2013)
16. F.M. Muntyanu, E.I. Gheorghitsa, A. Gilewski, V. Chistol, V. Bejan, V. Munteanu, On the peculiarities of Galvanomagnetic effects in high magnetic fields in twisting bicrystals of the 3D topological insulator Bi1–$x$Sb$x$($0 \leq x \leq 0.2$). Semiconductors **51**, 413 (2017)
17. F.M. Muntyanu, A. Gilewski, K. Nenkov, A.J. Zaleski, V. Chistol, Magnetic properties and superconductivity of nano-width crystallite interfaces of bicrystals and tricrystals OF $BI_{1-X}$–$Sb_x$ ($x \leq 0.2$) alloys. Phys. Status Solidi B **248**, 2903 (2011)
18. N.R. Werthamer, E. Helfand, P.C. Hohenberg, Temperature and purity dependence of the superconducting critical field, Hc2. III. Electron spin and spin-orbit effects. Phys. Rev. **147**, 295 (1966)
19. G. Grimvall, The *Electron-Phonon Interaction in Metals*, Selected Topics in Solid State Physics vol. XVI, ed. by E. Wohlfarth (North-Holland, New York, 1981)
20. L. LI, C. Richter, J. Mannhart, R.C. Ashoori, Coexistence of magnetic order and two-dimensional superconductivity at LAALO3/SRTIO3 interfaces. Nat. Phys. **7**, 762 (2011)
21. N. Pavlenko, T. Kopp, E.Y. Tsymbal, G.A. Sawatzky, J. Mannhart, Magnetism and superconductivity at LAO/STO-interfaces: the role of TI 3D interface electrons. Phys. Rev. B **85**, 020407 (2012)
22. M.G. Blamire, J.W.A. Robinson, The interface between superconductivity and magnetism: understanding and device prospects. J. Phys.: Condens. Matter **26**, 453201 (2014)

# Index


**A**
0-π transition, 43
Abrikosov vortices, 114
Aharonov-Bohm effect, 196, 199
Amplification, 187, 188, 192
Amplification point, 188
Andreev current, 91, 109
Andreev reflection, 109, 114
Antenna aperture, 149
Antenna characteristics, 121
Antenna slots, 121
Antennas, 118
Antiferromagnetic alignment, 4
(AP) alignment, 7
Array imaging system, 152, 153
Artificial atom, 175, 180, 181, 189, 190, 192
Asymmetric microcavities, 197, 218
Asymmetric microtube cavity, 216
Asymptotic range, 18

**B**
Band structure, 251
Basis conversion, 213, 216
Beam-width, 143
Bi bicrystals, 253
$Bi_{1-x}Sbx$ bicrystals, 254
Bicrystals, 250, 251, 256
Bicrystals of $Bi_{1-x}Sbx$, 260
Bismuth bicrystals, 252
Black body, 98
Bogoliubov-de Gennes equations, 8, 14, 20, 35
Boundary problem, 57, 61
Boundary transparency, 64
Boundary-value problem, 55, 56
Bragg frequency, 231
Bright temperature input, 158
Brightness temperature, 137
Brightness temperature difference, 135
Brillouin light scattering spectroscopy, 228
Brillouin spectroscopy, 233

**C**
Calibration coefficient, 139
Calibration method, 140
Calibration source, 141
Characteristic times of vortex dynamics, 209
Coherence length, 16, 23
Conversion of basis, 216
Conversion of the circular basis, 216
Cooper pair, 107, 182
Coupling constant, 188
Critical current, 40, 63, 83–85
Critical current amplitude, 88
Critical paramagnetic field, 260
Critical temperature, 12, 13, 16, 17, 20, 21, 36, 38, 98
Cross polarization pattern, 143
Cross-slot antenna, 118, 123, 126
Crystallite interface, 251
Cuprate superconductor, 73, 75, 77, 78, 87
Current density, 56
Current directions, 63
Current distribution, 65
Current responsivity, 114
Current-phase relation, 180
Cyclotron mass, 254

**D**
Data storage, 158
Decay length, 226




A. Sidorenko (ed.), *Functional Nanostructures and Metamaterials for Superconducting Spintronics*, NanoScience and Technology,
https://doi.org/10.1007/978-3-319-90481-8

Decay scales, 56
Defect mode, 233
Delocalization-to-localization transition, 204, 206
Diagonal coupling, 181
Diamagnetic response, 261
Dielectric lens, 148, 150, 151
Dielectric lens antenna, 147
Dielectric rod antenna, 142–144
Dielectric rod antenna array, 146
Diffusive limit, 7
Direct detection radiometer, 137, 152
Direct detection receiver, 138
Direct resonance, 184
Double-barrier junctions, 57
Dual-frequency receiver, 125
Dynes parameter, 109

**E**
Effects, 218
Eilenberger equations, 14
Eilenberger theory, 14
Electron coolers, 91
Electron cooling, 105, 107
Electron phonon interaction, 258
Electron temperature, 92, 99, 107
Electron-electron interaction, 102, 103
Electron-phonon relaxation, 102
Electron-phonon time constants, 104
Electronic band structure, 248
Electronic quantum transport, 247
Elementary spin valve, 10
Ellipsoidal reflector antenna, 152
$\phi$ - Josephson junctions, 50
$\phi$ -contacts, 51
$\phi$ -intervals, 62
$\phi$ -junction, 51, 52, 55
$\phi$ -shifters, 52
$\phi$ -state, 50, 58, 59, 62, 66, 67, 69
$\phi$ -structure, 59, 60, 67
Energy gap, 105, 106
Energy level, 180, 184
Energy spectrum, 180
Exchange biasing, 10
Exchange energies, 42
Exchange field, 3, 16, 74
Exchange interaction, 34
Exchange splitting, 5, 22, 32
External magnetic field, 85

**F**
Feed antenna, 149
Feed arrays, 153
Feeding waveguide, 142
Fermi distribution, 95, 104, 113
Fermi surface, 252
Ferromagnet, 58
Ferromagnetic interlayer, 83
Ferromagnetic layer, 42, 62, 75, 79
Ferromagnetic spin-valve, 87
Ferromagnetism and superconductivity, 261
FFLO state, 32
Focal spot, 148
Focus plane array imaging system, 155
Forbidden bands, 226, 229
Forbidden gap, 227
Fourier series, 58
Frequency characteristics, 118, 123
Frequency range, 142

**G**
Gamma-function, 58
Gaussian beam, 148
Gaussian beam method, 150, 152
Geometric phase, 196, 198, 199, 213, 214, 216, 218
Green's functions, 40

**H**
Harmonic amplitude, 58, 61, 67
Helical microcoil, 196, 197, 208, 210
Heterostructure, 5, 22, 35, 43, 64, 77, 80, 81

**I**
Image feeding antenna, 141
Imaging, 134
Imaging output pixels, 158
Imaging system, 129, 146, 152, 154, 157
Imaging technology, 130
Impedance, 121
Impedance matrix, 124
Induced magnetic moment, 87
Inhomogeneous twist, 205
Input antenna temperature, 140
Interaction region, 230
Interface, 39
Interface term, 59
Interlayer exchange interaction, 80
Inverse level, 176
Inverse spin valve effect, 10
Irregular magnonic waveguide, 238
Irregular waveguide, 238

**J**
Josephson circuits, 176
Josephson coupling energy, 178
Josephson $\phi$ -structures, 69
Josephson junctions, 51, 86

Josephson phase, 67
Josephson spin-valves, 40
Josephson structures, 42
Junction, 42
Junction model, 43

**K**
Kapitza resistance, 93

**L**
Landau level, 256
Landau–Zener transition, 191
Laser scribing technique, 224
Lasing, 175, 186, 190, 192
Lasing effect, 177
Layered nanostructures, 2
Linear approximation, 55

**M**
Möbius band, 200–204
Möbius ring, 195, 196, 204, 205, 211, 213, 217
Möbius ring with inhomogeneous twist, 204, 206
Möbius-ring resonator, 211, 212
Magnetic field, 77
Magnetic interlayer, 84
Magnetic metamaterials, 222, 223
Magnetic moment, 3, 6, 22, 78, 258
Magnetic strip, 238
Magnetic waveguides, 239
Magnetization distribution, 242
Magnetization vector, 42, 77
Magnetoelectronic devices, 233
Magnetostatic surface spin waves, 233
Magnetostatic wave, 229, 242
Magnon spintronics, 223
Magnonic crystal, 224
Magnonic forbidden bands, 232
Magnonic metamaterials, 221
Magnonic strips, 233
Magnonic structure, 231, 233, 235
Magnonic waveguide, 237
Magnonics, 222, 223
Matsubara frequencies, 53
Meissner effect, 259
Mesa-structure, 83, 84, 88
Metamaterials, 222
Micro- and nanoarchitectures, 196
Microstrip, 225
Microstrip antenna, 240
Microstrip lines, 121
Microtube, 207
Microwave antenna, 133
Microwave band, 132
Microwave frequency, 129
Microwave Network Analyzer, 240
Microwave transducers, 239
Microwave-frequency signals, 239
Millimeter wave band, 129, 147
Millimeter wave image, 153
Millimeter wave imaging picture, 155
Millimeter wave radiometer, 135, 139
Millimeter-wave, 141, 153
Mode approximation, 6
Mode beating length, 242
Multi-mode regime, 226
Multichroic, 118
Multichroic antenna, 117, 118, 121
Multichroic systems, 118
Multiferroic structure, 222
Multiferroic waveguide, 239
Multilayered structures, 52
Multiphoton processes, 190

**N**
Nanostructured microtubes, 196
Nanostructures, 11
Nanotube, 208, 209, 218
Narrow waveguide, 236
NIS junction, 91, 92, 96, 107
Noisy coefficient, 137
Non-Abelian, 214
Non-Abelian dynamics, 216
Non-Abelian evolution, 213, 216–218
Non-Abelian nature, 215
Non-collinear magnetizations, 5, 33, 36
Non-cyclic geometric phase, 216
Nonmonotonic dependence, 24
Normal-metal trap, 105, 112
Normalized amplitudes, 66
Numerical calculation, 62, 237
Numerical simulation, 121, 236, 242, 243
Numerical solution, 8

**O**
One-band superconductor, 260
One-mode approximation, 8
Open, 209
Open microtube, 208
Open Nb nanotube, 210
Open Nb tube, 207
Open superconductor microtube, 197
Open superconductor tube, 207
Open tubes, 197, 208, 209
Optical spin–orbit coupling, 213
Order parameter, 8
Oscillation effect, 17
Oscillatory behavior, 21, 37, 56

Oscillatory circuits, 126

**P**
Pair-breaking parameters, 9
Pairing function, 19
Pairing wave function, 5
Paramagnetic bicrystals, 259
Pattern of superconducting vortices, 206
Periodic magnonic structures, 229
Periodic waveguide, 226
Persistent current, 197, 200, 206
Phase difference, 43
Phase shift, 41
Phase shifter, 224
Phonon cooling, 107
Phonon escape, 104
Phonon temperature, 105
Phonon-electron process, 102
Photon counter, 100, 113
Planar antenna, 98
Planck blackbody formula, 133
Polarization, 119
Polarization resolution, 118
Port impedance, 121
Probability amplitudes, 191
Proximity effect, 1, 3, 4, 49, 77, 95
Pumping laser, 178
Pumping threshold, 182

**Q**
Quality factor, 177
Quantum efficiency, 100, 113
Quantum electrodynamics (QED), 176
Quantum oscillation, 249, 251, 253, 254, 256
Quantum phenomena, 176
Quantum ring, 195–197, 199, 200, 203, 205
Quantum systems, 175, 178
Quantum transport, 250
Quantum volcano, 199, 201, 202
Quantum-mechanical transparency, 10
Quasiclassical theory, 3, 19
Qubit energy, 179
Qubit level, 182
Qubit's ground state, 184
Qubits, 178

**R**
Rabi levels, 187
Rabi splitting, 184, 186
Rabi-like oscillation, 191
Rabi-split states, 189, 190
Rabi frequency, 184
Radiation characteristics, 143
Radiation detection, 131
Radiation pattern, 119, 123, 143
Radiation pattern parameters, 125
Radiation power, 131
Radiation source, 134
Radiometer, 134, 139
Radiometer array, 141, 154
Ramp-type junction, 66
Rayleigh-Jones formula, 133
Receiver, 136
Receiving system, 125
Reentrance, 9
Reentrance effect, 7
Reentrance of superconductivity, 6, 36
Reentrant superconductivity, 39
Reflection loss, 145
Regular waveguides, 229
Residual magnetization, 16
Resonance, 121
Resonance characteristic, 124
Resonance field, 80
Resonance structure, 121
Resonant field, 80
Resonant frequencies, 124
Resonator, 186
Ring-like system, 217
Rolled-up, 197
Rolled-up asymmetric microcavity, 213, 216
Rolled-up asymmetric microtube resonators, 216
Rotary spin valve, 42

**S**
S-NF-S junctions, 63
Saturation magnetization, 12
Seashell antenna, 119, 125
Second harmonic amplitude, 68
Security system, 130
Selective filters, 229
Self-assembled, 199, 200
Self-assembled micro- and nanostructures, 206
Self-sustained oscillations, 189
Serial resonance, 121
SFS structures, 52
Shapiro steps, 87, 88
Shubnikov-de Haas oscillations, 256, 258
Single atom, 178
Single atom lasing, 176, 187
Single-particle tunneling, 109
Singlet component, 19
SINIS bolometer, 92, 94, 95, 109, 114
SINIS detector, 97, 104
SINIS junctions, 51
SINIS receiver, 97
Spatial distribution, 234, 238, 242

Spatial propagation, 242
Spin polarization, 78
Spin projections, 35
Spin transport, 223
Spin valve, 1, 14, 73, 75, 82, 83
Spin wave, 221, 224, 226, 227, 235–237, 240
Spin wave energy, 243
Spin-orbit interaction, 214, 248
Spin-subbands, 5
Spin-triplet pairing, 34, 73
Spin-valve effect, 37
Spin-wave modes, 234
Spin-wave pattern, 238
Spin-wave propagation, 228
Spintronics, 2, 223, 224
State function, 18, 19
Stray field, 11, 12
Subgap current, 109
Superconducting Tc, 34
Superconducting artificial atoms, 182
Superconducting carriers, 77
Superconducting circuits, 180
Superconducting coherence length, 21
Superconducting correlation, 41, 56, 63, 82, 83
Superconducting current, 82, 83, 86
Superconducting electrodes, 86
Superconducting films, 42, 80
Superconducting material, 39
Superconducting order parameter, 14
Superconducting phase, 257, 258, 260
Superconducting resonators, 180
Superconducting spin valve, 6, 20, 22, 24, 33
Superconducting spin valve effect, 11
Superconducting spintronics, 1, 24, 33, 44
Superconducting state, 80
Superconducting transition, 37, 259–261
Superconductive electronics, 51
Superconductivity, 2, 53, 54, 57, 247, 249, 256, 259
Superconductivity and ferromagnetism, 32
Superconductor, 75, 81
Superconductor micro-, 218
Superconductor-ferromagnet, 43
Superconductor-ferromagnet hybrids, 23
Superconductor-manganite ferromagnet, 74
Supercurrent, 41, 53, 60, 61, 63, 68
Supercurrent density, 63
Supercurrent transfer, 63
Suppression parameter, 60
Suspended absorber, 95, 100
Suspended bolometer, 113
Suspended bridge, 93, 96
System spatial resolution, 158
System temperature sensitivity, 158

**T**
Taper waveguide, 235
Temperature sensitivity, 153
Terahertz radiation, 97
Topological defect, 206, 207
Topological effects, 195
Topological insulator, 248
Topological phase shift, 203
Topological quantum states, 248
Topology-driven, 218
Topology-driven effects, 200
Total current, 56
Total supercurrent, 68
Transfer matrix, 233
Transition frequencies, 186
Transition temperature, 3, 23
Transmission amplitude, 186
Transmission characteristic, 231
Transmission coefficient, 235
Transmission matrix, 231
Transmission matrix method, 230
Transmission response, 240
Transparency, 39
Transparency coefficient, 16
Transversal mode, 242
Triplet component, 19, 20, 35, 38
Triplet correlations, 77
Triplet effect, 39
Triplet pairing, 32, 35, 36
Triplet pairing effect, 15
Triplet superconducting correlations, 74
Triplet superconductivity, 41
Tunnel junction, 111, 178
Twisted fields, 205
Twisted space, 205
Twisting Bi bicrystals, 257
Twisting bicrystals, 254, 258
Two level system, 186
Two-dimensional superconductor, 254
Two-level quantum system, 184

**U**
Upper critical field, 260
Usadel equations, 7, 16, 53
Usadel Green's functions, 54
Usadel theory, 33

**V**
Vortex dynamics, 208–210
Vortex matter, 207
Vortex pattern, 210

**W**
Waveguide, 121, 224, 225, 230, 234, 235

Waveguide resonator, 183
Waveguide-to-microstrip, 138
Wavenumber, 237, 242
Weak coupling, 231

**Z**
Zero-current, 66
π-junction, 41